Université de Paris-Sud

U. F. R. Scientifque d'Orsay

Thèse

présentée par
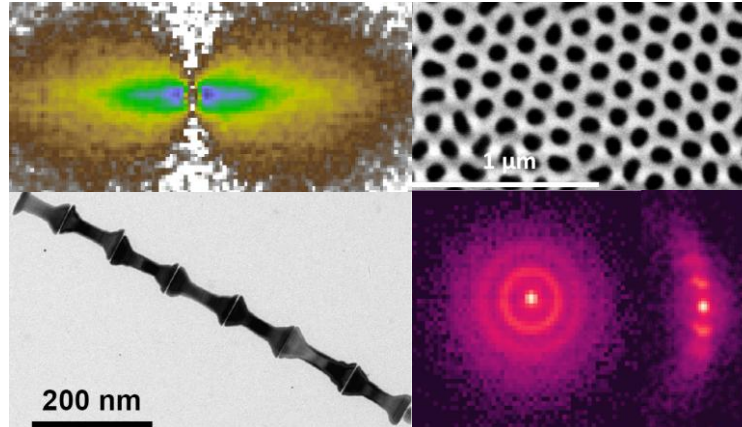
Thomas MAURER

Pour obtenir le titre de

Docteur de l'Université Paris XI Orsay

Spécialité : **Physique des Solides**

Magnetism of anisotropic nano-objects : Magnetic and neutron studies of Co$_{1-x}$Ni$_x$ nanowires

Soutenue le 10 novembre 2009

Composition du jury :

G. Chaboussant (Directeur de thèse)
V. Dupuis (Rapporteur)
O. Fruchart (Rapporteur)
F. Ott (Directeur de thèse)
L. Piraux
A. Thiaville (Président)
G. Viau

Magnetism of anisotropic nano-objects: Magnetic and neutron studies of $Co_{1-x}Ni_x$ nanowires

Thomas Maurer

Laboratoire Léon Brillouin UMR12 CEA/CNRS
Centre d'Etudes de Saclay F-91191 Gif sur Yvette, FRANCE
Version 1.0

April 6, 2010

ii

Remerciements

La thèse est une très bonne formation qui repose sur la transmission des connaissances et des méthodes de travail et qui donne aussi l'occasion d'initiatives et le temps de l'approfondissement. Ces trois années de thèse se sont révélées d'autant plus riches, tant scientifiquement qu'humainement, que j'ai eu la chance de faire de nombreuses rencontres.

Je remercie le CNRS et le CEA pour avoir cofinancé cette thèse au Laboratoire Léon Brillouin (LLB). Je remercie aussi toute l'équipe administrative du LLB pour m'avoir accueilli pendant ces trois années. En premier lieu, je tiens à remercier Philippe Mangin qui a été le directeur du LLB durant une grande partie de ma thèse. Je le remercie pour m'avoir introduit auprès de mes directeurs de thèse mais aussi pour ses conseils et la clarté pédagogique de ses cours lorsque j'étais étudiant à Nancy. Je remercie également Christiane Alba-Simionesco, actuelle directrice du LLB, qui m'a permis de terminer ma thèse dans les meilleures conditions possibles. Je remercie Suzanna Gota-Goldman, directrice adjointe du LLB, pour sa disponibilité et l'intérêt qu'elle a porté à mon travail. Je remercie Alain Ménelle qui grâce à ses nombreuses anecdotes m'a fait découvrir l'histoire du laboratoire et le monde des commissions. Je remercie Bernard Mailleret pour son aide précieuse et sa bonne humeur communicative. Je remercie aussi les secrétaires du laboratoire, Chantal Marais, Claude Rousse, Anne Mostefaoui, Chantal Pommeau et Catherine Doira pour avoir toujours pris le temps de m'accompagner dans les diverses démarches administratives.

Je tiens également à remercier les membres du jury qui ont pris le temps d'évaluer mon travail. Je remercie, en particulier, Véronique Dupuis et Olivier Fruchart, les rapporteurs de mon manuscrit, qui grâce à leurs commentaires détaillés m'ont permis d'améliorer ce travail et de réfléchir à de nouvelles pistes d'investigation. Je remercie André Thiaville pour avoir présidé le jury de thèse. Je remercie également Luc Piraux pour avoir accepté de juger ce travail et s'être déplacé depuis Louvain-la-Neuve. Je remercie enfin Guillaume Viau, membre du jury, sans qui ce sujet de thèse n'aurait pu naître puisqu'il est l'un des "créateurs" des objets étudiés. Il m'a, entre autres, initié à la synthèse organométallique et donné le goût pour les collaborations interdisciplinaires.

Mes plus sincères remerciements et ma plus profonde reconnaissance vont évidemment à mes directeurs de thèse, Grégory Chaboussant et Frédéric Ott qui m'ont formé tout au long de ces trois années. Cela a été une grande chance d'être encadré par deux jeunes chercheurs dynamiques, toujours disponibles et aux profils très complémentaires. Le sujet qu'ils ont proposé était suffisamment original pour que différentes difficultés expérimentales puissent surgir. J'ai alors eu la chance d'avoir une grande liberté d'initiative pour résoudre ces difficultés et de pouvoir faire évoluer le sujet au fur et à mesure des résultats. Néanmoins, au fur et à mesure que de nouvelles perspectives d'investigation surgissaient, Frédéric et Grégory ont su m'accompagner pour hiérarchiser les priorités et aller au fond

iii

des choses- ce qui n'a peut-être pas été toujours ma qualité première. Mais c'est ce qui m'a le plus motivé dans la fonction de jeune chercheur, savoir d'où l'on part mais ne jamais se douter de ce que l'on va découvrir. Je les remercie aussi d'avoir accepté que j'écrive ma thèse en anglais malgré le surplus de corrections syntaxiques et orthographiques. Je sais désormais qu'il est possible, et souhaitable, de faire des phrases sans utiliser des "some" constamment. Je crois, au final, que si cette thèse s'est révélée très enrichissante, tant scientifiquement qu'humainement, c'est avant tout grâce à Grégory et Frédéric pour qui j'ai une profonde estime.

Je remercie chaleureusement Sébastien Gautrot, technicien associé au spectromètre Papyrus et à mon projet de thèse. Il s'est montré très présent et très patient pour me former en cryogénie et m'aider à lancer les manips. Je remercie aussi Fatih Zighem qui est arrivé en post-doctorat dans l'équipe lors de ma dernière année de thèse. Son aide a été très précieuse lors de mes derniers mois de thèse, au moment où le temps commence à manquer et je lui en suis très reconnaissant. Je remercie aussi Vincent Klosek, originaire de Nancy lui aussi, et avec qui j'ai partagé de bons moments. Je regrette juste qu'il ait réussi à trouver de bonnes excuses pour ne venir ni à mon pot de thèse ni à mon pot de départ. Je remercie enfin Jacques Darpentigny pour sa gentillesse. Grâce à la bonne ambiance qui régnait dans l'équipe, c'est avec bonheur que je venais au laboratoire les matins et je ne garde que de bons souvenirs de mon passage dans l'équipe.

Je remercie aussi nos collaborateurs à ce projet dans le cadre de l'ANR MAGAFIL. En particulier, je remercie Jean-Yves Piquemal, Yaghoub Soumaré et Frédéric Herbst du laboratoire ITODYS (Paris 7) qui m'ont fourni plusieurs dizaines voire centaines de grammes de nanofils durant ma thèse et ont réalisé différentes études structurales. Cette collaboration a été très enrichissante et m'a donné un nouveau goût pour la chimie. Je garde un excellent souvenir de mes passages à l'ITODYS. Je remercie aussi Frédéric Schoenstein et Nourredine Jouini pour leur contribution lors de mes derniers mois de thèse. Je souhaite aussi exprimer ma reconnaissance à Jean-Baptiste Moussy (SPCSI, CEA Saclay), Michel Viret et Pierre Bonville (SPEC, CEA Saclay) qui m'ont beaucoup épaulé dans les mesures de magnétométrie et ont toujours pris le temps de répondre à mes questions et de s'intéresser à mes résultats.

Le LLB, parfois menacé ces dernières années, est un lieu privilégié pour faire une thèse puisqu'il réunit des compétences très variées autour de la diffusion neutronique. Ainsi, pour un sujet à l'interface de plusieurs disciplines tel que le mien, j'ai pu bénéficier de l'expertise de plusieurs membres du laboratoire. Je remercie d'abord François Boué, Fabrice Cousin, Jacques Jestin et Annie Brûlet qui se sont intéréssés à mon sujet et m'ont apporté leur expertise dans la fabrication de nanocomposites à base de polymère pour fabriquer mes échantillons. Je remercie Gilles André pour son aide lors des expériences de diffraction de neutrons. Je remercie aussi Daniel Petitgrand pour son aide lors des expérience de diffusion inélastique de neutrons et Alain Lapp pour m'avoir assisté lors de certaines expériences sur le spectromètre PAXY. Je remercie aussi l'ensemble des personnels du LLB pour s'être intéressé à mon travail à différents moments de ma thèse et pour la bonne ambiance qui règne dans le laboratoire. J'en profite pour remercier particulièrement les techniciens du laboratoire qui sont toujours montrés disponibles pour régler les différents problèmes qui surgissent de manière inopinée. Je remercie enfin l'ensemble des thésards et post-doctorants du LLB que j'ai rencontrés durant ma thèse. Parmi eux, je remercie particulièrement Nicolas Jouault qui m'a initié à la calorimétrie différentielle et

vi

Résumé

Le domaine du nanomagnétisme est actuellement en plein essor du fait de l'amélioration des techniques de synthèse et d'investigation. Diverses études ont été menées sur des systèmes 0D et 2D tels que les agrégats et couches minces magnétiques. Les techniques de synthèse actuelles permettent en effet de bien contrôler les dimensions et la texture de tels systèmes, ce qui permet de maîtriser les différents paramètres qui influent sur leurs propriétés magnétiques. Cependant, depuis quelques années, les objets 1D tels que les nanofils commencent à susciter un intérêt croissant dans la communauté du nanomagnétisme. De tels objets tirent bénéfice de leur anisotropie et présenter des propriétés magnétiques originales. S'il est actuellement toujours difficile, contrairement aux agrégats et films minces, d'obtenir des nanofils présentant une taille critique inférieure à $5\,nm$, les progrès des techniques de synthèse fournissent aujourd'hui des nanofils dont le diamètre peut varier d'une dizaine à plusieurs centaines de nanomètres et qui peuvent être ordonnés ou non. C'est dans ce contexte d'intérêt croissant pour les objets magnétiques anisotropes que s'inscrit cette thèse. Les motivations de ce travail ont été doubles, à la fois fondamentales et instrumentales. Elles ont consisté en:

1. Caractériser les propriétés magnétiques de nanofils de $Co_{1-x}Ni_x$ synthétisés par un procédé purement chimique, le procédé polyol développé par nos collègues Yaghoub Soumare et Jean-Yves Piquemal du laboratoire Interfaces, Traitements, Organisation et Dynamique des Systèmes (ITODYS, Université Paris-Diderot) et Guillaume Viau du Laboratoire de Physique et Chimie des Nano-Objets (LPCNO, INSA Toulouse). Ce procédé, purement chimique, présente l'avantage de fournir des objets d'un diamètre de l'ordre de $10\,nm$ et d'excellente qualité cristalline.

2. Développer la technique de Diffusion de Neutrons Polarisés aux Petits Angles pour sonder le magnétisme d'objets anisotropes. Si cette technique est bien adaptée à l'étude de nano-objets magnétiques, elle est presque exclusivement utilisée pour l'étude d'objets isotropes. L'anisotropie des nanofils augmente en effet la complexité d'utilisation de cette technique puisque l'orientation relative des objets devient un paramètre crucial.

Dans la partie I, nous nous sommes attachés à caractériser les propriétés magnétiques des nanofils synthétisés par le procédé polyol afin de mettre en lumière les perspectives d'utilisation de ce procédé. Dans le chapitre 2, le procédé polyol est d'abord décrit en détail ainsi que les objets que l'on peut obtenir. Ce procédé offre un large éventail de formes et de dimensions des objets synthétisés et leur confère une très bonne qualité cristalline. Les nanofils ainsi synthétisés ont donc des anisotropies de forme et magnétocristalline élevées et présentent des coercivités très élevées.

Le chapitre 3 illustre les propriétés magnétiques de ces objets en fonction de leur alignement. L'alignement des nanofils est un paramètre clef qui demande un intérêt particulier. Plusieurs méthodes ont été utilisées pour aligner les nanofils dans une matrice hôte, qu'elle soit solide ou liquide. Malheureusement, il subsiste toujours des difficultés à produire de tels échantillons, solides à température ambiante.

Dans le chapitre 4, nous avons essayé d'illustrer le rôle de la forme des objets ainsi que du rapport d'aspect dans le renversement de l'aimantation. De tels objets, d'un diamètre d'environ $10\,nm$, présentent un mode cohérent de renversement de l'aimantation. Cependant, la forme des extrêmités des fils, par exemple, peut conduire à la formation de vortex au moment du renversement de l'aimantation. Le rôle du nickel est donc important

non seulement du fait de la modification des propriétés magnétiques intrinsèques (M_S, T_C,...) mais aussi de la modification de la forme des objets.

Un autre enjeu dans la préparation de matériaux composites à base de ces nanofils est de réduire autant que possible leur oxydation. Leur manipulation au contact de l'air conduit à la formation d'une couche d'oxyde de cobalt à leur surface. Le chapitre 5 étudie l'influence du couplage entre le coeur ferromagnétique et la coquille d'oxyde antiferromagnétique de ces nanofils. Deux résultats importants ont été mis en évidence. Une étude par diffraction de neutrons a d'abord montré que la température de Néel de la coquille d'oxyde de cobalt est environ de $230\,\mathrm{K}$ soit à peu près $60\,\mathrm{K}$ de moins que sa valeur pour le matériau massif. D'autre part, si ce couplage ferromagnétique/antiferromagnétique donne naissance au phénomène attendu d'Exchange Bias en dessous de $T \sim 130\,\mathrm{K}$, il est aussi à l'origine d'une chute de coercivité de 30 à 50% de la coercivité entre la température de Néel ($\sim 230\,\mathrm{K}$) et la température d'Exchange Bias ($\sim 130\,\mathrm{K}$). Ce résultat expérimental, non reporté jusqu'à présent, met en évidence le rôle déterminant des fluctuations superparamagnétiques des grains antiferromagnétiques d'oxyde de cobalt dans le retournement de l'aimantation des nanofils et la mise en place du phénomène d'Exchange Bias.

Finalement, à partir des mesures magnétiques sur ces nanofils, alignés ou désordonnées, oxydés ou non, le chapitre 6 donne les perspectives d'utilisation de ces objets comme constituants de base d'aimants permanents. Des mesures magnétiques à haute température indiquent notamment que ces nanofils, grâce à leur anisotropie de forme, conservent une bonne partie de leurs propriétés magnétiques jusqu'à 250°C. Des aimants permanents fabriqués à partir de ces nanofils semblent pouvoir raisonnablement trouver une place au sein des grandes familles d'aimants permanents (ferrites, aimants à base de terre-rare,...).

La partie II s'attache quant à elle à mettre en évidence l'utilisation de la Diffusion de Neutrons Polarisés aux Petits Angles pour l'étude de nanofils magnétiques. Le chapitre 7 rappelle le formalisme associé à cette technique et l'applique à la géométrie cylindrique des nanofils. Il met en évidence le rôle déterminant de l'orientation relative des objets et donc de la distribution associée.

Le chapitre 8 illustre l'utilisation de cette technique pour l'étude des nanofils synthétisés par le procédé polyol. Il met en évidence la formation de larges agrégats (taille caractéristique supérieure à $180\,\mathrm{nm}$) dans le solvant, ce qui ne permet pas d'accéder aux propriétés magnétiques d'objets isolés.

Dans ce contexte, nous avons ouvert une collaboration avec Laurent Cagnon de l'Institut Néel à Grenoble afin d'étudier par Diffusion de Neutrons aux Petits Angles (DNPA) des nanofils de cobalt inclus dans des matrices d'alumine poreuse. Ces échantillons présentent l'avantage de fournir des nanofils isolés, bien ordonnés et parfaitement alignés. Leur étude par Diffusion de Neutrons Polarisés aux Petits Angles s'est révélée fructueuse puisqu'elle a permis d'obtenir la dépendance en Q du facteur de forme magnétique de ces objets. Cette étude ouvre la voie à une cartographie à l'échelle du nanomètre de l'aimantation dans ce type de nano-objets par DNPA.

Contents

II Small Angle Neutron Scattering (SANS) on magnetic nanowires 127

Preamble

One of the major breakthroughs in solid state physics in the past thirty years has been the miniaturization of materials down to the nanometer scale. The progress which have been made for the last decades have been so tremendous that the expression of "technological revolution" is often employed to qualify the field of nanotechnology. If the term "nano" has triggered hopes and fears at the same time, there is still some issuess around the impact of nanoparticles and their possible applications.

It is generally admitted that the term "nano" refers to materials whose at least one dimension is of the order of the nanometer. However, this definition seems trivial if one considers some natural nanoparticles such as the ones rejected by the volcanic eruptions and which do not present any specific properties. Precisely, a nano-object is so-called when its properties differ from the bulk ones. The size reduction indeed makes appear a threshold below which the physical and chemical properties of the nanomaterial vary from the bulk ones. The modification of the material properties in fact stems from the drastic increase of the ratio between the surface and the volume of the material. The size threshold of course depends on both the nature of the material and of the investigated properties. Moreover these properties become size-dependent in the nanoscale.

Furthermore the modification of properties as different as optical, mechanical, magnetic or thermal ones provides a large variety of possible applications: TiO_2 nanoparticles are added to solar cream to protect the skin from UV radiations, $CdSe$ particles whose size is in the $1 - 100$ nm range are used in the fabrication of laser diodes thanks to their size-depend fluorescent spectrum, the introduction of silica nanoparticles allows to reduce the rolling resistance of commercialized tyres,... The nanosciences are therefore one of the only fundamental research field which both requires and allows a close collaboration between chemists, physicists and even biologists. For instance in the Joint European Magnetic Symposia which took place in september 2008, Professor Quentin Pankhurst presented some research project about medical therapies via magnetic nanoparticles implying a cooperation between physicists, engineers, chemists and medics in the Royal Institution of Great Britain. It has for instance led to the development of a hand-held scanner that helps cancer surgeons determine the progression of cancer in a patient or a method for targeting magnetic nanoparticles to cancer cells in the liver so that they can be locally heated to help destroy cancer cells.

That is why in parallel with the progress of the techniques of characterization, lots of efforts have been made to set up new strategies of synthesis of these novel materials. Two approaches have been developed to synthesize nano-objects: the top-down and the bottom-up ones. The top-down approach consists in taking and etching a massive material down to the desired shape and size. The processes associated to it take advantage of their high reproductibility and find some immediate applications in the industry. After many improvements, this approach nowadays allows to produce structures as small as 20 nm in size. In order to go below this threshold, some synthesis routes based on the *bottom-up* approach have been developped for about fifteen years. The idea consists in assembling atoms to fabricate nano-objects. For the moment, large-scale applications are still limited with this approach. Nevertheless the great advantage of this approach is to provide nano-objects smaller than 20 nm and even 10 nm.

These two synthesis approaches are also used in the field of nanomagnetism to build-up nanostructures with specific magnetic properties. In the zoology of magnetic nano-objects, one often distinguishes thin films which exhibit a finite thickness from nanoparticles which

present at least two finite dimensions. It must be underlined that most studies have been performed on thin films since the progress in their synthesis allows nowadays to deposit layers of monoatomic thickness onto a substrate but also to control their roughness and their homogeneity. As for magnetic nanoparticles, it is still not possible to reduce the dimensions down to 1 nm. It implies that some effects observed in magnetic thin films such as the reduction of the Curie temperature T_C are not met in the case of magnetic nanoparticles. However some synthesis techniques such as for example *Mass Selected Low Energy Cluster Beam Deposition [Ala2004]* provide magnetic nano-objects of few nanometers such as 3 nm Co clusters. This corresponds to a limit which takes for granted the uniformity of the magnetization inside the particles made with usual magnetic materials such as Fe, Ni or Co. Contrary to magnetic thin films, the complex geometry of magnetic nanoparticles makes harder the analysis of the experimental results [Fru2007]. That is why it appears more convenient to work with monodomain and isotropic systems such as magnetic nanoclusters for which the demagnetizing field is uniform. Moreover, it is easier to synthesize monodisperse spherical magnetic nanostructures so that until now most studies have been performed on magnetic nanospheres.

The aim of my thesis was thus to investigate the magnetic properties of anisotropic nano-objects and in particular nanowires. The one-dimensional geometry of nanowires attracts more and more interest, partly because contrary to isotropic systems, the magnetic properties of nanowires will be essentially governed by their large shape anisotropy. This will confer them three advantages. First, a large shape anisotropy enhances the coercivity. Secondly, this contribution to the anisotropy is almost temperature independent which may lead to potential high-temperature application. Finally, this anisotropy prevents them from being superparamagnetic or at least decreases their blocking temperature.

The geometrical dimensions of magnetic anisotropic objects therefore plays a key role in their magnetic properties. Indeed the value of the shape anisotropy depends on the dimensions of the nanowires. When the nanowires are virtually infinitely long, the contribution of the shape anisotropy to the coercivity is $M_S/2$. It implies that for magnetic materials exhibiting high M_S such as Fe or Co, some very large coercivities may be expected. Moreover, the diameter of the nanowires also comes into play by determining the reversal mode of the magnetization. Depending on the nature of the material, there exists a threshold below which the magnetization reversal is coherent. Furthermore, the distance between neighbouring nanowires could play a critical role by triggering magnetic dipolar coupling between them.

Many questions thus arise: what is the role of the aspect ratio- defined by the ratio between the diameter and the length of the nanowires- in the magnetization configuration and reversal? How do the shape and magnetocrystalline anisotropies come into competition? What are the effects of the crystalline quality of the objects? How do the objects interact with each other via the dipolar interaction?

In most previous studies, the investigated magnetic nanowires have been electrodeposited in porous alumina membranes. The advantage of such a synthesis route is the high order and alignment of the objects. When the distance between neighbouring nanowires is large enough, the magnetic interaction between them can be neglected. However the crystalline quality of electrodeposited nanowires is often far from perfection which leads to magnetic inhomogeneities. In such case, the magnetization reversal becomes localized and no longer uniform. The motivation of this study has thus been to characterize the

magnetic properties of very well crystallized nanowires so that the magnetization can be considered as uniform inside the objects. This study therefore aims to probe the role of the nanowire dimensions on their magnetic properties and to give an answer to the above questions. This manuscript first begins with the introductive Chapter 1 which gives an overview on the magnetism of nano-objects.

Part I focuses on the magnetic properties of monocrystalline magnetic nanowires depending on their geometrical dimensions. This study has been led in collaboration with Yaghoub Soumare and Jean-Yves Piquemal from the ITODYS laboratory (Interfaces, Traitements, Organisation et Dynamique des Systèmes) at the Paris-Diderot university and with Guillaume Viau from the LPCNO (Laboratoire de Physique et Chimie des Nano-Objects) at the INSA Toulouse which contributed to the development of the polyol process during the last years. The polyol process is a pure chemical process which provides several grammes of $CoNi$ monocrystalline anisotropic nano-objects exhibiting very few stacking faults. Chapter 2 presents the polyol process and the magnetic nanowires synthesized via this route. In Chapter 3, I show the magnetic properties of different anisotropic nano-objects synthesized via this process and shows that magnetization reversal modes close to the coherent rotation model are expected. It implies that some large coercivities- close to the ones predicted by the Stoner-Wohlfarth model- are expected for such nano-objects. Micromagnetic simulations are presented in Chapter 4 to compare the experimental results to the predicted ones and to probe the role of the detailed shape of the anisotropic objects. It notably gives some answers to the role of both the aspect ratios and the shape of the tips of nanowires to the magnetic properties. Chapter 5 underlines how the oxidation of the investigated nanowires affects their hysteresis cycles because of the Exchange Bias phenomenon. This chapter shows how the superparamagnetic fluctuations of the antiferromagnetic CoO grains of the oxide affect the magnetization reversal of these objects. Finally, in Chapter 6, I discuss how such nanowires, taking advantage of both their large shape and magnetocrystalline anisotropy, could lie at the root of many applications and especially in the field of permanent magnets.

In Part II, I present the use of Polarized Small Angle Neutron Scattering to probe the magnetic properties of nanowires. Magnetic nanowires have already been investigated via different experimental techniques, principally magnetometry or ferromagnetic resonance. However, very few studies have been performed on magnetic nanowires via Polarized Small Angle Neutron Scattering which is well adapted to magnetic nanostuctures. Neutrons indeed carry a magnetic moment (spin) and consequently interact with the magnetic moments of the atoms. This property of neutrons lies at the root of their success in magnetism. Nevertheless, if many Polarized Small Angle Neutron Scattering studies have already been performed with success on magnetic nanospheres, nearly nothing has been done on objects presenting a more complex shape and consequently a shape anisotropy giving rise to dipolar interaction between the objects. The difficulty here is the fabrication of the samples. The strategy has been to elaborate a sample whose nano-objects are monodisperse, chemically identical, oriented in the same direction, well separated from each other to prevent them from interacting. Indeed, such a sample allows to get information about n identical objects without any average on their size or their orientation. Chapter 7 first presents the Polarized Small Angle Neutron Scattering technique and its related formalism. In Chapter 8, I present the results for the nanowires synthesized via the polyol process. However if the polyol process has many advantages,

it is still hard to fabricate some samples with separated and oriented nanowires. This is why a complementary Polarized Small Angle Neutron Scattering study, exposed in Chapter 9 has been performed on nanowires inserted in a porous alumina membrane. These samples have been synthesized by Laurent Cagnon fom the Institut Néel in Grenoble. In the long-term, such nanowires could be, for example, some constituents of the race track memories. Of course, one major challenge is to control the interaction between the objects. A Polarized Small Angle Neutron Scattering study on such arrays of nanowires should allow to characterize these interactions.

Chapter 1

Magnetism of nano-objects

During the last 20 years, the field of nanomagnetism has exploded and a huge number of new magnetic structures have appeared in which the nanometer scale plays a key role. Depending on the geometry, the size or the nature of the structures, different magnetic behaviors may be observed. This chapter aims at exposing the synthesis processes, magnetic properties and experimental tools to probe magnetism of nano-structures.

1.1 Magnetism going down to nano

Magnetism has always been fascinating since it lies at the root of interactions between objects which can be distant from each other. This phenomenon was observed in nature when iron dust was attracted by magnetizing stones such as magnetites. The first break-through in the understanding of magnetism was realized in the 19$^{\text{th}}$ century thanks to the Oersted's experiment [Ber1974, Coe2009]. Oersted showed in 1820 that an electric current injected in a compass needle can make it rotate. This experience was followed by Ampere's one in 1822 which proved that a coil can behave as a magnet when a current runs through it. These experiments were of the highest importance since they both showed for the first time that there was a direct link between electricity and magnetism. These experiments had then be supplemented by the discovery of the magnetic induction by Faraday in 1831 [Ber1974, Coe2009]. This major discovery led to the first mathematical formulation of the electromagnetic model by Maxwell in 1864.

At that time, magnetism was believed to be well understood. However some contradictions about magnetism were pointed out. If, as stated by Ampere, magnetism only comes from electric currents induced in materials, a 10 cm long iron magnetized bar whose magnetization is $1.7\,\text{MA.m}^{-1}$ should be run through by a current of 170000 A [Coe2009]. So why does this bar not melt? This is how at the beginning of the 20$^{\text{th}}$ century, physicists focused much more on the structure of matter. Lots of progress arose from Quantum Mechanics which allowed to understand magnetism far deeper. Goudsmit and Uhlenbeck demonstrated in 1925 [Gou1926, Uhl1925] that the electron carries an intrinsic quantum mechanical angular moment named *spin* which contributes, together with the orbital angular moment, to the magnetic moment of the atom. The next step came from Heisenberg [Hei1926] and Dirac [Dir1926] who independently understood in 1926 that the interaction between two spins was given by $H = -J\,\vec{S_1}.\vec{S_2}$ where H is the hamiltonian describing the interaction, J the exchange coupling constant and $\vec{S_1}$ and $\vec{S_2}$, the two interacting spins.

   Magnetism seemed to be finally understood in principle at the end of the first half
of the last century. The remaining difficulty consisted in solving the mathematical equa-
tions and therefore in predicting the magnetic behaviors of materials [Coe2009].   The
development of approximated models and micromagnetic simulations allowed to predict
quantitatively magnetic behaviors of many systems. Nevertheless, lots of questions have
kept the scientific community active in this research field.

   For instance, technological progresses have permitted a reduction of system dimensions
so that quantum effects may be observed. In fact, a non-negligible part of both theoretical
and technological breakthroughs came from the miniaturization of materials. To summa-
rize, when magnetism goes down to nano, quantum effects become visible and unexpected
magnetic behaviors can be discovered. As a matter of fact, these novel nanoscaled ma-
terials exhibit a characteristic size which is of the same order as the interaction lengths
[Blü2005]. For instance, new phenomena have appeared in confined systems (2D: thin
films, 1D: nanowires, 0D: nanoclusters) or at the interfaces of magnetic and non-magnetic
layered materials. Concerning confined systems, the reduction of one or several spatial
dimensions of a system brings many changes such as variations on the thermodynamic
properties, on the values of the spin and orbital moments, on the size of magnetic domains
or even on the dynamical properties [Blü2005]. It must however be reminded that prob-
ing low-dimensional systems does not only consist in investigating geometrical nanosized
systems but also larger systems which exhibit special properties on a 2D or 1D region (for
example Kohn anomaly in low-dimensional chains [Hoe2009], or conduction of electrons
through the Cu-O 2D-planes of cuprates superconductors). The dimensional reduction of
the exchange interaction (2D: $J_1 = J_2 \gg J_3$ or 1D: $J_1 \gg J_2 = J_3$) leads to collective prop-
erties in systems such as quasi-one-dimensional spin chains (for example $C_S NiCl_3$ and
$Ni(C_2H_8N_2)_2NO_2ClO_4$, both quasi-one-dimensional $S = 1$ chains [Aff1989]) or spin lad-
ders (for instance Cu-oxide-based ladders such as $Sr_{14-x}Ca_xCu_{24}O_{41}$ [Dag1999, Whi1996]
which consist in two ferro- or antiferro-magnetically coupled spin chains.

   Moreover, in order to probe the impact of the reduction of dimensions on the magnetic
properties, the example of the transition metals may be considered. From Hund's rules,
it is admitted that all of the 30 transition metal atoms bear a magnetic spin moment.
Nevertheless, only 5 of the 30 transition metals (Fe, Co, Ni, Cr and Mn) are magnetic
when they are in their bulk structure. The reduced dimension systems correspond to
the gap between the single atom limit and the bulk structure. A consequence is that
some other elements like V, Ru or Rh can become magnetic when they are deposited
as thin films onto a substrate [Gol1999, Rau1986, Wu1994]. An explanation comes from
the coordination reduction of confined systems. Indeed when the coordination is reduced,
less electrons contribute to the bonds and necessarily more electrons are unbounded which
leads to magnetism.

   Before entering into details, it should be mentioned that the material structure strongly
affects the magnetic properties. It is therefore useful to keep in mind that the formalism
and the theoretical models depend on the considered scale. Four scales can be approxi-
mately distinguished:

  1. The atomic scale ($< 1\,\mathrm{nm}$) for which the magnetization is governed by quantum
     effects.

  2. The nanoscopic scale ($\sim 1\,\mathrm{nm} - 100\,\mathrm{nm}$) for which the magnetic properties differ

from the ones of bulk materials. Therefore, nanomaterials exhibit a dual behaviour since they present both atomic and macroscopic aspects.

3. The mesoscopic scale ($\sim 100\,\text{nm} - 10\,\mu\text{m}$) for which there is apparition of magnetic domains so that magnetization can be considered uniform in norm but not in direction.

4. The macroscopic scale ($> 10\,\mu\text{m}$) where magnetization is given by the average on all the domains and is consequently considered once again as uniform.

The aim of the present work is to probe magnetism of nanowires whose diameter is of the order of 10 nm. This size corresponds to the nanoscopic scale and is at the limit between the microscopic and the mesoscopic scales. Therefore, the magnetic behaviour of such particles is expected to exhibit specific features.

1.2 Synthesis of nano-objects

For the past fifty years, one important challenge in microelectronics has been the miniaturization of electronic devices. This race to miniaturization follows the empirical Moore's law which predicts that the number of transistors on a surface, and thus the power of the devices, is doubled every eighteen months. The first approach to reduce the dimensions of the materials has been a top-down approach. It consists in "cutting" a material into the desired shape and size. The main advantage of the top-down approach is to easily allow a large scale reproduction of the same pattern.

The top-down approach has met a great success thanks to the technological progress in the lithographical techniques. After overcoming the diffraction limit ($\sim 50\,\text{nm}$ [Lah2006]), the resolution of optical lithography has been decreased down to only 20nm [Lah2006]. As for electronic lithography, the resolution can be better than 10 nm. However at that scale the cost and the fabrication time become prohibitive. That is why, for the past twenty years, lots of efforts have been focused to develop synthesis processes based on the opposite strategy: building some particles from the bricks of matter. This is known as the bottom-up technique.
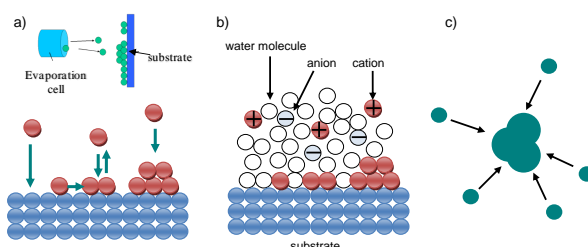
Figure 1.1: Examples for the three main routes to synthesize nanoparticles. (a) physical way: the atoms are evaporated onto a substrate. (b) electrochemical way: the cations are deposited on a substrate. The process may be reversible. (c) chemical way: the atoms self-assemble.

1.2.1   The bottom-up approach

The bottom-up technique consists in self-assembling atoms or molecules. In this approach, chemistry plays a key role as kinetic processes and thermodynamics are involved. Three main routes have been developed until now (see Figure 1.1).
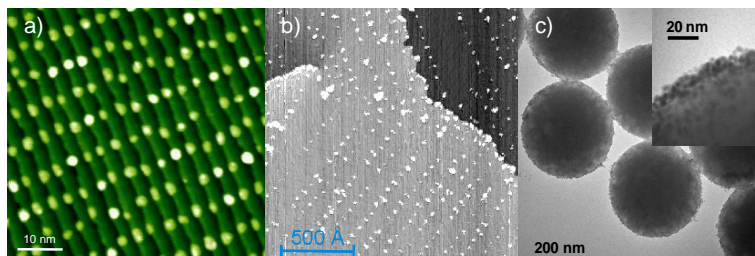
Figure 1.2: Examples of the three main routes to synthesize nanoparticles. (a) Co clusters evaporated and self-organized on a Au(788) surface [Rep2002]. (b) Ru clusters electro-chemically deposited on a Au(111) substrate [Str1999]. (c) FePt nanospheres synthesized via wet chemistry [Sal2005].

The first route is a physical way: in a vacuum chamber, atoms are evaporated from an evaporation cell onto a substrate (see Figure 1.1(a)). The key parameters are the deposition rate and the temperature. The surface of the substrate and the thermodynamic laws also play a key role. The surface curvature favors the adatoms diffusion in concave areas like holes or trenches whereas the elastic energy favors the growth of nanostructures in convex areas like edges or bumps. In order to take advantage of these thermodynamical considerations, a strategy consists in making some arrays of steps at the surface of a substrate. Such a surface is prepared using the vicinal surfaces which is a surface whose orientation is close to the one of a dense surface. Since the position of the atoms is imposed at the surface by the crystalline lattice, the surface is no longer flat but an array of steps. The nanoparticles can then be deposited onto the surface and tend to set near the step edges (see Figure 1.2(a)). Another typical example of such a physical way is the Buffer-Layer Assisted Growth (BLAG) technique which has been recently developed [Hua1998] and concentrates lots of efforts. This method allows to grow and organize magnetic nanoclusters on substrates. For example, nanoclusters of Co have been deposited onto boron-nitride layers by repeated BLAG cycles [Zha2008]. It must be precised that depositing atoms on surfaces is not the only way to form nanoclusters on substrates. Indeed, the Low-Energy Cluster Beam Deposition (LECBD) technique allows to deposit on some substrates some aggregates which have been nucleated in the gas phase on substrates [Ban2005]. This technique is well suited to the deposition and self-organization of transition metals (Fe, Ni or Co) magnetic clusters of well controlled (down to $2\,nm$) on various substrates [Per1997].

The second route is an electrochemical way which consists in depositing ions onto a substrate (see Figure 1.1(b)). In the electrochemical route, the key parameters are the ionic concentrations, the electrolyte and the electrical potential which governs the flux of ions and the temperature. This route may be reversible. A well-known example (see Figure 1.2(b)) is the deposition of Ru clusters on a Au(111) substrate [Str1999].

The third route is a pure chemical way named wet chemistry route (see Figure 1.1(c)). It consists in reducing some metallic salts and collecting them in a solvent. If the control

of the chemical reaction requires the control of many parameters, this route presents the advantage to allow a large-scale fabrication of nano-objects. This method has been preferentially used in order to synthesize monodisperse nanospheres such as FePt synthesized via wet chemistry (see Figure 1.2(c))[Sal2005, Sun2000].

1.2.2 Synthesis of nanowires via the bottom-up approach

One of the more recent challenge has been to control the shape of the nanostructures and to synthesize anisotropic objects such as nanowires instead of isotropic objects like clusters or nanospheres. Of course, there exists some top-down methods to synthesize such nano-objects. UV and X lithographies allow to go beyond the $100\,nm$ [Lah2006] threshold. Electron-beam lithography is a good route to fabricate nanowires of a few nanometers [Juh2005]. Unfortunately, this method does not permit any large scale fabrication [Lah2006].

The bottom-up approach appears to be the most promising alternative to synthesize nanowires exhibiting a diameter of a few nanometers. Four main routes have been developed since the 1990's:

1. The surface self-assembling route consists in using a template which exhibits some very selective and localized adsorption. The adsorbing sites act as anchoring sites for the growth of the nanostructures. For example the self-organization of W (110) trenches in a kinetically-limited growth regime, recently optimized at the Institut Néel [Bor2007], allows in a second step to deposit Fe nanowires in the trenches (see Figure 1.3(a)). It has also been shown that in the ion-sculpting technique, the interaction of a grazing-incidence defocused ion beam with an epitaxial film induces the self-organization of nanometer-scale surface ripples oriented along the projection of the ion-beam direction on the surface. It allows to synthesize monoatomic Fe steps on the surface of nanopatterned Fe/Ag(001) films [Bis2006, Bis2007]. Another well-known process is the use of vicinal surfaces. In this case, natural defects such as step edges act as anchoring sites. This is how molybdenum nanowires have been obtained via the electrodeposition of MoO_2 on Highly Oriented Pyrolytic Graphite (HPOG) [Zac2000].

2. The Vapor Liquid Solid (VLS) technique allows to grow nanowires from a metal melted drop [Wu2001]. In a high-temperature reactor ($\sim 900°$C), a drop is provided by a vapor phase coming from a target heated by a laser beam. Some nanowires exhibiting a few tenths of nanometers diameter for a length of several microns can thus be produced. For instance, Karaguchi et al. synthesized via the VLS process some $InAS/InP$ nanowires with a diameter of $30\,nm$ [Har1992] and S. R. Qi et al. [Qi2000] used a process involving VLS growth mechanism to fabricate TiC nanowires (see Figure 1.3(b)). The principle of VLS mechanism is in fact involved in other processes such as metallo-organic vapor phase epitaxy (MOVPE) [Par2002] (see Figure 1.3(d)).

3. The use of porous membranes. This method is based on porous membranes such as Al_2O_3 [Xu2000] or polycarbonate [Fer2003] exhibiting networks of vertical nanopores whose diameters and lengths respectively measure tenths of nanometers and microns. The second step consists in filling these nanopores with materials [San2003,

Dar2004, DeL2009] via electrodeposition, injection under high pressure or evaporation (see Figure 1.3(c)). This method takes advantage of the vertical order of the nanowire network.

4. The polyol process developed by F. Fiévet (ITODYS, Université Paris Diderot) [Fié1989]. It is a wet chemistry route which allows to get several grams of monodisperse and well-crystallized $CoNi$ nanowires [Ung2005, Ung2007] (see Figure 1.3(e)). Therefore besides the simplicity of this process (low temperature route), its main advantage is that it could pave the way for large scale fabrication of nanowires.
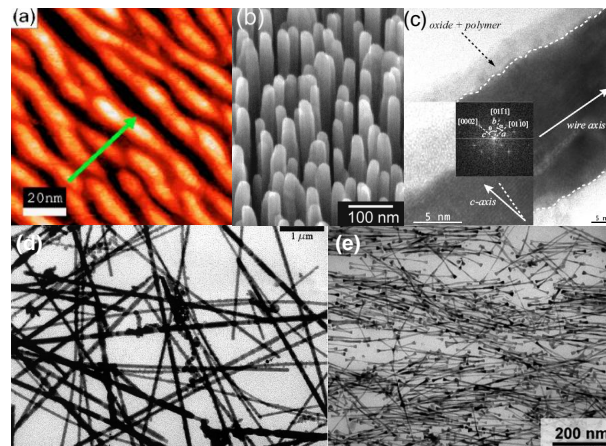
Figure 1.3: (a) $100\,\mathrm{nm}$ STM image of wires Fe (2.5 atomic layers)$/W$ [Bor2007], (b) ZnO nanorods with a mean diameter of $25\,\mathrm{nm}$ grown by MOVPE [Par2002], (c) TEM bright field image and diffraction pattern inset of a 30 nm diameter electrodeposited Co nanowire in a polycarbonate membrane [DeL2009], (d) Low magnification TEM image of TiC nanowires synthesized via VLS technique [Qi2000], (e) $Co_{80}Ni_{20}$ nanowires with a mean diameter of $7\,\mathrm{nm}$ synthesized via the polyol process [Sou2008].

In this context, I have investigated the magnetic properties of $CoNi$ nanowires synthesized via the polyol process for the past three years [Mau2007, Mau2009, Ott2009, Sou2008, Sou2009a]. These nanowires were synthesized by Yaghoub Soumare and Jean-Yves Piquemal from the ITODYS (Université Paris Diderot) and by Guillaume Viau from the LPCNO (INSA Toulouse). Part I presents both the polyol process and the characterization of the magnetic properties of such nanowires via magnetometric measurements. In Part II, the magnetic behaviour of such nanowires has been investigated via SANS measurements. Moreover, some arrays of Co and Ni nanowires electrodeposited in Al_2O_3 porous membranes have also been investigated via SANS measurements. These nanowires were produced by Laurent Cagnon from the Institut Néel in Grenoble.

1.3 Basic ingredients of magnetism

This section provides some basics about the field of magnetism. It starts with magnetism in atom to end with magnetism in fine particle such as the nanowires which have been investigated in this work.

1.3.1 Quantum origin of magnetism

To expose the origin of magnetism, it is convenient to first treat the magnetism of single atoms before considering two atoms and then crystals.

1.3.1.1 Origin of magnetic moments

In solids, magnetic moments have two main origins which are both provided by electrons. The first origin comes from the orbital motion of electrons. The expression of the amplitude of the magnetic orbital momentum $\left|\overrightarrow{M_L}\right|$ and its z-component $M_L|^z$ are:

$$\left|\overrightarrow{M_L}\right| = \gamma\hbar \left[l(l+1)\right]^{\frac{1}{2}} , \tag{1.1}$$

$$M_L|^z = \gamma\hbar m_l , \tag{1.2}$$

where γ is the gyromagnetic factor, l the orbital angular momentum quantum number and m_l the integer value comprised between $-l$ and l. It appears that the magnitude of the magnetic orbital moment is quantized and is of the order of $\gamma\hbar$ which is worth about 10^{-23}A.m^2.

The second origin of magnetic moments comes from the intrinsic spin angular momentum of electrons. The spin magnetic moment $\overrightarrow{M_S}$ is proportional to the spin momentum $\overrightarrow{S}$:

$$\overrightarrow{M_S} = g_S\mu_B\overrightarrow{S}, \tag{1.3}$$

where $g_S = 2.0023$ is the spin Landé factor. A mechanical treatment exposed in [O'H2000, Coh1973] leads to:

$$\left|\overrightarrow{M_S}\right| = \gamma\hbar \left[s(s+1)\right]^{\frac{1}{2}} , \tag{1.4}$$

$$M_S|^z = \gamma\hbar m_s , \tag{1.5}$$

where s is the spin quantum number and m_s the integer value comprised between $-s$ and s.

1.3.1.2 The spin-orbit coupling

The spin-orbit interaction couples the $\overrightarrow{L}$ and $\overrightarrow{S}$ quantum momenta so that the total angular momentum $\overrightarrow{J}$ defined as $\overrightarrow{J} = \overrightarrow{L} + \overrightarrow{S}$ is the conserved quantity. The spin-orbit coupling describes how the spin orientation is affected by electrons orbital motion.

1.3.1.3 Exchange interactions

Besides the spin-orbit coupling, properties of solids are also based on the exchange interaction. The exchange interaction can be either intra-atomic between the electrons of an atom or inter-atomic describing how strongly the atomic moments may couple parallel or antiparallel with each other.

The intra-atomic exchange interaction   The interaction between electrons is governed by the Coulomb repulsion. The second principle which lies at the root of interaction between electrons comes from the Pauli exclusion principle and leads to Hund's rules. If all atomic spins were aligned, the magnetic moments of atoms would be much larger than the ones measured. In fact the Pauli exclusion principle states that the total wave function of two identical electrons is antisymmetric. It implies that when two electrons have the quantum numbers n, l and m_l identical, the fourth quantum number m_s is opposite. The consequence is that the antiparallel spin pairs ($\uparrow\downarrow$) are privileged to the parallel ones ($\uparrow\uparrow$ *or* $\downarrow\downarrow$). It means that magnetism only concerns the transition-metal elements which exhibit unpaired electrons.

The inter-atomic exchange interaction   The inter-atomic exchange is a fundamental process that accounts for intrinsic magnetic properties such as magnetic orders (ferro-, antiferro-magnetism). This interaction is described by the Heisenberg hamiltonian[Sko1999, O'H2000]:

$$H_{exchange} = -\sum_{i<j} J_{ij} \overrightarrow{S_i}.\overrightarrow{S_j} , \qquad (1.6)$$

where the sum runs on the magnetic moments $\overrightarrow{S_i}$ of each atom in the structure.

1.3.1.4   Magnetic orders

Ferro- and antiferro- magnetism   The expression of the Heisenberg hamiltonian favors parallel alignment of the magnetic moments (ferromagnetism) when $J_{ij} > 0$ and antiparallel one (antiferromagnetism) when $J_{ij} < 0$. In the case of antiferromagnetism when the net magnetizations of the two sublattices are different, the system is said to be ferrimagnetic. Note that the Heisenberg hamiltonian suits particularly well to systems where electrons are well localized such as insulators. In other systems exhibiting more extended wave functions, the exchange interaction is much more complex. Some examples are detailed afterwards.

Magnetism in oxides: the superexchange interaction   In most oxides, the electrons remain well localized on the atomic sites so that the exchange model can be used to treat magnetism in such compounds. However this model is useless to explain magnetism of transition metal oxides. For such oxides, it is required to consider a more complex exchange interaction: the superexchange (or Kramers-Anderson superexchange [And1950, Kra1934]) . The superexchange interaction allows to explain antiferromagnetism in oxides such as MnO or FeO.

In order to have an idea of its principle, let's consider two transition metal ions- for instance Mn^{2+}- separated by an oxygen ion. The Mn^{2+} ion is a d ion and the O^{2-} ion is a p ion. The p orbital of the oxygen ion can exchange an electron with each 3d orbital of the Mn^{2+} ion. From Pauli exclusion principle, the two electrons of the p orbital have opposite spins. As shown on Figure 1.4, the superexchange interaction between the two Mn^{2+} ions via the p orbitals of the O^{2-} ion imposes that the two Mn^{2+} ions have opposite spin direction. Consequently, the superexchange interaction can induce antiferromagnetism in metal transition oxides.
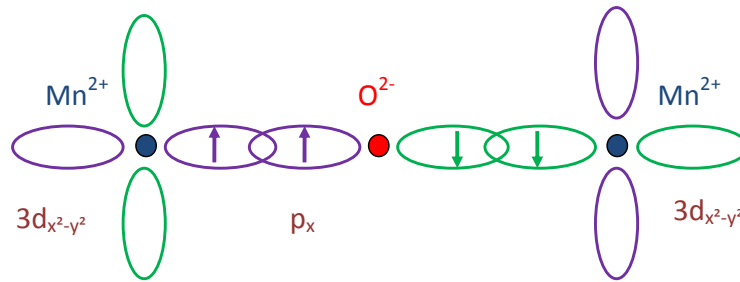
Figure 1.4: Schematic of superexchange in MnO antiferromagnet. Adapted from [O'H2000].

Magnetism in metals The Heisenberg and the superexchange interactions account for antiferromagnetism in compounds such as magnetic oxides where electrons are well localized and interact weakly with each other. Nevertheless the situation is much more complex for metals.

When magnetic electrons are itinerant, the model which should be considered is an electronic band model. This model gives rise to two half bands: one filled with electrons $|\uparrow\rangle$ and the other one filled with electrons $|\downarrow\rangle$. The occupation of these two bands comes from Hund's rules. When the density of states of these two bands is different, a net magnetization appears. This case concerns only few elements such as Fe, Co, Ni or Mn. The maximal value of the net magnetization is obtained for Fe which carries $2.2\,\mu_\mathrm{B}$/atom. The experimental values for net magnetization per atom is given by the Slater-Pauling curve [O'H2000].

When magnetic electrons are localized and some other ones itinerant, the exchange interaction becomes more complex. An interesting example is the one of rare-earth compounds. In rare-earth elements, magnetic electrons are the 4f ones which are very localized. There is however no direct interaction between the 4f electrons. However the 5d and 6s electrons of rare-earth elements interact with the 4f electrons of each atom. The exchange interaction between the 4f electrons occurs thanks to the itinerant 5d and 6s electrons and is named indirect exchange. This model is also referred as the RKKY (Ruderman, Kittel, Kasuya and Yosida) model.

1.3.2 Phase transition and ordering

One can distinguish three kinds of magnetism: diamagnetism, paramagnetism and ordered magnetism such as ferro-, ferri-, antiferro- and heli- magnetism.

Diamagnetism is a response to a magnetic field which induces current rings in the material because of the orbital motion of the electrons. These current rings create small magnetic moments which oppose to the applied magnetic field as expected from the Lenz law. A consequence is that the susceptibility of the system χ_T defined by $M = \chi_T H$ is negative.

Paramagnetism stems from the electron spins which tend to align along the magnetic applied field direction but are disordered because of thermal energy. This kind of magnetism is characterized by a positive susceptibility and strongly depends on the temperature. The Curie law states that the magnetic suceptibility of a paramagnetic material is inversely proportional to the temperature:

$$\chi_T = \frac{C}{T} \ , \tag{1.7}$$

where C is the Curie constant.

Magnetic ordering has been described above and is associated to a phase transition or the apparition of a spontaneous magnetization. The Heisenberg exchange interaction is usually used to model magnetic orders. Nevertheless as soon as one aims to describe the thermodynamical properties of magnetic orders, one has to make some approximations except in the case of a two dimensional system described without any approximation by Onsager [Ons1944]. For ferromagnets, the Curie law, valid for paramagnets, was extended to ferromagnets by Weiss [O'H2000]:

$$\chi_T = \frac{M}{H} = \frac{C}{T - T_C} \ , \tag{1.8}$$

with

$$T_C = \lambda C \tag{1.9}$$

where λ is the mean-field parameter. A useful method is the self-consistent field introduced by Weiss which consists in introducing a molecular field generated by all the neighbouring moments of the site i so that, in presence of an external field, the hamiltonian becomes:

$$\mathcal{H} = -\sum_{i,j} J\overrightarrow{S_i} < \overrightarrow{S_j} > -\mu_0 g\mu_B \overrightarrow{H} \sum_i \overrightarrow{S_i} = -zJS \sum_i S_i - \mu_0 g\mu_B H \sum_i S_i \ , \tag{1.10}$$

where g, z and S are respectively the Landé factor, the number of neighbouring spins of $\overrightarrow{S_i}$ and S the average value of the neighbouring spins. Everything happens as if there was an effective field $\overrightarrow{H_{eff}} = \frac{zJ}{\mu_0 g\mu_B}\overrightarrow{S} + \overrightarrow{H}$. Expressing the partition function of individual spins [O'H2000, Pap2002] leads to the following expression of the magnetization for spins $1/2$ only:

$$M = N\mu_0 tanh(\frac{\mu_0 H}{k_B T} + \frac{zJM}{N\mu_0 k_B T}) \ , \tag{1.11}$$

where N is the total number of spins. This self-consistent equation allows to define a critical temperature T^* which characterizes the phase transition. Below T^* there exists a solution $M \neq 0$ and thus a spontaneous magnetization. When $T > T^*$, there is no solution to the equation so that there is no longer any spontaneous magnetization. In the case of ferromagnetism T^* is the Curie temperature T_C whereas it is called the Néel temperature T_N for antiferromagnetism.

The Weiss molecular field does not take into account for the correlations between neighbouring sites. The Bethe method allows to treat this case and is detailed in [Pap2002].

1.3.3   Crystals and anisotropy

This section describes magnetism in crystals where the role of the crystal size and the formation of magnetic domains are discussed. The possible phase transitions are then detailed. Eventually, the stress is put on magnetism in single domain particles and especially in single domain nanowires which correspond to the framework of this study.

The magnetic properties of a crystal are governed by a competition between different energies. The configuration of the magnetic moments are indeed driven by the energy minimization of the system. The different energies in play are described below.

1.3.3.1 The Zeeman energy

When an external magnetic field $\overrightarrow{H_{ext}}$ is applied, the magnetic moments tend to align along the field direction. This energy E_Z named the *Zeeman energy* is expressed as:

$$E_Z = -\mu_0 \overrightarrow{M}.\overrightarrow{H_{ext}} , \tag{1.12}$$

where $\overrightarrow{M}$ is the magnetization of the sample.

1.3.3.2 Magnetic anisotropies

When the magnetic properties of a system are not isotropic, the system is said to be magnetically anisotropic. There are different origins to magnetic anisotropies: principally the crystal field and the sample shape.

Magnetocrystalline anisotropy One of the main origin of magnetic anisotropy is the magnetocrystalline anisotropy. Among all the magnetic anisotropy origins, the magnetocrystalline anisotropy is the only one which is intrinsic since it directly stems from the exchange interaction and the crystal symmetry. This can be indeed summarized as a coupling between the spins and the lattice via the orbital motion of the electrons: the spin-orbit lattice coupling. This coupling is responsible for the orientation of the spins depending on the lattice symmetries and tends to align the magnetic moments along some preferred crystallographic directions, giving rise to some easy and hard axes or planes of magnetization. The magnetization can be considered as uniform in norm but not in orientation. That is why the quantity of reduced magnetization is introduced.
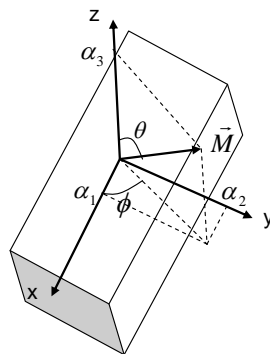
Figure 1.5: Definition of the parameters $(\alpha_1, \alpha_2, \alpha_3)$. They correspond to the spherical coordinates of $\overrightarrow{m} = \frac{\overrightarrow{M}}{M}$ calculated from θ and ϕ.

The notations are given in Figure 1.5 and the reduced magnetization $\overrightarrow{m} = \frac{\overrightarrow{M}}{M}$ is given by the parameters $(\alpha_1, \alpha_2, \alpha_3)$ given by:

$$\begin{cases} \alpha_1 = sin\theta cos\phi\,, \\ \alpha_2 = sin\theta sin\phi\,, \\ \quad \alpha_3 = cos\theta\,. \end{cases} \tag{1.13}$$

With this definition, the relation $\alpha_1^2 + \alpha_2^2 + \alpha_3^2 = 1$ is fulfilled.

Crystal structures of Fe, Ni and Co are respectively body-centered cubic, face-centered cubic and hexagonal. That is why the cubic and hexagonal crystal structures are presented below as well as numerical values of magnetocrystalline constants for Fe, Ni and Co.

The energy of cubic systems obeys the following symmetry rule:

$$E(\overrightarrow{M}) = E(-\overrightarrow{M})\,, \tag{1.14}$$

which implies that there is no odd order in the development of E_{MC}. Finally, the magnetocrystalline energy in cubic systems becomes:

$$E_{MC} = K_0 + K_1(\alpha_1^2\alpha_2^2 + \alpha_1^2\alpha_3^2 + \alpha_2^2\alpha_3^2) + K_2\alpha_1^2\alpha_2^2\alpha_3^2 + ...\,, \tag{1.15}$$

where K_i are the magnetocrystalline anisotropy constants. The magnetocrystalline energies following the different crystallographic directions can be calculated from $(\alpha_1, \alpha_2, \alpha_3)$.

- Calculation of E_{100}. The [100] direction corresponds to $\theta = 90°$ and $\phi = 0°$. It implies that $\alpha_1 = 0$ and $\alpha_2 = \alpha_3 = 0$. Finally, $E_{100} = K_0$.

- Calculation of E_{110}. The [110] direction corresponds to $\theta = 90°$ and $\phi = 45°$. It implies that $\alpha_1 = \alpha_2 = \frac{1}{\sqrt{2}}$ and $\alpha_3 = 0$. Finally, $E_{110} = K_0 + \frac{1}{4}K_1$.

- Calculation of E_{111}. The [111] direction corresponds to $\theta = 54.7°$ ($tan\,\theta = \sqrt{2}$) and $\phi = 45°$. It implies that $\alpha_1 = \alpha_2 = \alpha_3 = \frac{1}{\sqrt{3}}$ which leads to $E_{111} = K_0 + \frac{1}{3}K_1 + \frac{1}{27}K_2$.

For body-centered cubic crystals such as Fe, the easy and hard axes are respectively the [100] and the [111] directions. For faced-centered cubic crystals like Ni, the easy and hard axes directions are respectively the [111] and the [100] directions. The values of the corresponding anisotropy constants are given in Table 1.1.

For hexagonal crystals, the magnetocrystalline anisotropy is expressed as a function of the angle θ between the magnetization and the axis $\overrightarrow{c}$:

$$E_{MC} = K_0 + K_1 sin^2\theta + K_2 sin^4\theta + K_3 sin^6\theta + K_4 sin^6\theta cos\,6\phi\,. \tag{1.16}$$

For hexagonal crystals such as Co, the easy axis is the [001] direction and the hard axes are the [100] and the [010] directions which define the basal plane. The values of the corresponding anisotropy constants are given in Table 1.1.

	bcc-Fe	fcc-Ni	hcp-Co
$K_1(\text{J/m}^3)$	$4.8\,.\,10^4$	$-4.5\,.\,10^3$	$4.1\,.\,10^5$
$K_2(\text{J/m}^3)$	$-1.0\,.\,10^{-8}$	$-2.3\,.\,10^3$	$1.5\,.\,10^5$

Table 1.1: Magnitude of the magnetocrystalline anisotropy constants K_1 and K_2 of Fe, Ni and Co at room temperature [O'H2000].

The shape anisotropy and the demagnetizing field effect   A polycrystal without any preferred orientation of its grains does not exhibit any magneto-crystalline anisotropy. If the sample is not spherical, its shape can lead to one or more preferred orientations of the magnetization. This magnetic anisotropy, named *shape anisotropy*, comes directly from the dipolar interaction which is a long range interaction A magnetic dipole tends to align along the flux lines generated by all the other magnetic dipoles present in the sample. The consequence of the dipolar interaction is the demagnetizing field $\overrightarrow{H_d}$ generated in the dipole which tends to oppose to the magnetization of the dipole (see Figure 1.6).
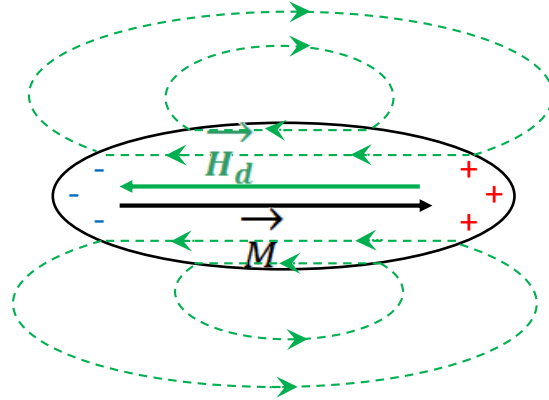
Figure 1.6: Demagnetizing field $\overrightarrow{H_d}$ inside an ellipsoid, opposed to the magnetization inside the ellipsoid $\overrightarrow{M}$.

The energy related to the demagnetizing field H_d is given by:

$$E_d = -\frac{1}{2} \int \mu_0 \overrightarrow{M}(\overrightarrow{r}).\overrightarrow{H_d}(\overrightarrow{r})dV \; , \tag{1.17}$$

The demagnetizing field $\overrightarrow{H_d}$ is related to the magnetization $\overrightarrow{M}$ via the demagnetizing tensor $\overline{\overline{N}}$:

$$\begin{pmatrix} H_{d_X} \\ H_{d_Y} \\ H_{d_Z} \end{pmatrix} = - \begin{pmatrix} N_{xx} & N_{xy} & N_{xz} \\ N_{yx} & N_{yy} & N_{yz} \\ N_{zx} & N_{zy} & N_{zz} \end{pmatrix} \begin{pmatrix} M_X \\ M_Y \\ M_Z \end{pmatrix} \tag{1.18}$$

where N_{ij} are the demagnetizing factors. The minus sign indicates that $\overrightarrow{H_d}$ and $\overrightarrow{M}$ point in opposite directions.

The calculation is very complex for a general shape but can be simplified for symmetric shapes and especially in the case of ellipsoids. If $\overrightarrow{a}$, $\overrightarrow{b}$ and $\overrightarrow{c}$ are the semi-axes of the ellipsoid of revolution, Equation 1.18 becomes :

$$\begin{pmatrix} H_{d_a} \\ H_{d_b} \\ H_{d_c} \end{pmatrix} = - \begin{pmatrix} N_\perp & 0 & 0 \\ 0 & N_\perp & 0 \\ 0 & 0 & N_{\shortparallel} \end{pmatrix} \begin{pmatrix} M_a \\ M_b \\ M_c \end{pmatrix} \quad tr(N) = 2N_\perp + N_{\shortparallel} = 1 \; . \tag{1.19}$$

Thus, the energy of the demagnetizing field is:

$$E_d = \frac{1}{2}\mu_0 V (N_\perp M_a^2 + N_\perp M_b^2 + N_\shortparallel M_c^2) \, . \tag{1.20}$$

In the $(\overrightarrow{a}, \overrightarrow{b}, \overrightarrow{c})$ base (see Figure 1.7), the magnetization vector can be expressed as:

$$\overrightarrow{M} = M_S(sin\theta \, sin\phi \, \overrightarrow{a} + sin\theta \, cos\phi \, \overrightarrow{b} + cos\theta \, \overrightarrow{c}) \, . \tag{1.21}$$

It leads to:

$$E_d = \frac{1}{2}\mu_0 M_S^2 V (N_\perp sin^2\theta + N_\shortparallel cos^2\theta) \, . \tag{1.22}$$

Since $2N_\perp + N_\shortparallel = 1$, Equation 1.22 becomes:

$$E_d = \frac{1}{2}\mu_0 N_\shortparallel M_S^2 v V + \frac{1}{4}\mu_0 M_S^2 V \left(1 - 3N_\shortparallel\right) sin^2\theta \, . \tag{1.23}$$

In this equation, the shape anisotropy is given by the $sin^2\theta$ term. There will thus be an easy-axis shape anisotropy as soon as $N_\shortparallel < 1/3$ (prolate ellipsoids) and there is no shape anisotropy contribution for magnetic spheres ($N_\shortparallel = 1/3$).

In uniformly magnetized ellipsoids, if the magnetization lies along a principle direction, then the demagnetizing field is also uniform and given by:

$$\overrightarrow{H_d} = -N\overrightarrow{M} \, , \tag{1.24}$$

where N is the demagnetizing tensor which is defined by [Sko1999]:

$$\begin{cases} N_\shortparallel = N \\ N_\perp = \frac{1-N}{2} \end{cases} \, . \tag{1.25}$$

.

The energy of the demagnetizing field then becomes:

$$E_d = \frac{1}{2}\mu_0 \int \overrightarrow{M} N \overrightarrow{M} dV = \frac{1}{2}\mu_0 V \overrightarrow{M} N \overrightarrow{M} \, , \tag{1.26}$$

where V is the volume of the ellipsoid.

The simplest case is the spherical one for which:

$$N_\perp = N_\shortparallel = \frac{1}{3} \, , \tag{1.27}$$

so that the energy of the demagnetizing field of a sphere is given by:

$$E_d = \frac{1}{6}\mu_0 V M_S^2 \, . \tag{1.28}$$

Table 1.2 summarizes the values of N for finite rods magnetized parallel to the axis. In this work, nanowires exhibiting some aspect ratio ($length/diameter$) larger than 10 have been investigated. For such objects, the demagnetizing factor N is expected to be smaller than 0.0172. The magnetization thus tends to be magnetized along the long axis of nanowires exhibiting such aspect ratios.

Aspect ratio ($Length/diameter$)	N
0	1
1	0.27
2	0.14
5	0.04
10	0.0172
20	0.00617
50	0.00129
100	0.00036
500	0.000014
1000	0.0000036

Table 1.2: Demagnetizing factors N for finite rods magnetized parallel to long axis. Adapted from [O'H2000].

When nanowires exhibit large aspect ratio so that they can be approximated by an infinitely long cylinder with $\overrightarrow{c}$ as the infinite axis (see Figure 1.7), the demagnetizing tensor thus becomes:

$$N = \begin{pmatrix} \frac{1}{2} & 0 & 0 \\ 0 & \frac{1}{2} & 0 \\ 0 & 0 & 0 \end{pmatrix} . \tag{1.29}$$

For spherical coordinates (see Figure 1.7), the energy of the demagnetizing field becomes:

$$E_d = \frac{1}{2}\mu_0 V M_S^2 \frac{1}{2}\left(sin^2\theta cos^2\phi + sin^2\theta sin^2\phi\right) = \frac{1}{4}\mu_0 V M_S^2 sin^2\theta . \tag{1.30}$$

Finally, the shape anisotropy governed by the energy of the demagnetizing field, tends to align the magnetization along the longer axes in absence of an applied magnetic field (E_d is minimum for $\theta = 0$).
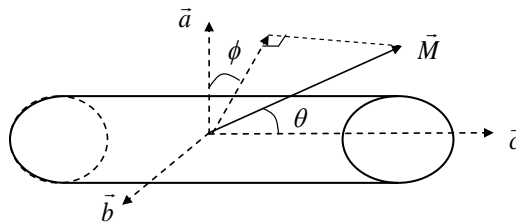
Figure 1.7: Definition of the θ and ϕ angles for an infinite cylinder.

1.3.4 Magnetic domain formation

Many magnetic materials do not exhibit any magnetization if no external magnetic field is applied. Weiss attributed this "absence" of magnetism to the formation of domains

in polycrystals: domains are magnetized in different directions so that the average net magnetization is almost zero (see Figure 1.8).

(a)   (b)
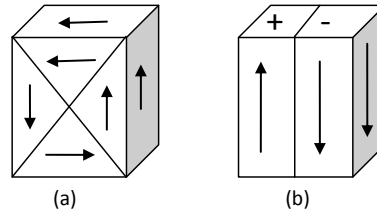
Figure 1.8: Schematic domain structures for (a) cubic and (b) uniaxial anisotropy. Adapted from [Sko1999].

1.3.4.1   Micromagnetic lengths

The formation of domains is in fact governed by the minimization of the total energy E:

$$E = E_Z + E_d + E_{MC} + E_{ex} \ . \tag{1.31}$$

The competitions between the energies which come into play are characterized by two micromagnetic lengths: the exchange length l_{ex} and the wall width parameter δ (see Figure 1.9).
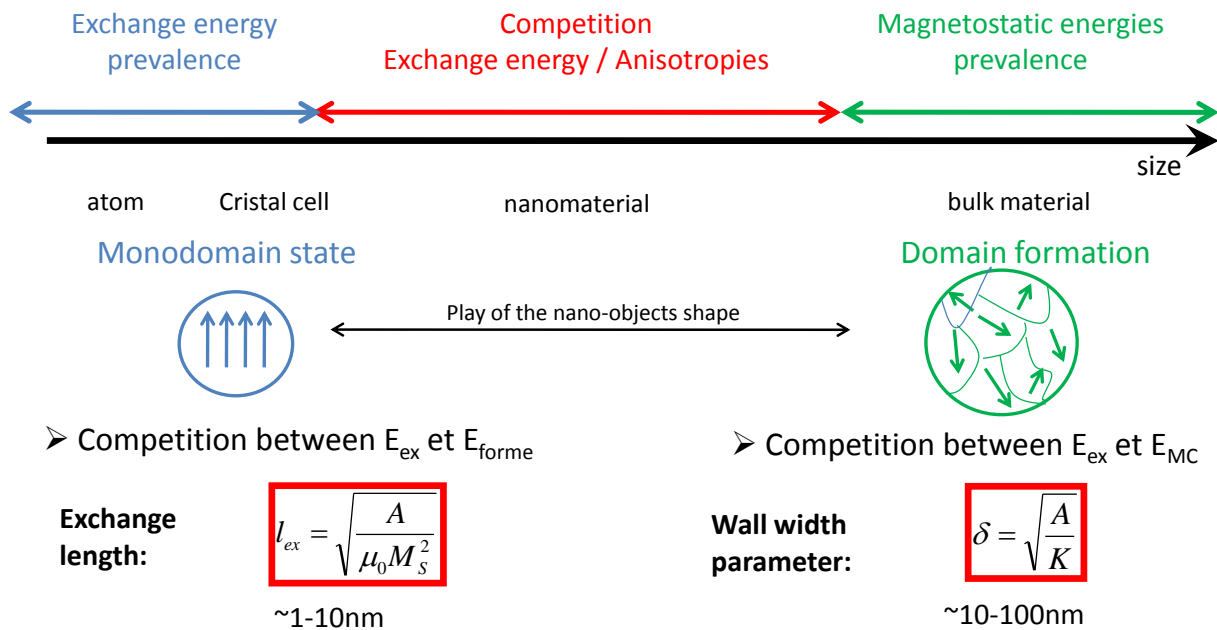
Figure 1.9: Schematic of energy competition in nanomaterials. The domain fomation is governed by the exchange length l_{ex} which accounts for the competition between the shape anisotropy and the exchange energy. The size of the domain walls is given by the wall width parameter δ.

The formation of magnetic domains stems from a competition between the exchange energy which tends to maintain spins aligned together and the demagnetizing energy

which prevents the formation of magnetic surface and volume charges. The role of the demagnetizing energy is illustrated by the *pole avoidance principle* which states that the magnetic surface and volume charges have to be minimized while the magnetic flux tends to be closed. The exchange legnth is the minimal length which is required so that the direction of the magnetic moments can change. It defines the threshold below which atomic exchange interaction prevails on the magnetostatic fields [Sko1999]:

$$l_{ex} = \sqrt{\frac{A}{\mu_0 M_S^2}} \ . \tag{1.32}$$

The exchange length is typically of order of few nanometers (see Table 1.3).

The second micromagnetic length is the wall width parameter δ which accounts for the competition between the exchange energy and the magnetocrystalline anisotropy. The wall width parameter characterizes the wall width which separates magnetic domains and is expressed as:

$$\delta = \sqrt{\frac{A}{K_1}} \ , \tag{1.33}$$

where A is the exchange stiffness constant which is related to the exchange interactions through:

$$A = \frac{S^2 a^2 J N'_\nu}{2} \ , \tag{1.34}$$

with N'_ν, S, a and J respectively the number of nearest-neighbour atoms per unit volume, the electronic spin of the atoms, the distance between spins and the exchange interaction. A is a macroscopic measure of the stiffness of coupling in the spin system and its value is comprised between 1×10^{-11} J/m and 2×10^{-11} J/m for most ferromagnets [O'H2000, Sko1999].
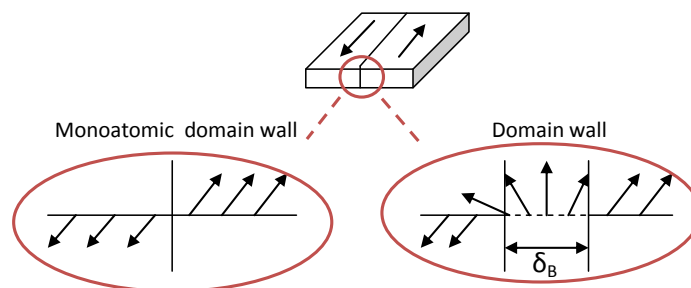
Figure 1.10: Schematics of a 180° domain wall. (a) a monoatomic domain wall, (b) a Bloch wall.

There are different kinds of domain walls. In materials with cubic anisotropy, the $< 100 >$ direction is the easy axis, 90° walls may be formed. However in systems exhibiting a uniaxial anisotropy, the magnetizations of the neighbouring domains are opposite and it gives rise to 180° domain walls. Some typical 180° walls are the Bloch and Néel walls. The Bloch wall corresponds to a rotation of the magnetic moments outside of the magnetization plane (see Figure 1.10) while the Néel wall is characterized by a rotation of the magnetic

moments inside the magnetization plane. It must be noted that Néel walls mainly concern surface geometry. As for Bloch walls, in the case of uniaxial magnetocrystalline anisotropy and of infinite wall, their width is given by the Bloch wall width:

$$\delta_B = \pi \sqrt{\frac{A}{K_1}} \ , \tag{1.35}$$

Table 1.3 gives the δ_B values for compounds such as transition metals or rare-earth magnets.

Material	δ_B (nm)	l_{ex} (nm)
Fe	40	1.5
Co	14	2
Ni	82	3.4
$SmCo_5$	3.6	4.9
$Nd_2Fe_{14}B$	3.9	1.9

Table 1.3: Values of δ_B for some transition and rare-earth metals [Sko1999].

1.3.4.2   Domain formation in nanowires

The situation is complex in nanowires as different configurations may arise depending on whether the anisotropy axis is along the nanowire axis or perpendicular to it. The nanowires which have been investigated crystallize in the hexagonal compact phase with the axis $\overrightarrow{c}$ along the geometrical axis. When their radii are large enough, a Bloch wall may be expected to arise as described in Figure 1.11.

The value of the threshold between monodomain and multidomain configurations in nanowires is defined from both the exchange length l_{ex} and the domain wall parameter δ. Indeed, the wall energiy per unit area γ is $\gamma = 4\sqrt{A\,K_1}$ under the hypothesis that K_2 can be ignored [Sko2002, Sko1999]. Considering the domain configuration shown in Figure 1.11, the wall energy is $\gamma 2RL$ where R and L are respectively the radius and the length of the nanowire. The gain of magnetostatic energy within this configuration may be assessed to half the single domain energy, that is $\mu_0 M_S^2 V/8$. It implies that domain formation is favored for nanowires whose radius exceeds the *critical single domain radius*:

$$R_{SD} = \frac{64 l_{ex}^2}{\pi \delta} = \frac{64 l_{ex}^2}{\delta_B} \tag{1.36}$$
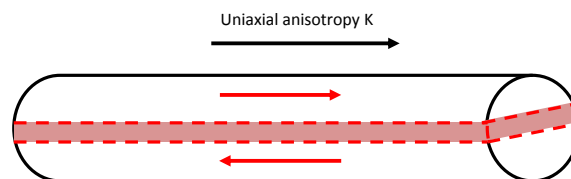
Figure 1.11: Schematics of a possible magnetization configuration for large nanowires exhibiting an uniaxial anisotropy along their geometrical axis.

1.3.5 Magnetism in single domain particles

As seen before the demagnetizing energy tends to divide a magnetic material into magnetic domains. However when the dimensions of the material are strongly reduced, there is a limit below which the particle is too small to contain a domain wall: the particle is said to be in a "single-domain state". The magnetization reversal of single-domain particles are - in many cases - well described by the Stoner-Wohlfarth model which is presented in Section 1.3.5.1. This model describes the reversal process as a coherent rotation of all moments in unisson. Nevertheless, other reversal modes are possible and are detailed in Section 1.3.5.2.

Furthermore, a competition between the anisotropy energy $E_{anisotropy} = KV$ (V is the volume of the particle) and the thermal energy $E_{thermal} = k_B T$ may occur and desta-bilize the magnetic order in the material. The physical limit is given by the case of a single-domain magnetic particle. In this section, a ferromagnetic single-domain particle is considered *i.e.* a particle carrying a macrospin. The magnetic order sets in below the Curie temperature T_C. When $KV \gg k_B T$, the ferromagnetic order cannot be disturbed by the thermal energy. The ferromagnetic regime can be approximated by the Stoner-Wohlfarth model which is only valid for T=0K. When KV is of order of $k_B T$, the magnetic order is destabilized by the thermal energy which gives rise to magnetic fluctuations: this is the superparamagnetic regime which is well described by the Néel-Brown (NB) model. Note that both Stoner-Wohlfarth (SW) and Néel-Brown models are only valid for the limit of single-domain particles insofar as the exchange coupling is able to suppress magnetic inhomogeneities and the magnetization reversal process arises only from coherent rotation of the magnetization vector.

1.3.5.1 The Stoner-Wohlfarth model (T=0K)

The Stoner-Wohlfarth model is the simplest micromagnetic model which describes magnetization reversal in single-domain particles. This model is based on the following hypothesis: the magnetization is uniform in the particle. The exchange interaction is thus constant and has no role in the minimization of the total energy. This is why the only considered energy contributions are:

1. The Zeeman energy E_Z which describes the interaction between the magnetic moments and the applied magnetic field H and is given by: $E_Z = -\mu_0 M_S H cos(\phi - \theta)$, where M_S is the saturated magnetization of the particles and $\phi - \theta$ the angle between $\overrightarrow{H}$ and the magnetization $\overrightarrow{M}$ (see Figure 1.12).

2. The magnetocrystalline anisotropy energy E_{MC} which is given by: $E_{MC} = K_{MC} sin^2\theta$, where K_{MC} is the anisotropy constant and θ the angle between $\overrightarrow{M}$ and the easy axis $\overrightarrow{z}$.

3. The shape anisotropy energy E_{shape} which is given by: $E_{shape} = K_{shape} sin^2\theta'$, where K_{shape} is the anisotropy constant and θ' the angle between $\overrightarrow{M}$ and the longer axis $\overrightarrow{z'}$.

In the particular case of a sphere, the shape anisotropy is zero and the anisotropy is reduced to the magnetocrystalline anisotropy. But for all other kind of ellipsoids, the

shape anisotropy has to be taken into account and the demagnetizing field thus plays a role in the magnetic behaviour of the single-domain ellipsoid.

Note that when the easy axis of the magnetocrystalline anisotropy is parallel to the longer axis of the ellipsoid, one has $\theta = \theta'$. The discussion is restricted to this case since it corresponds to nanowires synthesized via the polyol process which have been investigated (see Figure 1.12: $\overrightarrow{z} = \overrightarrow{z'}$).
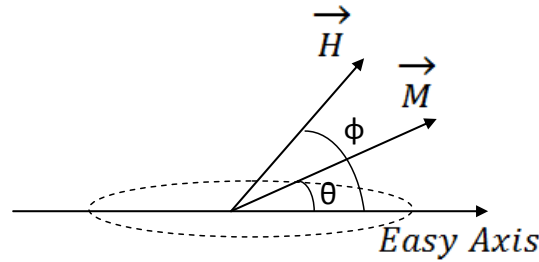
Figure 1.12: The Stoner-Wohlfarth geometry: definition of θ and ϕ

The free energy E of a magnetic single-domain ellipsoid is:

$$E = E_{MC} + E_{shape} + E_Z = \left[(K_{MC} + K_{shape})sin^2\theta - \mu_0 M_S H cos(\phi - \theta) \right] V \ . \qquad (1.37)$$

The anisotropy energy $K sin^2\theta$ includes both shape and magnetocrystalline anisotropies which may be expressed as follow:

- The magnetocrystalline anisotropy $E_{MC} = \frac{1}{2}\mu_0 M_S H_{MC} V sin^2\theta \equiv -\frac{1}{4}\mu_0 M_S H_{MC} V cos(2\theta)$ since constants can be neglected in the total energy expression. H_{MC} is designated as the anisotropy field and is worth $H_{MC} = \frac{2K_{MC}}{\mu_0 M_S}$.

- The shape anisotropy is $E_{shape} = \frac{1}{2}\mu_0 M_S^2 V (N_\perp cos\theta^2 + N_\| sin^2\theta) \equiv -\frac{1}{4}\mu_0 M_S^2 V (N_\| - N_\perp) cos(2\theta)$ where $N_\perp$ and $N_\|$ are the demagnetizing factors.

In order to write the expression of the adimensional Stoner-Wohlfarth energy η, we introduce the following reduced variables (provided that $N_\perp \neq N_\|$):

- $h = \frac{H}{(N_\| - N_\perp)M_S}$,

- $h_{MC} = \frac{H_{MC}}{(N_\| - N_\perp)M_S}$.

This leads to the following expression of the adimensional energy η:

$$\eta = -\frac{1}{4}(1 + h_{MC})cos(2\theta) - h\, cos(\phi - \theta) \ . \qquad (1.38)$$

The Stoner-Wohlfarth model allows to describe the influence of the magnetocrystalline anisotropy via H_A and the role of the shape of the particle via $\triangle N = N_\| - N_\perp = \frac{1}{2}(3N - 1)$.

The hysteresis cycle as a function of the angle ϕ between $\overrightarrow{H}$ and the easy axis can be calculated. Figure 1.13 shows that the value of the coercive field is strongly affected by

the angle ϕ. Note that when the particles are aligned along the magnetic field $\overrightarrow{H}$, the coercive field is the sum of two contributions, one from the magnetocrystalline anisotropy H_{MC} and another one from the shape anisotropy H_{shape}:

$$H_C = H_{MC} + H_{shape} = \frac{2K_{MC}}{\mu_0 M_S} + \frac{1}{2}(1 - 3N)M_S \ , \tag{1.39}$$

where K_{MC} is the anisotropy constant, M_S the saturation magnetization and N the demagnetizing factor. $N = 1/3$ for spheres and $N = 0$ for infinite cylinders. Some more accurate values of N as a function of the length and the radius of the cylinder are given in Table 1.2.
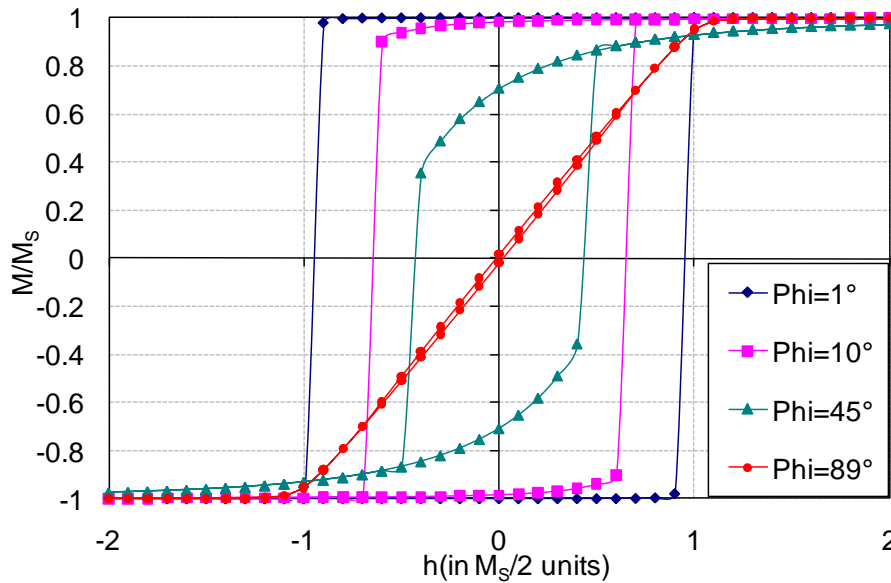
Figure 1.13: Hysteresis cycles in the Stoner-Wohlfarth model for different values of ϕ ($h_{MC} = 0$) in the case of infinitely long cylinders. The hysteresis cycle is square when the magnetic field is applied along the easy axis. It is closed when the magnetic field is applied perpendicularly to the easy axis ($\phi = 90°$) .

Figure 1.13 describes the case of a single particle. But the detection limit of magnetometry techniques such as SQUID or VSM implies to work on a collection of objects. The hysteresis cycles of randomly oriented particles have been calculated within the Stoner-Wohlfarth model by taking into account the contribution of the magnetocrystalline anisotropy. Note that it is only valid for uniaxial anisotropy. First it underlines the effect of the magnetocrystalline anisotropy on the hysteresis cycles (see Figure 1.14).

Secondly, Figure 1.14 shows that the remanence of randomly oriented particles is $0.5\,M_S$. This value strongly depends on the dimensionality of the system. The value of the remanence for randomly oriented particles is different when the particles are dispersed on a surface or in a volume:

$$M_r = \bar{M} = \frac{M_S \int_0^{\pi/2} cos\theta d\theta}{\int_0^{\pi/2} d\theta} = \frac{2M_S}{\pi} \quad for \ 2D \ distribution \ of \ easy \ axis, \tag{1.40}$$

$$M_r = \bar{M} = \frac{M_S \int_0^{\pi/2} cos\theta sin\theta d\theta}{\int_0^{\pi/2sin\theta} d\theta} = \frac{M_S}{2} \quad for\ 3D\ distribution\ of\ easy\ axis. \qquad (1.41)$$
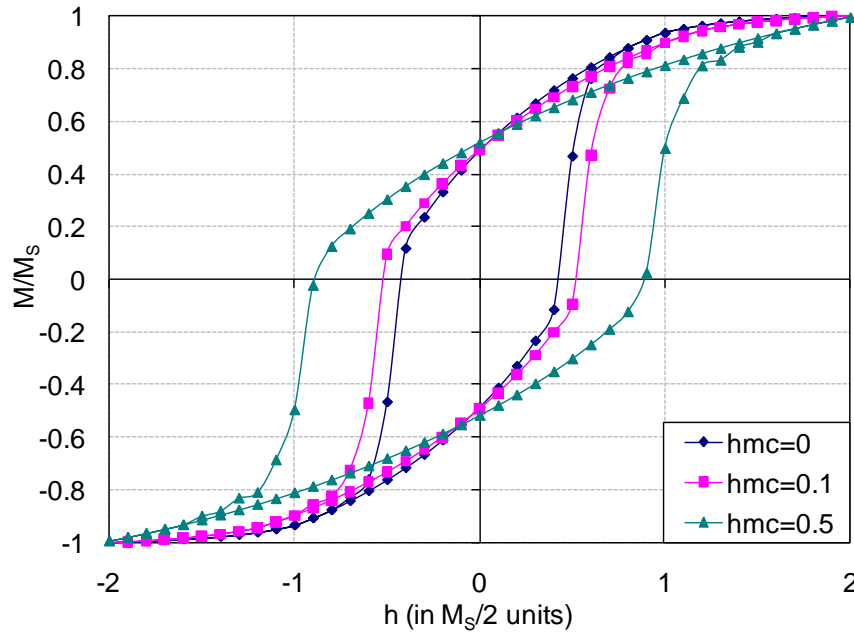
Figure 1.14: Hysteresis cycles of randomly oriented particles in the Stoner-Wohlfarth model for different values of h_{MC}. The considered particles are infinitely long cylinders and the magnetocrystalline anisotropy is supposed to be uniaxial.

Furthermore, the original Stoner-Wohlfarth model only takes the uniaxial shape or uniaxial magnetocrystalline anisotropies into account. However as shown on Figure 1.14, the magnetocrystalline anisotropy may have large effects on the hysteresis cycles. Therefore depending on the studied system, the other anisotropies such as the magnetocrystalline, the magnetoelastic or the surface ones have to be included. The generalization of the Stoner-Wohlfarth model has been developed in three dimensions by Thiaville [Thi1998, Thi2000] and applied to an arbitrary effective anisotropy.

1.3.5.2 Other reversal modes: curling and buckling

In single-domain particles, the reversal process is not necessarily uniform and cannot be always described by the Stoner-Wohlfarth model. Other reversal modes such as curling or buckling may occur and ease the reversal process. These two non-uniform modes lead to lower coercive fields than in the Stoner-Wohlfarth model. In these modes, the angle between the individual magnetic moments and the cylinder axis varies from a magnetic moment to another (see Figure 1.16). They are observed in structures exhibiting a radius larger than the coherence radius R_{coh}. Figure 1.15 summarizes the different possible reversal modes depending on the radius values.
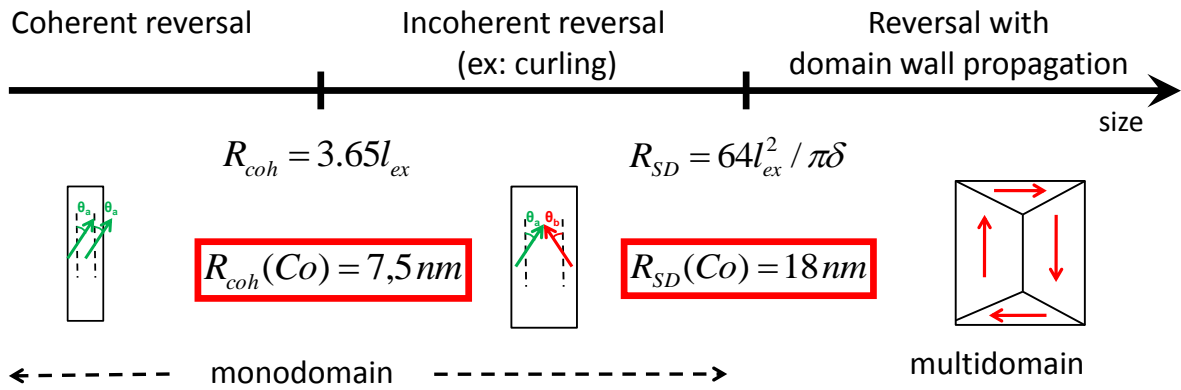
Figure 1.15: Magnetization reversal modes in nanowires. R_{SD} is the single-domain radius below wich the magnetization is monodomain. $R_{coh}$is the coherence rasius below which the magnetization reversal is expeted to be coherent.

In the case of spheres, the value of R_{coh} is [Sko1999]:

$$R_{coh} = \sqrt{24}\, l_{ex} \ , \tag{1.42}$$

where l_{ex} is defined in Equation 1.32.

In the case of cylinders, the value of R_{coh} becomes [Sko2000]:

$$R_{coh} = 3.65\, l_{ex} \ . \tag{1.43}$$

Equation 1.43 implies that the exchange length l_{ex} imposes the size limit below which the rotation is coherent. The curling mode (see Figure 1.16 (a)) is more frequently met in practice and is detailed below.

The magnetocrystalline anisotropy is here not taken into account. If the reversal process was coherent, the expected coercive field would be given by Equation 1.39. In a curling process, the exchange energy is increased but the magnetostatic energy is reduced as less magnetic moments point out of the easy axis at any step of the reversal process. The coercive field thus becomes:

$$H_C = \frac{2K_{MC}}{\mu_0 M_S} + \frac{c(D)A}{\mu_0 M_S R^2} \ , \tag{1.44}$$

where A is the exchange stiffness and $R = R_x = R_y$ refers to the two degenerate axes of the ellipsoid. $c(D)$ is a parameter which depends on the value of D and thus on the shape of the particle. For instance, $c = 8.666$ for spheres ($D = 1/3$) and $c = 6.678$ for needles ($D = 0$). As in the case of the Stoner-Wohlfarth model (see Equation 1.39, a shape anisotropy contribution to the coercivity can be extracted for a curling process and is expressed as:

$$H_C = \frac{c(D)A}{\mu_0 M_S R^2} \ . \tag{1.45}$$
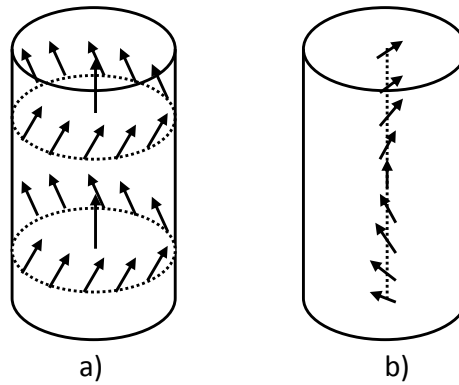
Figure 1.16: The (a) curling and (b) buckling nucleation modes in cylinders. Adapted from [Sko1999].

Figure 1.17 gives an overview of the dependence of H_{shape} as a function of the radius of the ellipsoid. When the radius becomes larger than R_{coh}, the contribution of the shape anisotropy to the coercivity decreases. Therefore it is crucial to synthesize particles as thin as possible as soon as one aims to obtain large coercivities. Incoherent rotation as well as domain wall lie at the root of large decrease of coercivities.
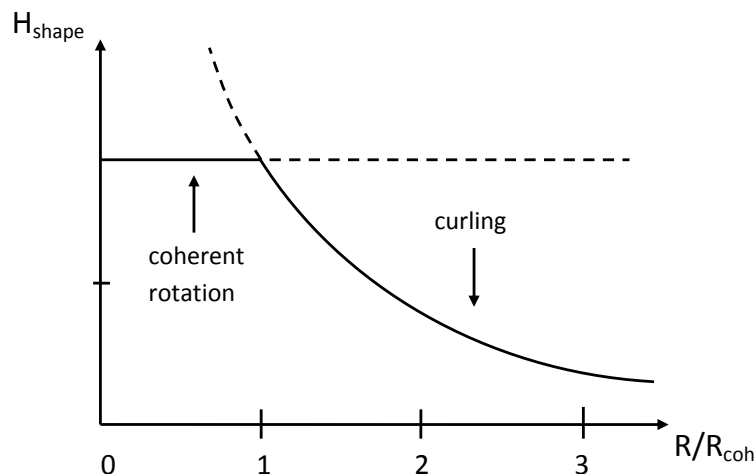
Figure 1.17: The shape anisotropy contribution to the coercivity for a prolate ellipsoid. Adapted from [Sko1999].

Finally it must also be precised that - besides coherent rotation and curling- a third mode of magnetization reversal may be observed [Sko1999, O'H2000]. This mode is named buckling (see figure 1.16 (b)) and occurs when the length L of ellipsoids exceeds $9.2R$ and the radius R satisfiess the relation: $R < 4l_{ex}$. This mode is characterized by a sinusoidal modulation of the magnetization in the z-direction.

1.3.5.3 Superparamagnetism $(T > 0\,K)$ in the Néel-Brown model

The Stoner-Wohlfarth model applies at T=0K and thus neglects the thermal fluctuations. When the thermal energy $E_{thermal} = k_B T$ is small compared to the anisotropy energy

$E_{anisotropy} = KV$, the Stoner-Wohlfarth model can be applied to single domain particles. However, when the size of the particle is so small that the thermal energy $E_{thermal} = k_B T$ becomes equivalent to $E_{anisotropy} = KV$, the Stoner-Wohlfarth model can no longer be applied [Dor1981, Kno2008]: this is the superparamagnetic limit.
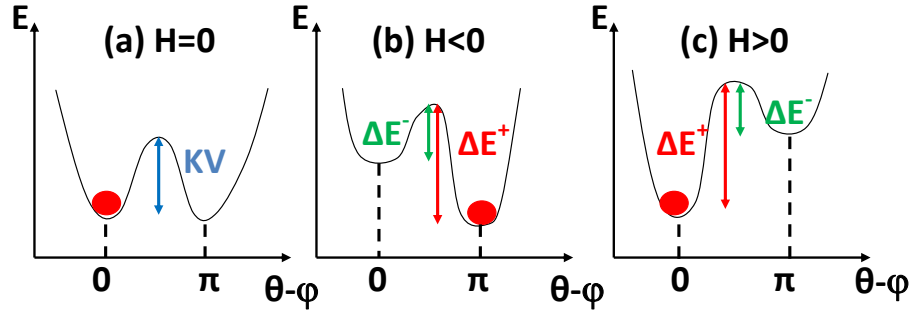
Figure 1.18: Diagram representing the energy profile as a function of θ, the angle between $\overrightarrow{M}$ and $\overrightarrow{H}$ defined in Figure 1.12 for: (a) $H = 0$, (b) $H < 0$ and (c) $H > 0$ when $H < \frac{2K}{\mu_0 M_S}$.

Let us consider a uniaxial single domain particle exhibiting a total magnetic anisotropy $KV sin^2\theta$ where θ is the angle between the magnetization and the easy axis. When an external magnetic field $\overrightarrow{H}$ is applied along the easy axis, the total energy is:

$$E = KV sin^2\theta - HM_S V cos\theta , \qquad (1.46)$$

where M_S is the saturation magnetization at the considered temperature. E exhibits a single minimum for $H > \frac{2K}{\mu_0 M_S}$ and there exists only one stable state. When $H < \frac{2K}{\mu_0 M_S}$, there are two minima ($\theta = 0$ *and* $\theta = \pi$). When there is no applied field, the energy barrier from $\theta = 0$ to $\theta = \pi$ is the same as the one from $\theta = \pi$ to $\theta = 0$ and is worth $(\triangle E)_{H=0} = KV$ (see Figure 1.18(a)). However when a positive (negative) magnetic field is applied, the symmetry of the energy barrier is lost and the barrier energy $\triangle E^-$ from $\theta = 0$ to $\theta = \pi$ (from $\theta = \pi$ to $\theta = 0$) becomes smaller than the one $\triangle E^+$ from $\theta = \pi$ to $\theta = 0$ (from $\theta = 0$ to $\theta = \pi$) [Dor1981, Fru2005] (see Figure 1.18(b) and (c)):

$$(\triangle E)_H^{\pm} = KV \left(1 \pm \frac{HM_S}{2KV}\right)^2 . \qquad (1.47)$$

In order to take into account the role of the temperature, the probability $f(\theta)d\theta$ to find the magnetization along the angle θ is introduced [Dor1981]:

$$f(\theta) = \frac{1}{C} exp(-\frac{E}{k_B T}) sin\theta , \qquad (1.48)$$

with the following condition of normalization:

$$\int_0^\pi f(\theta)\, d\theta = 1 ,$$

which leads to:

$$C = \int_0^\pi exp(-\frac{E}{k_B T}) sin\theta\, d\theta . \qquad (1.49)$$

When E is much larger than k_BT, $f(\theta)$ is finite only close to the minima of E. In this case (see Figure 1.19), the only possible states of magnetization correspond to these minima. In the case of $H = 0$, they are equiprobable. The probability that the magnetization jumps from one of these states to another is thus zero. It implies that a set of particles without any interaction between each other exhibits zero net magnetization in the absence of an applied field. However when E becomes equivalent to k_BT, $f(\theta)$ is larger around the energy minima and the magnetization can fluctuate around one or several states corresponding to energy minima. The magnetization is consequently given by the average of $cos\theta$ over the measuring time τ_m. It means that the measuring time τ_m affects the value of the measured magnetization. It can vary from large values (typically 100s) for magnetometry measurements down to small ones for techniques like Mössbauer (about 10^{-8}s). Thus if τ_m is much larger than the fluctuation time τ, the system reaches a thermodynamical equilibrium during the measurement: the particles are in a paramagnetic state. However if $\tau \gg \tau_m$, the fluctuations are very slow compared to the measuring time so that one can measure quasi-static properties: the particles are in the blocked regime.
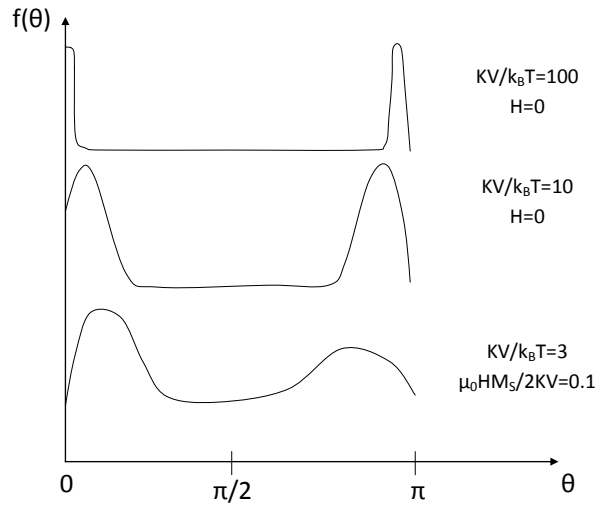
Figure 1.19: Probability $f(\theta)$ to find the magnetization oriented along θ as a function of $\frac{E}{k_BT}$ and H (adapted from [Dor1981]).

Two models are used to describe the superparamagnetic behaviour of fine particles. First, the Néel model considers that the magnetization follows an Arrhenius law with a characteristic relaxation time τ [Dor1981, Kno2008]:

$$\tau = \tau_0 exp\left(\frac{KV}{k_BT}\right) \, , \tag{1.50}$$

It must here be emphasized that the value of τ_0 is generally approximated to 10^{-9}s [Bea1956] but this value can largely vary from one material to another. Indeed, τ_0 depends on some characteristics of the material. The general expression of τ_0 is detailed in [Dor1981].

The temperature associated to the transition between the two regimes is called the blocking temperature and is noted T_B. Some precautions have thus to be taken since the

value of the blocking temperature T_B depends on the measuring time. Moreover the value of T_B is related to the value of the energy barrier which implies that T_B increases with increasing particle size. The value of T_B is expressed as:

$$T_B = \frac{KV}{k_B} ln\left(\frac{\tau}{\tau_0}\right) \ . \tag{1.51}$$

Some results about the Néel model are summarized in [Fru2005, Sha1994] and lead to the expression of the coercivity for a measurement performed during a time τ:

$$H_C(T, \tau) = H_C(T = 0K) \left(1 - \sqrt{\frac{k_B T}{KV} ln(\frac{\tau}{\tau_0})}\right) \ , \tag{1.52}$$

From this formula, it is possible to deduce [Fru2005] that for a fixed time scale τ, H_C becomes null for $T > T_B$. This is the superparamagnetic limit: below T_B the system is ferromagnetic and between T_B and T_C it is superparamagnetic.

In the case of uniaxial particles, the average magnetization is oriented along the field direction when a magnetic field is applied. When the magnetic anisotropy is weaker than the Zeeman energy, the average magnetization of the particles can be written as [Dor1981]:

$$< M >= M_S \mathcal{L}(\frac{\mu_0 M_S H V}{k_B T}) \ , \tag{1.53}$$

where $\mathcal{L}(x)$ is the Langevin function, defined as:

$$\mathcal{L}(x) = coth(x) - \frac{1}{x} \ . \tag{1.54}$$

The resolution of this self-consistent equation depending on approximations is described in [Dor1981, O'H2000, Kno2008].

The second model (the Brown model) is based on stochastic processes and the Gilbert equation and is obtained by adding a term describing the random forces which are applied to the system. The hypothesis on the random forces acting on the system are similar to the ones of the Brownian motion. The results are similar to those of the Néel model [Dor1981].

1.3.6   Specific properties of nanowires

Most investigated nanowires have been those electrodeposited in porous membranes [DeL2009, Dar2004, San2003]. The great advantage of such samples is the perfect alignment of the objects. In addition, the diameter, the length and the distance between the objects can be tuned from few tens nanometers up to hundreds of nanometers.

As detailed in the previous sections, the magnetic properties of nanowires are governed by their shape and magnetocrystalline anisotropies. The aim of this section is therefore to give an idea about the role of the diameter which governs the delocalized reversal mode, of the shape and of the imperfections which lead to localized reversal modes and of the interactions between nanowires which affects the magnetization state inside the nanowires.

1.3.6.1 Role of the diameter

The diameter d of the nanowires is a crucial parameter which governs the configuration of the magnetization. It has been shown in Section 1.3.5.2 that the diameter of nanowires govern their magnetization reversal modes. For diameters larger than R_{SD} (see Equation 1.36), the magnetic state is divided into lateral magnetic domains and the magnetization is reversed by domain wall propagation.

When the diameter is reduced down to a value smaller than $2R_{SD}$, the single-domain state becomes energetically favorable. For values of radius smaller than the coherent radius R_{coh}, the reversal mode is coherent and can be treated in the framework of the Stoner-Wohlfarth model (see Section 1.3.5.1). Neverthless, very few synthesis techniques (mainly pure chemical ones) allow to obtain nanowires with a radius smaller than R_{coh} [Sou2008, Sou2009a, Soul2009].

In fact, much more studies have been performed on nanowires whose radius is comprised between R_{coh} and R_{SD}. It principally concerns electrodeposited nanowires in porous membranes. For values of radius smaller than the coherent radius R_{coh}, the reversal mode is governed by the curling mode. It has been proved that one can find -for prolate spheroids- a third nucleation mode (besides coherent rotation or curling) if the aspect ratio L/d is larger than 500 [Aha1997].

Aharoni showed that in the case of curling, the coercive field H_C varies linearly with $1/d$. However, for very small diameters close to the threshold $2R_{coh}$ of the transition from curling to coherent reversal, thermal fluctuations may account for a decrease of H_C with decreasing diameters. This has been experimentally observed [Zen2002]. The length of nanowires also plays onto the coercivity value as it was found that for a constant diameter d, the coercivity value rapidly increases with increasing length values and is close to a maximal value for aspect ratios L/d superior to 5 [Zen2000, Zen2002, Zhe2000].

1.3.6.2 Role of the shape and of the imperfections: localization of the reversal modes

Coherent rotation and curling are delocalized modes meaning that the reversal nucleation is extended to the whole volume of the nanowire. However, the situation might be much more complex as illustrated in many studies.

For instance, the role of the diameter has been studied for hexagonally ordered 100 nm period nickel nanowire arrays [Nie2001]. As shown in Figure 1.20, the hysteresis cycles are deeply modified when the nanowire diameter varies from 55 nm down to 30 nm. When the diameter is 55 nm, the sample does not show any preferential magnetic orientation: the remanence is worth only 30% and the coercivity 600 Oe when the magnetic field is applied along the nanowires axes. However, when the diameter is reduced down to 30 nm, the sample clearly exhibits an easy and a hard magnetic axes: the remanence is increased up to 98% and the coercivity up to 1200 Oe when the magnetic field is applied along the nanowires axes. Nevertheless, for diameters of 30 nm, micromagnetic simulations [Nie2001] proved that neither the Stoner-Wohlfart model nor the curling mode can explain the hysteresis shape. In this case, a butterfly-type arrangement of the magnetization at the nanowires tips could account for such hysteresis cycles. Further micromagnetic simulations suggested that the magnetization reversal starts at the nanowire's extremities. Then at both ends of the nanowire, two 180° head-on-domain walls nucleate and

propagate through the nanowire. This has been confirmed by R. Hertel who performed micromagnetic simulations on 40nm diameter Ni nanowires [Her2002].
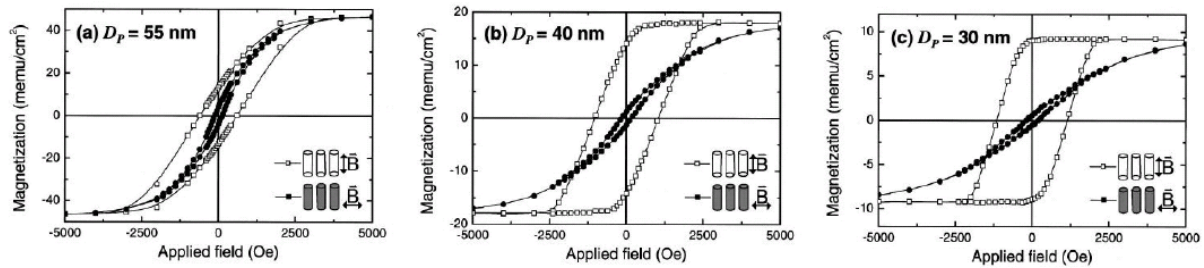
Figure 1.20: SQUID hysteresis loops for hexagonnaly ordered nanowire arrays with a pitch of 100 nm and pore diameters of (a) $D_P \approx 55$ nm, (b) $D_P \approx 40$ nm, (c) $D_P \approx 30$ nm. From [Nie2001].

In a general way, the cylindric shape of nanowires leads to the formation of a vertex at the end of nanowires to minimize the demagnetizing energy. A recent study [Wan2009] on a single 60nm Fe single nanowire combining MFM imaging and micromagnetic simulations confirmed the presence of such a vertex and showed that magnetic moments at the end of a nanowire first reverse at the nanowire's extremities with a curling mode and then reverse in the whole nanowire through domain wall propagation. Therefore, the extremities of nanowires play the role of nucleation point of the magnetization reversal. However, it was also showed that when the magnetic field direction deviates from the nanowire axis, a coherent rotation of the magnetic moments is observed [Esc2007].

The shape of nanowires and the deviation from the ellispoidal shape are the main, but not the only, origins of the reversal localization [Zen2002, Sko2002]. Polycrystallinity, wire-thickness fluctuations, defects or impurities can be reasons for reversal localization even for nanowires whose radius is smaller than R_{coh}[Sko2002, Zen2002].

1.3.6.3   Role of the interactions between the nanowires

As detailed in 1.3.3, the dipolar interaction plays a crucial role in the magnetization configuration and especially for nanowires. The stray field, originating from the dipolar interaction, may affect the magnetization of the surrounding nanowires, for instance by decreasing the coercivity and the remanence. The effects of the magnetostatic interactions between nanowires have been mainly investigated for arrays of nanowires such as nanowires electrodeposited in porous membranes. For instance, the results from [Nie2001] and presented in Figure 1.20 indicate that an increase of the nanowires diameter from 30 nm up to 55 nm and and thus an increase of the packing density lead to a decrease of both remanence and coercivity because of the increase of magnetostatic interactions between nanowires. Some micromagnetic simulations performed by R. Hertel on hexagonal arrays of 40 nm amorphous nanowires (pitch of $p = 100$ nm), in accordance with the arrays of Ni nanowires investigated by K. Nielsch et al. [Her2002] (see Figure 1.20 (b)), showed that the coercive field decreases with an increasing number N of nanowires and is of order of 100 mT for $N = 16$, in agreement with the experimental value ($\mu_0 H_C = 110$ mT) reported in [Nie2001].

It has also been shown [Vaz2004] that the pertinent parameter to characterize the interaction between nanowires is the ratio of the diameter d over the distance between the centers of the objects D ($D = p + d/2$). In agreement with the results presented in Figure 1.20, Figure 1.21(a) underlines the role of the packing density (through the increase of the diameter d) in the magnetization reversal. Figure 1.21(b) indicates that both the remanence and the coercivity decrease with increasing value of the ratio d/D. Encinas-Oropesa et al. expressed the effects of the dipolar coupling as a function of the porosity density P. Indeed, the effective anisotropy field H_{EF} is the sum of two contributions [Enc2001]:

$$H_{EF} = 2\pi M_S - H_U \quad (in\,CGS) \tag{1.55}$$

where $2\pi M_S$ is the self-demagnetizing field and H_U an additional uniaxial anisotropy field which comes from the dipolar coupling and favors an easy axis perpendicular to the wires. The additional uniaxial anisotropy field H_U can be expressed as [Enc2001]:

$$H_U = 6\pi P M_S \tag{1.56}$$

For instance, with $P = 0.1$ we have $H_U = 0.3 \times 2\pi M_S$ which is far from being negligible. Moreover, this model predicts that for P=1/3, the total effective anisotropy field H_{EF} is zero and therefore, the nanowires behave as if they were magnetically isotropic which has been experimentally confirmed in [Enc2001] via magnetic and ferromagnetic resonance experiments.
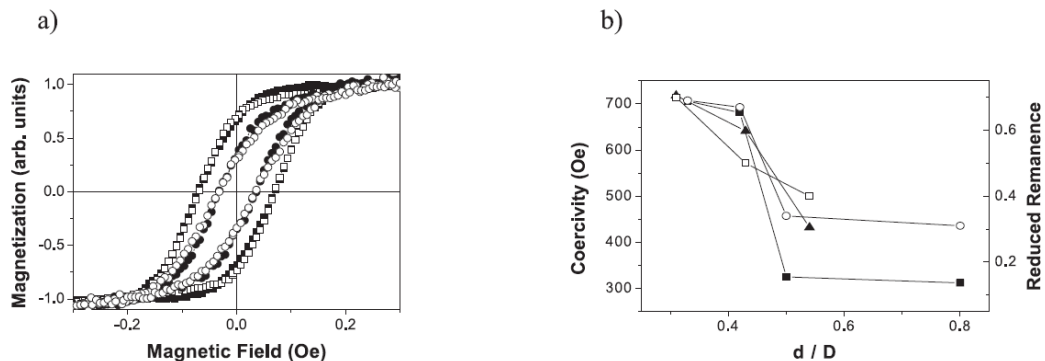
Figure 1.21: (a) Hysteresis loops as a function of the nanowire diameter for Ni nanowires separated 105 nm having diameters of 35 nm (■), 44 nm (□), 53 nm (•) and 83 nm (∘). (b) Dependence of coercivity [membranes prepared in oxalic (■) and sulphuric (▲) acids] and reduced remanence [oxalic (∘) and sulfuric membranes (□)] as a function of the ratio diameter to interwires distance d/D. From [Vaz2004].

Furthermore, it has been recently shown [Kho2009] that the resonance frequency of $Ni_{90}Fe_{10}$ in zero external field can be tuned from 8.2 to 11.7GHz by preparing the sample with different remanent state. Indeed, the resonance frequency in zero external field is linear with the remanent magnetization in sofar as the dipolar field is itself linear with the remanent magnetization. This is clearly due to the magnetostatic interactions between the nanowires.

A recent in-field MFM study [Wan2008] probed the role of the dipolar field in the magnetization reversal evidencing a switching field distribution in arrays of Co nanorods. The experimentally measured switching field distribution compared to the intrinsic switching field distribution (that is to say without taking into account the dipolar effects) indicates that the magnetization of some nanowires reversed without any negative applied field. It implies that the switching field distribution divides into two components: an intrinsic one which depends on the intrinsic properties of the nanowires (in particular their geometrical dimensions, their structure or their defects) and an extrinsic one which comes from the dipolar interactions between the objects. The dipolar field acting on a given nanorod at a random magnetization state has been assessed to $H_{dip} = 1.55 \, M/M_S$ (in kOe) [Wan2008, Wan2009].

The role of dipolar interactions has also been recently revisited for granular hard magnetic materials [Dob2009]. For such materials -in the case where the grains are weakly coupled- the demagnetizing field of a given grain is proportional to the spontaneous magnetization M_S not to the sample magnetization M. It implies that the self-demagnetizing field has to be considered as a contribution to the coercive field.

1.4 Oxidation of magnetic nanostructures: the Exchange Bias effect

The size reduction of systems presenting an interface between two compounds may lead to interfacial effects. Such systems can be for instance magnetic bilayers or magnetic particles in a matrix. One well-known example is the Exchange Bias effect which stems from the exchange coupling between the magnetic moments of ferromagnetic and antiferromagnetic layers at an interface. Metallic nanostructures are indeed known to oxidize when they get in contact with air creating an interface between a metallic core and an oxide shell. In 1956 two engineers from the General Electrics, Meiklejohn and Bean, studied fine Co particles (diameter around $20 \, nm$) embedded in their native antiferromagnetic oxide CoO [Mei1956]. They observed a shift of the hysteresis cycle on the field axis ($\sim 1kOe$) which they attributed to the interfacial exchange coupling between the ferromagnetic moments of the metal core and the antiferromagnetic moments of the oxide shell.

1.4.1 The Exchange Bias effect: phenomenology

In order to describe the principle of this exchange coupling, let us consider an interface between ferromagnetic and antiferromagnetic layers (see Figure 1.22). The Curie temperature T_C of the ferromagnet is assumed higher than the T_N of the antiferromagnet.When the temperature is above T_N, the antiferromagnet is in a paramagnetic state and has therefore no influence on the ferromagnet (see Figure 1.22(a)). The bilayer is then cooled down below T_N under a magnetic field and thus becomes ordered (see Figure 1.22(b)). At the interface between the magnetic moments of the ferromagnetic and antiferromagnetic layers, there is an exchange coupling which can be expressed via an Heisenberg hamiltonian:

$$\mathcal{H} = -J_{int}\vec{S}_{FM}\vec{S}_{AFM} \ , \tag{1.57}$$

where J_{int} is the interfacial coupling constant. The parameters $\vec{S}_{FM}$ and $\vec{S}_{AFM}$ are respectively the spins in the ferromagnetic and antiferromagnetic layers. This exchange coupling leads to an horizontal bias of the hysteresis cycle which can be positive or negative depending on the sign of J_{int}. After saturation, if the magnetic moments of both the ferromagnetic and antiferromagnetic layers are parallel at the interface, the bias is negative.
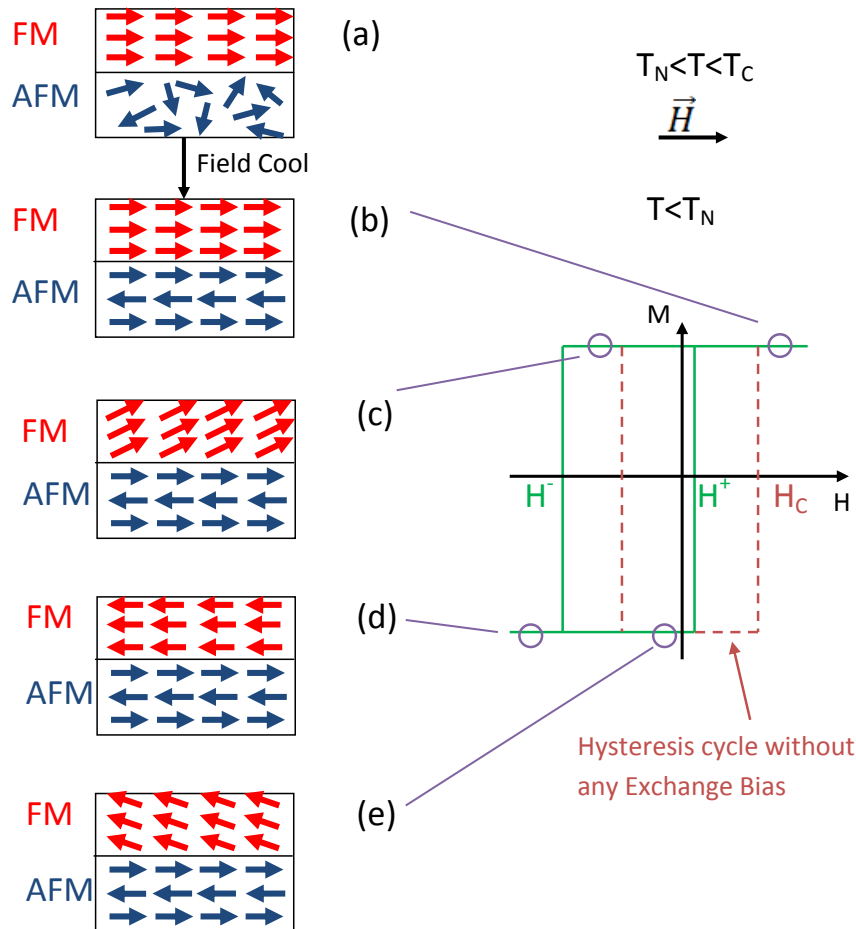
Figure 1.22: Naive principle of the exchange bias effect. Adapted from [Nog1999]

In Figure 1.22, the two intersections of the hysteresis cycle with the axis $M = 0$ are referred to as H^- and H^+ (see Figure 1.22). The interfacial constant J_{int} is a key parameter of the FM/AFM interfacial coupling. If Equation 1.57 seems to be a good starting point, the magnetic anisotropies of both ferromagnetic and antiferromagnetic layers also plays a role. If the magnetic anisotropy of the antiferromagnetic layer is smaller than the one of the ferromagnetic layer, the magnetic moments of the antiferromagnetic layer will reverse first while the magnetic moments of the ferromagnetic layer remain "frozen". However in most cases, the anisotropy of the antiferromagnetic layer is much larger than the one of the ferromagnetic layer so that the magnetic moments of the ferromagnetic layer reverse while the direction of the magnetic moments in the antiferromagnetic layer remain unchanged (see Figure 1.22(c)). In this configuration, the exchange coupling at the interface hinders

the magnetic moments reversal. Therefore the magnetic field which has to be applied to reverse the magnetic moments of the ferromagnetic layer is stronger than if there was no interfacial exchange coupling (see Figure 1.22). It implies that $H^- < -H_C$. When the bilayer is saturated in the opposite way (see Figure 1.22(d)), the nearest ferromagnetic and antiferromagnetic moments at the interface are in opposite directions. The magnetic field which has this time to be applied to reverse the magnetic moments of the ferromagnetic layer is smaller than if there was no interfacial exchange coupling (see Figure 1.22 (e)). It implies that $H^+ < H_C$.

It is customary to define this bias along the field axis as an exchange field H_E. The exchange and coercive fields are respectively defined by:

$$H_E = \frac{H^+ + H^-}{2} \, , \tag{1.58}$$

$$H_C = \frac{H^+ - H^-}{2} \, . \tag{1.59}$$

Note that the exchange coupling appears below a temperature lower than T_N but not necessarily equal to T_N. This temperature is referred to as the Exchange Bias Temperature T_{EB}. It is noted T_{EB} to avoid confusion with the blocking temperature of superparamagnetism, usually written T_B. It means that H_E appears only below T_{EB} and the AFM moments can be considered as blocked for $T < T_{EB}$ while between T_{EB} and T_N, the moments are ordered antiferromagnetically but they fluctuate altogether.

The temperature dependence of the exchange field H_{EB} has been extensively studied [Nog1999, Sta2000].

On the other hand, the temperature dependence of the coercivity is rarely studied although it can exhibit a variety of behaviors depending precisely on the anisotropy of the AFM layer [Nog1999]. As a matter of fact, it can be difficult to clearly distinguish the role of the exchange coupling from the role of the material microstructure in the temperature dependence of the coercivity [Nog1999]. It is first important to specify that in the case where the AFM anisotropy is much larger than the FM anisotropy, no influence on the coercive field H_C should arise from the exchange coupling. The FM and AFM moments are indeed decoupled.

However, it has been shown that, in the case of exchange-biased systems whose AFM layer exhibits a small anisotropy, a coercivity peak can arise around the blocking temperature [Nog1999]. To understand it, let us now consider that the AFM anisotropy is equivalent to the FM anisotropy. Below T_{EB} when the system is warmed up, the AFM anisotropy can become smaller than the FM anisotropy around T_{EB}. In this case, the FM and AFM moments are no longer decoupled. Therefore, when the FM moments rotate, they can drag the AFM moments irreversibly which leads to a slow down of the FM moments reversal. The direct consequence is an increase of the coercivity. Above T_{EB}, the AFM moments are no longer blocked so that they have no more effect on the FM moments reversal and thus on the coercivity. That is why a coercivity peak around T_{EB} is experimentally observed for such systems (see Figure 1.23). However, we will show in Chapter 5 that the coercivity of magnetic nanowires can be strongly affected by the AFM moments even above T_{EB}.
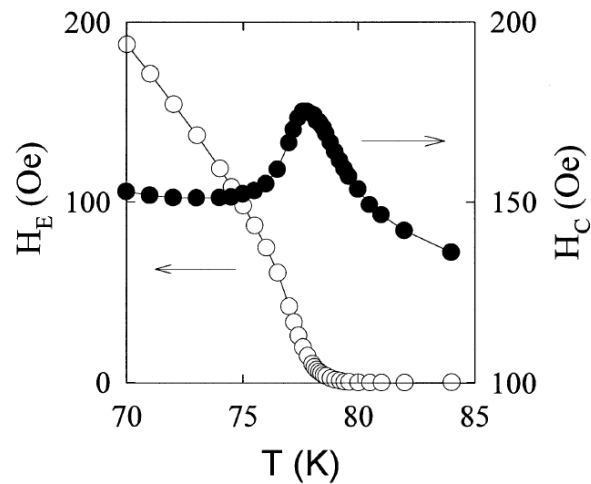
Figure 1.23: Exchange fields H_E and coercivity H_C versus temperature for an FeF_2/Fe bilayer after field cooling [Nog1999].

1.4.2   The Exchange Bias effect: modelling

Most of the recent studies of the exchange bias mechanism have been performed on thin film systems [Ber1999, Nog1999, Nog2005, Rad2008] since they permit a good control of the thickness and textures. If the Exchange Bias effect can be qualitatively understood, there is still a lack of quantitative prediction. Most models developed overestimate the value of the exchange field H_E. To check the proposed models, many efforts have been made to synthesize model systems where the dimensions, the structure or even the roughness of the system can be controlled. A phenomenological modelling for thin films geometry is reported in [Nog1999].

In this phenomenological model , it must be stressed that the following hypothesis are implicit [Rad2007]:

1. The FM layer rotates rigidly as a whole

2. Both FM and AFM layers are in a single domain state

3. The AFM/FM interface is atomically smooth

4. The AFM anisotropy is so large that the AFM moments remain fixed while the FM ones rotate

5. The uniaxial AFM anisotropy is in plane (in the case of a bilayer).

Let us now consider a Co thin film (ferromagnetic) whose thickness is t_{Co} and which is covered with a CoO layer (antiferromagnetic) exhibiting a thickness equal to t_{CoO} (see Figure 1.24). From the qualitative explanations considered above, the energy per unit surface E/S can be expressed as follows as soon as the magnetic moments of the ferromagnetic core rotate coherently:

$$\frac{E}{S} = -\mu_0 \, H \, M_{Co} \, t_{Co} \, cos(\theta - \beta) + K_{Co} \, t_{Co} \, sin^2(\beta) + K_{CoO} \, t_{CoO} \, sin^2(\alpha) - J_{INT} \, cos(\beta - \alpha) \, ,$$
(1.60)

where H is the applied field, M_{Co} the saturation magnetization, K_{Co} the anisotropy constant of the FM core, K_{CoO} the anisotropy constant of the AFM shell and J_{INT} the interface coupling constant. β, α and θ are respectively the angles between the magnetization M and the FM anisotropy axis, the AFM sublattice magnetization (M_{CoO}) and the AFM anisotropy axis, and the applied field and the FM anisotropy axis (see Figure 1.24). Note that the AFM and FM anisotropy axes are usually assumed to be collinear. The anisotropy constant K includes both the magneto-crystalline and the shape anisotropies.
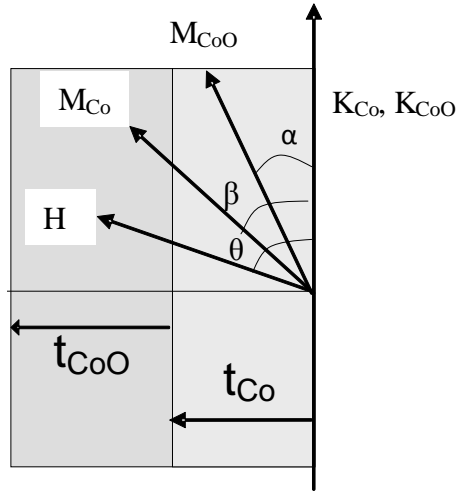
Figure 1.24: Geometry of the core-shell structure for a cylinder

Since the anisotropy of the ferromagnetic layer is supposed to be negligible compared to the one of the antiferromagnetic layer, the energy per unit area E/S becomes:

$$\frac{E}{S} = -\mu_0 \, H \, M_{Co} \, t_{Co} \, cos(\theta - \beta) + K_{CoO} \, t_{CoO} sin^2(\alpha) - J_{INT} \, cos(\beta - \alpha) \, . \qquad (1.61)$$

The hypothesis n°4 leads to:

$$\alpha \approx 0 \, . \qquad (1.62)$$

Moreover, if the magnetic field H is applied along the geometrical axis of the nanowire, then:

$$\theta = 0 \, . \qquad (1.63)$$

Thus the equation becomes $\beta - dependent$ and minimizing the equation leads to the loop shift:

$$H_E^{bil} = \frac{J_{INT}}{M_{Co} t_{Co}} \, . \qquad (1.64)$$

Thus, it appears that the exchange bias field H_E depends on the interface coupling constant J_{INT}. When J_{INT} is approximated to the ferromagnetic exchange, the deduced value for H_E is much larger than the experimental values [Jun1994].

Moreover, the value of the exchange field is inversely proportional to the thickness of the ferromagentic layer t_{Co}. Recently, M. De La Torre Medina et al. [DeL2009] et al. showed that in the case of nanowires, H_E is also inversely proportional to the diameter d of the non-oxidized wire core. This study concluded that the measured exchange bias energy in oxidized nanowires is about four times smaller than the energy in planar bilayers if d is considered as the ferromagnet thickness.

Of course, the model presented above is crude and does not exactly correspond to the experimental realities. That is why to account for such a mismatch between the predicted and experimental values of H_E, researchers focused on systems allowing to probe a key parameter. For instance it appears reasonable that the interface is not smooth (contrary to the interfaces in Figures 1.22 and 1.24). The roughness of the interface gives rise to a decrease of uncompensated spins at the interface [Tak1997] which may explain a lower value of H_E. Malozemoff postulated a random nature of exchange interactions at the interface since the roughness creates lateral variations of the exchange field which applies on the FM and AFM moments [Mal1987]. This model, known as the Malozemoff random field model, conducts the antiferromagnetic layer to break into domains.
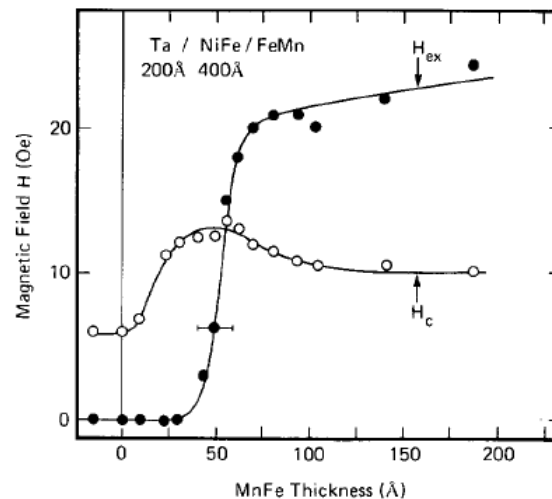
Figure 1.25: Exchange field (filled circles) and coercivity (open circles) versus MnFe thickness measured on $\text{Ta}\big(200\text{Å}\big)/\text{NiFe}(400\text{Å})/\text{MnFe}$ [Mau1987(2)].

Another reason can stem from the formation of domains in the antiferromagnetic [Mau1987, Née1967, Mal1974] or ferromagnetic [Sal1976, Zak1971] layers which lower the exchange coupling at the interface. A model has been proposed by Mauri [Mau1987] who postulates that the antiferromagnetic moments are no longer rigid and develop domain walls parallel to the surface which leads to a reduction of the exchange field.

Other origins like non-colinearity of the spins of the antiferromagnetic and ferromagnetic layers [Bro1970, San1974], grain size distribution [Nis1996] or even random anisotropy of the AFM layer [Ram1997] have also been proposed. Unfortunately, although these models suit well to a specific system, they do not account for the others.

Furthermore, Meiklejohn and Bean showed that the exchange field H_E vanishes when the CoO layer thickness decreases down to a certain threshold [O'H2000]. This loss of exchange coupling has also been evidenced in NiFe/FeMn bilayers where the exchange field vanished for a thickness of the antiferromagnetic layer FeMn lower than

50Å [Mau1987(2)](see Figure 1.25). This effect corresponds to the limit of weak antiferromagnet:

$$K_{AFM}t_{AFM} \ll J_{INT} \,, \tag{1.65}$$

where K_{AFM} and t_{AFM} are respectively the AFM layer anisotropy and thickness. This condition gives rise to a value of the AFM thickness t_{AFM}^c below which no exchange bias may be observed [Mau1987(2)]:

$$t_{AFM}^c = \frac{J_{INT}}{K_{AFM}} \,. \tag{1.66}$$

In this limit, the FM and AFM layers respond in unison to the applied field and the AFM moments are driven away from their preferred axis. The main consequence for such system is the disappearance of the unidirectional anisotropy of the AFM layer. In single domain particles or in thin films corresponding to the weak antiferromagnet limit, the hysteresis cycle should correspond to a coherent rotational process similar to the one of the Stoner-Wohlfarth model. However, the coherent rotation will be dictated by two processes: the coherent rotation between the FM or the AFM ones. It implies that the coercivity will be given by the harder of both processes. One can thus expect that the coercivity obeys to:

$$H_C \leq \frac{2K_{FM}t_{FM}}{\mu_0 M_{FM}t_{FM}} \quad and \quad H_C \leq \frac{2K_{AFM}t_{AFM}}{\mu_0 M_{FM}t_{FM}} \,,$$

where M_{FM}, t_{FM} and t_{AFM} are respectively the magnetization and the thickness of the FM layer and the thickness of the AFM layer.

1.4.3 The exchange Bias effect: applications

What is the most remarkable in the Exchange Bias effect, is that it allows for a ferromagnetic material to get an easy *direction* instead of an easy *axis* for its magnetization. Moreover, antiferromagnets exhibiting a very large anisotropy can be considered as magnetically neutral. Consequently, applications for the Exchange Bias effect take advantage of these two features.

A possible application is the enhancement of coercivity for small magnetic particles [Nog1999]. This is crucial in the case of small particles which are submitted to superparamagnetic fluctuations. The Exchange Bias effect therefore allows to increase the blocking temperature T_B of the particles. The enhancement of coercivity for small particles due to the exchange Bias effect has been studied for permanent magnets [LuB1962] and high density recording media [Gan1992].

Nevertheless, thin films attracted the attention of industrials and researchers because they allow to control very closely the growth of ferromagnetic and antiferromagnetic layers. Several applications based on the pinning of the ferromagnetic moments by the antiferromagnetic layer are used notably for fabricating magnetic recording media [Gla1972] or domain stabilizers in recording heads [Dev1997, Tan1984]. However the most promising route to apply the Exchange Bias effect has been opened by the Giant MagnetoResistance (GMR) effect. Exchange Bias is used in Spin Valves [Nog1999, Koo1996]. Usually, a spin valve is constituted of two ferromagnetic layers separated by an non-magnetic

layer (see Figure 1.26). If one of the ferromagnetic layer is in contact with an adjacent antiferromagnetic layer, the ferromagnetic magnetization of this layer will be pinned by the antiferromagnetic layer. It means that the magnetization of this ferromagnetic layer will not be affected when the magnetization of the other ferromagnetic layer is reversed [Die1991b, GruPat].

It must also be noted that some exchange Bias applications such as perpendicular magnetic recording media or read heads can also be devised from ferro-ferri systems [Bon1988, Oli1997].
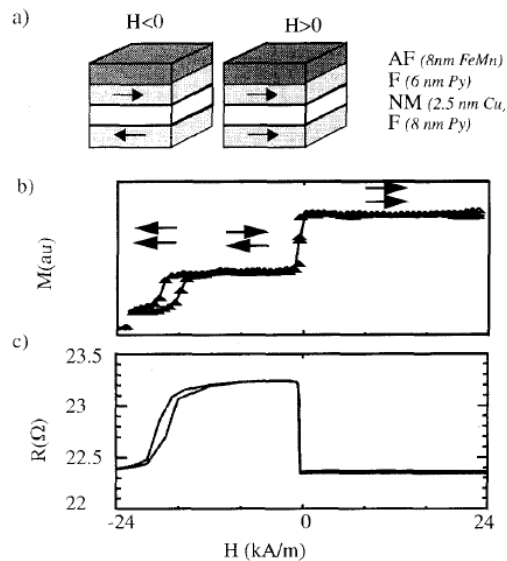
Figure 1.26: (a) Schematic configuration of a spin-valve (basic layout) (b) measured magnetization curve of a spin-valve (c) measured MagnetoResistance curve of a spin-valve [Koo1996].

1.5   Experimental methods to study magnetic nano-objects

Many experimental techniques have been developped to explore nanomagnetism. There are two main experimental approaches to probe the properties of materials. The first one consists in studying the properties of materials in the direct space. Of course, in the nanomaterials field, it requires observation techniques with high spatial resolution. Some huge progress have been made during the last decade, and here we focus on two techniques recently developed: the Spin-Polarized Scanning Tunneling Microscopy (SP-STM) and the electronic holography. These techniques allow to obtain a mapping of the magnetization at the nanoscopic scale. However, there are two main limitations to this approach:

1. Very small nanoparticles whose characteristic size is below the spatial resolution of the techniques can not be investigated

2. The provided information is only local. It is not sure that the information obtained for a piece of the sample is valid on the whole sample.

A third technique known as the micro-SQUID technique consists in fabricating a micro-sized SQUID around a nano-object. This technique allows to obtain the magnetic response of a single nano-object in an applied-field.

The second approach consists in studying the properties of materials in the reciprocal space. The associated techniques provide an access to a global information. However, if the nano-object do not have the same sizes or orientations, the information will be averaged over the size and orientation distributions. This approach allows to study both the static and dynamic magnetic properties of the material.

Note that this description of the experimental techniques used to probe nanomagnetism is not exhaustive and focuses on recently developed techniques suited to the study of nano-objects whose characteristic size is below $50\,nm$. In fact, each experimental technique presents some advantages and some limitations. Therefore, the choice of the experimental technique mainly depends on the characteristics of the sample. The techniques related to the direct space are very useful to probe the magnetic properties of individual nano-objects. The SP-STM technique and the Electron Holography both allow to probe the magnetic properties of very small nano-objects thanks to very good spatial resolution. When the aim is to study some arrays of nano-objects or some collective behaviours, the techniques related to the reciprocal space are well-adapted since they provide an information on the whole sample. Nevertheless it implies that the objects should be monodisperse and with the same orientation so that one has not to take some size and orientation distributions into account.

1.5.1 Experimental techniques in the direct space.

1.5.1.1 Spin-Polarized Scanning Tunneling Microscopy (SP-STM).

The SP-STM acts as a classical STM but the tip is covered with a magnetic material such as Fe. This magnetic material allows to polarize the conducting electrons. As a matter of fact, for non-magnetic tip, like in copper, half of the spins are "up" and the other half "down". For a tip covered with a magnetic material such as Fe, the conducting electrons at the Fermi level are polarized.

The SP-STM combines both the spatial resolution of the STM technique $\left(\sim 0.2\,\text{Å}\right)$ and its sensitivity to surface magnetization. Very recently, the SP-STM technique has been tuned to probe magnetic excitations in nanostructures. This process is based on the spin transfer torque so that the magnetization of the sample may be influenced by the injection of polarized electron current. The Inelastic Scanning Tunneling Spectroscopy (ISTS) has been successfully applied to probe the inelastic spin-torque effect in bulk Fe or in Co thin films [Bal2008], to investigate magnon dispersions and life times in thin Mn, Co and Ni films with an accuracy comparable to neutron inelastic scattering techniques [Gao2008] or even to determine the magnetic anisotropy of single Co and Fe atoms or clusters on Pt(111) substrate [Bal2009]. This recent technique is very well suited to magnetic nanostructures since it allows to study some magnetic systems out of reach with other scattering techniques such as Inelastic Neutron Scattering (INS) or Brillouin Light Scattering (BLS).

1.5.1.2   Electron Holography (EH).

Electron Holography (EH) is a recent development of Transmission Electron Microscopy (TEM). The EH technique is based on the measurement of the phase shift of the electronic wave after interacting with a static electromagnetic field (in this case, the electromagnetic field generated by the sample). The difficulty of this method consists in separating the electrostatic contribution from the magnetic contribution to the phase shift of the electronic wave. This very promising route to probe magnetic nanostructures has been developed in France by E. Snoeck and C. Gatel in CEMES in Toulouse and by A. Marty and P. Bayle in Grenoble. For instance, they succeeded in mapping the magnetization of nanodumbbells whose thickness of the central bar is smaller than 20 nm [Zig].

1.5.1.3   The Magneto-Optic Kerr-Effect.

The Magneto-Optic Kerr Effect (MOKE) gives an access to changes of both polarization and orientation of light by magnetic moments. This effect was discovered by John Kerr in 1877 and can be classified following the direction of the magnetization. If the transmitted wave is measured, the effect is called the Faraday effect. However, in most magnetic materials, the absorption is too large to study the transmission of light. That is why the reflected wave and thus the Kerr effect are most often measured. The Kerr effect mainly depends on the geometry of the magnetization. Indeed, there are three main cases:

1. The polar Kerr effect where the magnetization is perpendicular to the surface of reflection and parallel to the incident plane.

2. The longitudinal Kerr effect where the magnetization lies in the plane of incidence.

3. The transverse Kerr effect where the magnetization is perpendicular to the plane of incidence but parallel to the reflecting surface.

These three techniques allow to obtain imaging of magnetic domains.

1.5.1.4   Micro-SQUID.

The micro-SQUID technique was developed by A. Benoit and applied to magnetism by W. Wernsdorfer and B. Barbara fifteen years ago in order to measure the magnetic response of a single nanoparticle in an applied magnetic field. The idea consists in depositing a single nano-object on a micro-sized SQUID. This device gives an access to the magnetic properties of a single and isolated nanoparticle. After a decade of improvements and developments, the micro-SQUID technique is currently used to study clusters of a few nanometers such as 3nm Co nanoparticle embedded in a niobium matrix [Jam2001, Thi2002] for instance.

1.5.2   Experimental techniques related to the reciprocal space.

1.5.2.1   Neutron scattering.

Neutrons, thanks to their magnetic moment, are a powerful tool to probe magnetism in condensed matter. Neutrons have the following properties:

1. Neutrons easily penetrate thick materials because they are massive and electronically neutral.

2. Neutrons can interact totally differently with atoms whose atomic number is very close or even with different isotopes from the same atom species (see Figure 1.27). This is a great difference with X-Ray whose interaction with atoms is proportional to the square of the atomic number Z. It means that a large contrast can be observed between magnetic atoms like Fe, Ni or Co even though their atomic number Z is very close.

3. The neutron wavelength, comprised between 0.4Å and 20Å, gives access to both the interatomic lengths in crystals and the correlations between particles, polymers or molecules.

4. The neutron energy, comprised between 0.5 meV and 500 meV, allows to probe the excitations in both solids and liquids.

5. Neutrons carry a magnetic moment (spin) and consequently interact with the magnetic moments of the atoms. This property of neutrons lies at the root of their success in magnetism. In 1949 C.G. Shull and J. Samuel Smart performed neutron diffraction on MnO crystals in the Oak Ridge National Laboratory and gave the first proof of the existence of the antiferromagnetic order, which had been proposed by Louis Néel in 1932.

In fact, the main limitation to neutron scattering is the low intensity of the beam. As a matter of fact, the neutron flux is about 10^{15}neutrons.cm^{-2}.s^{-1}. This value is about nine orders of magnitude lower than the one of the third generation of synchrotron (10^{24}photons.cm^{-2}.s^{-1} for SOLEIL, 2005). From this limitation, neutron scattering thus requires large enough samples and long counting times.
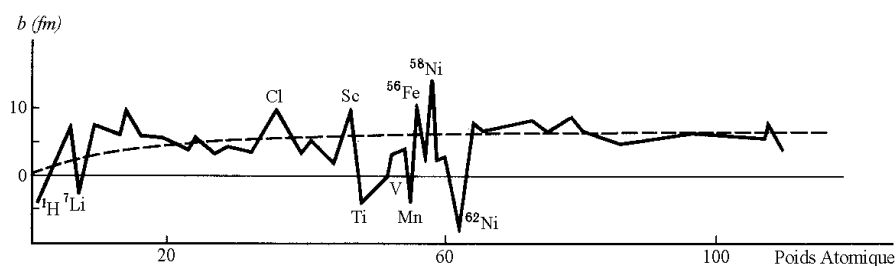
Figure 1.27: The neutron scattering length as a function of the atomic number.

Despite this limitation, neutron scattering remains a powerful tool to probe magnetism and different kinds of spectrometers are devoted to magnetic studies. Elastic neutron scattering studies can be performed such as neutron diffraction which gives an access to both the nuclear and magnetic structures or Polarized Small Angle Neutron Scattering (PSANS) which allows to determine the interactions between magnetic nano-objects. As for inelastic neutron scattering, "Triple Axes" spectrometers of "Time-of-Flight" spectrometers probe the lattice (phonons) and magnetic (magnons) excitations in the matter. Finally, neutron scattering is a good way to get access to both structural and dynamical magnetic properties provided the sample is well-adapted.

1.5.2.2 X-Ray scattering

X-rays are an electromagnetic field. This is why a magnetic interaction between X-Rays and the magnetic moments carried by the electrons in magnetic materials was expected in addition to the charge interactions. The first experimental proof was given in 1972 thanks to Bergevin and Brunel who performed magnetic X-rays magnetic scattering in NiO crystals using a commercial X-ray tube source in Grenoble [Ber1972]. The magnetic diffraction intensity was assessed to be six orders of magnitude lower than the charge scattering intensity, making such studies hard to be performed. The interest in the topic declined until 1985 when Gibbs et al. performed X-rays magnetic scattering on the rare-earth metal holmium, taking advantage of the high X-rays brilliance generated by the synchrotron source of the Brookhaven National Laboratory [Gib1985].

The main techniques which came out of the X-rays magnetic scattering are the X-rays Magnetic Linear Dichroïsm (XMLD) and the X-rays Magnetic Circular Dichroïsm (XMCD) spectroscopies. These both spectroscopies come from the X-rays Absorption Near Edge Structure (XANES) spectroscopy which is dependent to the polarization of X-rays. This feature lies at the root of XMLD and XMCD.

To sum up, XMLD allows to determine the spin order through charge order. Indeed, when the spins are ordered, the spin-orbit coupling is characterized by preferential charge order linked to the spin order. This technique is particularly suited to the determination of ferromagnetic and especially of antiferromagnetic spin direction.

As for the XMCD spectroscopy, it characterizes the difference in the absorption of right and left circularly polarized X-rays by magnetic moments. It allows to determine both spin and orbital magnetic moment of the atoms. Moreover, magnetic circular dichroïsm can lead to a magnetization mapping via the XMCD-PEEM technique (lateral resolution $\sim 20\,\mathrm{nm}$). This technique allowed for instance to investigate three-dimensional magnetization structures of Fe islands with hexagonal shapes and with thickness and lengths respectively up to $250\,\mathrm{nm}$ and $2.5\,\mu\mathrm{m}$ on Mo(110) buffer layers [Her2005]. Moreover, it allows to perform imaging of antiferromagnetic structures [Dür2009, Mig2009].

Finally, magnetic X-rays scattering and neutron scattering are complementary techniques. However, magnetic X-ray scattering is better suited to the investigation of surfaces.

Part I

Magnetic nanowires

In the zoology of magnetic nano-objects, nanowires are particulary interesting even though most experimental works have focused on magnetic nanospheres. The reason is the difficulty to synthesize well-crystallized anisotropic nano-objects. This part of the study is devoted to magnetic nanowires via a bottom-up process known as the polyol process. Chapter 2 describes the polyol process and shows that among the synthesis routes, the polyol process has turned as a good way to synthesize anisotropic magnetic nano-objects - especially nanowires- which are very well crystallized and exhibit aspect ratios as high as 30. This should confer to these objects both large shape and magnetocrystalline anisotropies.

In Chapter 3, the magnetic characterization of these objects at room temperature is presented and compared to the Stoner-Wohlfarth model. It is shown that nanowires randomly oriented exhibit coercivities up to 4.5kOe which is lower than the predicted value but much larger than magnetic nanowires synthesized via other routes. Moreover, the coercivity and the remanence are much better when the nanowires are aligned.

Then, the role of the shape of the objects in the magnetization reversal process is analyzed using micromagnetic simulations performed via the $Nmag$ software. The numerical results are compared to the experimental data and discussed in Chapter 4. It notably underlines the crucial influence of both the aspect ratio and the shape of the tips.

Furthermore, if these nanowires exhibit very good magnetic properties, their manipulation can conduct to a natural oxidation which strongly affects their properties. Chapter 5 details the magnetic properties of the objects from room temperature down to low temperature ($\sim 2.5\,\mathrm{K}$) when the oxide shell modifies the magnetization reversal through the Exchange Bias effect. The experimental results are of prime interest since they give evidence of the fundamental role of the superparamagnetic fluctuations of the CoO antiferromagnetic grains of the oxide shell in the Exchange Bias effect and in the magnetization reversal.

Finally, Chapter 6 discusses the possibility of using these objects for the fabrication of efficient permanent magnets. Such magnets could take advantage of the large shape anisotropy of the nanowires which is almost temperature independent and compete commercialized permanent magnets.

52

Chapter 2

Chemical synthesis and dispersion of magnetic nanowires

The polyol process allows to synthesize anisotropic magnetic objects. The principle is based on the reduction of metallic salts in a dialcohol solution. The nano-objects are collected from the dialcohol solution. In order to study the collected objects, it is possible to dry and press the objects into pellets or to disperse them and put them into form in another medium. The synthesis process is first described before presenting the fabrication of the different investigated samples.

2.1   Synthesis of nanowires

The polyol process has been developed by F. Fiévet et al. [Fig] and consists in dispersing metal precursors (hydroxide, acetate, oxide...) in a polyol solution (usually an $\alpha-diol$) and then in warming without exceeding the polyol boiling point ($\sim 230\,\mathrm{K}$). Polyols are used as solvents because they can act as reducing and polar solvents and also because of their high boiling temperature which allows to solubilize a large number of metal salts and to reduce the latter in a large temperature range. This process has been substantially improved for the past six years thanks to the works of two PhD students, Diane Ung [UngPhD] and Yaghoub Soumare [Sou2009b] under the supervision of Guillaume Viau and Jean-Yves Piquemal, in the Laboratoire ITODYS (Université Paris Diderot). They succeeded in synthesizing anisotropic nano-objects and especially $Co_{80}Ni_{20}$ and Co nanowires as detailed below.

The experimental protocol is relatively simple: the metal cobalt and nickel precursors are dissolved in a sodium hydroxide solution of polyol (metal concentration of $0.08\,\mathrm{M}$) and then reduced by heating the polyol solution. The proportion of cobalt and nickel carboxylates depends on the kind of desired objects. For instance, if the aim is to synthesize $Co_{50}Ni_{50}$ nano-objects, Co and Ni salts will be mixed in equal proportion. Indeed, the cobalt/nickel ratio measured by Energy-Dispersive X-ray spectroscopy in the final metal particles is very close to the ratio in the starting medium. A small amount of ruthenium chloride ($RuCl_3$) is added to seed the medium (the Ru/Co molar ratio is fixed equal to 2.5%). In some experiments a mixture of oleic acid (OA) and trioctylphosphine (TOP) is added to the solution at different times of the reaction in order to coat the surface of the nanowires with surfactants. This makes further wires dispersion easier. The

surfactant/metal molar ratio is 1 in every case.

The mixture is then heated at 170°C with a controlled temperature ramp. The solution turns to black progressively when the reduction occurs. After 30 min at 170°C the reduction is complete and the solution is cooled down. The magnetic powder is recovered by centrifugation, washed with absolute ethanol and dried under vacuum.

What should be underlined here is that after metallic salts dissolution and during the temperature ramp, two phenomena occur at the same time: the reduction of metallic ions in solution and the precipitation of a non-reduced intermediate solid phase which is in equilibrium with metallic species in solution. The growth of nanostructures is initiated from the metallic germs formed after the reduction of solvated species. The general mechanism indicates that several reactional parameters play a role in the formation of metallic particles. These parameters which allow to control the shape and the size of the nano-objects are listed below:

- The nature of the metallic precursors (proportion of cobalt and nickel)

- The basicity of the solution (0.1M)

- The optional addition of a nucleating agent ($RuCl_3$)

- The nature of the polyol (butanediol, propanediol,...)

- The temperature of reaction and the temperature ramp ($100°C - 200°C$)
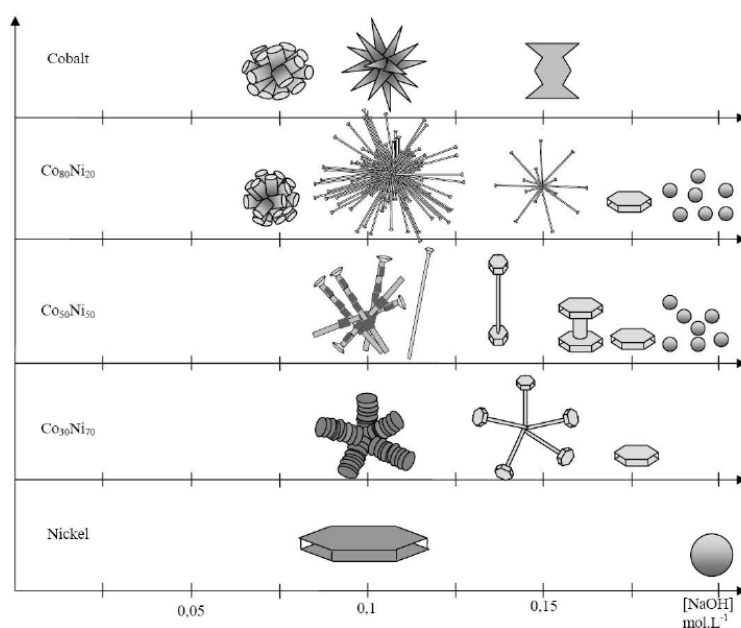
Figure 2.1: Evolution of $Co_{1-x}Ni_x$ nano-objects as a function of x and the basicity of the solution. From [UngPhD, Sou2009b].

The main advantage of the polyol process, except that it easily provides several grams of nano-objects, comes from the richness of the parameters which control the reaction. This allows to obtain a large variety of nanoparticles shapes and dimensions. For example,

the basicity of the solution and the proportion of metallic species are essential to obtain different nano-objects shapes, as detailed in Figure 2.1. The polyol process thus provides a great variety of shapes. Figure 2.1 shows the state of the art in 2005. The great progress which occured just before the beginning of my work has been the synthesis of individual $Co_{80}Ni_{20}$ nanowires. Then during this study, another breakthrough has been the synthesis of individual Co nanorods by Yaghoub Soumare, Jean-Yves Piquemal and Guillaume Viau. The other major advantage of these objects is their monodispersity in size so that there is little need to take any size distribution into account in the analysis of the magnetic measurements.

During my PhD work, I took part in a few sample syntheses under the supervision of Yaghoub Soumare. I realized then, that in spite of the simplicity of this chemical route, the quality of the synthesized nano-objects clearly stems from the good execution at the right time of the successive steps of the process.

2.2 Characterization of the nano-objects.

Figure 2.2 shows some examples of the variety of shapes provided by the polyol process. This process allows to synthesize nanowires (Figure 2.2 (c) and (d)) but also nano-objects with hybrid shapes like nanodiabolos (Figure 2.2 (a)) or nanodumbbells (Figure 2.2 (d)).
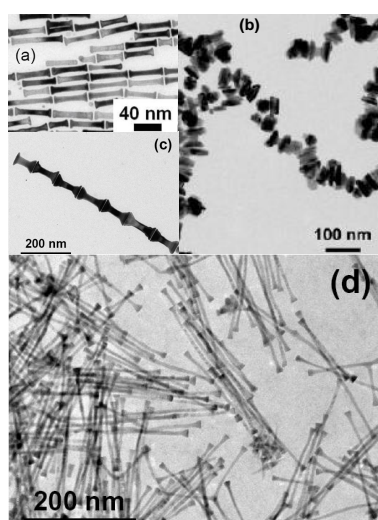
Figure 2.2: TEM images of nano-objects synthesized via the polyol process: (a) Co nanowires, (b) $Co_{50}Ni_{50}$ nanodiabolos, (c) Short Co nanorods and (d) $Co_{80}Ni_{20}$ nanowires. Adapted from [Sou2009a, Sou2008, Ung2007].

During my PhD work, I focussed on $Co_{80}Ni_{20}$ and Co nanowires which allows to compare the magnetic properties of nanowires exhibiting diffrent aspect ratios. In the case of $Co_{80}Ni_{20}$, the mean diameter, d_m, is in the range 7–10 nm and the standard deviation, σ_d, is very small, with a ratio $\sigma_d/d_m = 10\%$. The mean length, L_m, is always found in the range 200–300 nm. The length distribution is broader with a standard deviation generally higher than 25% of the mean length. In the case of Co nanowires, the mean diameter is in the range $10 - 30$ nm and the mean length in the range $100 - 250$ nm, depending on the experimental parameters (metal precursor, $[NaOH]$ and temperature ramp). The

standard deviation of the nanowires diameter distribution is also generally less than 10% of the mean diameter. The dimensions of the $Co_{80}Ni_{20}$ and Co nanowires are summarized in Table 2.1.

Dimension	$Co_{80}Ni_{20}$	Co
Diameter d (nm)	$7-10$	$10-30$
σ_d/d_m	10%	10%
Length L (nm)	$200-300$	$100-250$
σ_L/L_m	25%	25%

Table 2.1: Dimensions of the $Co_{80}Ni_{20}$ and Co nanowires

I also focussed on $Co_{50}Ni_{50}$ nanodumbbells which exhibit a more *hybrid* shape due to large caps at the tips of these objects. Their general shape is represented in Figure 2.3. It is defined by four characteristic lengths [Ung2005b]: l, the mean length of the central column, d, its diameter and D, the diameter of the caps and t their thickness. The total length of these objects, $l + 2t$, is 54 nm with a standard deviation of 17 nm. As for the diameter of the central column d,it is worth 13.5 nm with a standard deviation of 1.9 nm. The diameter of the caps D is 38 nm with a standard deviation of 4.2 nm.
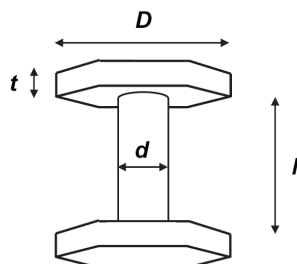
Figure 2.3: General scheme describing the hybrid shapes of the $Co_{50}Ni_{50}$ particles. Adapted from [Ung2005b]

A remarkable feature of these nanowires is their excellent crystallinity. First, in order to understand how Co and Ni are distributed in the nanowires, some EELS (Energy Electron Loss spectroscopy) analysis have been made on $Co_{50}Ni_{50}$ nanodumbbells where the proportions of Co and Ni are equal. The results are shown in Figure 2.4 and confirm that the two metals are partially segregated. Previous studies showed Ni enrichment at the surface compared to the core of spherical bimetallic $CoNi$ particles prepared by the polyol process [Via1996]. This composition gradient was attributed to a difference in the rate of reduction of the two metals. In fact, the formation of hybrid particles with intermediate $NaOH$ concentrations requires a mechanism with two well separated growth steps. The central column is thus formed in a first step that involves mainly the cobalt, and in a second step the caps which involve mainly the nickel. This feature is also transposed to Co and $Co_{80}Ni_{20}$ nanowires. It implies that both Co nanowires and the central column of $Co_{80}Ni_{20}$ nanowires are expected to crystallize in the hexagonal compact phase with the axis $\overrightarrow{c}$ along the geometrical axis while the tips of $Co_{80}Ni_{20}$ nanowires tend to crystallize in the cubic phase.
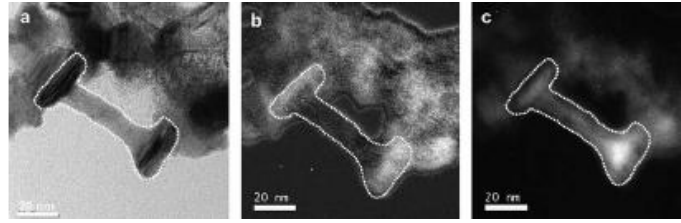
Figure 2.4: EELS analysis of a $Co_{50}Ni_{50}$ dumbbell-like particle: (a) bright field TEM image; (b) mapping of Ni; and (c) mapping of Co. Adapted from [Ung2005].

The powder X-ray diffraction patterns for $Co_{1-x}Ni_x$ show mainly the metallic hcp phase with the fcc phase as a minor phase. The proportion of the fcc phase never exceeds 7% and is generally zero in the samples prepared with surfactants. The XRD line broadening analysis reveals anisotropic crystallites. The crystallite size was calculated using the Scherrer formula. The average values for the hcp [002] and [100] directions are $L_{002} = 20\,$nm and $L_{100} = 5\,$nm, respectively, showing a preferential growth along the crystallographic $\overrightarrow{c}$ axis. This anisotropy is more pronounced in the wires prepared with surfactants. The XRD pattern of wires prepared in the absence of surfactants shows that the (101) line is always slightly broader than the (100) line (Figure 2.5 (a)). It is well known that the presence of stacking faults in the hcp phase has the consequence of broadening the (101) line [War1990]. Calculations allow the density of faults in the hcp phase (δ) to be determined [Cha2003]. It is noteworthy that the wires obtained with an addition of one equivalent of TOP (Trioctylphosphine) and OA (Oleic acid) do not present any faults in the hcp phase, $\delta = 0$ (Figure 2.5 (b)).
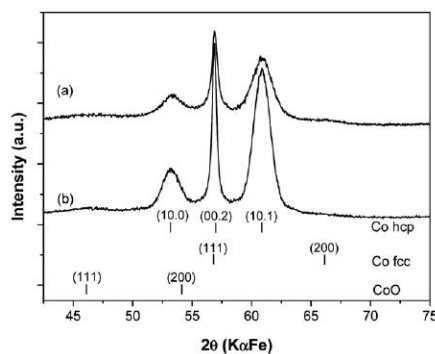
Figure 2.5: XRD patterns of $Co_{80}Ni_{20}$ nanowires prepared in a 0.15 M NaOH solution in 1,2-butanediol (a) without addition of surfactants ($x = 7\%$; $\delta = 0.16$; $L_{100} = 5\,$nm; $L_{002} = 18\,$nm); (b) adding one equivalent of oleic acid + one equivalent of trioctylphosphine at the end of reaction ($x = 0\%$; $\delta = 0$; $L_{100} = 5\,$nm; $L_{002} = 24\,$nm)

Finally, High Resolution Electron Transmission Microscopy (HRTEM) shows very well crystallized wires exhibiting the hcp structure with the crystallographic c-axis parallel to the wire long axis in agreement with XRD analysis shown in Figure 2.6 for Co nanowires.
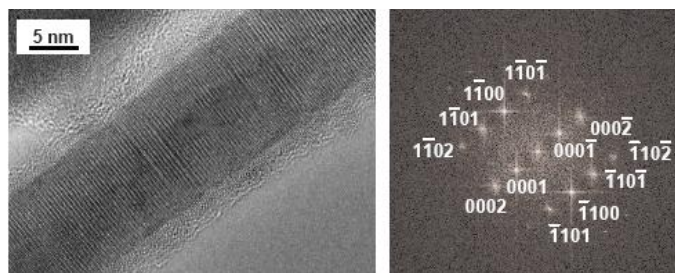
Figure 2.6: High-resolution image of a single cobalt rod in [1 1 2 0] zone axis and corresponding numerical diffraction pattern [C. Gatel].

2.3   Preparation of the samples: dispersion of the nanowires

As explained above, the high boiling point of the polyol ($\sim$ 230K for butanediol) is required for the reduction of metallic species in solution. However, this high boiling temperature prevents the substitution of the polyol by another more adequate solvent for the dispersion of the nanoparticles. Therefore it implies to collect the nanowires from the polyol solution by centrifugation and to wash them several times with ethanol. The samples obtained are thus a powder of nanowires.

To carry the neutron scattering experiments, the samples need to fulfill the conditions quoted in introduction and reminded here:

1. A large quantity of nanowires to get enough scattering signal.

2. Chemically identical and monodisperse objects to perform the scattering study on arrays of identical objects.

3. Same orientations of the nanowires to prevent their properties from being averaged following the orientation distribution. They also have to be sufficiently separated from each other to prevent them from interacting.

The first two conditions are fulfilled by the polyol process which provides several grammes of monodisperse and chemically identical nano-objects. A large amount of nanowires provided is precisely the advantage of the polyol process over other synthesis routes such as electrodeposition in porous membranes. One of the objectives was to separate the collected nanowires from each other and to disperse and align them in a matrix. This challenge is also crucial to improve the magnetic properties of the samples. (see Section 1.3.5.1). Two different strategies were implemented:

1. The particles were dispersed in a polymer solution (polystyrene or polymethyl methacrylate dissolved in toluene or dimethylacetamide) and the material solidified under a magnetic field while the solvent was evaporating. The nanowires are expected to align along the magnetic field direction.

2. The particles were dispersed in liquid toluene or dimethylacetamide where they are in principle to rotate. A magnetic field of $1T$ was then applied during the freezing

of the solution. Once the solution was frozen, the orientation of the particles was also frozen.

After dispersing the particles, we use Ultra-Sounds technique to separate the nanowires as some of them may be aggregated. The choice of solvent plays a key role in the success of these strategies and depends on the investigated nanowires. As a matter of fact, some acetate groups are grabbed at the surface of $Co_{80}Ni_{20}$ nanowires whereas surfactants such as laurate are present at the surface of Co ones. The choice of solvent is determined by the chemical groups at the surface of the objects and is thus different from one kind of objects to another one. When I began my PhD work, toluene was used to disperse every kind of objects. However, it was observed that the objects dispersed in toluene used to settle after about ten minutes. If it was not a problem for the second strategy since it takes only few minutes to apply a magnetic field and to freeze the toluene solution, it was a clear limitation of the fabrication of composite polymer films made with such objects since many hours are required to dry the polymer solution. After many attempts, I found that the dimethylacetamide was a suitable solvent for the dispersion of $Co_{80}Ni_{20}$ nanowires since the mixing of these nanowires with dimethylacetamide has been stable for many weeks. Unfortunately I did not find any solvent which allows a good dispersion of Co nanowires.

The other key factor to align the nanowires is the homogeneity of the magnetic field. Indeed, as long as the sample is liquid, an inhomogeneous magnetic field creates a field gradient that moves the objects from the center to the edges of the sample cell. The polymer solutions were dried in teflon moulds measuring 80mm $\times$ 70mm. These moulds allowed to make 40mm $\times$ 40mm polymer films. In order to make the polymer solutions dry in a oven, a system made of 2cm $\times$ 2cm $Nd_2Fe_{14}B$ permanent magnets of $1T$ and of Fe bars was constructed (see Figure 2.7). This device allowed to contains the 80mm $\times$ 80mm teflon moulds.
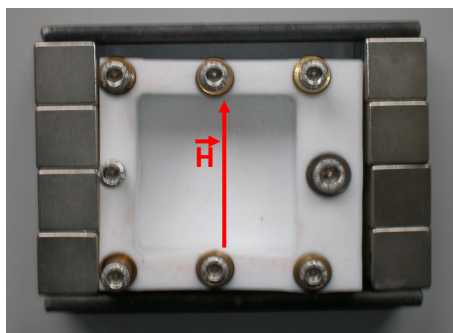
Figure 2.7: Device made of $Nd_2Fe_{14}B$ permanent magnets and of Fe bars.

Simulations performed with Finite Element Method Magnetics (FEMM) software gave an access to the homogeneity degree of the induced magnetic field by this set-up (see Figure 2.8). It proves that the magnetic field is very homogeneous in the central part of the mould. This is confirmed by the profiles (extracted from the color cuts of Figure 2.8) shown in Figure 2.9. The homogeneity of the magnetic field is about 2%.
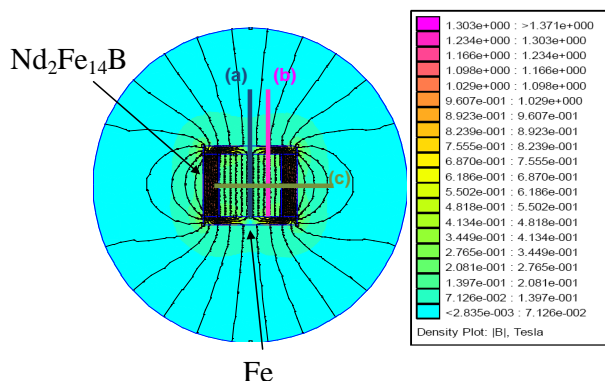
Figure 2.8: Magnetic field induced by the device of permanent magnets shown in Figure 2.7. The color lines (a), (b) and (c) define the sections giving the profile of the magnetic field for different position (see Figure 2.9).
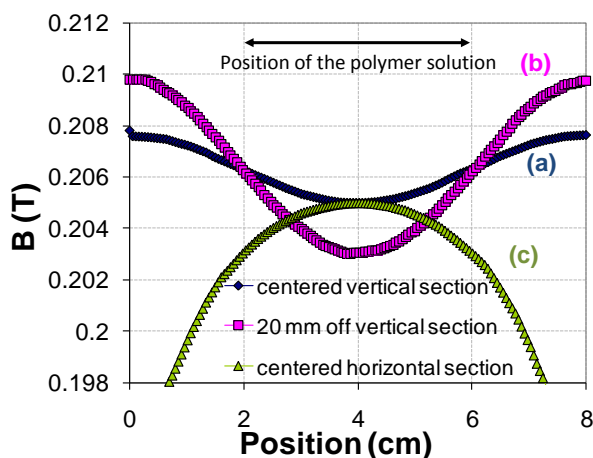
Figure 2.9: Magnetic field induced in the device of permanent magnets as a function of the position. The profiles (a), (b) and (c) refer to Figure 2.8.

The last crucial parameter to fabricate polymer films made with aligned nanowires is the concentration of nanowires in the host matrix. As a matter of fact, the higher the concentration, the more probable is the agglomeration of the nano-objects. At the same time, if the concentration is too low, the sample will not suit to neutron scattering. Some volumic concentrations between 1% and 10% have been tested.

2.4   Conclusion

Finally, the polyol process is a pure chemical route which allows to synthesize very thin nanowires ($d < 15 \, \mathrm{nm}$) so that a coherent magnetization reversal mode can be expected (see Section 1.3.5). Such nanowires are also very well crystallized which could help preventing from magnetic inhomogeneities. These nanowires have been dispersed and aligned in different matrixes (solvent, polymers). Magnetic characterizations of these samples are presented in Chapter 3.

Furthermore, the relative good monodispersity of these objects allows to study their dispersion and their magnetic properties via Small Angle Neutron Scattering techniques. The results are presented in Chapter 8.

Chapter 3

Magnetic characterization of the nano-objects at room temperature

The aim of the magnetometry measurements, performed at room temperature and presented here, is to determine whether the samples exhibit easy or hard magnetic axes. Vibrating-Sample Magnetometer (VSM) is well adapted to study the magnetic properties of samples depending on their orientation. Section 3.1 first presents the hysteresis cycles of nanowires powders. Then Section 3.2 characterizes the magnetic properties of samples with aligned nanowires. Finally Section 3.3 compares the magnetization of aligned nanowires with the Stoner-Wohlfarth model which is related to magnetization reversal mode via coherent rotation.

3.1 Magnetic characterization of nanowires powders

The hysteresis cycles of randomly oriented Co and $Co_{80}Ni_{20}$ nanowires and $Co_{50}Ni_{50}$ nanodumbbells have been investigated. The investigated objects are presented in Figure 3.1 and their corresponding total lengths and diameters of the central column are provided in Table 3.1.

	Co	$Co_{80}Ni_{20}$	$Co_{50}Ni_{50}$
Diameter d (nm)	15	7	15
Length L (nm)	150	240	55
Coercivity $\mu_0 H_C$ (T)	0.52	0.36	0.15
predicted $\mu_0 M_S$ (T)	1.76	1.53	1.19
predicted K_1 (J/m^3) at RT [O'H2000, Ono1979]	5×10^5	3.9×10^5	2.3×10^5

Table 3.1: Dimensions and coercivity of randomly oriented $Co_{80}Ni_{20}$ nanowires, Co nanowires and $Co_{50}Ni_{50}$ nanodumbbells. The corresponding predicted saturated magnetization and magnetocrystalline anisotropy of such objects are also indicated.

The hysteresis cycles, measured on non-oriented powders at room temperature, are presented in Figure 3.2. The coercive fields H_C are respectively 0.52 T, 0.36 T and 0.15 T for Co nanowires, $Co_{80}Ni_{20}$ nanowires and $Co_{50}Ni_{50}$ nanodumbbells. Several reasons may explain that the coercivity decreases with increasing proportion of Ni:

1. The saturated magnetization M_S, which contributes to the shape anisotropy of nanowires (see Section 1.3.5.1), is much larger for Co ($\mu_0 M_S = 1.76\,\text{T}$) than for Ni ($\mu_0 M_S = 0.62\,\text{T}$).

2. Co is mainly present in the central colum and crystallizes with the axis $\overrightarrow{c}$ along the geometrical axis (see Figure 2.6) which contributes to maintain the magnetization along the geometrical axis. Ni, on the other hand, is mainly present at the tips of the objects and crystallizes in the cubic phase so that magnetization reversal is made easier from the tips.
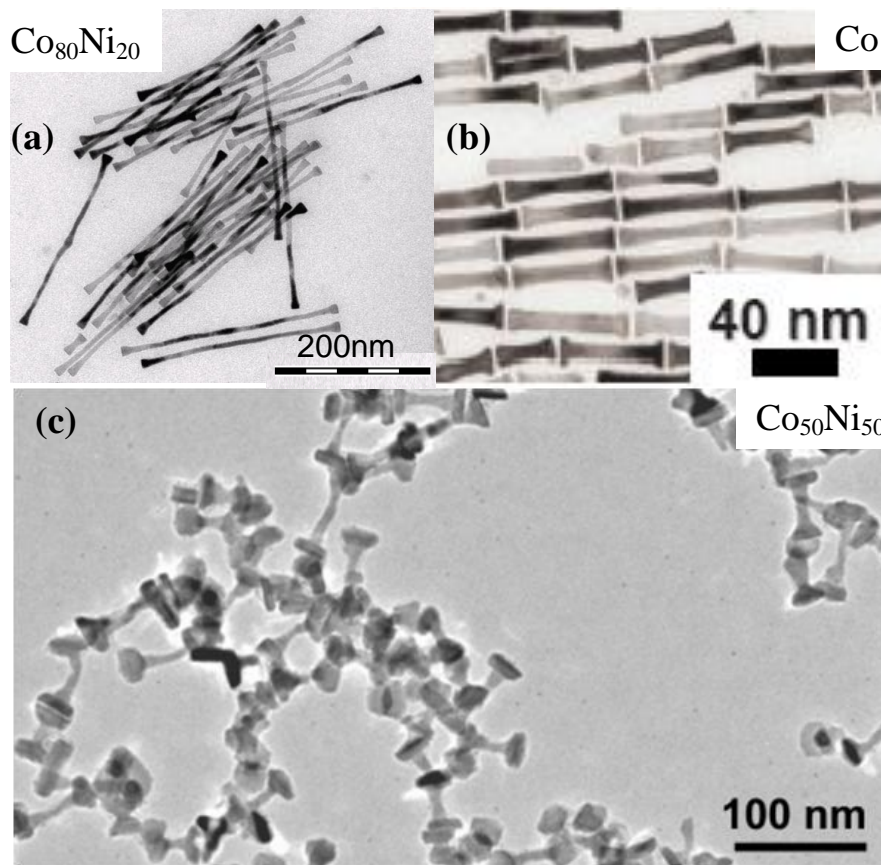
Figure 3.1: TEM images of (a) $Co_{80}Ni_{20}$ nanowires, (b) Co nanowires and (c) $Co_{50}Ni_{50}$ nanodumbbells.

The other feature of these hysteresis cycles which needs to be clarified is the difference between the remanence of $Co_{50}Ni_{50}$ nanodumbbells and the one of Co and $Co_{80}Ni_{20}$ nanowires. Indeed, $Co_{50}Ni_{50}$ nanodumbbells exhibit remanence of $M_R/M(H = 2\text{T}) = 0.5$ whereas Co and $Co_{80}Ni_{20}$ both exhibit remanence of $M_R/M(H = 2\text{T}) = 0.67$. It has been shown in Section 1.3.5.1 that within the Stoner-Wohlfarth model, 3D-systems exibits a remanence of $0.5\,M_S$. The remanence of $Co_{50}Ni_{50}$ nanodumbbells is therefore in agreement with the Stoner-Wohlfarth model. The experimental value measured for Co and $Co_{80}Ni_{20}$ nanowires is higher than the one expected for randomly oriented objects. This may be attributed to the fact that the external magnetic field $H = 2\text{T}$ provided by the VSM is not large enough to saturate the Co and $Co_{80}Ni_{20}$ nanowires.
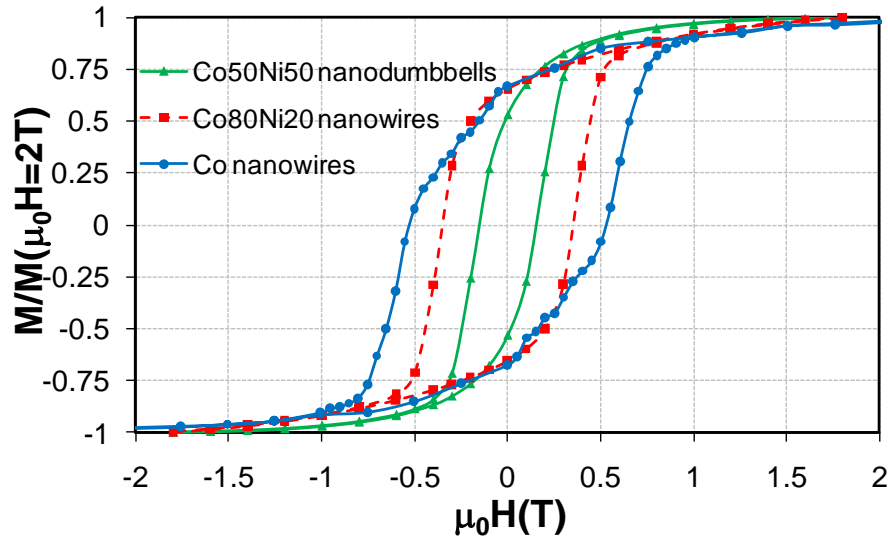
Figure 3.2: Hysteresis cycles at 300K of randomly oriented nano-objects: *Co* nanowires, $Co_{80}Ni_{20}$ nanowires and $Co_{50}Ni_{50}$ nanodumbbells measured with a VSM.

The hysteresis cycles of similar nanowire powders were then measured with a SQUID (Superconducting Quantum Interference Device) which provides magnetic fields up to $H = 5T$ (see Figure 3.3). This time, the remanence $M_R/M(H = 5T) \approx 0.5$ is in agreement with the Stoner-Wohlfarth model which confirms that saturation of *Co* and $Co_{80}Ni_{20}$ nanowires requires large magnetic fields.
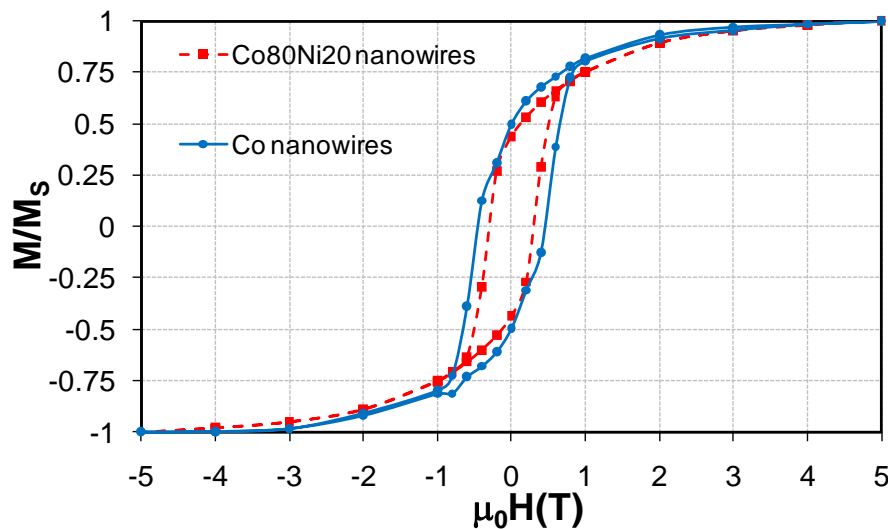
Figure 3.3: Hysteresis cycles at $300K$ of randomly oriented nano-objects: *Co* and $Co_{80}Ni_{20}$ nanowires measured with a SQUID (magnetic fields up to 5T).

3.2 Magnetic characterization of aligned nanowires

Simulations presented in Section 1.3.5.1 showed that both the remanence and the coercivity depend on the relative orientation of the nanowires. Therefore, I tried to disperse

and align nanowires in a host (solid or liquid). This section presents the magnetic characterization of the different investigated samples.

3.2.1   Nanowires aligned in a polymer matrix

In order to produce solid samples at room temperature, I first tried to disperse and align nanowires in a polymer matrix. A polymer was disolved in a solvent in order to obtain a polymer solution. Then nanowires were added to the polymer solution and the mixture solidified under a magnetic field (see the device presented in Section 2.3) while the solvent was evaporating. The nanowires are expected to align along the magnetic field direction.
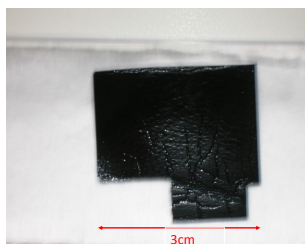
Figure 3.4: Photography of a polystyrene film made with a $Co_{80}Ni_{20}$ nanowire volumic concentration of 5%.
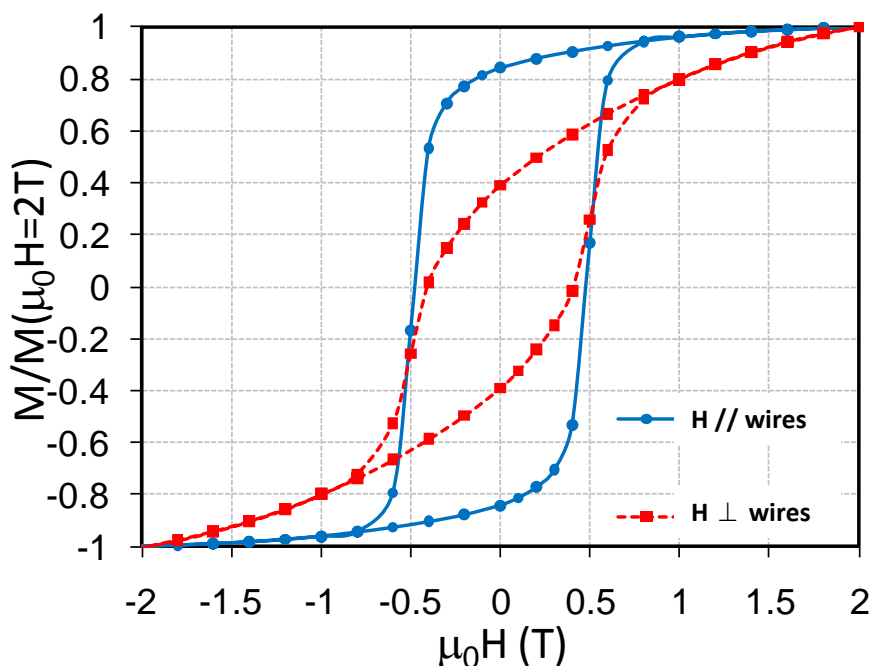
Figure 3.5: Magnetization of $Co_{80}Ni_{20}$ nanowires dispersed in PMMA with the magnetic field applied along the nanowires and perpendicular to the nanowires axis at T=300 K.

During my PhD work, I made attempts with different polymers (principally poly(methylmethacrylate) (PMMA) and polystyrene) and different solvents (toluene, dimethylformamide,...) (see Figure 3.4). The best results were obtained for $Co_{80}Ni_{20}$ nanowires with toluene and

PMMA. The corresponding hysteresis cycle is presented in Figure 3.5. Due to a partial alignment of the particles, the magnetic characteristics have been improved compared to those of non-oriented nanowires. The sample clearly exhibits easy and hard magnetic axes. The remanence has increased to $0.85 M_S$ in $Co_{80}Ni_{20}$ nanowires with their easy axis aligned along $\overrightarrow{H}$ compared to $0.67 M_S$ for powder samples (see Figure 3.2). Similarly, the coercive field has increased from 0.36T to $0.48T$ (see Figure 3.2).

However, as precised in Section 2.3, toluene is not an appropriate solvent for the dispersion of both Co and $Co_{80}Ni_{20}$ nanowires since the particles demix after about ten minutes whereas many hours or days are required to dry the polymer solution. At the end of my PhD, I found that dimethylacetamide (DMAC) allows a good dispersion of $Co_{80}Ni_{20}$ nanowires and that the solution remains stable during many weeks. Unfortunately I did not have enough time to make successful attempts.

3.2.2 Nanowires aligned onto flat surfaces

In order to have better aligned nanowires in solid forms, some drops of toluene solution containing some Co nanowires onto flat surfaces (Si substrates) were dried under a magnetic field. Figure 3.6 (a) shows that the deposited Co nanowires tend to form some microscopic structures looking like some *cigars* and Figure 3.6 (b) illustrates that the wires can be aligned with an external magnetic field inside these microstructures. The magnetization curve of the Co nanowires deposited on Si substrates under an external magnetic field applied during the evaporation of the solvent was measured at 300 K. A coercivity $\mu_0 H_C = 0.55$T and a remanence to saturation ratio $Mr/Ms = 0.9$ were obtained (see Figure 3.7). The rather high value of this ratio confirms the Scanning Electron Microscope images presented in Figure 3.6 and indicates that the alignment of the nanowires on the surface is good. If these samples provide a good alignment of the nanowires, they unfortunately do not exhibit enough quantities of matter to be studied via neutron scattering.
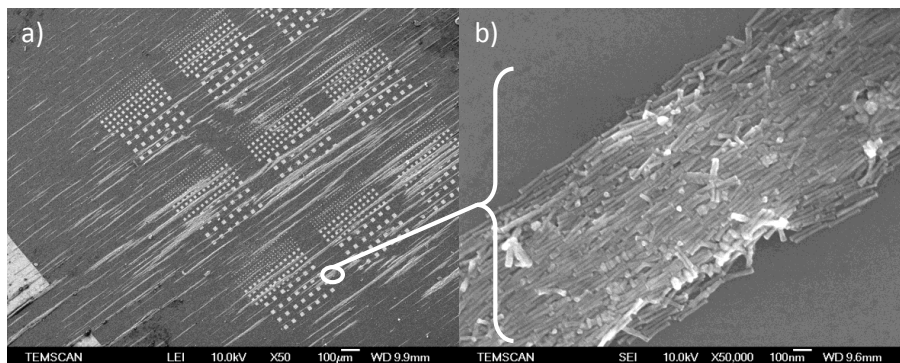
Figure 3.6: Scanning Electron Microscope images of Co nanowires deposited under a magnetic field onto a Si substrate: a) at the microscopic scale, the objects form some microstructures with *cigar* shape, b) Co nanowires are rather well aligned inside these microscopic structures
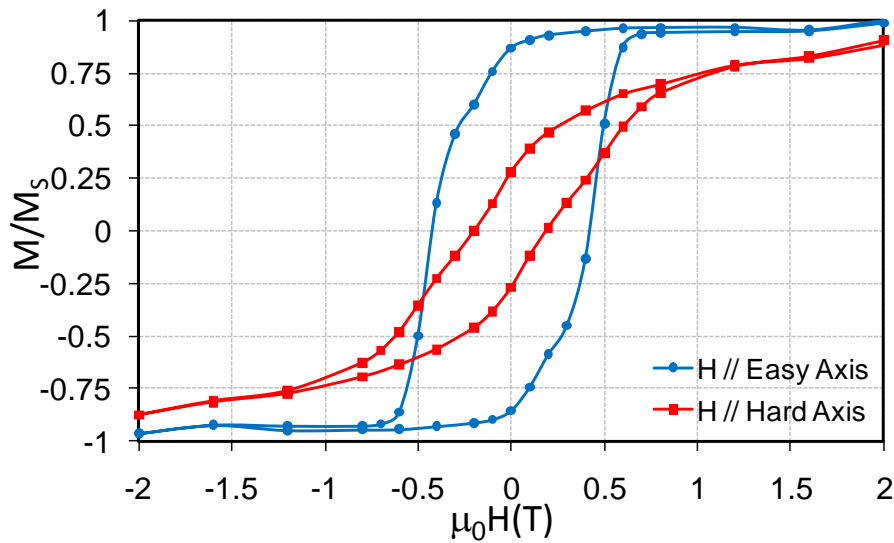
Figure 3.7: Magnetization curve of Co nanowires deposited on a Si substrate with an external magnetic field

3.2.3 Nanowires aligned in a frozen liquid solution

In order to fabricate samples exhibiting a better alignment of nanowires, I conceived a third process. The idea consisted in dispersing the nano-objects in liquid toluene where they are freeer to rotate than in a polymer solution. Then a magnetic field of $1T$ was applied during the freezing of the solution . The magnetization was measured at $140\,\mathrm{K}$ which is below the freezing point of toluene ($T_f = 180\,K$) (see Figure 3.8). I performed the magnetic measurements on a SQUID since the VSM did not allow to perform measurements at low temperature.

	$Co_{80}Ni_{20}$	Co	$Co_{50}Ni_{50}$
Coercivity $\mu_0 H_C(\mathrm{T})$ at $T = 140\,\mathrm{K}$	0.65	0.9	0.42

Table 3.2: Coercivity of the investigated $Co_{80}Ni_{20}$ and Co nanowires and $Co_{50}Ni_{50}$ nanodumbbells.

The square shape of the hysteresis loops suggests that the particles are well aligned in the solid toluene matrix. The characteristics of the sample are significantly improved: the coercive field is increased to $0.42\,\mathrm{T}$ for $Co_{50}Ni_{50}$ nanodumbbells, to $0.65\,\mathrm{T}$ for $Co_{80}Ni_{20}$ nanowires and to 0.9T for Co nanowires (see Table 3.2), compared to respectively $0.15\,\mathrm{T}$, $0.36\,\mathrm{T}$ and $0.52\,\mathrm{T}$ for powder samples. Of course, the temperature of measurement ($140\,\mathrm{K}$) can be expected to increase the coercivity. However, in Section 5.1.2, it will be seen that $T = 140\,\mathrm{K}$ is not a temperature which necessarily provides larger coercivities than room temperature due to the oxidation of the nano-objects. Moreover, the increase of remanence up to $0.87\,M_S$ for $Co_{50}Ni_{50}$ nanodumbbells, up to $0.95\,M_S$ for Co nanowires and up to $0.974\,M_S$ for $Co_{80}Ni_{20}$ nanowires indicates that these objects are very well aligned in the frozen toluen matrix. Therefore, the nanowire alignment has significantly enhanced the anisotropy effects as it is shown in the next section for Co and $Co_{80}Ni_{20}$ nanowires. This

process, however, requires to work at low temperatures to freeze the particle solvent which may be an handicap for other studies such as neutron scattering.
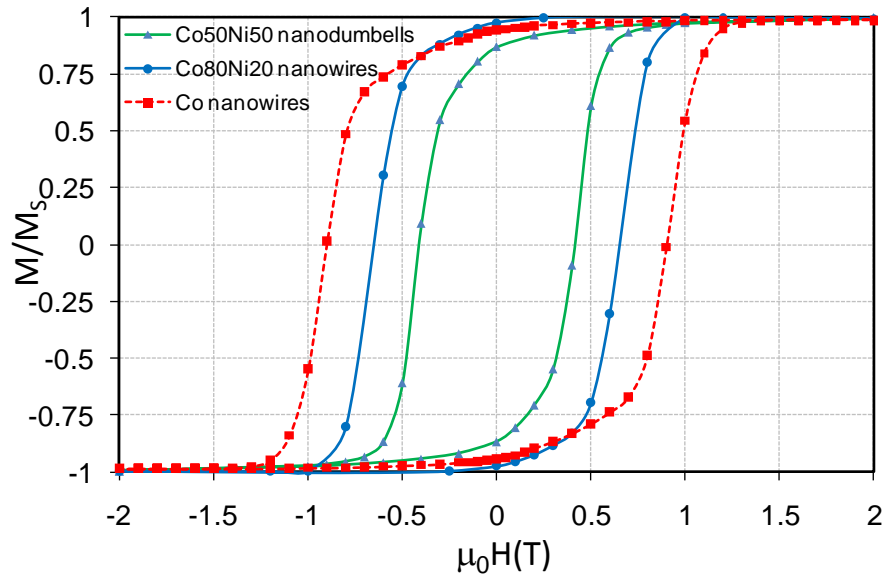
Figure 3.8: SQUID measurements on Co and $Co_{80}Ni_{20}$ nanowires dispersed and aligned in a frozen toluene under an external magnetic field of 1 T. The measurements were made at 140 K.

3.3 Modelling the magnetization of aligned nanowires with the Stoner-Wohlfarth model

To extract quantitative information about the ordering of the particles in the frozen solution, the Stoner-Wohlfahrt model [O'H2000] has been considered. It has been shown in Section 1.3.5.1 that the shape of the hysteresis cycles strongly depends on the relative orientation of the nanowires. Therefore I performed similar simulations to characterize the orientation distribution of the objects in the frozen toluene solution. The contributions of both the magnetocrystalline and shape anisotropies are also expected to be deduced from these simulations.

The Stoner-Wohlfarth model is well suited since nanowires are a limiting case of very elongated ellipsoids, almost monodisperse and with excellent crystallinity. Moreover , the diameter of the wires is sufficiently small to ensure that they are in a single domain state [O'H2000, Sel2000]. Three magnetic energies are considered: the magnetostatic energy, the magnetocrystalline energy, and the Zeeman energy. The free parameters of the model are the angular distribution of the wire directions, which is assumed to be the gaussian and the magnetocrystalline anisotropy field.
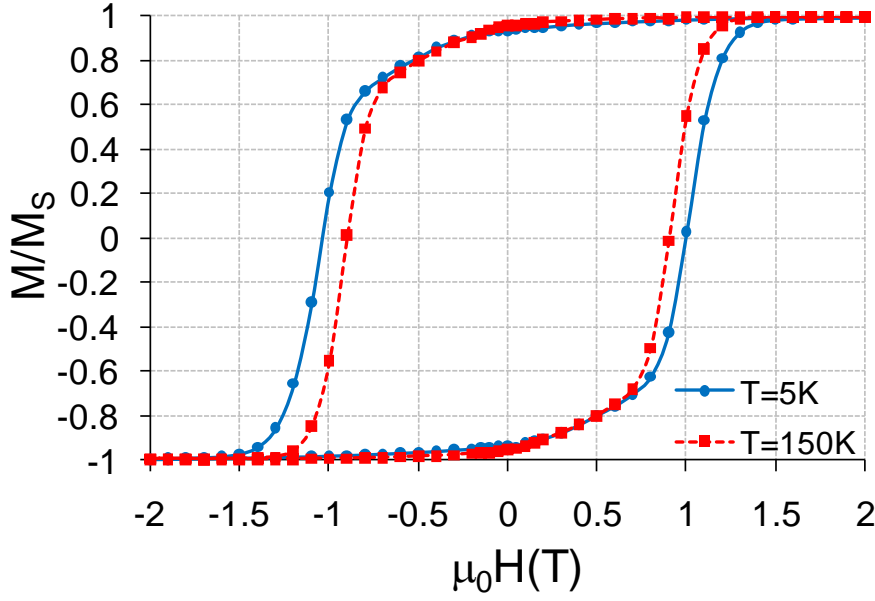
Figure 3.9: SQUID measurements on *Co* nanowires dispersed and aligned in a frozen toluene under an external magnetic field of 1 T. The measurements were made at 150 K and 5 K.

The Stoner-Wohlfarth model is only valid for T=0K that is to say when there are no thermal fluctuations. The question arises whether this model can be applied at $T \approx$ 140 K. The diameter of the objects is such that the Curie temperature is close to bulk *Co* ($T_C = 1390$ K). Measurements are performed at $T_C/10$ which ensures that the exchange energy is not weakened by temperature effects. Furthermore, to ensure that the Stoner-Wohlfarth model can be applied at $T \approx 140$ K, the energies into play have to be assessed. The thermal fluctuations are characterized by an energy $E_{th} = k_B T$ which is of the order of $E_{th} \approx 2 \times 10^{-21}$ J at $T \approx 140$ K. The shape anisotropy energy of a nanowire of diameter and length 100 n*m* ($V \approx 8 \times 10^{-24}$ m^3) is of the order of $E_{sh} = \frac{1}{4}\mu_0 M_S^2 V \approx 5 \times 10^{-18}$ J and the magnetocrystalline anisotropy of $E_{MC} = K_{Co} V \approx 5 \times 10^{-18}$ J. The ratio between the total anisotropy energy and the thermal fluctuations is therefore:

$$\frac{E_{sh} + E_{MC}}{E_{th}} \approx 5000. \tag{3.1}$$

It means that thermal fluctuations at $T = 140$ K can be neglected for such nanowires so that the Stoner-Wohlfarth model can be applied. Moreover, this calculation indicates that the contribution of the shape and magnetocrystalline anisotropies are of the same order of magnitude for such nanowires.

This is experimentally confirmed by Figure 3.9 which shows the hysteresis cycles of aligned Co nanorods in toluene solution at $T = 150$ K and at $T = 5$ K. No major difference between the magnetic behaviour at $T = 150$ K and at low temperature is observed. The coercivity loss of 10% from $T = 5$ K to $T = 150$ K mainly stems from the magnetocrystalline anisotropy temperature dependence (see Figure 6.6).
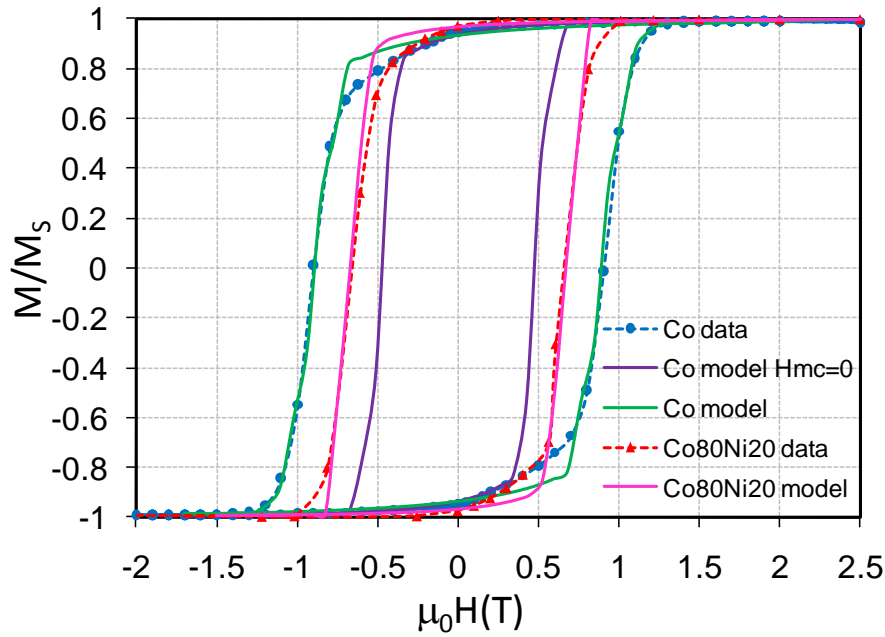
Figure 3.10: Comparison between the hysteresis loops of Co and $Co_{80}Ni_{20}$ nanowires aligned in a frozen toluene solution at $T = 140\,\mathrm{K}$ and simulations using a Stoner-Wohlfarth model. The free parameters are the orientation distribution ($\sigma_\theta = 10°$ for $Co_{80}Ni_{20}$ nanowires and $\sigma_\theta = 15°$ for Co ones) and the contribution of the magnetocrystalline anisotropy to the coercivity ($\mu_0 H_{MC} = 0.3\,\mathrm{T}$ for $Co_{80}Ni_{20}$ nanowires and $\mu_0 H_{MC} = 0.42\,\mathrm{T}$ for Co ones).

The magnetization measurements of both Co and $Co_{80}Ni_{20}$ nanowires (presented in Figure 3.8) have thus been modeled within the Stoner-Wohlfarth model. The comparison between the experimental data and the simulations is shown in Figure 3.10. The experimental hysteresis cycles have first been modeled by considering a gaussian distribution of the nanowire orientation. The value of σ_θ (half-width at half maximum) has been adjusted to fit the remanence (see Figure 3.10, purple curve for Co nanorods). The fit of the remanence led to $\sigma_\theta = 10°$ and $\sigma_\theta = 15°$ for respectively $Co_{80}Ni_{20}$ and Co nanowires. However, there is a large mismatch between the modelled and experimental values of the coercivity (see figure 3.10, comparison between the purple and dashed blue curves). For the moment, in the model, the onlycontribution to the anisotropy is the shape one. That is why, in order to correct this micmatch, the magnetocrystalline anisotropy has been taken into account which allows to well fit the experimental data (see Figure 3.10, green and pink curves for respectively Co and $Co_{80}Ni_{20}$).

The experimental hysteresis cycles have thus been modeled with a reasonable accuracy by considering a dispersion of the nanowire orientation of $\sigma_\theta = 10°$ (half-width at half maximum) and $\sigma_\theta = 15°$ for respectively $Co_{80}Ni_{20}$ and Co nanowires and by introducing a magnetocrystalline anisotropy field $\mu_0 H_{MC} = 0.3\,\mathrm{T}$ for $Co_{80}Ni_{20}$ nanowires and $\mu_0 H_{MC} = 0.42\,\mathrm{T}$ for Co nanowires. This leads to the conclusion that the observed coercivity $\mu_0 H_C = 0.65\,\mathrm{T}$ for $Co_{80}Ni_{20}$ nanowires ($\mu_0 H_C = 0.9\,\mathrm{T}$ for Co nanowires) is the sum of the two equivalent contributions: a magnetocrystalline anisotropy $\mu_0 H_{MC} = 0.3\,\mathrm{T}$ (respectively $\mu_0 H_{MC} = 0.42\,\mathrm{T}$) which is very close to the value for bulk hexagonal cobalt and a shape

anisotropy which contributes to $\mu_0 H_{shape} = 0.35$ T (respectively $\mu_0 H_{shape} = 0.48$ T) to the coercive field. The contribution of the shape anisotropy is rather disappointing since, for perfectly aligned nanowires, one would expect $\mu_0 H_{shape} = \mu_0 M s/2$, which would be 0.75 T for $Co_{80}Ni_{20}$ nanowires and 0.9 T for Co nanowires. However the experimental coercivities of these nanowires are much larger than the ones of nanowires synthesized via other processes which barely exceed 0.1 T even for perfectly aligned nanowires in porous membranes [Sel2000]. The large coercivities of these nanowires compared to the ones of other systems is due to their very small diameter and to their high quality of crystallinity which both favors a coherent rotation process.

3.4   Influence of the interactions between nanowires

A remaining question concerns the interactions between the objects in suspension in the solvent. Figure 3.6 shows that nanowires tend to form microscopic aggregates so that there can be magnetic interactions between the objects when they are not enough separated. The dried nanowires are covered with an oxide shell which is typically $1 - 2$ nm thick so that the distance between the ferromagnetic cores is of the order of 4 nm. Figure 3.11(a) indicates that the dipolar field of nanowires is very localized near their tips (in a volume with a typical size given by the radius of the nanowires). It implies that when the nanowires are side to side (see Figure 3.11(b)), the interaction between each other can be neglected. Moreover when the nanowires are head to head (see Figure 3.11(c)), the distance of 4 nm between the objects is large enough to consider that the interaction between each other is weak ($H_{dipolar}$ is of the order of $0.5 - 1$ kG which is five to ten times smaller than the coercive field). Nevertheless, if in Figure 3.11(c), the distance between the objects is reduced down to zero, there will be formation of a longer nanowire. The initial value of the diameter takes the coherent rotation for granted and the extended length should provide both higher remanence and coercivity. Thus, it appears reasonable to neglect the magnetic interactions between the objects in a first approximation.
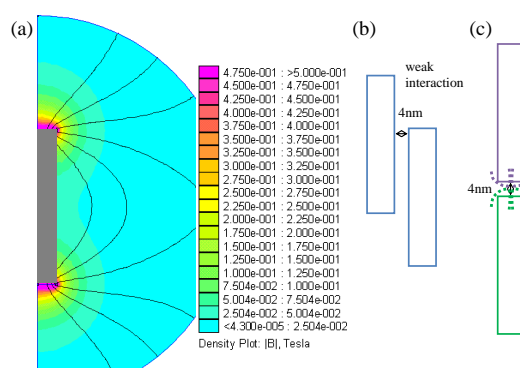
Figure 3.11: (a) Dipolar field of a nanowire with a diameter of 8 nm and a length of 100 nm.The dipolar field is localized near the tips of the nanowires, (b) when the nanowires are side to side, the interaction between each other is weak, (c) when the nanowires are head to head, they are enough separated because of the oxide shell and the solvents at their surface to consider the interaction between each other as weak.

In order to put into evidence the influence of the dipolar interactions between nanowires

on their hysteresis cycles, micromagnetic simulations have been performed on different kind of aggregates (see Figure 3.12) via the Nmag software [Fis2007, Nmag]. The studied model nanowire is a 100 nm long, 10 nm diameter cylindrical wire (see Figure 3.12 (a)) which is representative of the experimental objects which exhibit an aspect ratio around 10. The magnetic parameters used correspond to typical values for *hcp* cobalt epitaxial thin films [Tan1961], saturation magnetization $M_S = 1400 \, \text{kA.m}^{-1}$, exchange constant $A = 1.2 \times 10^{-11} \, \text{J/m}$. The magnetocrystalline anisotropy has been set to $K_1 = 2.5 \times 10^5 \, \text{J.m}^{-3}$. The distance between two nodes of the mesh $(1 - 2 \, \text{nm})$ has been chosen smaller than the exchange length $\ell_{ex} = \sqrt{A/\mu_0 M_S^2} \approx 2.2 \, \text{nm}$.
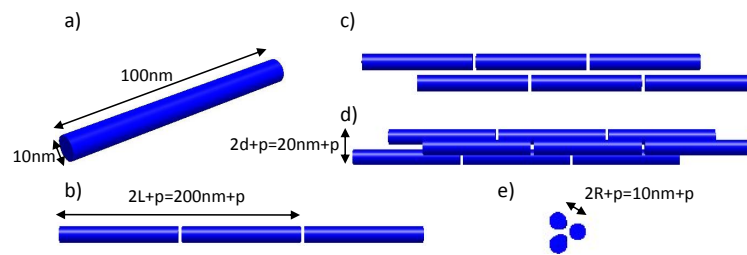
Figure 3.12: Representation of the different simulated aggregates. (a) The nanowires which constitue these aggregates exhibit a diameter of 10 nm for a length of 100 nm. (b) Chain of nanowires separated by a picth p which can be 3, 10 or 20 nm. Chains made of 2, 3 or 5 nanowires have been investigated. (c) Two chains of nanowires which are side to side. The distance between nanowires has been set to 3 nm and aggregates of 4, 6 or 10 nanowires have been investigated. (d and e) Side and front views of nanowires which are in staggered rows. The distance between the nanowires is 3 nm and the number of the nanowires which constitute the aggregates is 3, 6, 9 or 15.

Moreover, TEM images showed that the distance betwwen nanowires in aggregates is at least $3 - 4 \, \text{nm}$ because of the oxide shell and organic matter at the surface. That is why the pitch p between nanowires has been set to 3 nm. In the case of chains of nanowires (see figure 3.12 (b)), further simulations have been performed with $p = 10 \, \text{nm}$ and 20 nm.

Figure 3.13 represents some examples of the simulated hysteresis cycles for an applied field with an angle of 5.7° with the long axis of the nanowires. The coercive field and the remanence of an isolated nanowire are respectively $H_C = 647.01 \, \text{mT}$ and $M_R/M_S = 0.9948$. The comparison between the hysteresis cycle of isolated nanowires (dark curve) and the hysteresis cycles of the simulated aggregates indicate very slight changes in their shape but also in the values of the remanence and the coercive field.

These simulations show that in the case of chains of nanowires (see Figure 3.12 (b)), both the coercive field and the remanence are improved in very slight proportions (see Table 3.4) so that there is no real difference with the case of a single nanowire. Major changes occur when the nanowires are side to side (see Figure 3.12 (c)) or in staggered rows (see Figure 3.12 (d) and (e)). Indeed, when the nanowires are side to side, the coercive field is lowered to about 609.36 mT (see Table 3.5) which corresponds to a decrease of only 6% compared to the case of isolated nanowires. No real change in the values of the remanence is noticed. When the nanowires are in staggered rows, the coercive field is lowered to about 634.5 mT (see Table 3.6) which corresponds to a decrease of only 2% compared to the case of isolated nanowires. Once again, no real change in the values of

the remanence is noticed.
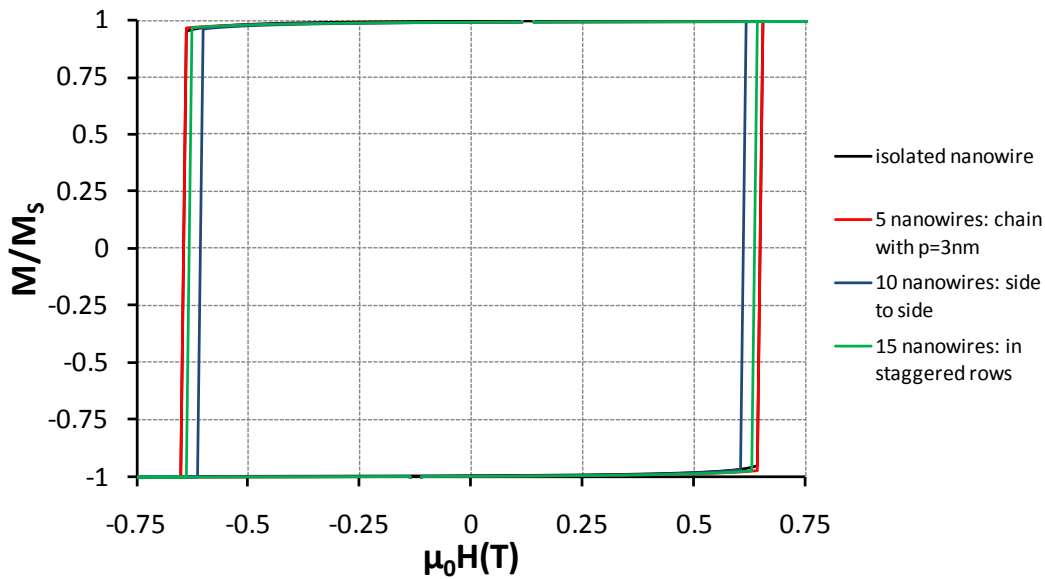
Figure 3.13: Hysteresis cycles of: (dark) an isolated nanowire (see Figure 3.12 (a)), (red) a chain of 5 nanowires separated with a pitch of 3 nm (see Figure 3.12 (b)), (blue) 10 nanowires side to side separated with a pitch of 3 nm (see Figure 3.12 (c)) and (green) 15 nanowires in staggered rows with a pitch of 3 nm (see Figure 3.12 (d) and (e)). The applied field is set with an angle of 5.7° with the long axis of the nanowires.

The different configurations correspond to the different possible geometries of aggregates of nanowires. The results of the simulations prove that no major changes are observed in the shape of the hysteresis cycles and in the values of the coercivity so that the interactions between nanowires can be neglected in a first approximation. The stray field is indeed localized near the tips of the nanowires. In 2D arrays of nanowires (see Section 1.3.6), the stray field between nanowires affects in large proportions both the remanence and the coercivity for porosities of only 10% [Enc2001, Nie2001]. Nevertheless, the geometric configurations of chains or aggregates prevent the stray field between nanowires from largely affecting their magnetization reversal.

	2 nanowires	3 nanowires	5 nanowires
$p = 3$ nm	$H_C = 647.05$ mT $M_R/M_S = 0.9948$	$H_C = 647.07$ mT $M_R/M_S = 0.9949$	$H_C = 647.08$ mT $M_R/M_S = 0.9949$
$p = 10$ nm	$H_C = 647.04$ mT $M_R/M_S = 0.9948$	$H_C = 647.05$ mT $M_R/M_S = 0.9948$	$H_C = 647.06$ mT $M_R/M_S = 0.9948$
$p = 20$ nm	$H_C = 647.03$ mT $M_R/M_S = 0.9948$	$H_C = 647.03$ mT $M_R/M_S = 0.9948$	$H_C = 647.04$ mT $M_R/M_S = 0.9948$

Table 3.4: Values of the coercive field and the remanence for chains of nanowires (see Figure 3.12 (b)).

4 nanowires	6 nanowires	10 nanowires
$H_C = 609.33\,\text{mT}$	$H_C = 609.35\,\text{mT}$	$H_C = 609.36\,\text{mT}$
$M_R/M_S = 0.9943$	$M_R/M_S = 0.9946$	$M_R/M_S = 0.9953$

Table 3.5: Values of the coercive field and the remanence for nanowires side to side (see Figure 3.12 (c)).

3 nanowires	6 nanowires	9 nanowires	15 nanowires
$H_C = 634.48\,\text{mT}$	$H_C = 634.49\,\text{mT}$	$H_C = 634.51\,\text{mT}$	$H_C = 634.51\,\text{m}T$
$M_R/M_S = 0.9953$	$M_R/M_S = 0.9951$	$M_R/M_S = 0.9950$	$M_R/M_S = 0.9950$

Table 3.6: Values of the coercive field and the remanence for nanowires staggered in rows (see Figure 3.12 (d) and (e)).

3.5 Conclusion

Powders of nanowires synthesized via the polyol process exhibit large coercivities ($\sim 0.4\,\text{T}$ at room temperature). The values of coercivities are largely improved when the nanowires are well aligned ($\sim 0.9\,\text{T}$ at $140\,\text{K}$). However, even if such values of coercivities are among the largest ever measured for Co-Ni nanowires [Soul2009], the contribution of the shape anisotropy is rather disappointing (about half the predicted value).

It can be argued that the discrepancy between the experimental and predicted contributions of the shape anisotropy comes from the detailled geometrical shape of the objects, and particularly from the geometrical shape of their extremities. In order to put into evidence the role of the nanowire geometry in the magnetization reversal, micromagnetic simulations have been performed with the Nmag software [Nmag, Fis2007] and have been compared to the experimental data in Chapter 4.

Chapter 4

Micromagnetic simulations

The polyol process allows to synthesize anisotropic nano-objects of both different shapes and aspect ratios. It has been shown that the objects provided by the polyol process exhibit large coercivities. One reason stems from their large shape anisotropy. However the contribution of the shape anisotropy to the coercive field is about half the predicted value by a coherent reversal model. The aim of this chapter is therefore to understand why there is such a discrepancy between the predicted and experimental values.

As detailed in Section 1.3.6, previous experimental studies coupled with micromagnetic simulations [Nie2001, Her2002] showed that arrays of Ni nanowires with small enough diameters ($\sim 30 - 40$ nm) do not exhibit any delocalized reversal modes (in particularly curling) but localized ones characterized firstly by the nucleation of the magnetization reversal in the extremities and secondly by the propagation of the magnetization reversal via a domain wall. A systematic study [Uhl2004] of the magnetization reversal in Co and $NiFe$ nanolines of thickness 16 nm and of width ranging from 65 to 1130 nm showed that nucleation governs the magnetization reversal and that the magnetization switching is controlled by the ends of the nanolines. Therefore a small area of the nanolines governs the magnetization reversal of the whole object.

The objective consists here in determining how the magnetization reversal and the coercivity are affected by the detailed shape of the extremities and the aspect ratio of such objects. To answer this question, micromagnetic simulations [Ott2009] have been performed using the Nmag software [Fis2007, Nmag]. Then the micromagnetic simulations have been compared with experimental data.

4.1   Relation between the shape of a nanowire and its coercivity

In a first approximation, nano-objects synthesized via the polyol process behave as elongated ellipsoids. In the case of ellipsoids, if one assumes a coherent rotation of the magnetization, the shape anisotropy field is given by $H_a = M_s.\Delta N$ where ΔN is the difference between the long and short axis demagnetizing factors. For infinitely long ellipsoids $\Delta N = 1/2$; for an aspect ratio of 5, ΔN is equal to 0.42. Thus in the case of 3d magnetic materials such as Co, the shape anisotropy field should have values of the order of 0.9 T. However, such high values are experimentally never observed [Sel2000]. The main reason

for this discrepancy lies in the coherent rotation behavior assumption. The single domain radius limit is of the order of 15 nm for Co (see Section 1.3.5). The case of nanowires corresponds to an intermediate situation where the diameter of the wires is smaller than the single domain limit whereas the length of the wires is significantly larger. Complex magnetization reversal mechanisms such as curling or localized reversal modes are thus likely to occur (see Section 1.3.5).

The numerical micromagnetic simulations presented here underline which parameters are important in the shape of magnetic nanowires to provide the highest magnetic coercivity. The starting point are the different types of magnetic nano-objects which have been synthesized via the polyol process by Guillaume Viau, Jean-Yves Piquemal and Yaghoub Soumare during the last few years.

Following the experimental observations detailed in Chapter 2, the particles have been divided in a few different possible types (see Table 4.1):

    a. Ellipsoids, which are uses as reference objects,

    b. Cylinders,

    c. Cylinders with rounded edged,

    d and e. Dumbbells (cylinders with spherical ends),

    f and g. Diabolos (cylinders with conical ends),
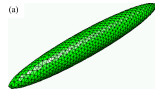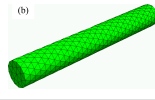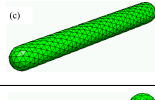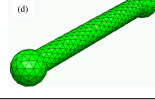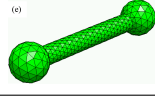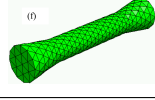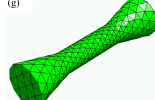
		Features
	Ellipsoids	Long axis L , short axis D
	Cylinder	Length L , diameter D
	Capped cyl.	Half-sphere of diameter D at both ends
	Dumbbell 1	Spheres of diameter 1.5D at both ends
	Dumbbell 2	Spheres of diameter 2D at both ends
	Diabolo 1	Cones of base 1.5D and length 1.5D
	Diabolo 2	Cones of base 2D and length 2D

Table 4.1: Parameters describing the different objects. The length L of the objects is set at 100 nm, the diameter D ranges from 5 to 28 nm.

For these different types of objects, aspects ratios ranging between 3.6 and 20 have been considered (see Table 4.1). This aspect ratio is defined as the ratio between the length

of the object L and its middle diameter D. The length was fixed to $L = 100\,\text{nm}$ which is an average size for these objects. The aim was not to model specific objects but rather to draw general trends which should help in the choice of appropriate shapes for the magnetic properties optimization. In *all* the simulations, the wires were made of cobalt ($M = 1400\,\text{kA/m}$) even though real systems are often $CoNi$ alloys. This was necessary to be able to quantitatively compare the different results and focus on geometrical aspects. Note that the magneto-crystalline anisotropy has not been included to avoid mixing different sources of coercivity. We only focus here on the influence of the shape anisotropy.

The micromagnetic simulation software which has been used is the *Nmag package* [Nmag, Fis2007] to perform 3D simulations on the various types of nanowires geometries. The meshes have been created using *Netgen* [Net]. The number of nodes ranged from about 800 for the smallest aspect ratio (~ 3.6) up to 5000 for the highest aspects ratios objects (~ 20). The use of a finer mesh did not change the results (as checked in a few cases). This number of nodes was sufficient to give a value of the coercive field with an accuracy better than 10 kA/m (10mT) which is well below the requirement for the discussion.
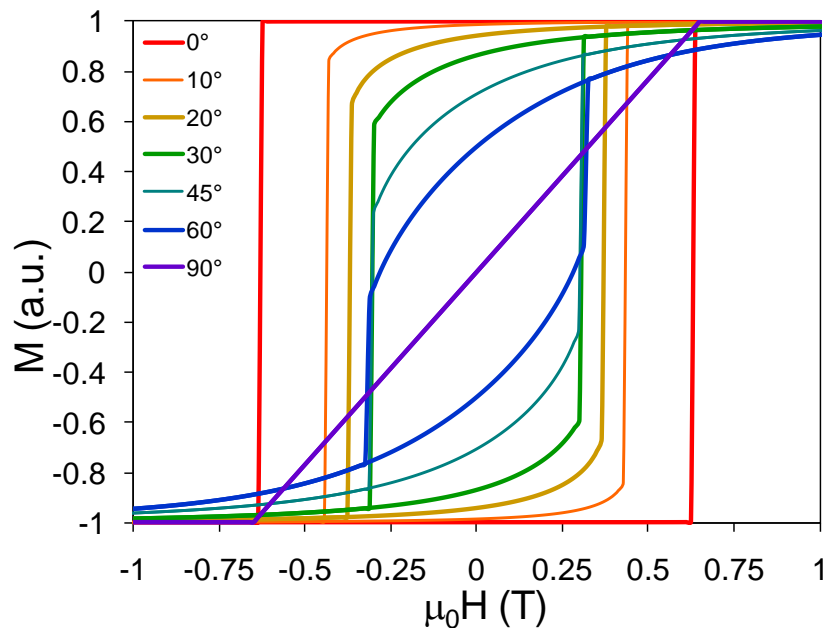
Figure 4.1: Evolution of the hysteresis loop as calculated in the Stoner-Wohlfahrt model for an ellipsoid with an aspect ratio of 3.6 for different orientations of the applied field with respect to the easy axis. The numerical micromagnetic calculations for the ellipsoids (5.7°, 30°, 45°, 60°) agree perfectly with these analytical curves.

Some calculation of hysteresis loops have also been performed for various orientations of the magnetic field with respect to the wires. Figure 4.1 shows the evolution of the hysteresis cycles in the analytical Stoner-Wohlfahrt model in the case of an ellipsoid with an aspect ratio of 3.6. The values of the coercive field vary little when the applied field angle is between 30° and 60° whereas the shape of the hysteresis changes dramatically. When the field is perpendicular to the object, the hysteresis cycle closes. As for the case of magnetic fields applied along the nanowire geometrical axis, I considered an applied

field making a finite angle of 5.7° (i.e. H parallel to the vector $h = [1, 0.1, 0]$) with respect to the object easy axis. This is of the order of the best alignments of the nano-objects that can be experimentally achieved and is thus closer to realistic conditions. By the way, this also ensures a faster convergence of the calculations.

The role of the tip shape and the aspect ratio are discussed in the following subsections. How do the shape of the tips and the aspect ratio of the object modify the hysteresis loops?

4.1.1   Role of the tip shape

The Stoner-Wohlfarth model which assumes a coherent rotation of the magnetic moments is only valid for ellipsoids with small enough diameters (typically of the order of the exchange length). However real systems may exhibit other shapes as presented in Table 4.1. It can be guessed that a shape different from an ellipsoid may give rise to other reversal processes of the magnetic moments even for radius smaller than the coherent radius.

Figure 4.2 compares the hysteresis curves for the different types of particles when the magnetic field is applied at an angle of 5.7°. The highest coercive fields are obtained for ellipsoids or objects whose shape is close to ellipsoid (cylinders and capped cylinders). The lowest coercive fields correspond to the *Diabolo 2* and *Dumbbell 2* objects which exhibit large extremities. The hysteresis loop of the *Diabolo 2* is more significantly rounded but nevertheless the coercivity is higher than for *Dumbbell 2* objects. This suggests that the reversal mechanism is rather different between these objects. Note that the cases of *Dumbell 2* and *Diabolo 2* respectively correspond to the real $Co_{80}Ni_{20}$ and Co nanowires and is detailed in Section 4.2.
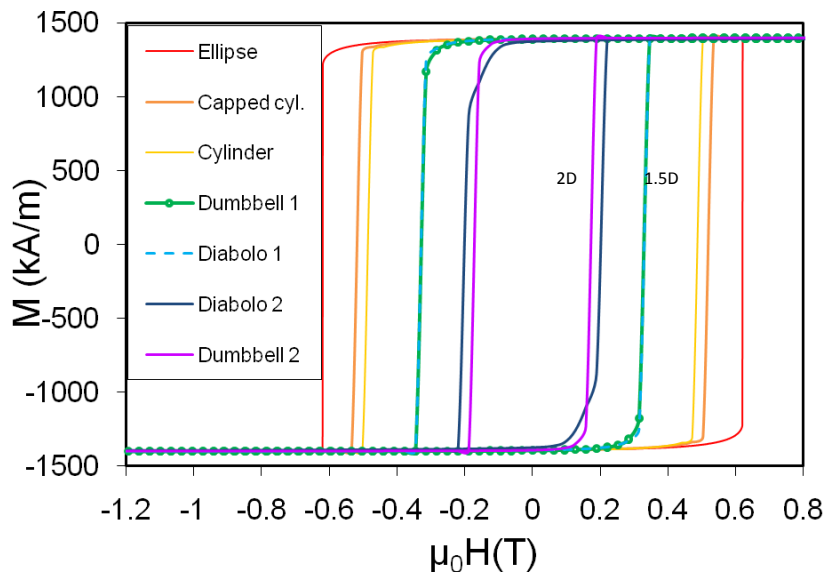
Figure 4.2: Hysteresis curves for the different types of objects when the field is applied at an angle of 5.7° with respect to the easy axis. The curves correspond to objects with $R = 5\,\mathrm{nm}$ (aspect ratio of 10).

The link between high coercivities and the ellipsoidal shape of the objects is even more obvious when the hysteresis loops are compared for different applied field directions. For

objects such as the nanowires and the capped nanowires, the behavior is very close to ellipsoids. The coercive field increases very quickly as the applied field direction decreases from 30° to 0° (see Figure 4.3(a)). In the case of the *Diabolo 2* and the *Dumbbell 2* objects (R=10nm), the coercive field does not really increase as the field is better aligned with the wire but the cycles become simply squarer.
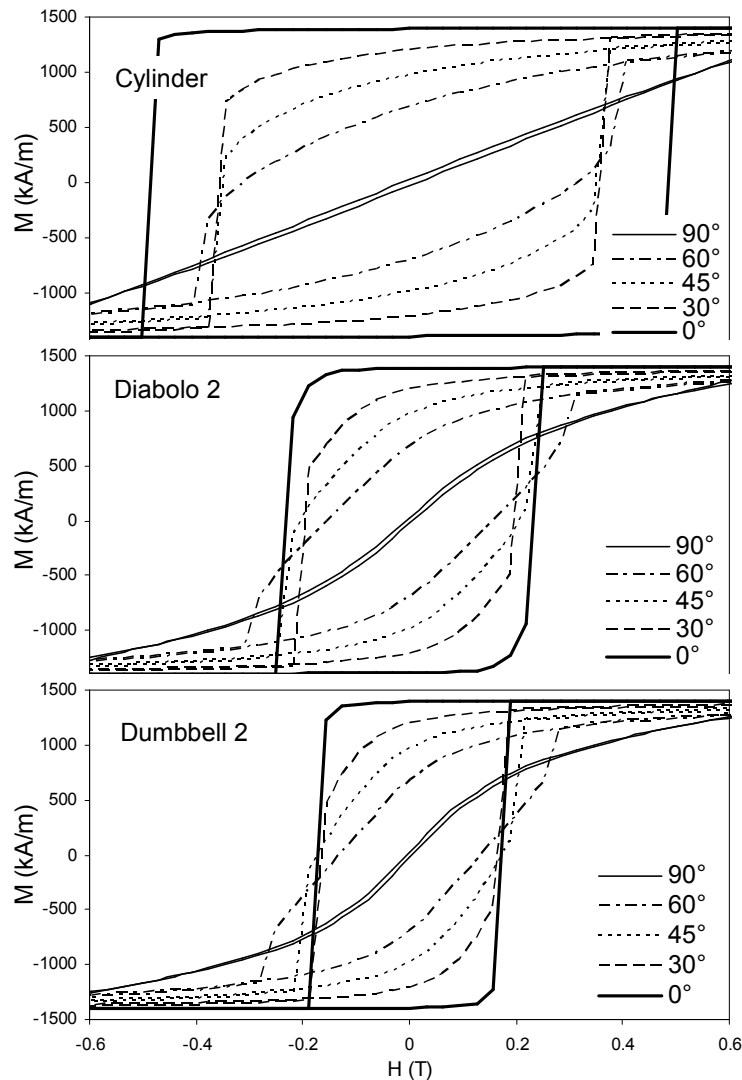
Figure 4.3: Hysteresis curves for *Cylinders*, *Diabolo 2* and *Dumbbell 2* as a function of the applied field direction. The curves correspond to objects with $R = 10$ nm (aspect ratio of 10).

In order to understand the micromagnetic mechanism of reversal in these different objects, the 3D micromagnetic state of the different objects has been plotted just before the magnetization reversal. The magnetic scalar potential ϕ is defined as $\overrightarrow{H_{demag}} = -\overrightarrow{grad}\phi$. The demagnetizing field lines are thus perpendicular to the magnetic scalar potential iso-surfaces. The case of the ellipsoid is provided as an illustration of the canonical case (see Figure 4.4). At remanence, the magnetization is aligned along the ellipsoid long direction and the demagnetization field is homogeneous. Since the demagnetizing field is homo-

geneous, the ϕ isosurfaces are flat. During the reversal, the magnetization is tilted with respect to the long axis, the demagnetizing field is still homogeneous, and the magnetic potential isosurfaces are still flat. The magnetization reversal in the ellipsoid is perfectly coherent. This explains the high coercivity of these objects.
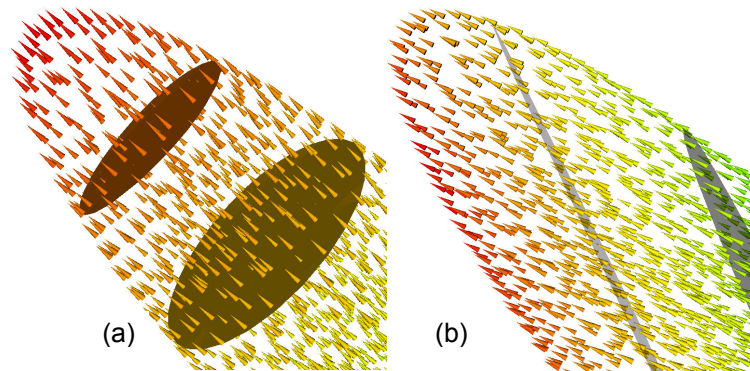
Figure 4.4: Demagnetizing field and magnetic potential of an ellipsoid. (a) at remanence, (b) during reversal. The iso-surfaces indicate the magnetic potential iso-surfaces. The demagnetizing field lines are perpendicular to these surfaces.
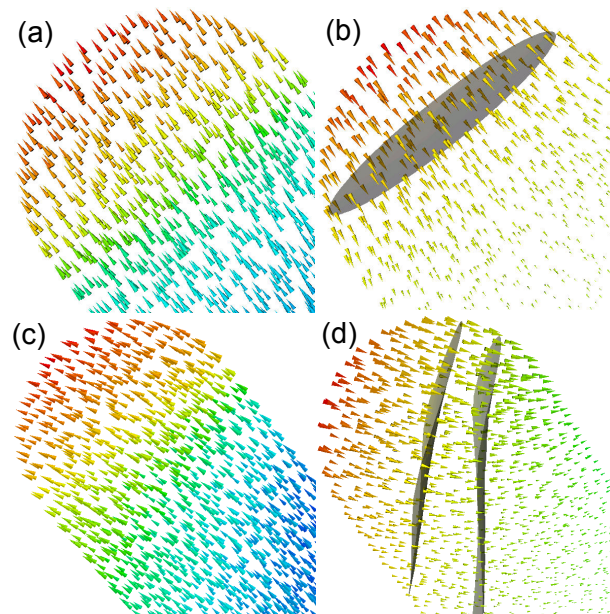
Figure 4.5: Magnetic state of a capped cylinder. (top) at remanence, magnetization and demagnetizing field; (bottom) before reversal, magnetization and demagnetizing field. (a) At remanence, the magnetization is almost perfectly collinear; (b) the demagnetizing field follows the one of a sphere in the tips and is very low in the rod. (c) Before reversal, the magnetization rotates at the wire tip in a C-shape form; (d) the demagnetizing field is close to the one of an ellipsoid. The magnetic potential iso-surfaces are almost flat.
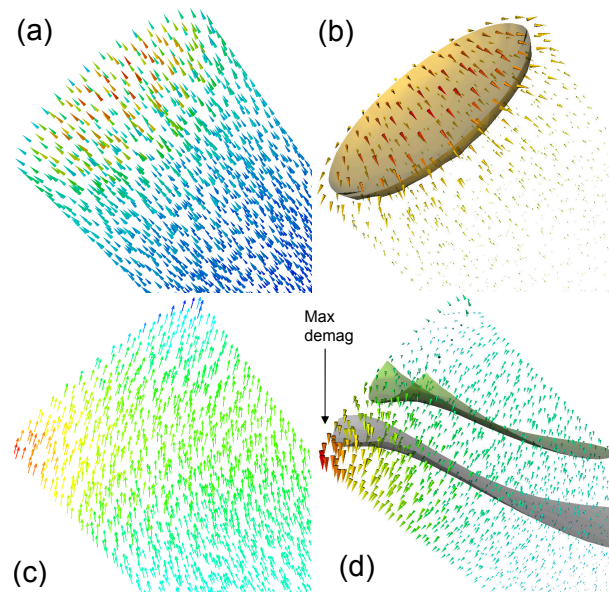
Figure 4.6: Magnetic state of a *Cylinder*. (top) at remanence, magnetization and demagnetizing field; (bottom) before reversal, magnetization and demagnetizing field. (a) At remanence, the magnetization is almost perfectly collinear except at the edges of the wire; (b) the demagnetizing field is zero except at these edges. (c) Before reversal, the magnetization rotates at the wire tip in a C-shape form; (d) the demagnetizing field becomes very high at on edge of the tip.

The case of the capped nanowires is very close to the ellipsoid (see Figure 4.5). At remanence, the magnetization is collinear in the whole object. The demagnetizing field is very low in the rod and reduced at the tips. It remains parallel to the wire axis (see magnetic potential iso-surface). During the reversal, the demagnetizing field remains low. The magnetization rotates in the tip in a C-shape form (Figure 4.5(c)). The magnetic potential iso-surfaces are rather flat indicating that the rotation takes place in an almost coherent way in the tips. This eventually leads to the flipping of the whole rod.

In the case of cylindrical objects, the sharp edges give rise to a "flower" state [Uso1994] at the tips of the nanowires (see Figure 4.6(a)). The demagnetizing field is rather high but remains very localized at these tips (see Figure 4.6(b)). During reversal, the magnetization rotates in a C-shape form (see Figure 4.6(c)). The magnetic potential iso-surfaces are not flat any more at the tip as in the case of the capped nanowires and the demagnetizing field becomes very high at one edge of the cylinder (see Figure 4.6(d)). This seed point is difficult to create because it costs locally quite a lot of energy. The coercivity of the wires remains very high.

In the case of *Diabolo 2* particles, the magnetization is in a "flower-vortex" state which is strongly accentuated by the shape of the object (see Figure 4.7(a)). During reversal, the magnetization develops in a full vortex state (see Figure 4.7(c)) similarly to a curling process which eventually promotes the flipping of the magnetization in the rod. The magnetic potential iso-surfaces remain almost perpendicular to the long axis during the reversal. The symmetry of the object is kept during almost the whole reversal process.
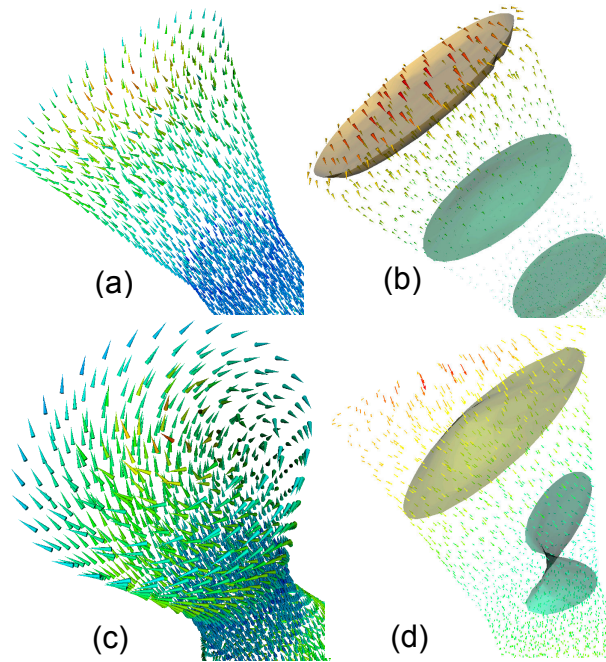
Figure 4.7: Magnetic state of a *Diabolo 2*. (top) at remanence, magnetization and demagnetizing field; (bottom) before reversal, magnetization and demagnetizing field. (a) At remanence, the magnetization forms a flower state and a slight vertex is already present; (b) the demagnetizing field has a rather complex variation; at the connection between the edge and the rod, the demagnetizing field is very low. (c) Before reversal, the magnetization forms a vertex; (d) the demagnetizing field remains almost along the wire long axis. At the connection between the tip and the rod, it follows a rather complex shape.

In the case of dumbbell type objects, the magnetization is in a slight vortex state at remanence (see Figure 4.8). The demagnetizing field is low because the object has only rounded edges. The demagnetizing field follows the one of a sphere in the tips except at the joint between the tip and the rod where it follows a complex profile. While the field is reversed, the vortex fully develops inside the sphere but since the sphere is isotropic, the vortex axis rotates with respect to the long axis of the nanowire. The symmetry is lost during reversal and this promotes an easy reversal of the magnetization in the spherical end. This then initiate the rotation of the magnetization in the rod. The demagnetizing field remains low during the whole process.

Table 4.2 shows that the maximum demagnetizing field amplitude can hardly be related to the coercivity of the systems. High coercivities are achieved for systems in which the demagnetizing field remains low (*ellipsoids* and *capped cylinders*) but also in *cylinders* in which the local demagnetizing fields reach the highest values (though only very locally). On the other hand, the demagnetizing field remains rather low in the *Dumbbell* system but the system exhibits only modest coercivities because a vortex state is naturally formed. These different calculations illustrate the different magnetization reversal processes in various nano-objects and show that they can be qualitatively different between objects which have globally rather similar shapes. A key parameter is therefore the shape of the nanowires tips.
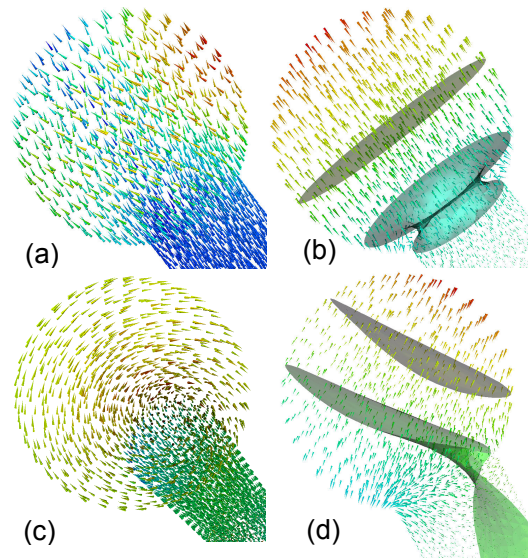
Figure 4.8: Magnetic state of a *Dumbbell 2.* (top) at remanence, magnetization and demagnetizing field; (bottom) before reversal, magnetization and demagnetizing field. (a) At remanence, the magnetization is almost parallel to the long axis though a slight vertex is already present; (b) the demagnetizing field follows the one of a sphere in the tip, but the sharp edge between tip and rod gives rise to a complex variation of the demagnetizing field. (c) Before reversal, the magnetization forms a vertex tilted at 45° with respect to the long axis. (d) The demagnetizing field is also tilted at 45°. Beware that the (c) and (d) views are not from the same camera point of view, (c) is viewed along the vertex kernel, (d) is viewed perpendicular to the vertex kernel.

	$H_c(\mathrm{kA/m})$	$H_{demag}(\mathrm{kA/m})$ *at remanence*	$H_{demag}(\mathrm{kA/m})$ *before reversal*
Ellipsoids	421	82	230
Capped cyl.	325	378	379
Cylinder	300	688	865
Diabolo 1	205	779	708
Dumbbell 1	190	443	596
Diabolo 2	155	776	539
Dumbbell 2	115	458	529

Table 4.2: Maximum magnitude of the demagnetizing field for the various types of particles.

4.1.2 Role of the dimensions: diameter and aspect ratio

The role of the dimensions has been assessed for the different objects presented in Table 4.1. Figure 4.9 shows the evolution of the coercive field H_C for different aspect ratios and for a field applied at 5.7° with respect to the easy axis. Since the length of the objects is set to 100 nm, the variation of the aspect ratio is equivalent to the variation of the diameter.
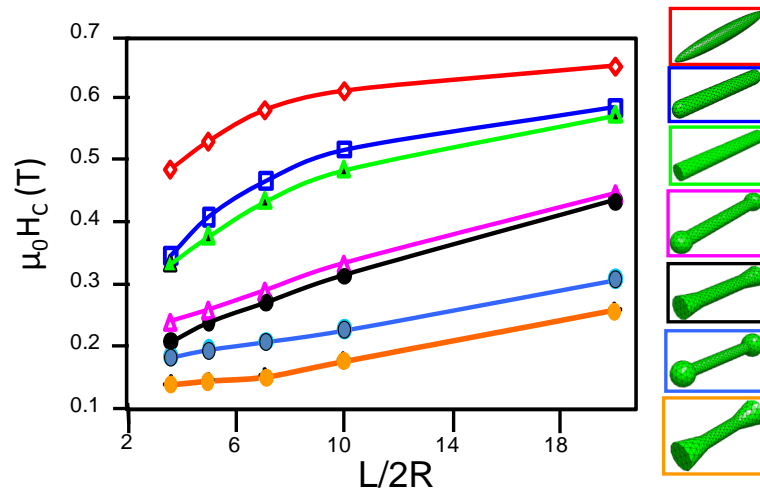
Figure 4.9: Evolution of the coercive field as a function of the aspect ratio for the different types of objects. The magnetic field is applied at 5.7° with respect to the object easy axis.

The ellipsoids will be used as the reference objects since they set the upper limit of the shape anisotropy that can be achieved in the limit of the Stoner-Wohlfarth model. Figure 4.10 shows the evolution of the coercive field H_C depending on the angle between the applied field and the easy axis of the ellipsoid. The comparison between the simulations and the analytical solution provided by the stoner-Wohlfarth model is in good agreement. One can note that as soon as the angle of the applied field is not parallel to the object, the coercive field drops very quickly.
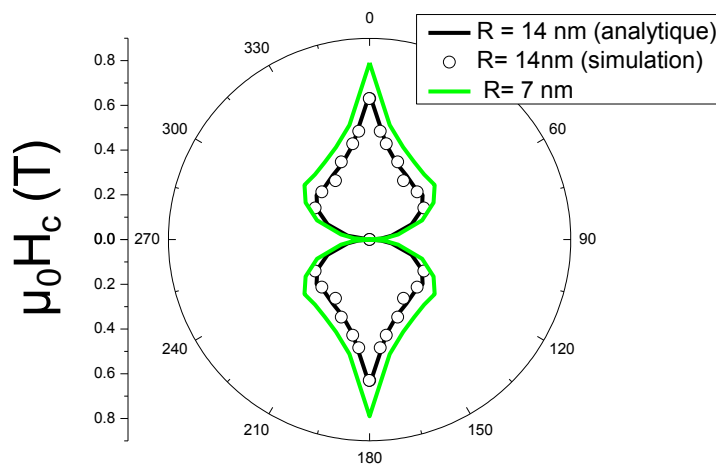
Figure 4.10: Evolution of the coercivity $\mu_0 H_C$ as a fonction of the angle between the applied field and the easy axis for ellipsoids. The results from the simulations for an ellipsoid with $R = 14 \, \text{nm}$ (aspect ratio of 3.6) is compared to the analytical solution provided by the Stoner-Wohlfarth model. The green curve corresponding to an ellipsoid with $R = 7 \, \text{nm}$ (aspect ratio of 7.2) indicates that the coercive field increases with decreasing values of the radius.

The cylindrical geometry (Table 4.1(b)) provides a rather good shape anisotropy which ranges from 70% for low aspect ratios (3.6-5) up to 90% of the maximal theoretical

coercivity for the higher aspect ratios. The capped cylinders (Table 4.1(c)) behave very closely to normal cylinders and provide slightly improved performances. Figure 4.11 shows the evolution of the coercive field H_C depending on the angle ϕ between the applied field and the easy axis of the object for various sizes of the nanowires and capped nanowires. From Equation 1.43 and the parameters introduced in these simulations, the coherent diameter of nanowires is 25nm. The shape of the curve $H_C(\phi)$ (see Figure 4.11) is rather similar to the shape of the curve $H_C(\phi)$ corresponding to the ellipsoid (see Figure 4.10) when the diameter is below 20nm which is almost in agreement with the predicted value of the coherent radius. Moreover, from Figure 4.11, it appears that when the nanowires are capped, the coercivity is slightly improved, especially for larger diameters (2R⩾20nm).
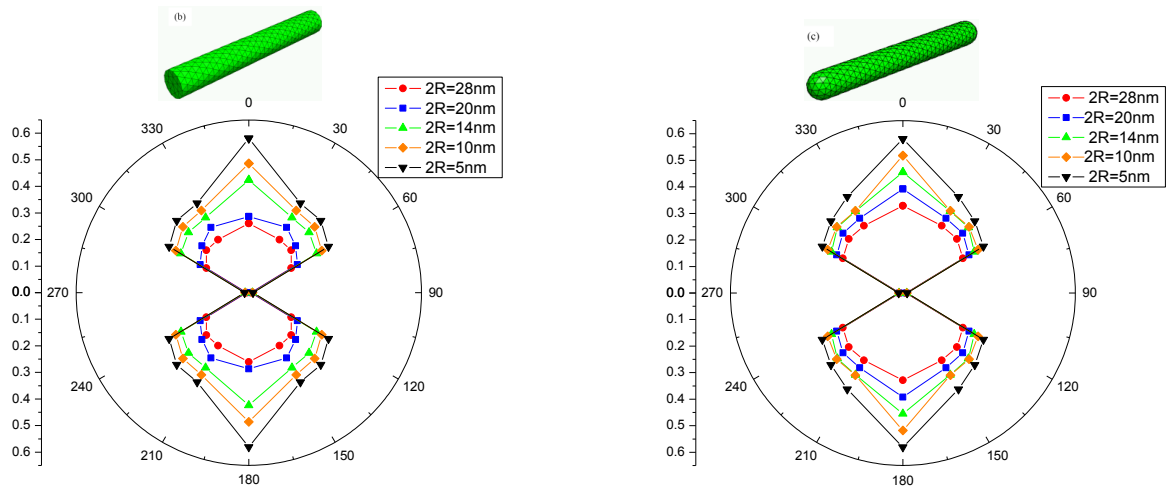
Figure 4.11: Evolution of the coercivity $\mu_0 H_C$ as a fonction of the angle between the applied field and the easy axis for nanowires (object of type b) and capped nanowires (object of type c). The results from the simulations are compared for various values of diameter.

The particles with small conical endings (*Diabolos 1*, Table 4.1(c)) and with small spherical endings (*Dumbbells 1*, Table 4.1(d)) show a very significant drop of coercivity with respect to the ideal case by about a factor 2 (see Figure 4.9).

The situation gets worse when the endings are increased in size (*Diabolos 2*, Table 4.1(f), and *Dumbbells 2*, Table 4.1(e)). The coercivity is only about a third of the maximal theoretical value. For the highest aspect ratios, the situation improves for the particles with small and bigger endings since the coercivity increases respectively to $\sim 70\%$ and $\sim 50\%$ of the maximal theoretical value.

Figure 4.12 shows the evolution of the coercivity H_C as a fonction of the angle between the applied field and the easy axis for the objects with spherical or conical endings depending on the values of the core diameter 2R (and consequently on the values of the spherical endings 2R'). It clearly indicates that the coercivity is significantly lowered for large endings. In particularly, for dumbbells with small (R'=1.5R) or large (R'=2R) spherical endings, the coercivity is lowered for $R' > 18 nm$ which corresponds to the coherent radius for a sphere (defined from the parameters introduced in these simulations). Moreover, the larger the endings are (R'=2R), the lower the coercive field is, as shown on Figures 4.9 and 4.12. It confirms that the extremities of these objects play the role of

nucleation points which promote the magnetization reversal.

Finally the micromagnetic simulations presented here show that the wire tip plays a key role in the reversal mechanism and on the magnitude of the coercive field and that the aspect ratio plays a much lesser role as shown on Figure 4.9.
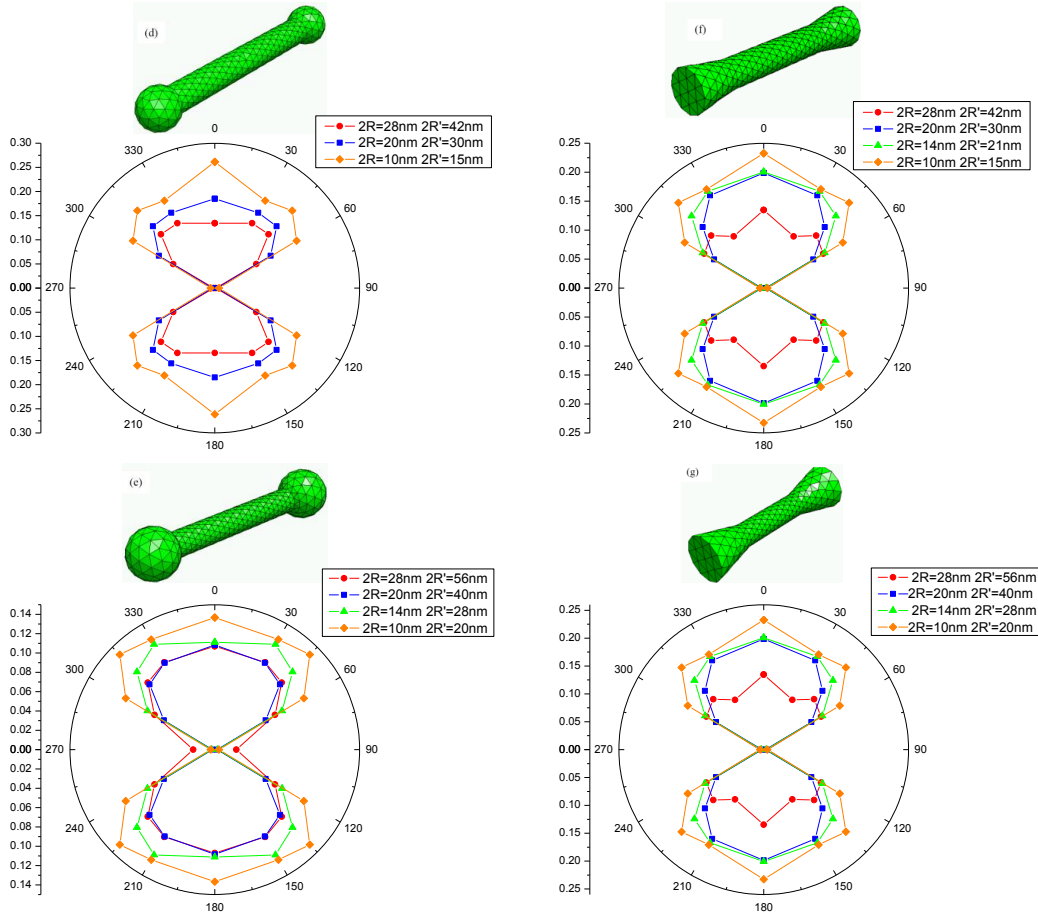
Figure 4.12: Evolution of the coercivity $\mu_0 H_C$ as a fonction of the angle between the applied field and the easy axis for nano-objects with spherical extremities (objects of type d and f) and with conical extremities (object of type e and g). 2R is the diameter of the core and 2R' the diameter of the spherical extremities or of the base of the conical extrimities (see Table 4.1). The results from the simulations are compared for various values of diameter.

4.2   Comparison with experimental data

In this section, the numerical results are compared with experimental measurements. The following nano-objects are considered: *Cylinders* (Co nanorods on Figure 4.13(b)), *Dumbbells* ($Co_{80}Ni_{20}$ nanowires on Figure 4.13(c)) and *Diabolos* (short $Co_{50}Ni_{50}$ nanowires on Figure 4.13(d)). The shape and the aspect ratio of these objects is rather different. The Co nanorods are very close to cylindrical objects with an aspect ratio of ~ 10 ($L \sim 200\,\text{nm}$, $D \sim 20$) whereas the $Co_{80}Ni_{20}$ nanowires are closer to small dumbbells with an aspect ratio of ~ 35 ($L \sim 240\,\text{nm}$, $D \sim 7\,\text{nm}$). Short $Co_{50}Ni_{50}$ nanowires have a global aspect

ratio of ~ 6 ($L \sim 60$ nm, $D \sim 10$ nm in the central part). The case of *Co* nanorods (see Figure 4.13(a)) is discussed in Sub-Section 4.2.2. Indeed these objects can be considered as *cylinders* in a first approximation which explains their high coercivity. In order to explain the shape of their hysteresis cycles, it is however required to take the shape of their tips into account (long *Diabolos 2*).
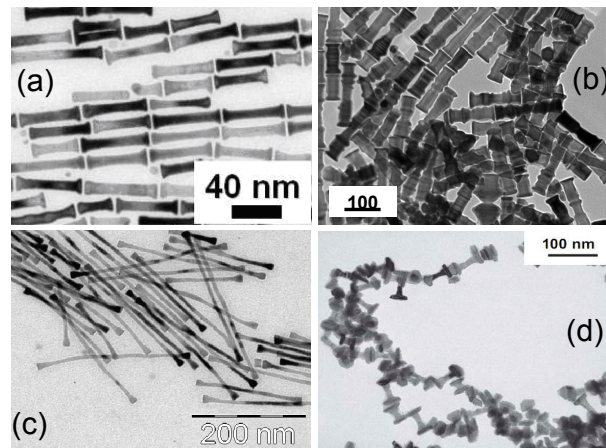
Figure 4.13: TEM images of magnetic nano-wires synthesized in various conditions. (a) *Co* nanorods; (b) *Co* nanorods of length 100 nm; (c) long (200 nm) and thin (7 nm) $Co_{80}Ni_{20}$ nanowires with rounded tips; (d) $Co_{50}Ni_{50}$ dumbbells [Ung2005].

4.2.1 Qualitative comparison

Direct comparisons with experimental results are not straightforward because in the simulations the intrinsic magneto-crystalline anisotropy is not taken into account. The magneto-crystalline anisotropy of our nano-objects is of the order of 0.3 T at 300 K [Mau2007]. Note also that this magneto-crystalline anisotropy is temperature dependent [Ono1980, Ono1979]. Thus we will only make relative comparisons of the coercive fields of these different types of nanowires and not absolute comparisons of the H_c values. The second issue is related to the interaction between wires. In the measured powders or suspensions, the wires are clustered so that magneto-static interactions between wires are taking place. However, direct magneto-static interactions between wires represent small energies compared to the magnetic exchange energies in a single wire so that the bias introduced by the wires interactions can be neglected in a first approximation. Comparison between the modelling of a single wire and real materials is not straightforward. So we restrict our aim to interpret qualitatively some of the general trends in the behavior of the nanowires.

In order to obtain an assembly of co-aligned wires, the nanowires were oriented in a toluene solution following a procedure described in [Mau2007]. Freezing the toluene solution required working at 150 K. The hysteresis loops are presented on Figure 4.14. One can note that the measured coercivity goes up to 1 T which is a value higher than what would be expected from a simple shape anisotropy contribution. Since the c-axis of the wires is aligned along the measuring direction, the magneto-crystalline provides an extra contribution to the coercivity. The coercive fields are 0.9 T, 0.65 T and 0.42 T for *Cylinders*, *Dumbbells* and *Diabolos* respectively. If one refers to Figure 4.9, the expected

coercive field for the different objects (*Cylinders* of aspect ratio 10, *Dumbbells1* of aspect ratio 35 and *Diabolos2* of aspect ratio 6) one would expect coercive fields of $0.5\,T$, $0.4\,T$ and $0.25\,T$. The hierarchy is preserved even though the difference in the measured coercivity is much higher in the experimental data. This can be accounted for by the fact that (i) the modeling of the shapes of the objects is not perfect and (ii) the magneto-crystalline anisotropy is likely to be smaller for $Co_{50}Ni_{50}$ compared to Co. If we make this last assumption, it would correspond to a magneto-crystalline anisotropies of $0.4\,T$, $0.25\,T$ and $0.22\,T$ for Co , $Co_{80}Ni_{20}$ and $Co_{50}Ni_{50}$ respectively at $150\,K$. These values are plausible.
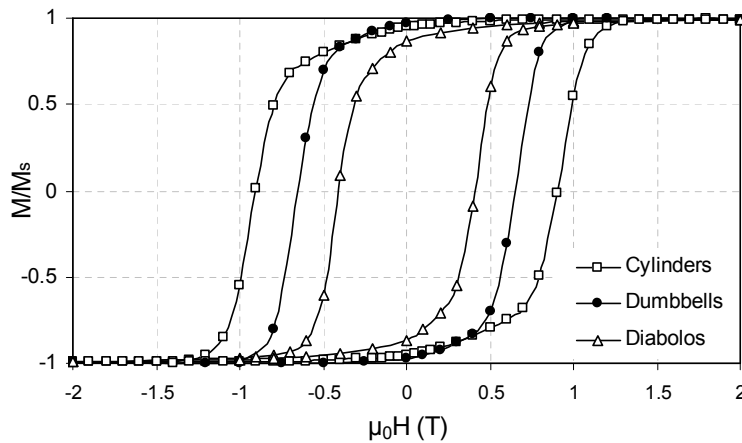
Figure 4.14: Hysteresis cycles at 150K of different types of oriented nanowires: Cylinders (Co nanorods), Dumbbells ($Co_{80}Ni_{20}$ nanowires) and Diabolos (short $Co_{50}Ni_{50}$ nanowires).
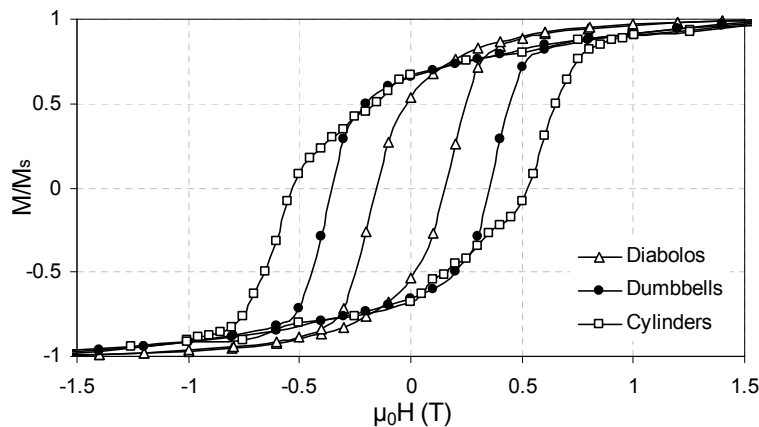
Figure 4.15: Hysteresis cycles at 300K of different powders of nanowires (non oriented): Cylinders (Co nanorods), Dumbbells ($Co_{80}Ni_{20}$ nanowires) and Diabolos (short $Co_{50}Ni_{50}$ nanowires).

Measurements on non-oriented powders at room temperature are presented on Figure 4.15. The measured coercive fields are $0.52\,T$, $0.35\,T$ and $0.15\,T$ for *Cylinders*, *Dumbbells* and *Diabolos* respectively. These values follow qualitatively the numerical results ($0.5\,T$,

0.4 T and 0.25 T). Between the different types of nano-objects, a difference of coercive field of the order $0.15 - 0.2$ T is observed which is in agreement with the results of the simulations.

4.2.2 Role of the tip shape on the hysteresis loop shape: example of Co nanowires

The magnetic measurements presented in Chapter 3 show that the hysteresis cycles of Co nanowires exhibit a kink in the magnetization loop (see Figure 3.7 for instance). This effect is observed only for Co nanowires. No such effect have been measured for $Co_{80}Ni_{20}$ nanowires or $Co_{50}Ni_{50}$. It suggests that the shape of Co nanowires is at the origin of the apparition of this effect.
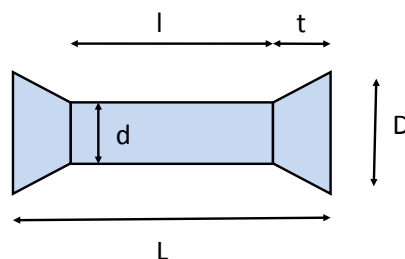
Figure 4.16: Geometry of Co nanowires: $L = 100-150$ nm, $d = 10-15$ nm, $D = 30-50$ nm and $t = 15 - 25$ nm.

The geometry of Co nanowires is presented in Figure 4.16. In Section 4.2.1, Co nanowires were considered as cylinders. However, TEM images showed that they have a tip whose shape is described in Figure 4.16. To illustrate the investigated effect, some magnetic measurements have been performed on two different batches of samples (see Figure 4.17):

- Co nanowires aligned in a frozen butanediol solution. They have a diameter of 16 nm for a length of 153 nm. This sample is referred to as Sample 1.

- Co nanowires randomly oriented in a butanediol solution. They exhibit a diameter of 18 nm for a length of 175 nm. This sample is referred to as Sample 2.
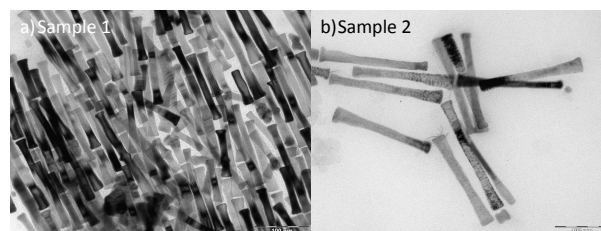
Figure 4.17: TEM images of Co nanowires from a) Sample 1 and b) Sample 2.

Figure 4.18 presents the hysteresis cycle of Sample 1 at $T = 140$ K and Figure 4.19 presents the hysteresis cycle of Sample 2 from room temperature down to $T = 5$ K and shows that this effect is present at all temperatures.
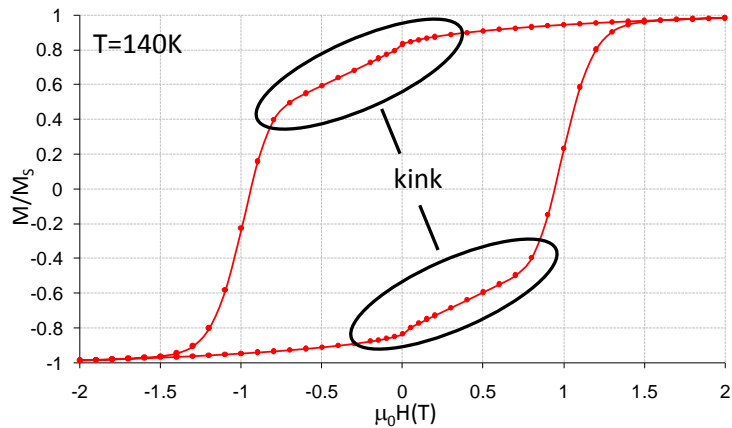
Figure 4.18: Hysteresis cycles of *Co* nanorods aligned in a butanediol solution at $T = 140\,\mathrm{K}$ (Sample 1). One observes q kink in the loop below remanence.
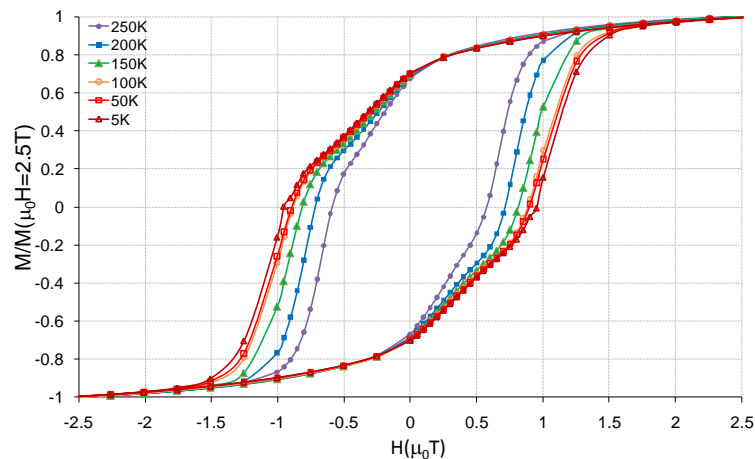
Figure 4.19: Hysteresis cycles of *Co* nanorods randomly oriented in a butanediol solution from room temperature down to $T = 5\,\mathrm{K}$ (Sample2).

In order to probe the role of the shape of the tip in the investigated effect, I performed micromagnetic simulations with the *Nmag* software on objects with the geometry presented in Figure 4.16 and whose dimensions are given in Table 4.3. The hysteresis cycles deduced from the simulations performed on these objects are presented in Figure 4.20. The simulated hysteresis cycles are characterized by a similar effect to the one observed in the experiments. This confirms that the shape of the tip plays a key role in the rapid decrease of magnetization which starts as soon as the remanent state is reached. However, these simulations show that, depending on the dimensions of the objects, this effect may start above or below $H = 0\,\mathrm{T}$.

Further micromagnetic simulations are required to put into evidence the exact role of each of the parameters L, l, d, D and t.

simulations	L (nm)	l (nm)	d (nm)	D (nm)	t (nm)
Simul	200	150	15	30	25
Simul2	160	130	20	30	15
Simul3	220	190	20	30	15
Simul4	160	130	20	60	15
Simul5	160	130	20	40	15

Table 4.3: Dimensions L, l, t, d and D (see Figure 4.16) of the simulated objects.
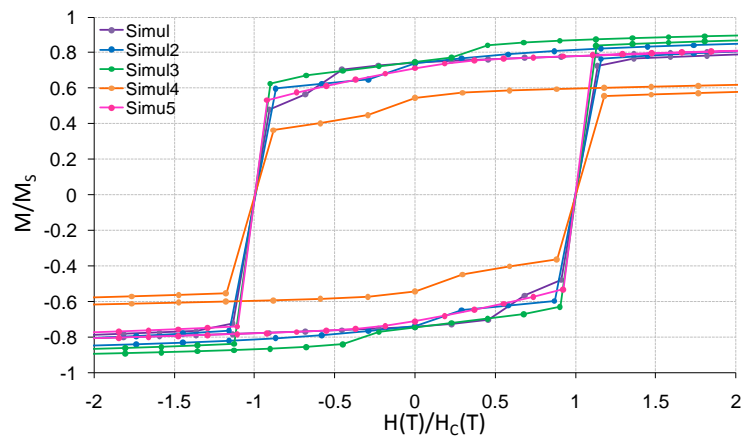
Figure 4.20: Hysteresis cycles calculated from the micromagnetic simulations performed with the *Nmag* software on the objects presented in Figure 4.16 and with the dimensions listed in Table 4.3.

4.3   Conclusion

In Chapter 3, it has been established that the contribution of the shape anisotropy to the coercivity is about half the predicted value by the Stoner-Wohlfarth model (assuming a coherent rotation). Micromagnetic simulations showed that the detailed shape of the objects play a key role in the magnetization reversal and in the value of the coercive field. These simulations put into evidence the crucial role of the endings of the objects. Indeed, the endings of the objects act as nucleation points which help the magnetization reversal and conduct to a decrease of the coercive field. The simulations are in qualitative agreement with the experimental data and allow to explain the kink in the magnetization at the remanence experimentally observed fo Co nanowires (conical endings). Moreover, these simulations also put into evidence the role of the dimensions of the objects and especially the role of the endings size.

Besides the effect of the detailed shape of the objects on the coerivity values, the oxydation of the nanowires -due to their manipulation in the air- may affect their magnetic properties via the formation of an interface between a Co ferromagnetic core and a CoO antiferromagnetic shell. A study of the effects of the oxydation on the magnetization reversal is presented in Chapter 5.

Chapter 5

Exchange bias in magnetic nanowires

Magnetic properties of metallic nanowires may be strongly affected by their oxidation. Indeed when they get in contact with air, they may oxidize until passivation occurs and thus be covered with a finite sized shell of oxide. The consequences are twofold: (i) the moment of the objects will be reduced due to a decrease of the magnetic volume and (ii) the hysteresis cycle can be biased due to the Exchange Bias effect (see Section 1.4). This chapter focuses on the consequences of the exchange bias on the magnetic properties of anisotropic nano-objects, principally nanowires. In particular, it will be shown that the coercive field H_C of the nanowires exhibits an unusual temperature dependence which has not been reported until now. This temperature dependence of H_C gives a new insight of the exchange bias and shows that superparamagnetic fluctuations of the antiferromagnetic CoO grains present at the surface of the nanowires play a key role in the flipping of the magnetization reversal. The effect is first put into evidence for Co nanowires, then a comparison with $Co_{80}Ni_{20}$ nanowires and $Co_{50}Ni_{50}$ nanodumbbells is discussed. As shown in Chapter 2, the influence of Ni principally plays on the shape of the particles. Eventually, the role of the oxide thickness is investigated which gives a better overview on the interaction between the ferromagnetic core and the antiferromagnetic shell.

5.1 Exchange Bias in oxidized Co nanowires

The phenomenon of Exchange Bias in oxidized Co nanowires is studied. Section 5.1.1 provides a neutron diffraction characterization of the CoO oxide shell. It notably allows to determine the Néel temperature T_N of the oxide shell. Then Section 5.1.2 presents the modification of the hysteresis cycles with decreasing temperature. The main result is a coercivity drop from the Néel temperature T_N down to the Exchange Bias temperature T_{EB} with decreasing temperature. Such a coercivity drop has not been reported in the litterature until now. To find an interpretation of this phenomenon, some magnetic relaxation measurements have been performed and are exposed in Section 5.1.3. These measurements suggest an interpretation for the coercivity drop which has been experimentally observed. This interpretation unravels the role of the superparamagnetic fluctuations of the antiferromagnetic CoO grains in the magnetization reversal of the ferromagnetic Co core. This interpration is eventually compared to micromagnetic simulations.

5.1.1 Oxidation of the nanowires: characterization of the cobalt oxide shell

In order to perform magnetic characterizations, the nanowires are collected by centrifugation, washed several times with ethanol [Ung2005, Ung2007]. In this case, the wires oxidize at their surface. After a few weeks the system reaches a stable magnetic state via a passivation mechanism [Gal2005, Gan1993]. No change in the magnetic behavior could be observed in wires at a 1-year interval which confirms that passivation sets in and prevents the magnetic objects from corrosion.
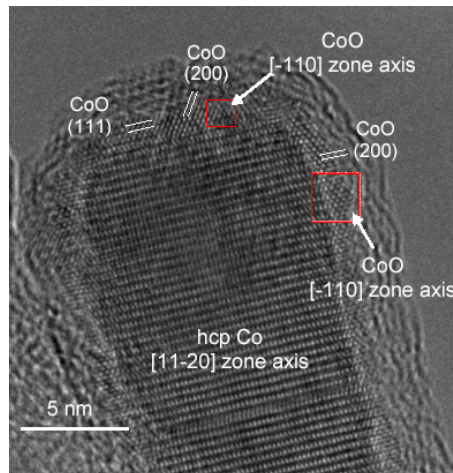
Figure 5.1: HRTEM image of the tip of a Co wire showing the local structure of the Co wire surrounded by a CoO shell (1.2 nm thickness). Performed by C. Gatel [Mau2009].

X-ray diffraction patterns, presented in Chapter 2 (see Figure 2.5), showed that the nanowires were very well crystallized wires in the metallic *hcp* phase with the crystallographic $\overrightarrow{c} - axis$ parallel to the wires axis but also suggest the presence of CoO oxide. In order to characterize the CoO shell around the nanowires, HRTEM (High-resolution Transmission Electronic Microscopy) was performed by Christophe Gatel from the CEMES in Toulouse. The typical HRTEM image presented on Figure 5.1 shows a wire with a mean diameter of 13 nm that consists of a core of metallic cobalt coated by a thin oxide layer of CoO. The diffraction pattern calculated from the image of the Co core was indexed as the $[11\bar{2}0]$ zone axis of the *hcp* structure showing that the $\overrightarrow{c} - axis$ is parallel to the wire axis. The metal core is nearly single crystal since only few stacking faults diffuse lines are observed perpendicular to the [0002] direction. The CoO oxide layer is continuous all over the wire edges. Its thickness inferred from HRTEM images is estimated to 1.2 ± 0.1 nm on the edge of the wires and to 1.4 ± 0.1 nm on the tips. Diffraction patterns calculated on the edge and on the tip of the wire are indexed as the [110] zone axis of the *fcc* structure with two distances of 0.212 nm and four distances of 0.245 nm corresponding respectively to the (002) and (111) reflections of the $Fm3m$ cubic cobalt oxide CoO [JCPD]. The crystallographic orientation relationships between the native oxide and the metal are: CoO $[\bar{1}10]$ (111) // Co $[11\bar{2}0]$ (0001) and CoO $[\bar{1}10]$ (110) // Co $[11\bar{2}0]$ $(1\bar{1}00)$ on the tip and the edges, respectively. These relationships allow to (i) minimize the mismatch between cobalt oxide and cobalt parameters on the edges:

0.212 nm and 0.202 nm for the (200) oxide and (0002) cobalt distances, respectively, and (ii) retain the hexagonal symmetry of the *hcp Co* (0001) plane in the *CoO* (111) plane on the tip. The oxide layer appears monocrystalline both on the tip and on the edges but is globally polycrystalline because of the different orientations on the wire facets. Therefore, from the bulk measurement point of view, the CoO layer will be considered as disordered and composed of crystallites of various sizes.

Moreover, the roughness of the interface between the *Co* core and the oxide layer is smaller than 0.5 nm showing that we have very well defined interfaces, with very few surface defects, of quality equivalent to thin films deposited by vacuum techniques.

Bulk *CoO* is an antiferromagnet with a Néel temperature $T_N = 293$ K. In the form of very thin film, the Néel temperature of *CoO* is only slightly changed: it has been shown that *CoO* layers as thin as 1 nm on oxidized *Co* particles still present antiferromagnetic order close to room temperature [Gan1993, Sku2003] and that the Néel temperature in very thin epitaxial *CoO* layers can even be increased well above room temperature [VdZ2000]. In the case of *Co/CoO* nanospheres, a T_N of about 235 K was reported [Ind2008].

I performed neutron powder diffraction experiments with G. André on the G4.1 spectrometer at the LLB-Orphée laboratory in order to determine T_N (see Figure 5.2 (a)). It has been shown that above T_N, bulk *CoO* has the rocksalt structure [Sch1951][1] whereas below T_N there is a small trigonal and tetragonal distorsion [Ind2008, Jau2001, Tom2004]. Thus bulk *CoO* crystal structure becomes monoclinic (C2/m phase) when the antiferromagnetic order sets in. However we indexed the peaks following the cubic lattice diffraction pattern in a first approximation as it is usually done. At room temperature we observe the two nuclear peaks (111) and (200) at respectively 2.54 Å^{-1} and 2.94 Å^{-1}. When the temperature is lowered, three magnetic peaks appear: the $\left(\frac{1}{2} \frac{1}{2} \frac{1}{2}\right)$ and $\left(\frac{3}{2} \frac{1}{2} \frac{1}{2}\right)$ peaks at respectively $q_{2,a} = 1.27$ Å^{-1} and $q_{2,b} = 2.43$ Å^{-1} from the AFM-II order and the (100) peak at $q_1 = 1.47$ Å^{-1} from the AFM-I order. The temperature dependence of the AFM-II peaks intensity (see Figure 5.2 (b)) shows that the AFM order sets in around 230 K. This is comparable to what has been observed in *Co/CoO* spherical particles [Ind2008]. The (100) peak of the AFM-I order is barely visible. However Gaussian fits of the pattern suggest that the (100) peak appears only below 150 K, contrary to what was observed in [Ind2008]. In addition, above 250 K a very broad magnetic diffuse scattering is observed around the $\left(\frac{1}{2} \frac{1}{2} \frac{1}{2}\right)$ position suggesting that AF correlations already exist at higher temperatures. Nevertheless, we consider that the Néel temperature of the *CoO* shell is around $T_N = 230$ K, which is lower than the bulk value. Using the Scherrer formula, the width of the $\left(\frac{1}{2} \frac{1}{2} \frac{1}{2}\right)$ peak corresponds to a magnetic correlation length of $1 - 2$ nm. This is in agreement with the structure of the oxide shell. Note that neutron diffraction measures an instantaneous picture of the AF ordering of the *CoO* shell so that it is not sensitive to super-paramagnetic fluctuations (slower than 10^{-14}s) of the small CoO crystallites. The measured T_N temperature thus does not correspond to the blocking temperature of the *CoO* crystallites.

Eventually, XRD and HRTEM allowed to detect the presence of an *CoO* shell around the *Co* core and to characterize its structure. The use of neutron diffraction was here crucial to determine that the transition temperature between the antiferromagnetic and

---

[1]Note that the 2ϑ scale of Figures 9 and 10 are not correct.

the paramagnetic phases of CoO is around $240\,\mathrm{K}$ either around $50\,\mathrm{K}$ below the bulk value. It means that, if we except the loss of magnetization linked to the oxidation, the magnetic properties of the nanowires may be affected by the oxide shell only below $T_N = 240\,\mathrm{K}$ when the oxide is magnetically ordered.
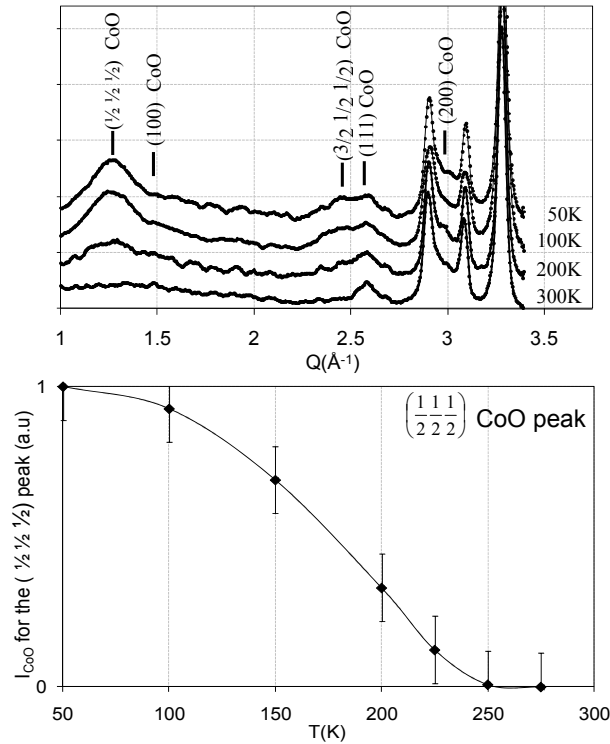
Figure 5.2: (a) Neutron diffraction pattern for oxidized Co nanowires for temperatures between 50K and 300K [Mau2009]. The CoO peaks are indexed following the cubic lattice diffraction pattern [Sch1951]. The three non-indexed peaks above $Q = 2.89\,\text{Å}^{-1}$ correspond to the Co structural diffraction peaks [Sou2009a, Sou2009b]. (b) Intensity of the $\left(\frac{1}{2}\,\frac{1}{2}\,\frac{1}{2}\right)$ CoO diffraction peak as a function of the temperature. The CoO shell orders anti-ferromagnetically between $220\,\mathrm{K}$ and $250\,\mathrm{K}$.

5.1.2 Exchange bias and coercive field

The nanowire powders were characterized by SQUID magnetometry. We considered two different types of samples: (i) non oxidized Co wires, which were used as reference samples and kept in their butane-diol synthesis solution, (ii) Co dried powders exposed to air which led to a natural oxidation as reported in Section 5.1.1.

In order to probe the influence of the antiferromagnetic CoO shell on the magnetization reversal of the ferromagnetic Co core, the samples have been cooled down to $T = 5\,\mathrm{K}$ under a magnetic field $H = 5\,\mathrm{T}$. Then hysteresis cycles have been measured while increasing the temperature from $5\,\mathrm{K}$ to $300\,\mathrm{K}$. Figure 5.3 (a) shows the hysteresis cycles at $T = 200\,\mathrm{K}$ for both oxidized and non-oxidized Co nanowires. Figure 5.3 (b) presents the evolutions of the exchange bias field H_{EB} and coercive field H_C for these systems as a function of temperature and magnetic history.

tel-00471180, version 1 - 7 Apr 2010

In the case of non-oxidized samples, no exchange bias is observed and the coercive field decreases monotonously from $\mu_0 H_c \sim 0.9\,\text{T}$ at low temperatures to $0.5\,\text{T}$ at room temperature. In the case of oxidized Co nanowires, an exchange bias field H_{EB} appears below $T_{EB} \approx 120\,\text{K}$. This exchange bias field reaches $0.2\,\text{T}$ at low temperatures. The most striking feature is that the coercive field H_C dependence is not monotonous since the coercive field decreases down to a *minimum* at T_{EB}, then reaches a maximum at about $200\,\text{K}$, and finally decreases again when reaching room temperature. It thus appears that H_C is maximum at $T \approx T_N \approx 200\,\text{K}$.
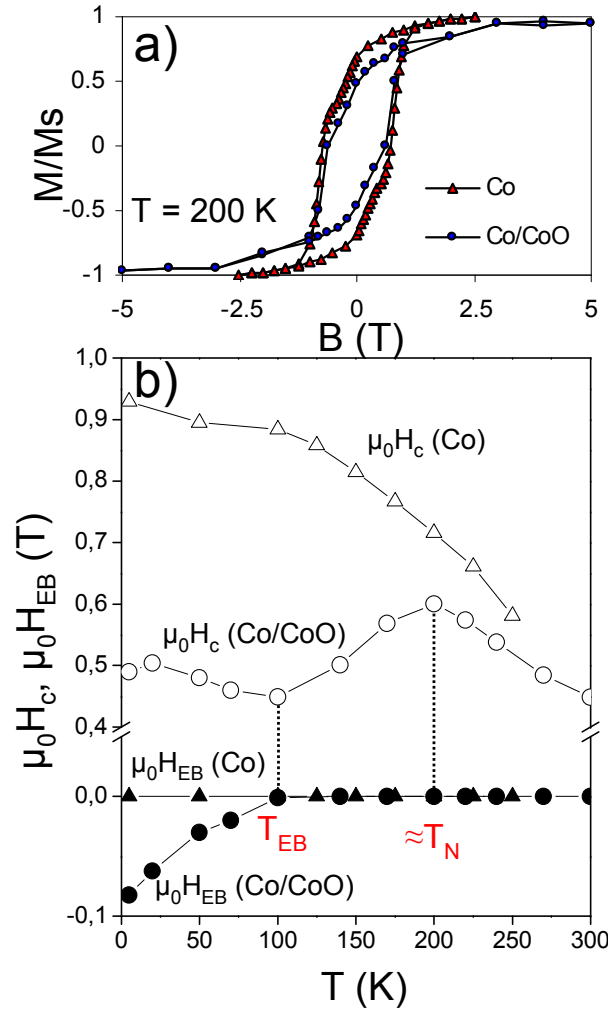
Figure 5.3: (a) Hysteresis cycles obtained from the Co and Co/CoO nanowires. (b) Temperature dependence of the coercive field $\mu_0 H_C$ (open symbols) and the exchange bias field $\mu_0 H_{EB}$ (filled symbols) for non oxidized Co (triangles) and oxidized Co (circles) nanowires. The samples were cooled under $B = 5\,\text{T}$ and the measurements were performed with an increasing temperature. The lines are guided for the eyes.

Below T_{EB}, the increase of the coercive field with decreasing temperature, along with the increase of the exchange bias field, is in qualitative agreement with previous studies [Ber1999, Nog1999, Pen2000, Lun2004, Igl2008, Gru2007]. However, the fact that the coercivity goes up upon warming between T_{EB} and T_N is unexpected. As we shall argue,

this is due to the presence of superparamagnetic fluctuations of the AFM CoO grains.

For elongated systems, the main contributions to the coercivity of the system arise from the shape anisotropy K_{sh} of the wires which is quasi temperature independent and from the Co uniaxial magneto-crystalline anisotropy K_{mc} which decreases from 7×10^5 J/m^3 at 5 K down to zero at 550 K [Ono1979, Ono1980]. Thus a monotonous variation of the coercive field would be expected. The measurements presented here unambiguously show that the temperature behavior of the coercive field is related to the Exchange Bias phenomenon. The comparison of the measurements on non-oxidized and oxidized Co wires (see Figure 5.3 (b)) indeed shows that the oxidation, and thus the Exchange Bias mechanism, leads to a drop of the coercivity of about 0.15 T from T_N down to T_{EB}.

All reports on the Co/CoO system in the literature indicate that the coercive field monotonously increases below T_{EB} [Pen2000, Lun2004]. In a few reports, on some other exchange bias systems, a maximum of the coercive field around the onset of the exchange-bias temperature T_{EB} is observed ([Nog1999] and references therein, [Nis1998, Eft2005]). It should pointed out that these observations have been made on very low coercivity systems where the coercive field increase is only of a few mT and is attributed to the increase of the antiferromagnetic anisotropy around T_{EB}. In the present case the effect is in the *opposite direction* since a *coercivity minimum* is observed at T_{EB}. As evidenced by the temperature dependence of H_C, the antiferromagnetic surface layer modifies the core ferromagnetic magnetization up to almost T_N, which is well above the onset of a static Exchange Bias at T_{EB}.

In order to have a deeper understanding of the coercivity, it is required to probe the frequency temperature dependence of the superparamagnetic fluctuations of the antiferro-magnetic CoO grains. Magnetization relaxation measurements have thus been carried out to assert whether the observed exchange bias effects is concomitant with a slowing down of the superparamagnetic fluctuations of the antiferromagnetic grains at the nanowires surface.

5.1.3   Relaxation measurements on oxidized nanowires powders

To probe the influence on the antiferromagnetic shell on the magnetization reversal of the ferromagnetic core, I performed relaxation measurements. When nanowires are non-oxidized and are purely ferromagnetic, their magnetization is expected to be constant in time. Nevertheless, the CoO oxide shell is so thin that the related grains are expected: (i) to carry some uncompensated moments [Roy2005, Roy2007] and (ii) to exhibit some superparamagnetic fluctuations for a certain temperature range. The aim of the relaxation measurements is to answer these questions.

The magnetization relaxation was measured at small positive fields (3 mT) after saturation under 5 T (see Figure 5.4 (a)). The time decay of the magnetization was fitted using a phenomenological stretched exponential expression:

$$M(t) = M_c + M_0 e^{(-t/\tau)^\beta} \, , \tag{5.1}$$

where M_c is the magnetization at infinitely long times (static part), M_0 is the magnetic moment of the fluctuating volume, τ is the relaxation time and $\beta = 0.4$ is a stretch factor, indicative of a distribution of relaxation times in the sample. For single-size particles, we

would have $\beta = 1$. The fact the β is for far off unity is strongly indicative of a broad size distribution.

For monodisperse superparamagnetic objects with uniaxial anisotropy K, the temperature dependence of the relaxation time τ is related to the energy barrier $\triangle E$ separating the two stable states through the Arrhenius expression:

$$\tau = \tau_0 e^{\triangle E/k_B T} , \tag{5.2}$$

where the energy barrier is driven by the total anisotropy energy K and the volume V of the particles:

$$\triangle E = KV . \tag{5.3}$$

As shown in Figure 5.4 (b), the relaxation time τ is first very short above T_N and then increases quickly upon decreasing temperature down to 50 K where it finally levels off down to the lowest temperature. The behavior of the relaxation time, characterized by a progressive slowing down of the relaxation, and the broad temperature range between T_N and T_{EB} suggest that the *CoO* layer is composed of a collection of antiferromagnetic grains with a broad size distribution which will relax with a characteristic time controlled by their respective energy barriers $\triangle E$. This is confirmed by the indicative value of 0.4 for β.

In the case of wide (almost flat) distribution of particle size and anisotropy barriers, the behavior of the magnetization can be described phenomenologically by the relation [Kne1962]:

$$M(t) = M_0 - S(T) \, ln \, (t - t_0) , \tag{5.4}$$

where $S(T)$ is called the magnetic viscosity. This dependence is well followed in the time range $t > 100$ s (see Figure 5.4 (a)) in agreement with the limitation of this model. The viscosity parameter is presented on Figure 5.4 (c). At low temperatures, the viscosity $S(T)$ is low because most of grains are blocked and thus only a very small fraction of the sample can relax. Upon warming, we observe a round maximum at 50 K and then a steady decrease at higher temperatures. The broad size distribution of the antiferromagnetic grains means that, at a given temperature, larger grains will tend to order along the ferromagnetic magnetization while smaller grains remain superparamagnetic. At low temperatures, only the smallest grains will be superparamagnetic while the larger ones are locked into one of their stable magnetization configuration; hence a longer relaxation time in average and a smaller viscosity. At high temperatures, the global viscosity of the system decreases due to the fact that only the few remaining large grains are contributing to the relaxation [Paj2007].

From the temperature dependence of the viscosity $S(T)$, some quantitative information can be extracted as follows. The viscosity $S(T)$ is related to the distribution of energy barriers through:

$$S(T) = k_B T M_S / \triangle E_{m,T} , \tag{5.5}$$

where M_S is the spontaneous magnetization of the *CoO* layer and $\triangle E_{m,T}$ is the mean energy barrier of the remaining grains that still relax at a temperature T [Woh1984, Gau1986, StP2001]. Larger grains, with higher energy barrier, are blocked while smaller grains relax more rapidly than the time window of the measurement. The quantity $\triangle E_{m,T}$ is equivalent to the inverse of a distribution function $f(\triangle E_m)$ with:

$$\int_0^\infty f(\triangle E_m) d\triangle E_m = 1 . \tag{5.6}$$

The form of $f(\triangle E_m)$ can be either a flat distribution:

$$f(\triangle E_m) = 1/W \, , \tag{5.7}$$

where the two extrema are separated by W or a Gaussian-like distribution around a mean activated energy $k_B T^*$:

$$f(\triangle E_m) = A.e^{-(k_B(T^*-T)/W)^2} \, , \tag{5.8}$$

with

$$A = (1/\sqrt{\pi}W)(T^*/T) \, . \tag{5.9}$$
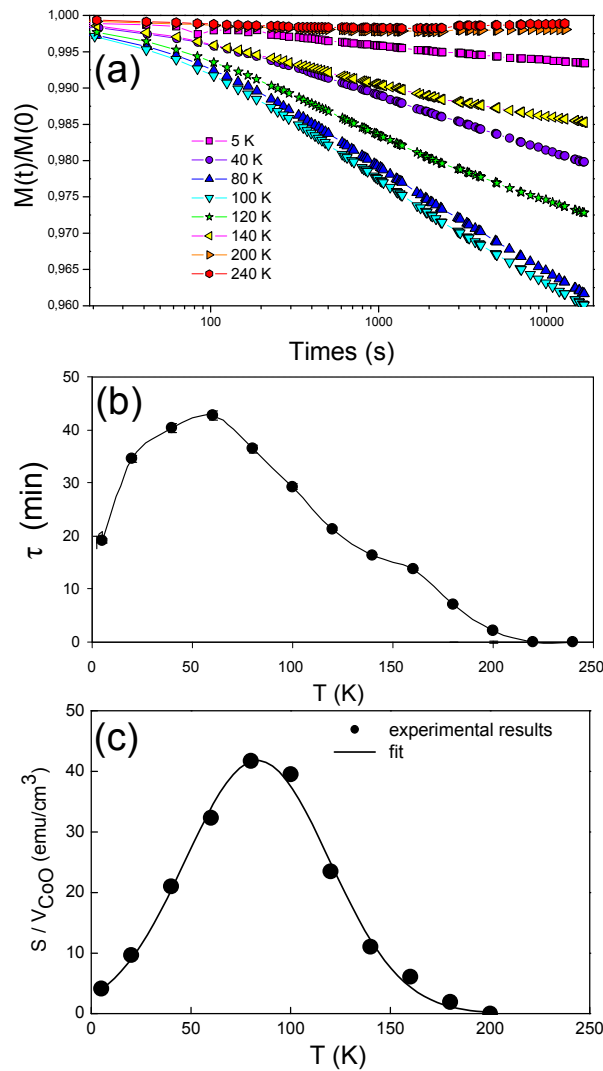
Figure 5.4: (a) $M(t)/M(t=0)$ as a function of time for oxidized Co nanowires under $3\,\mathrm{mT}$ after saturation at $5\,\mathrm{T}$. (b) Temperature dependence of the magnetization relaxation time for oxidized Co nanowires extracted from the expression $M(t) = M_c + M_0 \exp\left(-t/\tau\right)^{\beta}$ with $\beta = 0.4$ kept fixed throughout. (c) magnetic viscosity $S(T)$, as a function of the temperature, extracted from the expression $M(t) = M_0 - S(T) \, ln\,(t - t_0)$.

The best agreement is found for the latter model with $k_B T^* = 83 \pm 1\,\mathrm{K}$ and a width $W = 35 \pm 2\,\mathrm{K}$ as shown in Figure 5.4 (c). From the absolute values of the viscosity

$S(T)$, normalized by the volume fraction of CoO present in the nanowire (assuming a 1.5 nm shell thickness), the spontaneous magnetization of the CoO shell is found to be $M_S = 15.2 \pm 0.1$ emu/cm^3, a value much lower than the theoretical value. Indeed, it has been estimated [Dut2008] that in CoO, a saturation magnetization of 224 emu/g results if all Co spins in bulk CoO were to order ferromagnetically with a spin only moment of $3\mu_B$). It implies that the volume fraction which is "active" represents only $1-2\%$ of the total volume of CoO in the materials. A similar result trend was found in the case of granular CoO layers [Gru2007] or powders [Dut2008]. Equating the obtained mean activated energies $k_B T^*$ for both compounds with the usual expression for the energy barrier ($\triangle E = KV$) leads to active volumes of the CoO grains which are in the range of $1.6-2.4$ nm^3 if one assumes that the uniaxial anisotropy is $K = 5 \times 10^5$ J/m^3 [Gan1993, Mei1957].

To summarize, below T_N, the antiferromagnetic moment fluctuations of the CoO freeze progressively as the temperature is decreased [Sca2000]; leading to a low temperature rise of the relaxation time and a maximum of viscosity below T_{EB}. The physical origin of the superparamagnetism can be attributed to a small fraction ($\sim 7\%$ as found from the experiment) of uncompensated spins at the FM/AFM interface as recently shown [Roy2005, Tom2006, Roy2007, Bla2008, Ind2008].

5.1.4   Exchange bias in nanowires: interpretation

The previous measurements underline the role of the superparamagnetic fluctuations of the CoO grains in the magnetization reversal of the Co core. It allows to imagine that the magnetic moments of the antiferromagnetic shell can couple with the magnetic moments of the ferromagnetic core in spite of the superparamagnetic fluctuations of the former. This gives the following insight into the way the exchange bias mechanism sets in:

- Usually, the different models proposed are static ones and overestimate the quantitative values of the exchange field. The following description of the phenomenon (see Figure 5.5) is based on the key role played by the dynamical effects of the superparamagnetic fluctuations of the antiferromagnetic grains which compose the CoO shell. A dynamical $AFM - FM$ coupling appears as soon as T_N is reached (~ 230 K) even when the CoO grains are in a superparamagnetic state.

- Above T_N, the paramagnetic state of the CoO grains impedes any influence on the magnetization of the ferromagnetic core. Below T_N, the relaxation time τ increases by one order of magnitude and, correlatively, the coercivity decreases (see Figures 5.3 and 5.4). In this temperature regime, the average fluctuations of the antiferromagnetic CoO grains become slow enough so that the magnetic moments of the antiferromagnetic grains can couple with the nearest magnetic moments of the ferromagnetic core, opening a relaxation channel for the ferromagnetic core. This induces a significant drop of the coercivity with decreasing temperature as the average fluctuations of the antiferromagnetic grains become slower in frequency.

- The exchange bias temperature T_{EB} ($T_{EB} \approx 120$ K for Co nanowires) acts then as a threshold where the average relaxation time of the antiferromagnetic CoO grains is sufficiently long enough to trigger a static Exchange Bias mechanism. As long as the

antiferromagnetic grains fluctuate fast enough, no net bias field can appear. Below T_{EB} , these fluctuations are slow enough so that the antiferromagnetic moments can be considered as nearly blocked compared to the measurement time. At the lowest temperatures, the $AFM - FM$ coupling increases linearly and the exchange field H_{EB} increases as usually observed [Nog1999, Pen2000, Igl2008, Lun2004, Gan1993]. In parallel, the coercive field H_C starts to increase again with decreasing temperature below T_{EB} due to a ferromagnetic core microstructure which is no longer sensitive to the antiferromagnetic fluctuations.

This scenario reconciles the observation showing antiferromagnetic order [VdZ2000] as well as $FM - AFM$ exchange coupling [Sku2003] well above the blocking temperature T_{EB}. However, it remains to validate this interpretation via some micromagnetic simulations providing quantitative information.
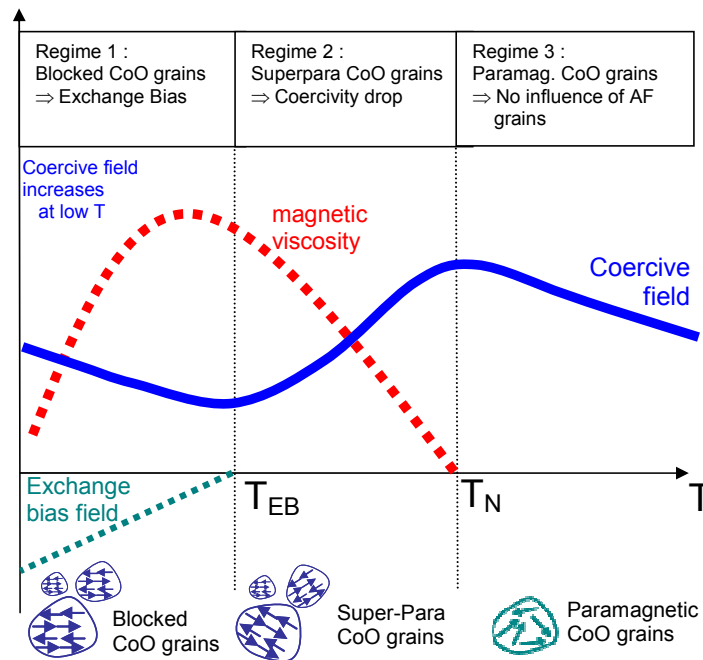
Figure 5.5: Schematics of the magnetization and relaxation processes in the oxidized nanowires. The solid line represents the temperature dependence of the coercive field of the ferromagnetic metallic core with a local maximum around T_N and a local minimum at T_{EB}, temperature below which a finite Exchange Bias is observed. The dashed line represents the magnetic viscosity.

5.1.5   Exchange bias in nanowires: modelling

As described above, the magnetic behavior of nanowires is strongly influenced by the oxide shell surrounding them. In order to qualitatively understand the role of the interactions between a magnetic Co wire and its CoO shell, some micromagnetic simulations have been performed with the *Nmag* micromagnetic modelling package [Fis2007] by Fatih Zighem. The aim of these simulations is to show that the coupling at the interface between the moments of the ferromagnetic core and those of the antiferromagnetic grains can lead

to a drop of coercivity. Since it is not possible with the Nmag software to simulate antiferromagnetic grains around a ferromagnetic core, the simulated objects have been ferromagnetic cores coated with small ferromagnetic half hemispheres. Moreover, the Nmag software does not allow to choose a material different from the one of the core for the half-hemispheres. That is why these simulations only give qualitative information. Depending on the temperature regime, the moments of the ferromagnetic half hemispheres are either blocked ($T < T_{EB}$) or free to rotate ($T_{EB} < T < T_N$).
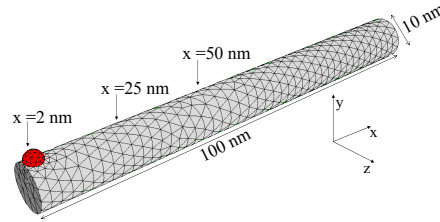
Figure 5.6: Typical mesh used for the micromagnetic calculations in presence of one hemisphere placed at the edge of the wire.

The studied model object is a 100 nm long, 10 nm diameter cylindrical wire which is representative of the experimental objects which exhibit an aspect ratio around 10 (see Figure 5.6). The magnetic parameters used correspond to typical values for *hcp* cobalt epitaxial thin films [Tan1961], saturation magnetization $M_S = 1400$ kA.m^{-1}, exchange constant $A = 1.2 \times 10^{-11}$ J/m. The magnetocrystalline anisotropy is neglected. The distance between two nodes of the mesh has been chosen smaller than the exchange length $\ell_{ex} = \sqrt{A/\mu_0 M_S^2} \approx 2.2$ nm.

As stated above, the key ingredients are the nanometer size CoO particles which compose the shell around the wire. For the simulations, 3 different regimes are considered:

- (i) below the Exchange Bias temperature $T < T_{EB}$, the CoO particles are blocked and a finite exchange bias field appears,

- (ii) between the Exchange Bias temperature and the Néel temperature $T_{EB} < T < T_N$, the CoO particles are antiferromagnetically ordered but are subject to super-paramagnetic fluctuations,

- (iii) above T_N, the CoO shell is not magnetically ordered and there is no effective interaction between the wire core and the shell.

In the high temperature regime $T > T_N$, the simulation is straightforward and leads to a coercive field of 471 mT when the field is aligned along the wire axis. Of course, in the case of randomly aligned wires with respect to the field, the coercive field due to the shape anisotropy is reduced by a few tens of mT due to the misalignment of the field with the wires. It can be noted that in the experimental measurements, when the temperature is decreased from room temperature to $220 - 230$ K, the coercive field increases as expected from the magneto-crystalline anisotropy linear temperature dependence of Co between 200 and 300 K [Ono1980] ($K_{mc} \approx 5 \times 10^5$ J/m^3 at 300 K and $\approx 6.5 \times 10^5$ J/m^3 at 200 K).
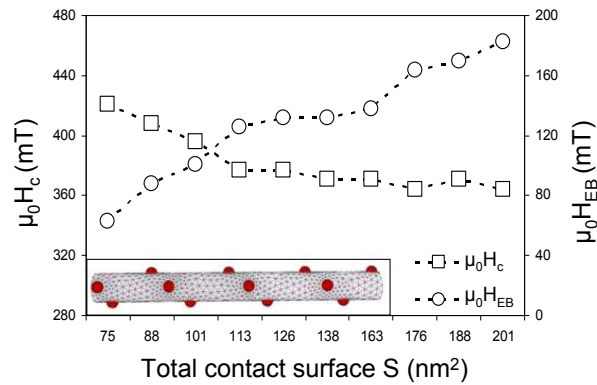
Figure 5.7: $\mu_0 H_{EB}$ and $\mu_0 H_C$ measured on the hysteresis cycle calculated along the wire axis in presence of more and more blocked particles around the wire. S is the total surface in contact between the blocked particles and the wire. The particles are homogeneously placed along the wire as we can see it in the insert.

In the low temperature regime, $T < T_{EB}$, the wire can be considered as coated with small particles, whose magnetic moments are blocked along the x direction. These particles are modelled as half hemispheres (see Figure 5.6) and correspond to the blocked CoO particles. However, because of some limitations due to the Nmag software, these half-hemispheres are modelled as Co ones. When the temperature decreases the number of blocked antiferromagnetic particles increases. Thus, in the simulations, a wire is modelled as coated with an increasing number of such small blocked particles with a diameter of 4 nm. Figure 5.7 presents the evolution of the exchange bias field H_{EB} as a function of the total biased surface S around the wire. The total surface of the wire is 3100 nm^2. It is shown that a few pinning points which represent only a small fraction of the wire surface (7%) are sufficient to induce large exchange bias fields (~ 0.2 T), which are of the same order of magnitude as what is experimentally observed. Note however, that the exchange at the interface was taken as $A_{FM-AFM} = 1.2 \times 10^{-11}$ J/m which overestimates the efficiency of the exchange bias field. Note also that the emergence of blocked grains barely affects the coercive field. The coercive field is reduced from 470 mT without bias to 370 mT with 7% of biased surface. This qualitatively explains why at low temperatures, when most of the antiferromagnetic grains are blocked, the coercive field is not fully recovered in the oxidized wires compared to the non oxidized wires (see Figure 5.3 (b)). It suggests that the CoO grains act as nucleation points which promote the reversal of the wires and reduce the coercivity.

In the intermediate regime, $T_{EB} < T < T_N$, the situation is more complex. The relaxation measurements have shown that the CoO grains in the shell have a broad size distribution range so that there is also a broad distribution of the antiferromagnetic fluctuation frequencies. It is presently impossible or at least very difficult to tackle numerically such a complex problem in the dynamic regime. Nevertheless, in this intermediate regime, it can be contemplated to give some insight of the role of fluctuating magnetic grains at the surface of the wires provided some approximations are made. The first point to note is that the characteristic reversal time of a 100 nm Co wire is of 4 ns, as obtained from dynamic micromagnetic simulations using a damping constant $\alpha = 0.02$.
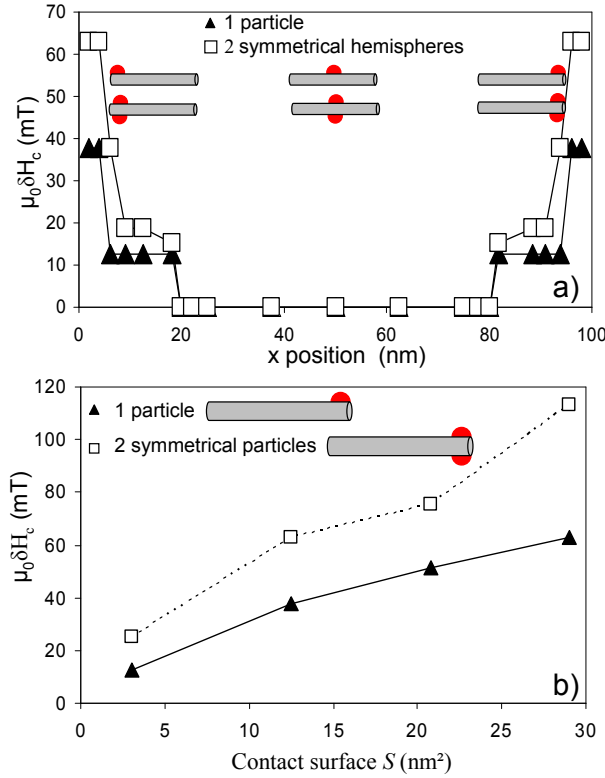
Figure 5.8: $\mu_0 H_{EB}$ and $\mu_0 H_C$ measured on the hysteresis cycle calculated along the wire axis in presence of more and more blocked particles around the wire. S is the total surface in contact between the blocked particles and the wire. The particles are homogeneously placed along the wire as we can see it in the insert.

In the theory of superparamagnetism, the relaxation time τ is related to the energy barrier $\triangle E$ separating two stable states of a magnetic particle through the Arrhenius expression: $\tau = \tau_0 exp\left(\triangle E / k_B T\right)$. The energy barrier is essentially driven by the uniaxial anisotropy energy K and the volume V of the particles: $\triangle E = KV$. The relaxation constant τ_0 is of the order of 10^{-9} s. In order to take the fluctuations of the antiferromagnetic grains into account, a constant anisotropy $K = 5 \times 10^5 J/m^3$ is introduced [Mei1957, Gan1993]. The characteristic reversal time of $4ns$ thus corresponds to a volume of the antiferromagnetic particles of the order of $10\,\text{nm}^3$. Smaller particles will fluctuate much faster than the reversal time of the wire and their interaction with the wire is likely to average out to zero. Bigger particles will fluctuate much slower and can be considered as static during the wire reversal. Thus one can make the assumption that the very small CoO grains will not play a key role in this intermediate regime while the bigger particles will behave as static objects with respect to the wire reversal so that static micromagnetic calculations may provide realistic account of the interactions between the Co wire and the CoO grains. The second assumption made is that the CoO grains behave mostly as nucleation points for the magnetic reversal of the wires. In order to model the CoO grains as nucleation points, they were modelled as small ferromagnetic grains with their magnetization free to rotate coupled to the Co wire with an exchange constant $A = 1.2 \times 10^{-11}$ J/m.

The first step considered in assessing the role of the position of these nucleation points

along the Co wire (see Figure 5.8). The calculation was performed with hemispheres of volume $17\,\text{nm}^3$ (2 nm radius), the surface S in contact with the ferromagnetic wire thus being $12.5\,\text{n}m^2$. It was found that the addition of such an hemisphere at the surface of the wire can induce a significant drop $\triangle H_c$ in the coercive field ($\sim 40\,\text{mT}$) when it is placed close to the wire tip ($\triangle H_c$ represents the difference of coercive field between the value obtained from the isolated wire (471 mT) and the value obtained from the wire surrounded by particles). On the other hand, such nucleation points placed in the middle of the wire do not induce any drop in the coercive field. The coercive drop can be almost doubled to ($\sim 70\,\text{mT}$) by simply putting a second symmetrical nucleation point. The sensitivity to the nucleation point position can be explained by the distribution of the demagnetizing field which is localized near the tips of the wire and close to zero in the rest of the wire [Ott2009]. In the presence of an hemisphere located close to the tips of the wire, the demagnetizing field interacts with the nucleation point. This promotes an easier magnetization reversal and thus a smaller applied field. It is thus likely that it is mostly the CoO particles located near the tips of the wires which are responsible for the coercivity drop observed in the investigated systems.

The effect of the nucleation point volume or contact surface were also investigated. Nucleation points of increasing contact surfaces with the Co wire were considered (from 3 to $28\,\text{nm}^2$). Figure 5.8 (b) represents the drop in coercivity as a function of the contact surface. It varies quasi-linearly from 12 to $60\,\text{m}T$ for surfaces S varying from 3 to $30\,\text{nm}^2$. The coercivity drop can be doubled if two particles are placed symmetrically at the end of the wire. These calculated drops are of the same order of magnitude as the ones experimentally observed. In the same way as before, large grains placed far from the wires tips do not have any influence on the coercive field.

Contrary to the case of antiferromagnetic grains at the surface of a thin film, where an increase of the coercive field is usually observed near the Exchange Bias temperature [Gri2003, Lei2002], a drop of coercivity is observed in the nanowires when the antiferromagnetic grains interact with the wire. This is due to the $1D$ geometry which is very sensitive to the antiferromagnetic grains which behave as nucleation points promoting a magnetization reversal contrary to the case of thin films, where antiferromagnetic grains usually behave as pinning centers which drag the magnetization.
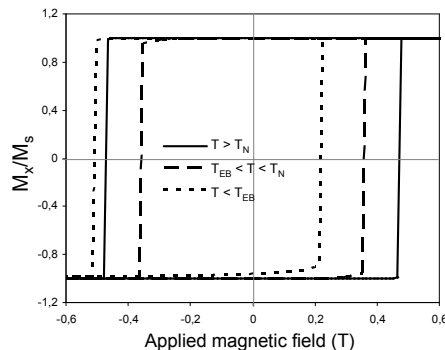
Figure 5.9: Typical hysteresis cycles calculated in the three temperature regimes. Solid line: $\mu_0 H_c = 471\,\text{mT}$, long dashed line: $\mu_0 H_c = 360\,\text{mT}$, short dashed line: $\mu_0 H_c = 365\,\text{mT}$ and $\mu_0 H_{EB} = 145\,\text{mT}$.

To make these micromagnetic simulations more understandable, Figure 5.9 presents three typical hysteresis in the three different temperature regimes, for a magnetic field applied along the wire. The solid line cycle corresponds to an isolated wire having no interaction with the CoO particles ($\mu_0 H_c \approx 471$ mT). The long dash cycle corresponds to a wire coated with nucleation points (2 nm radius hemispheres) covering 7% of the wire surface. The coercive field is reduced to 360 mT. The short dash cycle corresponds to a wire coated with pinning points (2 nm radius hemispheres) covering 7% of the wire surface. The coercive field is still reduced to 360 mT and a finite exchange bias field appears $\mu_0 H_{EB} \approx 145$ mT.

These micromagnetic simulations underline the effects of the CoO grains position along the wire and of their relative contact surface. These simulations have been performed for the same shape and size of the Co nanowire. In order to get a deeper understanding of the mechanisms into play, further experimental investaigations have been performed to probe the effects of the nanowires shape, of the magnetic history and of the CoO shell tickness.

5.2 Exchange Bias in nanowires: influence of the shape

In order to probe the role of the shape of the nanoparticles in the exchange bias mechanism, three types of samples have been investigated: (i) Co nanowires, (ii) $Co_{80}Ni_{20}$ nanowires and (iii) $Co_{50}Ni_{50}$ nanodumbbells (see Figure 2.2). Of course, the difficulty here is that the shape of the particles is linked to the chemical composition of the particles (proportion of Co and Ni) so that some precautions have to be taken to interpret correctly the following data. These three kinds of objects have been described in Section 2.

5.2.1 Temperature dependence of the exchange and coercive fields

Figure 5.10 presents the evolutions of the exchange bias field H_{EB} and coercive field H_C for these systems as a function of temperature and magnetic history. The characteristics of $H_{EB}(\mathrm{T})$ and $H_C(\mathrm{T})$ are summarized in Table 5.1 and compared to the geometrical dimensions of the investigated objects.

	d (nm)	L (nm)	L/d	$\mu_0 H_{EB}(\mathrm{T}) at 5\mathrm{K}$	$\mu_0 H_C^{max}(\mathrm{T})$	$\triangle\mu_0 H_C(\mathrm{T})$	$\triangle H_C/H_C^{max}$
$Co_{80}Ni_{20}$	7	240	34.3	-0.185	0.43	0.23	0.53
Co	15	130	8.7	-0.082	0.6	0.15	0.25
$Co_{50}Ni_{50}$	15	55	3.7	-0.071	0.136	0.0125	0.09

Table 5.1: Summary of the some characteristics of $\mu_0 H_{EB}(T)$ and $\mu_0 H_C(T)$ versus the dimensions of the different investigated nanoparticles. d and L are respectively the diameter and the length of the objects. $\triangle\mu_0 H_C$ represents the coercivity drop between $\mu_0 H_C^{max}(T \sim 200-230\,\mathrm{K})$ and $\mu_0 H_C(T_{EB})$.

The temperature dependence of H_{EB} is first analyzed. It appears that the exchange bias temperature T_{EB} is about 130 K for $Co_{80}Ni_{20}$ nanowires whereas it is about 100 K for both Co nanowires and $Co_{50}Ni_{50}$ nanodumbbells. Moreover, at $T = 5$ K, H_{EB} is

respectively -0.185 T, -0.082 T and -0.071 T for $Co_{80}Ni_{20}$ nanowires, Co nanowires and $Co_{50}Ni_{50}$ nanodumbbells. T_{EB} and $H_{EB}(5\,K)$ are similar for the three kinds of objects, probably due to the similar value of their diameters (see Section 1.4.2). However it must be noted that from Equation 1.64 one would have expected a ratio between $H_{EB}(5\,K)$ for Co nanowires and $Co_{50}Ni_{50}$ nanodumbbells of about:

$$\frac{H_{EB}^{Co}(5K)}{H_{EB}^{Co_{50}Ni_{50}}(5K)} = \frac{M_{Co_{50}Ni_{50}}}{M_{Co}} = 0.67 \, , \tag{5.10}$$

since both objects exhibit the same value of diameter. In fact, the experimental value of this ratio is:

$$\frac{H_{EB}^{Co}(5K)}{H_{EB}^{Co_{50}Ni_{50}}(5K)} \approx 1.15 \, . \tag{5.11}$$
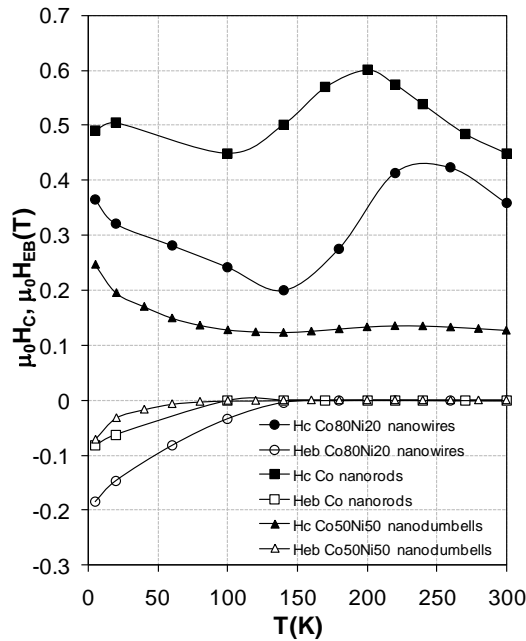
Figure 5.10: Temperature dependence of the coercive field $\mu_0 H_C$ (open symbols) and the exchange bias field $\mu_0 H_{EB}$ (filled symbols) for oxidized $Co_{80}Ni_{20}$ (circles) nanowires, oxidized Co nanowires (squares) and oxidized $Co_{50}Ni_{50}$ nanodumbbells (triangles). The samples were cooled under $\mu_0 H = 5\,T$ and the measurements were performed with an increasing temperature. The lines are guided for the eyes.

The difference between the experimental and predicted values may be explained by different factors: for instance the shape of the tip or the chemical composition of the core and the oxide shell which may lead to different values of J_{INT}. As for the value of $H_E(5\,K)$ for $Co_{80}Ni_{20}$ nanowires, it is about twice larger than the one of the Co nanowires. This can be qualitatively attributed to the fact that the antiferromagnetic layer represents 60% in volume of the total wire for $Co_{80}Ni_{20}$ ($< D >= 6.8\,\text{nm}$) and only 20% for the Co wires ($< D >= 15\,\text{nm}$).

As for the coercive field H_C, the three samples present qualitatively similar temperature dependence but in different proportions. The description of $\mu_0 H_C(\mathrm{T})$ for Co nanowires has been made in Section 5.1.2. For $Co_{80}Ni_{20}$ nanowires the coercivity H_C exhibit a local maximum at $T \sim 230\,\mathrm{K}$ and then decreases with decreasing temperatures down to $T_{EB} \approx 130\,\mathrm{K}$ and finally increases again with decreasing temperatures below T_{EB}. The behaviour of $H_C(\mathrm{T})$ is thus very similar for Co and $Co_{80}Ni_{20}$ nanowires. The main differences are the value of the exchange bias temperature T_{EB} and of the temperature T^* corresponding to the local maximum H_C^{max} just above the coercivity drop ($\sim 200\,\mathrm{K}$ for Co nanowires and $\sim 230\,\mathrm{K}$ for $Co_{80}Ni_{20}$ ones). The difference between the values of T_{EB} between these samples probably comes from the difference between the values of diameter as explained above. As for T^*, the value of this temperature is linked to the Néel temperature T_N when the CoO grains inside the oxide shell begin to order antiferromagnetically. The presence of NiO inside the oxide shell certainly affects the value of the Néel temperature T_N. Nevertheless, it is experimentally hard to distinguish the presence of NiO from the one of CoO since both oxides have the same crystallographic structure ($NaCl$) and their lattice parameter are very similar ($a = 0.4258\,\mathrm{nm}$ for CoO and $a = 0.4177\,\mathrm{nm}$ for NiO). Nevertheless, the Néel temperature of bulk NiO ($T_N = 523\,\mathrm{K}$) is larger than the one of bulk CoO ($T_N = 293\,\mathrm{K}$) so that one can indeed expect a higher value of T_N for the oxide shell of the oxidized $Co_{80}Ni_{20}$ nanowires. Another difference between the temperature dependence of H_C of the Co and $Co_{80}Ni_{20}$ nanowires is the amplitude $\triangle\mu H_{0C}$ of the coercivity drop. This coercivity drop is about twice larger in proportion for $Co_{80}Ni_{20}$ nanowires than for Co nanowires (see Table 5.1).

For the $Co_{50}Ni_{50}$ nanodumbbells, the coercivity H_C exhibits a local maximum at $T \sim 230\,\mathrm{K}$ and then decreases with decreasing temperatures down to $T \approx 130\,\mathrm{K}$ and finally increases again with decreasing temperatures below $T \approx 130\,\mathrm{K}$. For this sample there is a slight difference between the exchange bias temperature $T_{EB} \approx 100\,\mathrm{K}$ and the temperature corresponding to the local minimum of coercivity $T \approx 130\,\mathrm{K}$. Furthermore, it must be pointed out that even if the temperature dependence of the coercivity for this sample is similar to the ones of the other samples, the coercivity drop is here very slight since its amplitude is worth about $\triangle\mu H_{0C} \approx 0.0125\,\mathrm{T}$ either only 9% in proportion. The proportion of the coercivity drops compared to the aspect ratio L/d of the corresponding nano-objects underlines the role of the anisotropy in this effect. As a matter of fact, the larger is the aspect ratio, the larger in proportion is the coercivity drop as indicated in Table 5.1. Of course, some precautions have to be taken with this affirmation since the shapes of the tips are very different from an object to another. Indeed in Section 5.1.5, it has been shown that the superparamagnetic fluctuations of the antiferromagnetic grains are most effective to reverse the magnetization when the grains are localized near the tips of the objects.

5.2.2 Relaxation properties

I measured the magnetization relaxation of oxidized $Co_{80}Ni_{20}$ nanowires at small positive fields ($3\,\mathrm{mT}$) after saturation under $5\,\mathrm{T}$ (see Figure 5.11 (a)) and compared these results to the one of Co nanowires. As it has been done in Section 5.1.3 for oxidized Co nanowires, the time decay of the magnetization was fitted using a phenomenological stretched exponential expression: $M(t) = M_c + M_0 \exp{(-t/\tau)}^\beta$, where M_c is the magneti-

zation at infinitely long times (static part), M_0 is the magnetic moment of the fluctuating volume, τ is the relaxation time and β is a stretch factor, indicative of a distribution of relaxation times in the sample. Figure 5.11 (b) compares the temperature dependence of the relaxation time τ for oxidized $Co_{80}Ni_{20}$ and Co nanowires. Note that in both cases, β is 0.4 which indicates that the relaxation time distribution and thus the oxide grain size distribution is similar for both samples. As shown in Figure 5.11 (b), the temperature dependence of τ is similar for both samples: the relaxation time τ is first very short above T_N and then increases quickly upon decreasing temperature down to $50\,\mathrm{K}$ where it finally levels off down to the lowest temperature.
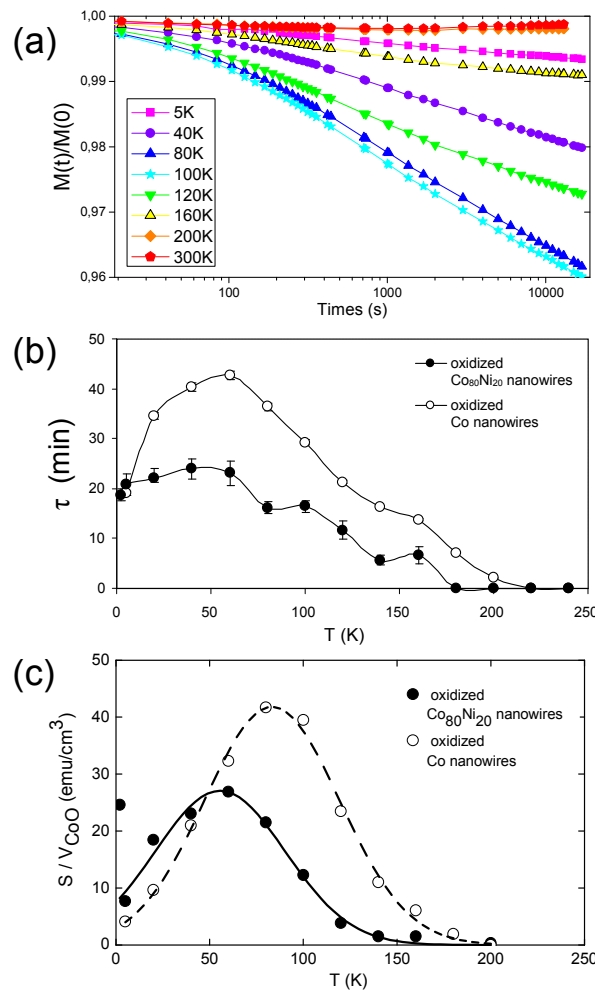
Figure 5.11: (a) $M(t)/M(t=0)$ as a function of time for $Co_{80}Ni_{20}$ nanowires under $3\,\mathrm{mT}$ after saturation at 5T. (b) Temperature dependence of the magnetization relaxation time for oxidized $Co_{80}Ni_{20}$ and Co nanowires extracted from the expression $M(t) = M_c + M_0 \exp{(-t/\tau)}^{\beta}$ with $\beta = 0.4$ kept fixed throughout. (c) magnetic viscosity $S(T)$, as a function of the temperature, extracted from the expression $M(t) = M_0 - S(T) ln{(t - t_0)}$.

Since β is 0.4 for oxidized $Co_{80}Ni_{20}$ nanowires, the distribution of particle size and anisotropy barriers can be considered as almost flat so that the behavior of the magnetization can also be described phenomenologically by the relation [Kne1962]: $M(t) = M_0 - S(T) ln{(t - t_0)}$, where $S(T)$ is the magnetic viscosity. The viscosity parameter is

compared on Figure 5.11 (c) for oxidized Co and $Co_{80}Ni_{20}$ nanowires. Its temperature dependence is very similar for both samples so that the interpretation is the same as the one presented in Section 5.1.3. The only difference is the value of $k_B T^*$ which is found to be $k_B T^* = 55 \pm 1$ K for the oxidized $Co_{80}Ni_{20}$ nanowires whereas it was found to be $k_B T^* = 83 \pm 1$ K for the oxidized Co nanowires (see Section 5.1.3). The value of W is the same for both samples and is $W = 35 \pm 2$ K. From the absolute values of the viscosity $S(T)$, normalised by the volume fraction of CoO present in the nanowire (assuming a 1.5 nm shell thickness), the spontaneous magnetization of the CoO shell for oxidized $Co_{80}Ni_{20}$ nanowires is $M_S = 15.2 \pm 0.1$ emu/cm^3. This is the same value as the one deduced in the case of oxidized Co nanowires. It implies that the volume fraction which is "active" also represents only $1 - 2\%$ of the total volume of CoO in the oxidized $Co_{80}Ni_{20}$ nanowires.

Finally, the relaxation measurements performed on oxidized $Co_{80}Ni_{20}$ nanowires indicate that the mechanisms which come into play in these oxidized nanowires are the same as the ones proposed for oxidized Co nanowires and that the shape of wires nor their composition does not affect the behaviour of the CoO shell.

5.3 Exchange Bias in nanowires: influence of the magnetic history

Figure 5.12 presents the temperature dependence of the exchange bias field H_{EB} and coercive field H_C for oxidized $Co_{80}Ni_{20}$ nanowires as a function of magnetic history. In a first series of measurements, the samples were field-cooled under $5T$ and the hysteresis cycles were measured while increasing the temperature from 5 K to 300 K. A second experimental procedure consisted in measuring the hysteresis cycles with decreasing temperature.
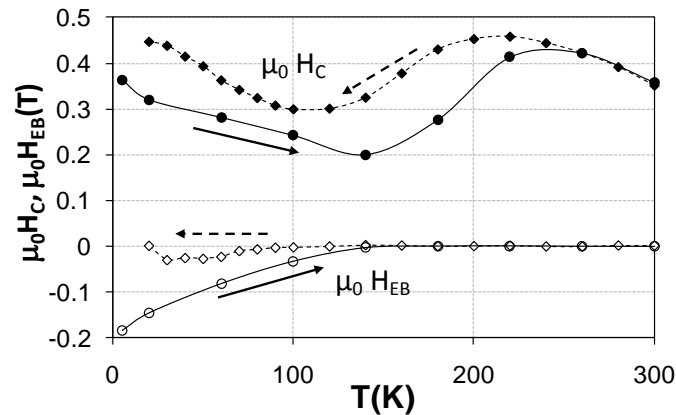
Figure 5.12: Comparison between the case where the temperature is increased (from a field cooled state) (solid line) and when the temperature is decreased (dotted line).

The results are qualitatively the same apart from the fact that H_{EB} is significantly smaller and appears at lower temperatures, while the coercive field is larger but still presents a marked minimum at T_{EB}. Indeed, when the sample is field cooled without any external magnetic field, the antiferromagnetic CoO grains do not exhibit any preferential orientation. This explains why both H_{EB} and the coercivity drop are smaller than when

the sample is field cooled and the CoO grains oriented along the same direction. These measurements indicate that the coercivity of the system strongly depends on the magnetic history which would not be the case without exchange bias contribution.

5.4   Conclusion

In this chapter, the effects of the oxidation on the magnetic properties of $Co_{1-x}Ni_x$ nanowires have been investigated. It has first been shown that the AF ordering temperature of CoO oxidation shell is rather high ($T_N \sim 230\,\mathrm{K}$) compared to the bulk value ($T_N \sim 293\,\mathrm{K}$). The exchange-bias field reaches values on the order of $0.2\,\mathrm{T}$ at low temperatures. A minimum of coercivity is observed around the blocking temperature $T_{EB} \sim 100\,\mathrm{K}$ which is unambiguously related to the exchange-bias mechanism. Magnetization relaxation measurements show that this effect finds its origin in the superparamagnetic fluctuations of the oxidized AFM CoO layer. This proves that the exchange-bias mechanism sets in well above T_{EB}. Such a dramatic effect on the coercivity properties was not observed in previous studies because zero-dimensional systems spheres [Gan1993, Sku2003, Lun2004] and two-dimensional systems thin films [Dev1997, Ful1972, Hou2000, Nog1999, Sku2003] have a high degree of symmetry and low coercivities. On the other hand, in the 1D geometry of nanowires, the coercivity is dominated by shape anisotropy effects. The large drop of coercivity can thus be due to blocked AFM particles which act as nucleation points and promote the magnetization reversal of the wires. Therefore, the results presented in this chapter underline the importance of the AFM superparamagnetic fluctuations in the exchange-bias mechanism.

Furthermore, a complementary study has been led and allows to compare different degrees of oxidation. This study is presented in Annexe and show surprising results for slightly oxidized nanowires, in particularly large increase of saturation magnetization with decreasing temperature, giant coercivity drop with decreasing temperature below 50K and even a decrease of the exchange field with decreasing temperature.

Chapter 6

Fabrication of permanent magnets using magnetic nanowires

The magnetic characterizations at room temperature of nanowires synthesized via the polyol process (presented in Chapter 3) indicate that these objects exhibit large coercivities. This allows to imagine using these nanowires as permanent magnets.

The efficiency of a permanent magnet is given by its maximum energy product (see Figure 6.1). This energy product can be deduced from the $B - H$ loop. B is here defined as the magnetic induction which is expressed as:

$$B = \mu_0(H + M) \, . \tag{6.1}$$

From Figure 6.1, it is evident that large coercivities and a square $M - H$ loop are required to obtain high energy products . Of course, the energy product of a permanent magnet is not the only criterion for its use. The microstructure, the temperature dependence, the shape, the mechanical properties or the cost also play a key role in the choice of a permanent magnet depending on the desired application. For instance, the commercialized Crovac magnets [O'H2000, VAC]- which are made of Fe, Cr and Co- are often employed when permanent magnets rolled into thin sheets are required for specific applications. Therefore, since there exists a large range of possible applications in the field of permanent magnets (electronic devices, cars, generators, motors, loudspeakers, wireless devices, actuators...), one can wonder if permanent magnets made with such nanowires could compete with other kinds of permanent magnets for some applications.

Today, commercialized permanent magnets are divided in four main families: ferrites, AlNiCo magnets, bonded rare-earth magnets and sintered rare-earth magnets. Ferrites are the most commercialized permanent magnets because of their low price in spite of their limited performances. AlNiCo magnets are less and less sold because they are quite expensive compared to their performances but find applications when excellent temperature stability is required such as in instrumentation. Rare-earth permanent magnets are the most powerful ones but are very expensive and sensitive to corrosion.

In the 1960s, permanent magnets made with $Fe - Co$ ESD (Elongated Single Domain) particles were commercialized under the name of Lodex [Deg2001]. The properties of ESD particles came from their large shape anisotropy which is almost temperature independent. However, the performances of Lodex at room temperature were limited and they were superseded in the 1970s by rare-earth magnets [Deg2001].

The first magnetic characterizations at room temperature of the nanowires synthesized via the polyol process suggest larger coercivities for our nanowires than for Lodex ($\sim$ 1 kOe). Consequently, can magnetic nanowires be considered as efficient ESD particles? Here the subject is revisited and the question is simply to know whether these nanowires could find an application in industry.

First, the properties of Lodex permanent magnets are detailed in order to understand why they could not compete with rare-earth magnets. Then the magnetic properties of the nanowires and their high temperature behaviour are discussed before comparing them to other commercialized permanent magnets.
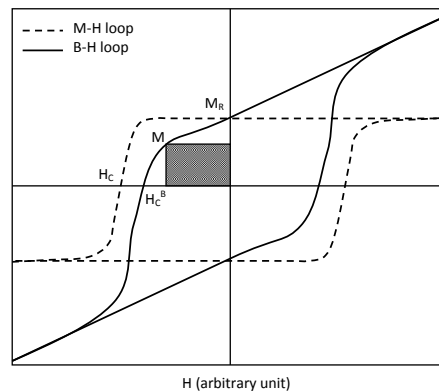
Figure 6.1: The energy product of a hard magnetic material is defined as the larger rectangle in the top left quarter of the $B - H$ hysteresis loop [Deg2001].

6.1 Lodex: an example of permanent magnet made of ESD particles

In 1942, permanent magnets prepared from pure Fe or $Fe_{1-x}Co_x$ ($0.3 < x < 0.35$) powders, respectively designed under the name PF1 and PF2, were elaborated in France. They were obtained after compacting and sintering the spherical particles (diameter comprised between 10 nm and 100 nm) in a reducing environment at around 400°C. Their performances are presented in Table 6.1. Their commercialization was stopped because of their low magnetocrystalline anisotropy ($K_1 \approx 4,7 \times 10^4$ J.m^{-3}) [Deg2001].

ESD magnet	B_R (T)	H_C (kA.m^{-1})	H_C (Oe)	$(BH)_{max}$ (kJ.m^{-3})	$(BH)_{max}$ (MG.Oe)
PF1	0.6	38	475	8.8	1.1
PF2	0.86	32.5	410	13	1.65
Lodex: isotropic Fe-Co	0.48	78	970	10	1.24
Lodex: Fe-Co anisotropic	0.68	80	1000	24	3

Table 6.1: Magnetic performances of ESD permanent magnets (PF1, PF2 and Lodex) [Deg2001].

However, a leading innovation arose in the United States in 1954 [Cra1967, Men1955,

FaL1966]. It consisted in giving a very elongated shape to the *Fe* or *FeCo* particles (diameter around 20 nm for a length around 100 nm) and in aligning them (see Figure 6.2). The elongated shape of the particles was obtained thanks to electrolytical deposition on a mercury cathode. Then, annealing the material allowed to increase the shape anisotropy of the needles and therefore increase the coercivity. It could even be improved further if a small quantity of tin or lead covered the needles ($H_C \simeq 1\,\mathrm{kOe}$). Their performances are shown in Table 6.1.

Figure 6.2: Image of ESD Fe particles [Men1955].

At that time, the key advantage of these permanent magnets was their large shape anisotropy leading to quite large coercivities. Nevertheless, the energy product of such permanent magnets ($\sim 3\,\mathrm{MGOe}$) could not compete with the one of RE magnets ($\sim 50\,\mathrm{MGOe}$) which were developed in the 1970's (see Figure 6.3). Moreover, the use of mercury to fabricate these permanent magnets hastened of such materials.
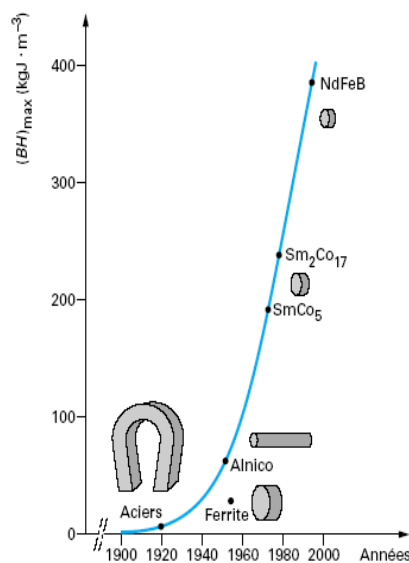
Figure 6.3: Magnetic performances of classical permanent magnets [Deg2001].

6.2 Magnetic performances of nanowires and high temperature behaviour

As detailed in Chapter 3, the nanowires synthesized via the polyol process exhibit very interesting magnetic properties at room temperature, in particular a large coercivity. Moreover, in nanowires, the large shape anisotropy mostly governs their magnetic properties. The key advantage of this feature is that the shape anisotropy is almost temperature independent far below the Curie temperature T_C. This suggests that these materials may keep their coercivity at higher temperatures. Knowing that the coercivity of RE magnets collapse above 250°C, such nanowires may compete with RE magnets at high temperatures.

6.2.1 Magnetic properties at room temperature

From the magnetic characterizations of $Co_{80}Ni_{20}$ and Co nanowires presented in Chapter 3, the energy product of a material made of such nanowires at room temperature have been assessed.

6.2.1.1 $Co_{80}Ni_{20}$ nanowires pressed powder: an assessment of the energy product.

Dried powders were compressed using a manual press. The density of the pressed powders was $4.4\,g.cm^{-3}$ (*i.e.* 50% of Co bulk density). A typical hysteresis cycle is presented in Figure 6.4. The sample exhibits a relatively high coercive field, $H_C = 286\,\text{kA/m} = 3.6\,\text{kOe}$. The saturation magnetization of the powder is in the range of 8.2×10^{-5}–$10.7 \times 10^{-5}\,\text{Tm}^3/\text{kg}$ $(65$–$85\,\text{emu.g}^{-1})$. If normalized by the bulk density of the material, one obtains $M = 581$–$758\,\text{kA/m}$ $(4\pi M = 7.3$–$9.4\,\text{kG})$. This is lower than the bulk values for $Co_{80}Ni_{20}$ alloys $M = 1230\,\text{kA.m}^{-1}$ $(4\pi M = 15.4\,\text{kG})$. This reduced magnetization is attributed to superficial oxidation of the nanowires observed with high resolution TEM. The Curie temperature T_C of these nano-objects is expected to be relatively high since the magnetization is reduced by only 10% at 240°C (see Figure 6.4). T_C is thus at least above 600°C. Further magnetic measurements at higher temperatures are presented in Section 6.2.2.2.
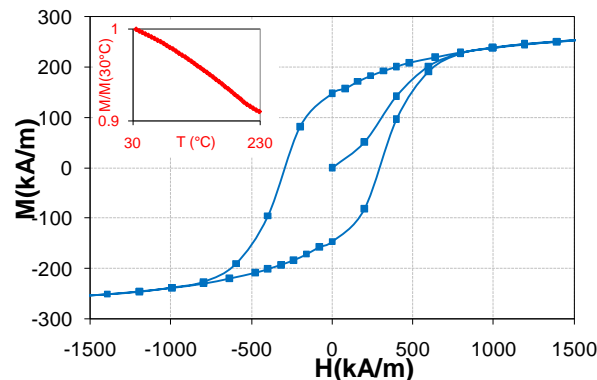
Figure 6.4: Magnetization VSM of a pressed powder sample $T = 300\,\text{K}$. (Inset) Variation of saturation magnetization with temperature.

From these results, the energy product of material made of such nanowires is estimated. A density of about half the bulk value can be reasonably used while keeping the shape anisotropy properties. This would lead to a magnetization of about $7.5\,$kG for the bulk material and the energy product would be of the order of $BH_{max} = 3.5\,$kOe $\times\, 3.5\,$kG $\approx$ $12\,$MGOe $(95\,$kJ/m$^3)$. Such energy products are not competitive with high performances of $NdFeB$ permanent magnets at room temperature [Gut2000] but can be compared to other kinds of permanent magnets.

6.2.1.2   Assessment of the energy product of Co nanowires

For Co nanorods, the measured saturation magnetization is $113\,$emu.g^{-1} close to 70% of the bulk value. This can be explained by a partial oxidation of the wires as well as the presence of organic residue in the sample. The coercivity of wires randomly deposited on a substrate is as high as $5.2\,kOe\,(414\,$kA/m$)$ (see Figure 6.5). This value can be improved by aligning the wires. The coercivity of a frozen solution of aligned wires is as high as $9\,$kOe $(716\,$kA/m$)$ at $140\,$K with a remanence of $0.95 M_S$ (see Figure 6.5). At $140K$, the Co powders have thus an energy product of the order of $6\,$kG $\times\, 4.5\,$kOe $\approx$ $27\,$MGOe $(215\,$kJ/m$^3)$ which ranks them at the level of $SmCo$ RE magnets (see Figure 6.3). Of course, such an assessment at $140\,$K probably overestimates the energy product expected at room temperature since saturation magnetization and coercivity usually decrease with increasing temperature. Nevertheless, the magnetic measurements were performed on oxidized nanowires and as shown in Chapter 5, the coercivity of such oxidized nanowires are equivalent at room temperature and at $140\,$K. It means that the energy product of permanent magnets made of Co nanowires can theoretically be as large as $25\,$MGOe $(\sim 200\,$kJ/m$^3)$ at room temperature.
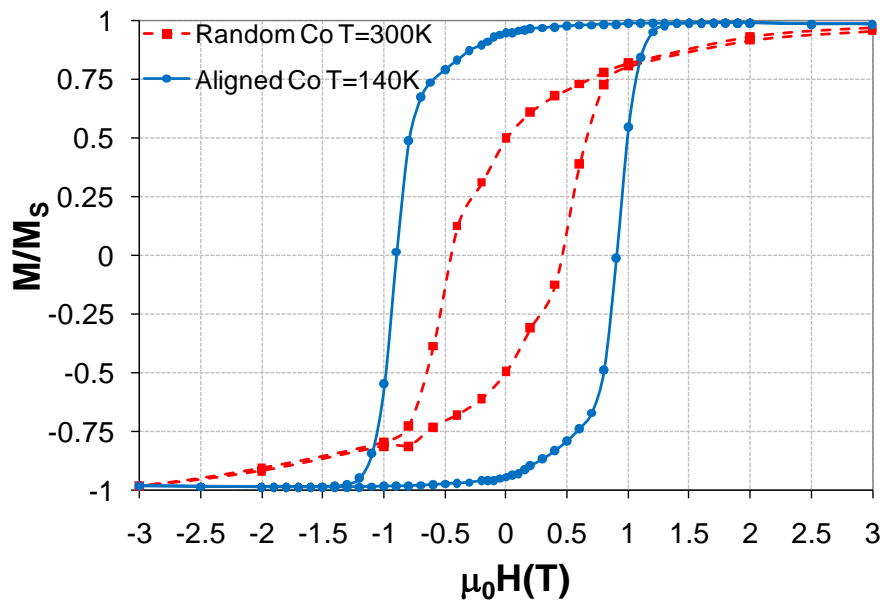
Figure 6.5: Magnetization curve on Co nanorods randomly deposited on an Al substrate ($300\,$K data) and on Co nanorods aligned in liquid toluene and frozen at $140\,$K.

6.2.2 Magnetic properties at high temperature

In Section 3.3, it has been observed that about half of the coercivity came from the shape anisotropy of the nanowires while the other half came from their magnetocrystalline one. Since the shape anisotropy is almost temperature independent, a part of the magnetic properties of the nanowires are expected to be preserved at high temperature. However, several experimental studies [Car1958, Ono1979, Ono1980] gave evidence of a strong decrease of the magnetocrystalline anistropy at high temperature (see Figure 6.6) leading to an inversion of its sign at around $T = 515\,\mathrm{K}$. Therefore, magnetic measurements on the nanowires at high temperatures are presented in this section to consider their ability to keep their coercivity at high temperatures.
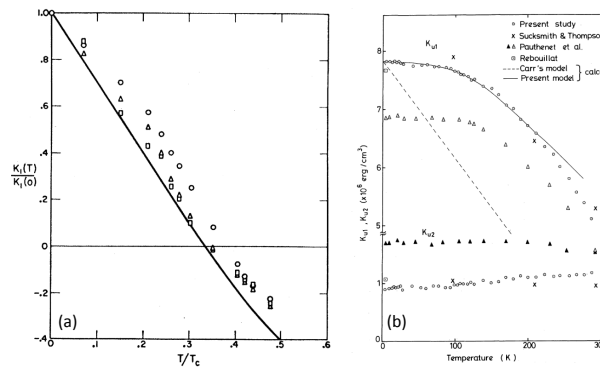
Figure 6.6: (a) Temperature dependence of the uniaxial magnetocrystalline anisotropy constant K_{u1} determined by Carr [Car1958], (b) Temperature dependence of the uniaxial magnetocrystalline anisotropy constants, K_{u1} and K_{u2}, of *hcp* cobalt determined by Ono. The different experimental results are compared to Carr's relation and to Ono's model. Note that Carr's model temperature dependence is only valid for $T > 150\,\mathrm{K}$ where K_{u1} exhibits a linear temperature dependence. [Ono1979, Ono1980]

6.2.2.1 Measurements on *Co* nanowires

Two kinds of samples have been investigated: *Co* nanorods pressed into pellets and *Co* nanorods deposited on an *Al* substrate. The samples were measured in a SQUID under reduced pressure of helium at high temperature.

First, the saturated magnetization and the remanent magnetization of the pressed pellets are rather stable up to $550\,\mathrm{K}$ (see Figure 6.7). M_S decreases by less than 1%. At $550\,K$, an increase of the magnetization is observed. It is explained by the decomposition of remaining organo-metallic matter at the surface of the rods which causes the apparition of added metallic *Co*. At higher temperatures (up to $800\,\mathrm{K}$, the saturation magnetization decreases only moderately (10%). However, the starting *Co* nanowires were characterized as pure *hcp Co* but after the heating procedure the coexistence of *hcp* and *fcc Co* phases was observed. The reason is a phase transition $hcp \rightarrow fcc$ which occurs at about $725\,\mathrm{K}$ for bulk cobalt.
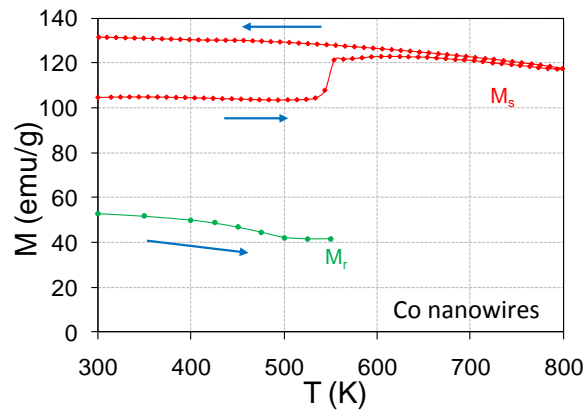
Figure 6.7: Saturation magnetization and remanence as a function of temperature for a pellet of Co nanorods.

As for the coercive field, it has a linear temperature dependence (see Figure 6.8). The behaviour of the two samples are quite different. The coercive field at room temperature of the measured pellet wass relatively low ($H_C \sim 2.2\,\text{kOe}$) compared to the other pellets usually studied ($H_C \sim 5.2\,\text{kOe}$). The coercivity of the pellet decreases linearly from $300\,\text{K}$ to $500\,\text{K}$ and drops sharply around $550\,\text{K}$. This suggests that the nanowires structure and the shape anisotropy are lost as early as $550\,\text{K}$. A possible explanation could be the sintering of the wires in the pellets at $550\,\text{K}$.

In the case of wires deposited on an Al substrate, the coercivity decreases but does not drop sharply at least up to $600\,\text{K}$ (see Figure 6.8). In this case, the nanowires are quite well separated which prevents them from sintering at high temperature.
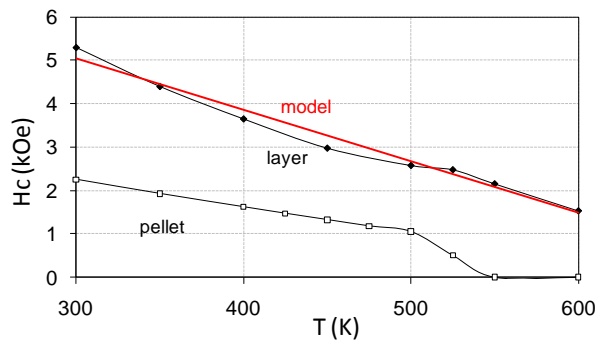
Figure 6.8: Evolution of the coercive field for Co nanowires pressed into pellets and deposited as a layer on an Al substrate. The red line is a linear fit to the experimental data of the nanowires deposited on an Al substrate. The red line is given by $H_C = A \times (1 - B \times T)$ with $A = 8.6141 \pm 0.32608$ and $B = 0.001386 \pm 8.06337 \times 10^{-5}$.

These measurements at high temperature give us a first idea of the energy product which could be expected at high temperature. The measurement of the pressed pellet shows that at $800\,\text{K}$ the sample can keep $85 - 90\%$ of its saturated magnetization. The measurements on the Al substrate indicate that the sample can keep 50% of its coercivity at $500\,\text{K}$ and 30% at $600\,\text{K}$. Thus the energy products would be at least of the order of $7.5\,\text{MGOe}\,(60\,\text{kJ/m}^3)$ at $500\,\text{K}$ and $4\,\text{MGOe}\,(32\,\text{kJ/m}^3)$ at $600\,\text{K}$.

Furthermore, the temperature dependence of the coercive field is probably related to the temperature dependence of the magnetocrystalline anisotropy since both are linear. In Section 6.2.2.3, the experimental temperature dependence of H_C is compared to the predicted one given in [Ono1979, Ono1980, Car1958]. It will allow to assess if the decrease of the coercivity with increasing temperature only stems from the magnetocrystalline anisotropy.

6.2.2.2   Measurements on $Co_{80}Ni_{20}$ nanowires

The case of $Co_{80}Ni_{20}$ is very similar (see Figure 6.9). The saturation magnetization is rather stable up to 550 K. The coercive field also decreases almost linearly up to 550 K. Even though this sample was not heated at too high temperature the coercive field was reduced by about 40% at room temperature which proves that the nanowire structure has been altered. It means that particular attention must be paid to the structural modifications of the nanowires at higher temperatures. In other words, one of the main challenge in order to fabricate permanent magnets made of such nanowires would consist in dispersing them in a suitable matrix which prevents them from altering or sintering.
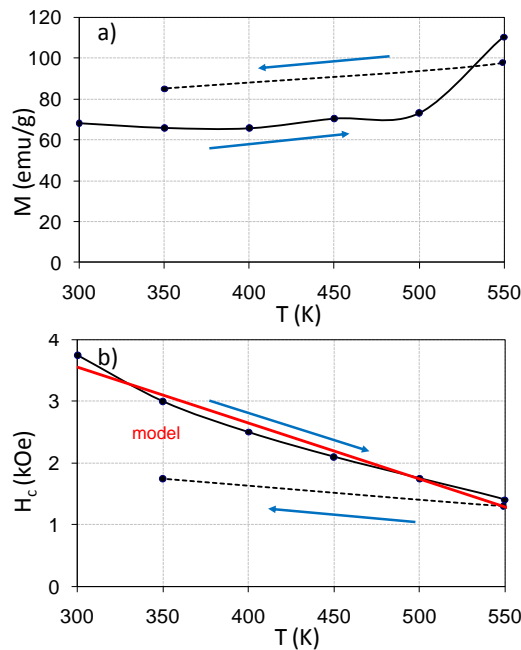
Figure 6.9: Evolution of (a) the saturated magnetization of $Co_{80}Ni_{20}$ nanowires and (b) the coercive field. The red line allows to fit the experimental coercivity from the model developed in Equation . The red line is given by $H_C = A \times (1 - B \times T)$ with $A = 6.27128 \pm 0.25662$ and $B = 0.001446 \pm 9.0568 \times 10^{-5}$.

6.2.2.3   Determination of the magneto-crystalline anisotropy temperature dependence

The magnetic measurements at high temperature allow to assess the contributions of the shape anisotropy H_{shape} and the magnetocrystalline anisotropy H_{MC} to the coercivity.

In this section, the experimental results on Co nanowires are compared to the magneto-crystalline anisotropy of *bulk Co*. From the theory of Zener [Zen1954], it has been predicted and experimentally confirmed [Car1958] that the uniaxial anisotropy constant K_1 of Co varies as :

$$\frac{K_1(T)}{K_1(0)} = \left(1 - \frac{3T}{T_C}\right) \left(\frac{M(T)}{M(0)}\right)^3 . \tag{6.2}$$

Since the Curie temperature of Co is $T_C = 1360\,\text{K}$, the temperature variations of the magnetization can be neglected in the temperature range $300\,\text{K} - 800\,\text{K}$ and it thus leads to the following dependence:

$$K_1(T) = K_1(0) \times (1 - 0.0021 \times T) . \tag{6.3}$$

The magneto-crystalline anisotropy thus varies linearly with temperature and becomes negative at 475 K. However, further investigations from F. Ono and O. Yamada [Ono1979, Ono1980] led to the conclusion that the temperature dependence of the *bulk Co* magnetocrystalline anisotropy was linear only for temperature above 150 K as shown in Figure 6.6. Indeed, Equation 6.2 (Carr's relation) was obtained from the Zener's theory by considering the effect of the change of the parameter ratio c/a with temperature. W. J. Carr made the assumption that the thermal expansion of c/a exhibited a constant coefficient. However as explained in [Ono1979, Ono1980], this assumption cannot be applied at low temperature where a very small change in the values of a and c are expected. The results obtained by F. Ono and presented in Figure 6.6 imply that the Co magnetocrystalline anisotropy has a linear temperature dependence for temperatures above 150 K with $K_{MC} \approx 6.5 \times 10^5\,\text{J/m}^3$ at $T = 200\,\text{K}$ and $K_{MC} \approx 5 \times 10^5\,\text{J/m}^3$ at $T = 300\,\text{K}$. It finally leads to an inversion of the sign of K_{MC} at $T \approx 515\,\text{K}$ and to a linear temperature dependence above $T = 200\,\text{K}$ estimated to:

$$K_1(T) = 9.5 \times 10^5 \times (1 - 0.00156 \times T) \ \ in \ J/m^3 . \tag{6.4}$$

The slope of the magnetocrystalline anisotropy decrease with increasing temperature is therefore slightly modified compared to Equation 6.2 .

The coercive field H_C of nanowires is given by (see Section 1.3.5.1):

$$H_C = 2(K_{MC} + K_{shape})/\mu_0 M_S . \tag{6.5}$$

The shape anisotropy is supposed to be temperature independent, so that the coercive field can be expected to follow a linear dependence as a function of temperature:

$$H_C(T) = H_{shape} + H_{MC}(300K) \times (1 - 0.00156 \times T) . \tag{6.6}$$

.

This is what is experimentally observed in the range $300-500\,\mathrm{K}$ since the coercivities of Co and $Co_{80}Ni_{20}$ nanowires follow the respective temperature dependencies (see Figures 6.8 and 6.9):

$$\left\{ \begin{array}{l} H_C(T) = H_C(0K) \times (1 - 0.00138 \times T)\,, \\ H_C(T) = H_C(0K) \times (1 - 0.00144 \times T)\,. \end{array} \right. \qquad (6.7)$$

The measured temperature coefficients ($0.00138\,\mathrm{K}^{-1}$ and $0.00144\,\mathrm{K}^{-1}$) are not too far from the theoretical one (within 12%). This temperature dependence corresponds mostly to the intrinsic magneto-crystalline anisotropy of Co. Thus, it is possible to extract the contribution of the shape anisotropy to the coercivity from the measurement at $515\,\mathrm{K}$ when the magneto-crystalline anisotropy is expected to vanish. The shape anisotropy contribution is of the order of only $1.7\,\mathrm{kO}e$ and $2.6\,\mathrm{kO}e$ for respectively $Co_{80}Ni_{20}$ and Co nanowires. This result is about half the value of the previous assessments obtained by fitting room temperature hysteresis curves shown in Chapter 3 ($3.5\,\mathrm{kO}e$ for $Co_{80}Ni_{20}$ nanowires [Mau2007] and $4.8\,\mathrm{kO}e$ for Co nanowires). However, the difference observed here between the values obtained from the Stoner-Wohlfarth modelling at room temperature and from the magnetic measurements at $515\,\mathrm{K}$ comes from the fact that, in this procedure, the wires are not aligned but randomly oriented. Indeed, for randomly oriented nanowires, the angular average reduces the contribution of the shape anisotropy to the coercivity by a factor 0.5 using a simple Stoner Wohlfahrt model (see Section 1.3.5.1).

Finally, it appears that the temperature dependence of the Co magneto-crystalline anisotropy is a real limitation to the performances of permanent magnets made with these nanowires at high temperature. Indeed K_{MC} not only vanishes at $515\,\mathrm{K}$ but becomes negative above this temperature.

6.3   Comparison with commercial permanent magnets

From the measurements shown in this chapter, these materials seem to present some potential for the fabrication of permanent magnetic materials. Their advantages and limitations are detailed in this section and compared to the performances of commercial permanent magnets.

First, the polyol process is a low temperature chemical process which does not need any advanced metallurgical skills and which can easily be scaled to large volumes. Moreover, the use of 3d transition metals such as Co provides high remanence and high T_C.

In addition, the nanowires synthesized via the polyol process are very well crystallized. Consequently, their single crystal structure provides an extra magneto-crystalline anisotropy. Most importantly, through their strong shape anisotropy, they provide a large coercivity, almost temperature independent far below T_C, so that these nanowires could potentially be used as high temperature permanent magnets as $AlNiCo$ magnets. At room temperature, coercivities as high a $7.5\,\mathrm{kO}e$ ($0.6\,\mathrm{MA/m}$) were already achieved (but not confirmed) and this value could be improved. The magnetization of the pressed powder is of the order of $12\,\mathrm{kOe}$ but it would be difficult to improve it without loosing the nanowires structures. Thus at room temperature, the energy product of the nanowires is

of the order of 20 MGOe which nearly rank them among at the level of $SmCo$ RE magnets (see Figure 6.10).

Unfortunately, the performances of these nanowires at higher temperatures are limited by the fact that the magneto-crystalline anisotropy of Co drops rather quickly with temperature and vanishes at about 175°C. The nanostructure of the material is also temperature sensitive and seems to be lost above 300°C for the samples studied. However, their performances at high temperature can all the same be considered as competitive with the ones of $AlNiCo$ or RE magnets (see Figure 6.11).
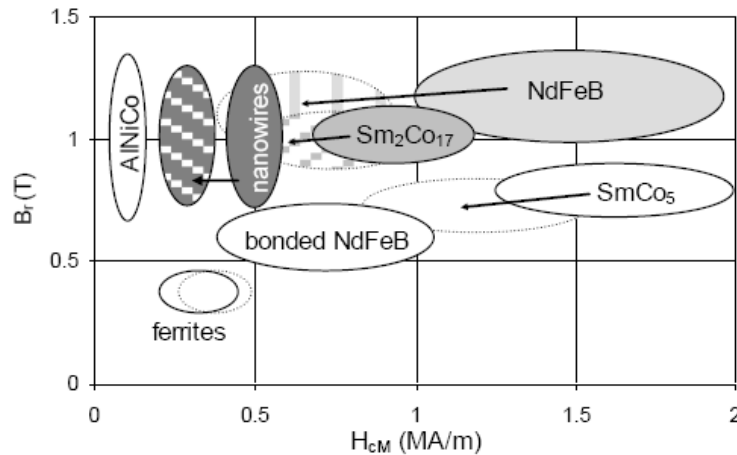
Figure 6.10: Remanence and coercivity of the usual permanent magnets materials at 20°C. The values at 120°C are indicated as hashed surfaces (adapted from [Deg2001], [Mau2007] and [Via2009]).

As shown in Figure 6.10, they could fill a gap between RE magnets such as $SmCo$ [Gut2000] and $AlNiCo$ magnets [Cro1966]. RE magnets have higher coercivities but they show stronger softening upon warming, while $AlNiCo$ magnets exhibit much lower coercivities in the whole temperature range of interest.

Material	Price (€/kg)
Fe	0.065
Co	30
Ni	13

Table 6.2: Price of Fe, Co and Ni (September 2009).

Besides, magnetic performances cannot be considered as the only criterion for the choice of a permanent magnet. The cost of a permanent magnet combined with the desired application is of course a key factor in the choice of a permanent magnet. Table 6.2 gives an estimation of the price of Fe, Co and Ni . Fe is a very cheap material which makes ferrite very attractive. To the contrary, the price of $NdFeB$ is relatively high ($\sim$ 50€/kg) since Nd is very expensive. As for permanent magnets made with $CoNi$ nanowires, an estimated price is about 30€/kg. This intermediate price for intermediate performances between ferrites and rare-earth permanent magnets could justify its use for

applications requiring good magnetic performances or temperature stability. Moreover another advantage is that such nanowires can be dispersed in metals as well as in polymers. Consequently, with these nanowires it is possible to produce some permanent magnets exhibiting different shapes (thanks to some specific moulds), which is not possible with rare-earth permanent magnets because they are very hard to manufacture. One can even imagine to fabricate some micro-sized permanent magnets with nanowires in order to use them in microelectronics.
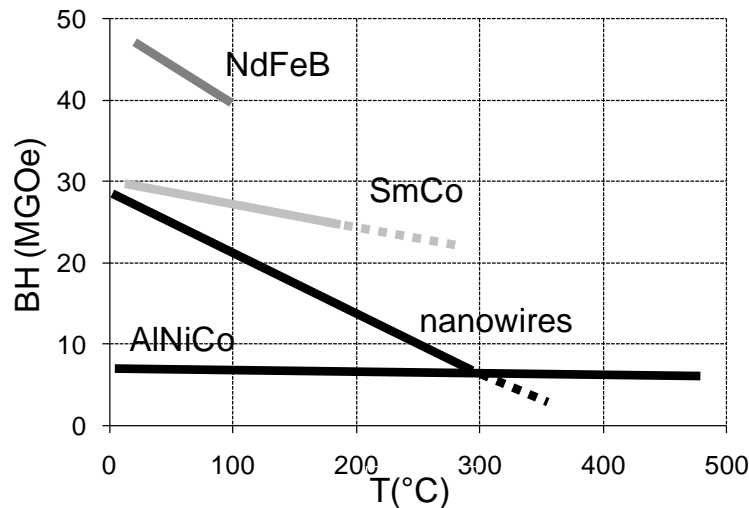
Figure 6.11: Temperature dependence of permanent magnets made with nanowires and other kinds of permanent magnets.

6.4   Perspectives

These nanowires may have some potential for the fabrication of permanent magnets and now lots of efforts have to be done in the metallurgical field so that they can be dispersed in an appropriate material. That is why a collaboration has started with the Laboratoire des Propriétés Mécaniques et Thermodynamiques des Matériaux (LPMTM) in Paris-XIII. Their expertise in metallurgy would be useful to press the nanowires under a magnetic field or to disperse the nanowires in a suitable metal under a magnetic field. For the latter point, the idea consists in using tin or lead which both exhibit a low boiling temperature.

Besides, since it will not be possible to improve the magneto-crystalline properties of Co, the most promising route to improve the magnetic performances of the nanowires might be to consider the fabrication of similar materials based on iron which would both provide a higher remanence (and thus a higher shape anisotropy) and a cheaper cost for large scale applications. Such materials could then be competitive with bonded $NdFeB$ materials for room temperature applications or with $SmCo_5$ for high temperature applications up to 250°C.

Finally, what could be also very useful concerning the use of these nanowires are their dimensions. Their nanosize could lead to applications in microelectronics by using only small quantities of them. For instance, another potential application of these materials is their use in magnetic recording media. Their properties are already twice as good as existing materials used for magnetic tape recording [Wan2007, Deg2001].

Part II

Small Angle Neutron Scattering (SANS) on magnetic nanowires

Small Angle Scattering (SAS) is a technique developed by Guinier and Fournet in the 1940's and 1950's [Gui1955]. Guinier first discovered SAS during X-Ray diffraction measurements on metal alloys [Gui1939]. He observed a small deviation of the beam after it interacted with structures larger than its wavelength. From this deflection of the beam, he built up a theory which allowed to characterize the shape, the orientation and the organization of particles dispersed in a continuous medium. This technique permits to study colloidal particles (nano-objects, ferrofluids, ...), surfactant aggregates like micelles, polymers, liquid crystals or even biological objects like proteins. It must be precised that SAS includes three techniques based on three different radiations: Small Angle Light Scattering (SALS), Small Angle X-Ray Scattering (SAXS) and Small Angle Neutron Scattering (SANS).

The following work consists in using the SANS technique to probe the magnetic properties of nanowires. Many works have been carried out on magnetic nanosphere but very few have been devoted to more complex objects such as magnetic nanowires. The complexity of such anisotropic systems mainly stems from both the complexity of their nuclear and magnetic form factors but also from the inhomogeneity of their demagnetizing field. Two different systems have been studied during this work. "Aligned" powders made of the magnetic nanowires presented in Part I have first been investigated. The second part of the work has consisted in studying magnetic nanowires perfectly oriented in porous alumina membranes.

In this part of the manuscript, Chapter 7 aims at theoretically treating the case of SANS measurements on magnetic nanowires. In Chapter 8, I discuss the SANS results on the aligned powders of magnetic nanowires. Finally Chapter 9 presents results on perfectly ordered systems made of nanowires included in porous alumina membranes.

130

Chapter 7

SANS formalism applied to the study of magnetic nanowires

Most magnetic nano-objects investigated via Polarized SANS measurements are nanospheres [Löf2005]. Unfortunately, there has been no deep investigations on anisotropic magnetic nano-objects such as nanowires. Until now, the only published paper [Gri2007a] about Polarized SANS experiments on magnetic nanowires does not focus on polarized intensities but only on the magnetic field dependence of the general intensity and thus provides no real information about the magnetism of the nanowires. Two reasons for this lack of investigation on magnetic nanowires may be mentioned:

1. The SANS intensity for a general shape of particles depends on their relative orientations with respect to the incident beam.

2. The demagnetizing field is not homogeneous in nanowires making more complex the determination of the magnetic form factor.

For the past three years, I have explored the possibility of studying magnetic nanowires via polarized SANS in the Laboratoire Léon Brillouin. I have performed SANS experiments on the PAXE spectrometer and Polarized SANS experiments on the PAPYRUS spectrometer. This chapter provides the general formalism of Polarized SANS and how it applies to magnetic nanowires. It is illustrated with some simulations performed via the SpectraProcessor software [Spe]. The technical details about neutron scattering and the course of a SANS experiment are described in Annexes 11 and 12 .

7.1   Mathematical formalism of SANS

This Section describes the basics of the SANS formalism. It begins with the treatment of non polarized SANS which leads to the structural characterization of the investigated system. Then it illustrates how Polarized SANS is adapted to probe magnetism in nanostructures.

7.1.1   SANS geometry

In an elastic scattering process, the norm of the wave vector is conserved so that:

$$\left|\overrightarrow{k_s}\right| = \left|\overrightarrow{k_i}\right| = k = \frac{2\pi}{\lambda_i} \ , \tag{7.1}$$

where $\overrightarrow{k_s}$, $\overrightarrow{k_i}$ and λ_i are respectively the scattered wave vector, the incident wave vector and the incident wavelength. The scattering wave vector $\overrightarrow{Q}$ is defined by (see Figure 7.1):

$$\overrightarrow{Q} = \overrightarrow{k_s} - \overrightarrow{k_i} = \frac{4\pi}{\lambda}sin\theta \ . \tag{7.2}$$
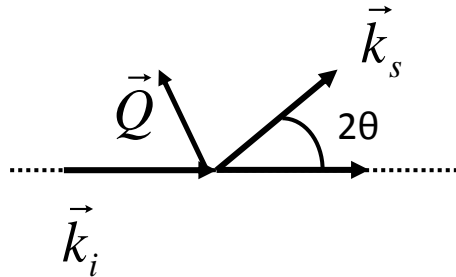
Figure 7.1: Geometry of any scattering event

From this formula, the accessible Q range strongly depends on the wavelength and on the accessible θ range which both are imposed by the technical specifications of the spectrometers (see Annexe 11). The SANS experiments presented in Chapters 8 and 9 have been performed on the PAPYRUS and PAXE spectrometers (see Annexe 12). For the PAPYRUS spectrometer, the accessible Q range is $0.002\text{Å}^{-1} < Q < 0.24\text{Å}^{-1}$. For the PAXE spectrometer, the accessible Q range is $0.001\text{Å}^{-1} < Q < 0.5\text{Å}^{-1}$. The corresponding characteristic sizes ξ are summarized in Table 7.1 and given by:

$$\xi = \frac{2\pi}{Q} \ . \tag{7.3}$$

Table 7.1 indicates that both the PAXE and PAPYRUS spectrometers are adapted to the study of nano-objects whose characteristic sizes are in the range $3-300\,\text{nm}$. In particular, they are adapted to the study of the nanowires presented in Part I.

	PAPYRUS	PAXE
$Q_{min}\,(\text{Å}^{-1})$	0.002	0.001
$Q_{max}\,(\text{Å}^{-1})$	0.24	0.5
$\xi_{min}\,(\text{nm})$	2.6	1.25
$\xi_{max}\,(\text{nm})$	314	628

Table 7.1: Q_{min}, Q_{max}, ξ_{min} and ξ_{max} for the PAXE and PAPYRUS spectrometers.

7.1.2 Non-Polarized SANS: structure and nuclear form factors

In Small Angle Neutron Scattering, the optical approximation is allowed so that this technique in fact probes continuous medium. It is then convenient to introduce a scattering length density $\rho(\vec{r})$ which characterizes the scattering ability of the medium. The

scattering length density is defined as:

$$\rho = \sum_i \frac{c_i b_i}{V_i} \, , \tag{7.4}$$

where c_i, b_i and V_i are the atomic concentration, the nuclear scattering length and the atomic volume of the constituent i in the sample, respectively. Note that contrary to X-rays, neutron scattering lengths b_i are real constants and therefore do not present any spatial dependence. More details are given in Annexe 11.

The scattering amplitude $A(\overrightarrow{Q})$ is expressed as [Rav2006, Gri2008]:

$$A(\overrightarrow{Q}) = \int_V \rho(\overrightarrow{r}) e^{-i\overrightarrow{Q}.\overrightarrow{r}} d^3\overrightarrow{r} \, , \tag{7.5}$$

where V is the sample volume and $\rho(\overrightarrow{r})$ the scattering length density of the sample.

In Equation 7.5, the temporal dependence of the scattering length density is not taken into account. If this approximation is valid for X-Rays [Gla1982] since they exhibit frequencies ($\sim 10^{18}$Hz) much larger than atomic vibrations ($\sim 10^{12}$Hz), it is not the case for neutrons [Rav2006]. However only elastic scattering is here considered. Consequently the lattice vibrations are neglected and the intensity measured in a SANS experiment is the temporal average of the instantaneous intensity.

It is first shown that SANS is only sensitive to nuclear contrast and measures nuclear form factors. Moreover, for assemblies of correlated particles , SANS experiments can give access to the distribution of the particles via the measurement of the structure factor.

7.1.2.1 Particles with no spatial correlation: definition of the nuclear form factor

In order to express the SANS intensity, it is convenient to consider the spatial average $\langle \rho \rangle$ of $\rho(\overrightarrow{r})$ and its spatial fluctuations $\delta\rho(r)$ so that the scattering length density can be written as:

$$\rho(\overrightarrow{r}) = \langle \rho \rangle + \delta\rho(\overrightarrow{r}) \, . \tag{7.6}$$

This reduces $A(\overrightarrow{Q})$, defined in Equation 7.5, into:

$$A(\overrightarrow{Q}) = \int_V \delta\rho(\overrightarrow{r}) e^{-i\overrightarrow{Q}.\overrightarrow{r}} d^3\overrightarrow{r} \, . \tag{7.7}$$

Equation 7.7 is fundamental since it clearly shows that SANS is only sensitive to the contrast of the nuclear scattering length density. This allows to understand why SANS experiments are particularly well suited to the study of particles dispersed in a continuous medium.

The measured scattered intensity per unit volume becomes [Gri2008]:

$$I(\overrightarrow{Q}) = \frac{\left|A(\overrightarrow{Q})\right|^2}{V} = \frac{1}{V} \int_V \int_V \delta\rho(\overrightarrow{r}) \delta\rho(\overrightarrow{r'}) e^{-i\overrightarrow{Q}.(\overrightarrow{r}-\overrightarrow{r'})} d^3\overrightarrow{r} d^3\overrightarrow{r'} \, . \tag{7.8}$$

The experiments presented in this manuscript were performed on particles dispersed in solvents or included in alumina membranes. Therefore these systems can be modelled

as particles of volume V_P with a scattering length density ρ_P dispersed in a medium exhibiting a scattering length density ρ_M. It implies that:

$$\delta\rho(\overrightarrow{r}) = \delta\rho(\overrightarrow{r'}) = \rho_P - \rho_M \ , \tag{7.9}$$

so that the scattered intensity per unit volume becomes:

$$I(\overrightarrow{Q}) = \frac{1}{V}(\rho_P - \rho_M)^2 \int_{V_P} \int_{V_P} e^{-i\overrightarrow{Q}.(\overrightarrow{r}-\overrightarrow{r'})} d^3\overrightarrow{r} d^3\overrightarrow{r'} = \frac{(\triangle\rho)^2}{V} \int_{V_P} \int_{V_P} e^{-i\overrightarrow{Q}.(\overrightarrow{r}-\overrightarrow{r'})} d^3\overrightarrow{r} d^3\overrightarrow{r'} \ , \tag{7.10}$$

with

$$\triangle\rho = \rho_P - \rho_M \ . \tag{7.11}$$

Let's consider a system with N identical particles of volume V_P. From the *Born approximation*, when the scattering intensity is small compared to the total intensity, scattering by a given center can be considered as independent from the other scattering centers. It means the amplitude scattered by the N particles is the sum of the amplitudes scattered by each one so that Equation 7.7 becomes:

$$A(\overrightarrow{Q}) = \delta\rho \sum_N \int_{V_P} \delta\rho(\overrightarrow{r}) e^{-i\overrightarrow{Q}.\overrightarrow{r}} d^3\overrightarrow{r} \ . \tag{7.12}$$

Equation 7.10 thus makes appear the nuclear form factor $F_N(Q)$ of the particles defined by [Gla2001]:

$$F_N(\overrightarrow{Q}) = \frac{\triangle\rho}{V_P} \int_{V_P} e^{-i\overrightarrow{Q}.\overrightarrow{r}} d^3\overrightarrow{r} \ . \tag{7.13}$$

This allows to express the SANS intensity as:

$$I(\overrightarrow{Q}) = \frac{V_P^2}{V} N \left| F_N(\overrightarrow{Q}) \right|^2 = \Phi V_P \left| F_N(\overrightarrow{Q}) \right|^2 \ , \tag{7.14}$$

where Φ is the volume fraction of particles defined as:

$$\Phi = \frac{N V_P}{V} \ . \tag{7.15}$$

Finally, Equation 7.14 provides an expression of the scattered intensity whose Q-dependence only stems from the nuclear form factor. The nuclear form factor can be a priori calculated since it only depends on the shape of the particles via the geometrical form factor $F(Q)$:

$$F(\overrightarrow{Q}) = \int_{V_P} e^{-i\overrightarrow{Q}.\overrightarrow{r}} d^3\overrightarrow{r} \ . \tag{7.16}$$

7.1.2.2   Spatially correlated particles: definition of the structure factor

If the N identical particles are now spatially correlated, the scattered intensity per unit volume becomes [Rav2006]:

$$I(\overrightarrow{Q}) = \frac{\left| A(\overrightarrow{Q}) \right|^2}{V} = \frac{1}{V} \left\langle \int_V \rho(\overrightarrow{r}) e^{-i\overrightarrow{Q}.\overrightarrow{r}} d^3\overrightarrow{r} \int_V \rho(\overrightarrow{r'}) e^{i\overrightarrow{Q}.\overrightarrow{r'}} d^3\overrightarrow{r'} \right\rangle \ . \tag{7.17}$$

The position j of each particle can be expressed as $r = r_j + u$ where r_j and u are respectively the mass center of the particles and the distance to the mass center. The introduction of these quantities allows to rewrite the scattered intensity per unit volume as:

$$I(\overrightarrow{Q}) = \frac{1}{V} \left\langle \sum_j e^{-i\overrightarrow{Q}.\overrightarrow{r_j}} \int_{V_P} \rho(\overrightarrow{u}) e^{-i\overrightarrow{Q}.\overrightarrow{u}} d^3\overrightarrow{u} \sum_k e^{i\overrightarrow{Q}.\overrightarrow{r_k}} \int_{V_P} \rho(\overrightarrow{v}) e^{i\overrightarrow{Q}.\overrightarrow{v}} d^3\overrightarrow{v} \right\rangle . \qquad (7.18)$$

Let's now consider that the correlations between the particles are identical so that the average of the product is equal to the product of the averages [Gri2008]:

$$I(\overrightarrow{Q}) = \frac{N}{V} \left\langle \frac{1}{N} \sum_{j=1}^{N} \sum_{k=1}^{N} e^{-i\overrightarrow{Q}(\overrightarrow{r_j}-\overrightarrow{r_k})} \right\rangle \left(\int_{V_P} \int_{V_P} \rho(\overrightarrow{u})\rho(\overrightarrow{u}) e^{-i\overrightarrow{Q}.(\overrightarrow{u}-\overrightarrow{v})} d^3\overrightarrow{u} d^3\overrightarrow{v} \right) . \qquad (7.19)$$

The last term of this expression can be recognized as $V_P^2 \left| F_N(\overrightarrow{Q}) \right|$ of the particles which has been previously introduced. The first term is defined as the structure factor $S(\overrightarrow{Q})$ and expressed as:

$$S(\overrightarrow{Q}) = \left\langle \frac{1}{N} \sum_{j=1}^{N} \sum_{k=1}^{N} e^{-i\overrightarrow{Q}.(\overrightarrow{r_j}-\overrightarrow{r_k})} \right\rangle . \qquad (7.20)$$

The structure factor is so-called because it stems from the spatial correlations between the mass centers of the particles. Eventually, the scattered intensity may be written under the following simple expression:

$$I(\overrightarrow{Q}) = \Phi V_P (\triangle\rho) \left| F(\overrightarrow{Q}) \right|^2 S(\overrightarrow{Q}) . \qquad (7.21)$$

Finally, the physical parameters which are relevant in SANS studies are the geometric form of the particles, their spatial correlations and their chemical composition which are respectively described by the geometrical form factor $F(\overrightarrow{Q})$, the structure factor $S(\overrightarrow{Q})$ and the nuclear contrast $\triangle\rho$.

7.1.3 Polarized SANS: the magnetic form factor

One of the advantages of neutron scattering comes from the interaction with the magnetic moments of the samples. The magnetic interaction between neutrons and the sample is now discussed.

Neutrons and electrons are particles carrying a spin $\frac{1}{2}$ and their magnetic moments are defined as follows:

$$Neutron: \quad \overrightarrow{M_N} = -g_N\mu_N\overrightarrow{\sigma} , \qquad (7.22)$$

$$Electron: \quad \overrightarrow{M_S} = -g\mu_B\overrightarrow{S} . \qquad (7.23)$$

$g = 2$ and $g_N = -1.932$ are respectively the Landé factors for electron and neutron. $\overrightarrow{\sigma}$ and $\overrightarrow{S}$ are respectively the spin operators of neutrons and electrons. μ_B and μ_N are respectively the Bohr and nuclear magnetons. They are defined as:

$$\mu_B = \frac{e\hbar}{2m_e} \simeq 9.274 \times 10^{-24} J.T^{-1} , \qquad (7.24)$$

and

$$\mu_N = \frac{e\hbar}{2m_N} \simeq 5.051 \times 10^{-27} J.T^{-1} \,. \tag{7.25}$$

Note that μ_N is 1836 times smaller than μ_B.

The aim is now to take the neutron spin state into account in the scattering. $|\psi_i\rangle$ and $|\psi_s\rangle$ are respectively the incident and scattered wave functions of the *neutron-sample* system , $|\sigma_i\rangle$ and $|\sigma_s\rangle$ are respectively the incident and scattered neutron spin states and $\mathcal{P}_{i,\sigma_i} = \mathcal{P}_i\mathcal{P}_{\sigma_i}$ the probability that the *neutron-sample* system is in the $|\psi_i\rangle$ state and the incident neutron in the spin state $|\sigma_i\rangle$. The energies and wave functions of the initial and final states for the neutron-sample system are listed below:

$$initial\ state\ \ |\psi_i\rangle\ :\ \psi_i = \frac{1}{\sqrt{\mathsf{V}}}e^{i\,\overrightarrow{k_i}.\overrightarrow{r}}\,\phi_i \quad \varepsilon_i = E_i + \frac{p_i^2}{2m}\,, \tag{7.26}$$

$$final\ state\ \ \ |\psi_s\rangle\ :\ \psi_s = \frac{1}{\sqrt{\mathsf{V}}}e^{i\,\overrightarrow{k_s}.\overrightarrow{r}}\,\phi_s \quad \varepsilon_s = E_s + \frac{p_s^2}{2m}\,. \tag{7.27}$$

V is a volume normalizing the wave functions of the neutron. Note that it has no influence on the final result (Van Hove formula). ϕ_i and ϕ_s are respectively the initial and final wave functions of the sample. $\overrightarrow{p_i}$ and $\overrightarrow{p_s}$ are respectively the initial and final impulsion of the neutron and are defined by $\overrightarrow{p_i} = \hbar\,\overrightarrow{k_i}$ and $\overrightarrow{p_s} = \hbar\,\overrightarrow{k_s}$. E_i, E_s, $\frac{p_i^2}{2m}$ and $\frac{p_s^2}{2m}$ are respectively the energies of the initial and final states of the sample and of the neutron. From the energy and momentum conservation, the energy and momentum transfers are:

$$\hbar\omega = E_s - E_i\,, \tag{7.28}$$

$$\hbar\overrightarrow{Q} = \hbar\overrightarrow{k_s} - \hbar\overrightarrow{k_i}\,. \tag{7.29}$$

The external magnetic field $\overrightarrow{H}$ defines the quantization *z-axis*. The neutron spin state is given by its projection on the *z-axis* noted $|+\rangle$ or $|-\rangle$. The neutron spin states $|+\rangle$ and $|-\rangle$ respectively refer to neutrons polarized parallel and antiparallel to the applied field axis *z*. When polarized neutrons are considered, one has to distinguish the different possible scattering processes depending on the spin state. There are in fact four possible scattering processes [Rav2006, Gla2001]:

$$Non\ spin - flip\ processes\ :\ |+\rangle \longmapsto |+\rangle\,,$$

$$|-\rangle \longmapsto |-\rangle\,,$$

$$Spin - flip\ processes\ :\quad |+\rangle \longmapsto |-\rangle\,,$$

$$|-\rangle \longmapsto |+\rangle\,.$$

It appears that the spin degrees of freedom have to be taken into account in order to calculate the partial differential cross section from Fermi's golden rule [Gri2008]:

$$\frac{d^2\sigma}{d\Omega dE} = \frac{k_s}{k_i}\left(\frac{\mathsf{V}\,m}{2\pi\hbar^2}\right)^2 \sum_{i,\sigma_i}\mathcal{P}_{i,\sigma_i}\sum_{s,\sigma_s}|\langle\psi_s,\sigma_s\,|H|\,\psi_i,\sigma_i\rangle|^2\,\delta(E_s - E_i + \hbar\omega)\,, \tag{7.30}$$

where H is the interaction hamiltonian between the neutron and the sample.

Neutrons can in fact be subject to two kinds of magnetic scattering [Rav2006]:

- A magnetic nuclear scattering coming from the interaction of the neutron with nuclei carrying a spin. Apart at very low temperature ($T \ll 1K$), these spins are disordered so that it leads to incoherent scattering. Only few nuclei carry a spin. The typical case is the one of the hydrogen nucleus which carries a spin $\frac{1}{2}$ which leads to huge incoherent scattering. This is why in most neutron scattering experiments, one tries to get rid of hydrogen. A possibility is to substitute deuterium to hydrogen.

- A scattering process coming from the dipolar interaction of the neutron with the electronic magnetic moments of the atoms. This electromagnetic interaction allows the study of the magnetic structure of solids.

If the nuclear spin scattering can be neglected, it is possible to show [Rav2006] that the total scattering length b is the sum of a nuclear scattering with the nuclear scattering length b_N coming from the neutron-nucleus interaction and of a magnetic scattering length b_M coming from the electromagnetic interaction of the neutron with the spin and orbital moments so that:

$$b = b_N + b_M = b_N + 2\overrightarrow{\sigma}.\overrightarrow{A} \,, \tag{7.31}$$

with the scattering amplitude for magnetic scattering $\overrightarrow{A}$ expressed as:

$$\overrightarrow{A}(\overrightarrow{Q}) = -\frac{g_N r_0}{2\mu_B}\overrightarrow{\sigma}\,\overrightarrow{M_\perp}(\overrightarrow{Q}) \,, \tag{7.32}$$

where $r_0 = \frac{e^2}{m_e c^2}$ is the electron radius and $\overrightarrow{M_\perp}(\overrightarrow{Q})$ the Fourier transform of the sample magnetization which is perpendicular to the scattering vector $\overrightarrow{Q}$. It is important to underline that only the component of the magnetization *perpendicular* to the scattering vector $\overrightarrow{Q}$ contributes to the magnetic scattering.

To put into evidence the *spin-flip* and *non-spin-flip* processes, it is convenient to introduce the Pauli-spin matrices:

$$\sigma_x = \begin{pmatrix} 0 & 1 \\ 1 & 0 \end{pmatrix}, \ \sigma_y = \begin{pmatrix} 0 & -i \\ i & 0 \end{pmatrix}, \ \sigma_z = \begin{pmatrix} 1 & 0 \\ 0 & -1 \end{pmatrix} . \tag{7.33}$$

This allows to introduce the following relations:

$$\begin{cases} \sigma_x \left|+\right\rangle = \left|-\right\rangle, \ \sigma_x \left|-\right\rangle = \left|+\right\rangle \\ \sigma_y \left|+\right\rangle = i \left|-\right\rangle, \ \sigma_y \left|-\right\rangle = -i \left|+\right\rangle \\ \sigma_z \left|+\right\rangle = \left|+\right\rangle, \ \sigma_z \left|-\right\rangle = - \left|-\right\rangle \end{cases} \tag{7.34}$$

It allows to calculate the scattering length densities for the four possible scattering processes:

$$\begin{cases} \langle+|\,b\,|+\rangle = b_N - \frac{\gamma_n r_0}{2\mu_B} M_{\perp z}(\overrightarrow{Q}) \\ \langle-|\,b\,|-\rangle = b_N + \frac{\gamma_n r_0}{2\mu_B} M_{\perp z}(\overrightarrow{Q}) \\ \langle+|\,b\,|-\rangle = -\frac{\gamma_n r_0}{2\mu_B}\left(M_{\perp x}(\overrightarrow{Q}) - iM_{\perp y}(\overrightarrow{Q})\right) \\ \langle-|\,b\,|+\rangle = -\frac{\gamma_n r_0}{2\mu_B}\left(M_{\perp x}(\overrightarrow{Q}) + iM_{\perp y}(\overrightarrow{Q})\right) \end{cases} \tag{7.35}$$

Since the neutron polarization is parallel to the *z-axis* defined by the applied magnetic field, it is possible to obtain, from Equation 7.35, two rules for the magnetic scattering [Brü2002]:

1. The *spin-flip* processes are observed for the component $\overrightarrow{M_\perp}(\overrightarrow{Q})$ which is perpendicular to the neutron polarization.

2. The *non-spin-flip* processes are observed for the component $\overrightarrow{M_\perp}(\overrightarrow{Q})$ which is parallel to the neutron polarization.

This leads to the definition of the magnetic form factor for a magnetic atom which refers to the magnetic part of scattering [Gla2001]:

$$F_M(\overrightarrow{Q}) = \frac{1}{V}\frac{g_N r_0}{2} \int \overrightarrow{\sigma}.\overrightarrow{M_\perp}(\overrightarrow{r})\, e^{i\overrightarrow{Q}.\overrightarrow{r}}\;. \tag{7.36}$$

$F_M(\overrightarrow{Q})$ is thus proportional to the Fourier transform of $\overrightarrow{M_\perp}(\overrightarrow{r})$.

The magnetic scattering length density is defined as:

$$\eta_M = \frac{e^2\gamma}{2mc^2} \sum_i \frac{c_i}{V_i} M_i^\perp\;, \tag{7.37}$$

where c_i and V_i are respectively the atomic concentration and the atomic volume of the particle constituent. $M_i^\perp$ (expressed in Bohr magnetons) is the projection of the magnetic moment onto the plane perpendicular to the scattering wave vector. $e^2\gamma/(2m^2)$ is the magnetic scattering length of $1\,\mu_\mathrm{B}$ and is equal to:

$$\frac{e^2\gamma}{2mc^2} = 0.27 \times 10^{-12} cm\;. \tag{7.38}$$

The definition of the magnetic form factor, given by Equation 7.36, can therefore be extended to a magnetic particle by introducing the magnetic contrast density $\triangle\eta_M$:

$$F_M(\overrightarrow{Q}) = \iiint_V \triangle\eta_M e^{i\overrightarrow{Q}.\overrightarrow{r}} d^3\overrightarrow{r}\;, \tag{7.39}$$

with

$$\triangle\eta_M = \eta_M(particles) - \eta_M(medium)\;. \tag{7.40}$$

Since the magnetic moments of the neutrons are sensitive to the magnetic moments of the particle, the scattering function consequently depends on the polarization of the neutrons. The spectrometer PAPYRUS on which the Polarized SANS experiments have been performed allows to polarize the spins of the incident neutrons but does not permit any analysis of the spins of the scattered neutrons. It is consequently possible to separate the scattered intensity of incident neutrons polarized $|+\rangle$ noted I^+ from the one of neutrons polarized $|-\rangle$ noted I^- [Gla2001, Rav2006]:

$$I^+(\overrightarrow{Q}) = \frac{d\sigma^{++}}{d\Omega} + \frac{d\sigma^{+-}}{d\Omega} = S(\overrightarrow{Q})\left[|F_N|^2 + (|F_M|^2 - 2PF_N F_M)sin^2\alpha\right]\;, \tag{7.41}$$

$$I^-(\overrightarrow{Q}) = \frac{d\sigma^{-+}}{d\Omega} + \frac{d\sigma^{--}}{d\Omega} = S(\overrightarrow{Q})\left[|F_N|^2 + (|F_M|^2 + 2P\varepsilon F_N F_M)sin^2\alpha\right]\;. \tag{7.42}$$

where ε is the spin-flipper efficiency and α the angle $\left(\overrightarrow{Q},\overrightarrow{M}\right)$. P is the polarization rate and is defined by:

$$P = \frac{n^+ - n^-}{n^+ + n^-}\;, \tag{7.43}$$

with n^+ and n^- are the neutrons respectively polarized $|+\rangle$ and $|-\rangle$. P is generally worth of the order of 0.95 during Polarized SANS experiments.

Making the sum and the difference of $I^+(\overrightarrow{Q})$ and $I^-(\overrightarrow{Q})$ gets an easier access to the contribution of the magnetic form factor F_M to the scattering:

$$I(\overrightarrow{Q}) = I^+(\overrightarrow{Q}) + I^-(\overrightarrow{Q}) \simeq S(\overrightarrow{Q}) \times \left(2\left|F_N(\overrightarrow{Q})\right|^2 + 2sin^2\alpha \left|F_M(\overrightarrow{Q})\right|^2 \right) \; for \; \varepsilon \simeq 1 \, , \quad (7.44)$$

$$\triangle I(\overrightarrow{Q}) = I^+(\overrightarrow{Q}) - I^-(\overrightarrow{Q}) = S(\overrightarrow{Q}) \times \left(-4PF_N(\overrightarrow{Q})F_M(\overrightarrow{Q})sin^2\alpha \right) . \quad (7.45)$$

The magnetic contrast $\triangle I(\overrightarrow{Q})$ is proportional to the magnetic form factor $F_M(\overrightarrow{Q})$. A Polarized SANS experiment therefore aims at studying the magnetic contrast $\triangle I(\overrightarrow{Q})$ in order to access at $F_M(\overrightarrow{Q})$. Finally, it is possible to extract $S(\overrightarrow{Q})$, $F_N(\overrightarrow{Q})$ and $F_M(\overrightarrow{Q})$ via a Polarized SANS experiment which justifies the use of polarized SANS to extract quantitative information about the magnetic properties of the sample.

7.2 SANS applied to magnetic nanowires

Section 7.1 showed that the SANS intensity depends on five quantities:

1. The nuclear contrast $\triangle\rho$ which comes from the chemical composition of the sample. As explained in Annexe 11, one great advantage of neutrons is to provide atomic scattering lengths b which strongly vary from one element to another. It means that the choice of solvents and particles is crucial to obtain large nuclear contrast.

2. The form factor $F(\overrightarrow{Q})$ which is governed by the shape of the particles. To simplify the problem, it is thus recommended to work on monodisperse particles so that it is not necessary to take the size distribution into account. It also implies that for a general shape of particles, the relative orientations of the particles have to be considered. This is the reason why most SANS studies are performed on isotropic particles such as nanospheres.

3. The magnetic form factor $F_M(\overrightarrow{Q})$ which is linked to $\overrightarrow{M_\perp}(\overrightarrow{Q})$ and therefore provides information on the magnetization of the sample.

4. The structure factor $S(\overrightarrow{Q})$ which underlines the spatial correlations between the particles.

5. In the case of particles which are, for instance, antiferromagnetically coupled, there can be a magnetic structure factor.

This section aims at applying the mathematical formalism developed in Section 7.1 to magnetic nanowires. The nanowire geometry only plays a role in the expression of the geometrical and magnetic form factors. Simulations performed via the *SpectraProcessor* software [Spe] first illustrate the role of the cylindric geometry in the form factors.

7.2.1   The geometrical form factor $F(\overrightarrow{Q})$

The geometrical form factor has been defined in Equation 7.16. To express the geometrical form factor $F(\overrightarrow{Q})$ of nanowires, these particles are modelled as cylinders with a radius R and a length L. Their relative orientation with respect to the incident wave vector $\overrightarrow{k_i}$ plays a key role in the determination of $F(\overrightarrow{Q})$ (see Figure 7.2). In SANS, when the detector is flat, it is possible to consider $\overrightarrow{Q}$ contained in the detector plane. It leads to the following approximation:

$$\overrightarrow{Q} \perp \overrightarrow{k_i} \; . \tag{7.46}$$

The geometrical form factor of a cylinder is thus expressed as :

$$F_{cyl}(\overrightarrow{Q}) = \frac{2J_1(Q_\perp R)}{Q_\perp R}.\frac{sin(\frac{1}{2}Q_{\shortparallel}L)}{\frac{1}{2}Q_{\shortparallel}L} \; , \tag{7.47}$$

where $J_1(x)$ is the first-order Bessel function of the first kind. $Q_{\shortparallel}$ and $Q_\perp$ are respectively the projections of the scattering wave-vector $\overrightarrow{Q}$ along the cylinder long axis and in a plane perpendicular to the cylinder long axis. These quantities are defined in Figure 7.2:

$$\begin{cases} Q_{\shortparallel} = Q\,sin\beta \\ Q_\perp = Q\,cos\beta \end{cases} , \tag{7.48}$$

where β is the angle between the normal to the incoming wave-vector $\overrightarrow{k_i}$ and the cylinder long axis. Equation 7.47 shows that the influences of the radius R and the length L of nanowires are well separated in the expression of the form factor $F(\overrightarrow{Q})$.
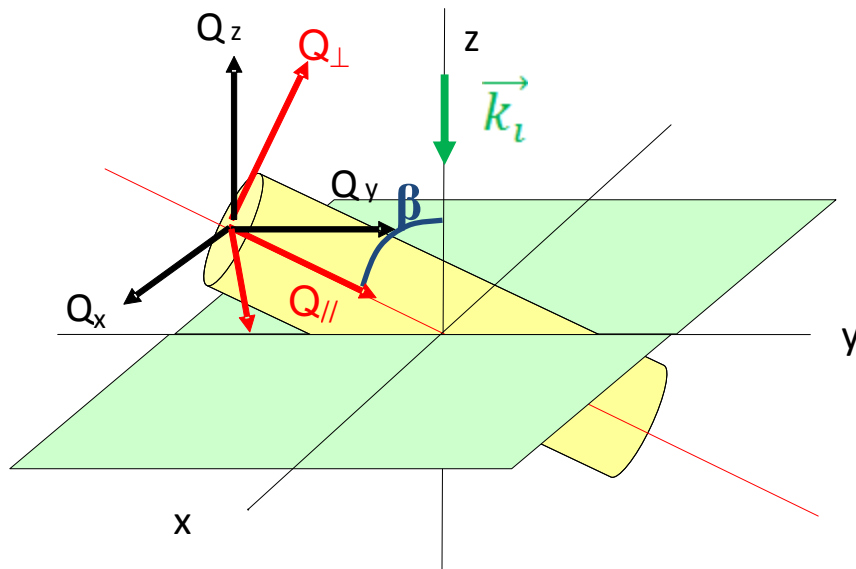
Figure 7.2: Representation of $\overrightarrow{Q_{\shortparallel}}$ and $\overrightarrow{Q_\perp}$ in the detector axis $(\overrightarrow{x}, \overrightarrow{y}, \overrightarrow{z})$. The normal to the incoming wave-vector $\overrightarrow{k_i}$ makes an angle β with the cylinder long axis.

It implies that when the cylinder is aligned along the incoming wave-vector $\overrightarrow{k_i}$ ($\beta = 0$), the geometrical form factor becomes an Airy function depending only on the radius of

the nanowire:

$$F_{cyl}(\overrightarrow{Q}) = \frac{2J_1(QR)}{QR} \tag{7.49}$$

Figure 7.3(a) presents the contribution $\left|F(\overrightarrow{Q})\right|^2$ of this form factor to the SANS intensity when the nanowire is along the incident beam. Note that the form factor of a cylinder aligned along the incident beam is similar to the one of a flat disk. It means that in this configuration, the length of the nanowires plays no role in the scattering.

When the cylinder is perpendicular to the incoming wave-vector $\overrightarrow{k_i}$ ($\beta = \frac{\pi}{2}$), the geometrical form factor is this time simplified as a function depending only on the length of the nanowire:

$$F_{cyl}(\overrightarrow{Q}) = \frac{sin(\frac{1}{2}QL)}{\frac{1}{2}QL} \tag{7.50}$$

Figure 7.3(b) presents the contribution $\left|F(\overrightarrow{Q})\right|^2$ of this form factor to the SANS intensity when the nanowire is perpendicular to the incident beam. Besides, Figure 7.3(c) presents the contribution $\left|F(\overrightarrow{Q})\right|^2$ of the form factor to the SANS intensity when $\beta = \pi/4$. In this configuration, the radius and the length of the nanowire both contribute to the scattering.
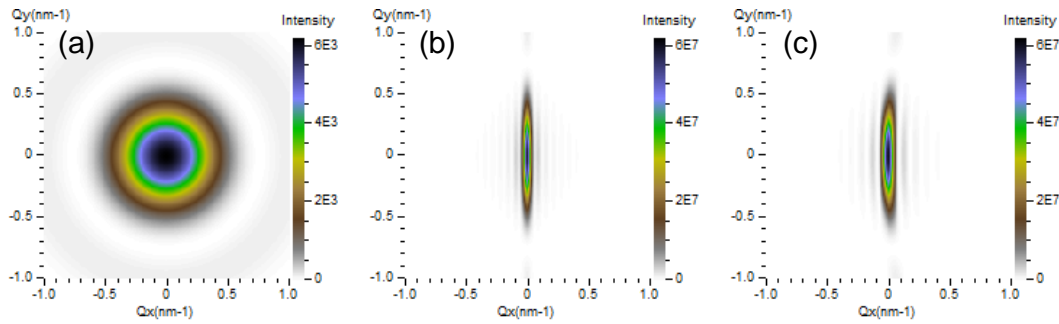
Figure 7.3: Simulations of $\left|F(\overrightarrow{Q})\right|^2$ performed via the spectraprocessor software for a nanowire with a diameter of $10\,nm$ and a length of $100\,nm$ depending on its orientation to the incident beam: (a) $\beta = 0$ (aligned to $\overrightarrow{k_i}$), (b) $\beta = \pi/2$ (perpendicular to $\overrightarrow{k_i}$), (c) $\beta = \pi/4$.

The SANS intensity is thus strongly affected by the relative orientations of nanowires. Equation 7.47 suits to cylinders perfectly aligned. However, during a SANS experiment, nanowires may exhibit different orientations so that when the cylinders are disordered, one has to take the distribution of orientations into account. For instance when the cylinders are randomly oriented, the value of the geometrical form factor comes from an integration over the Euler angles (β, φ) related to spherical coordinates :

$$F_{cyl}(\overrightarrow{Q}) = \int_0^{2\pi} \int_0^{\pi} \left[\frac{2J_1(Q_\perp R)}{Q_\perp R} \cdot \frac{sin(\frac{1}{2}Q_\parallel L)}{\frac{1}{2}Q_\parallel L} \right]^2 sin\beta d\beta d\varphi \ . \tag{7.51}$$

7.2.2 The magnetic form factor $F_M(\overrightarrow{Q})$

The expression of the magnetic contrast, presented in Equation 7.45, reveals as crucial the role of α, the angle between the magnetization and the scattering vector $\overrightarrow{Q}$, in the

magnetic contribution to the scattering. The PAPYRUS spectrometer allows to apply a magnetic field along or perpendicular to the incident wave vector $\overrightarrow{k_i}$. When the magnetization of nanowires is along the incident beam, $\alpha = \pi/2$. When it is perpendicular to the incident beam, α is defined in the detector plane and can vary from 0 to 2π.
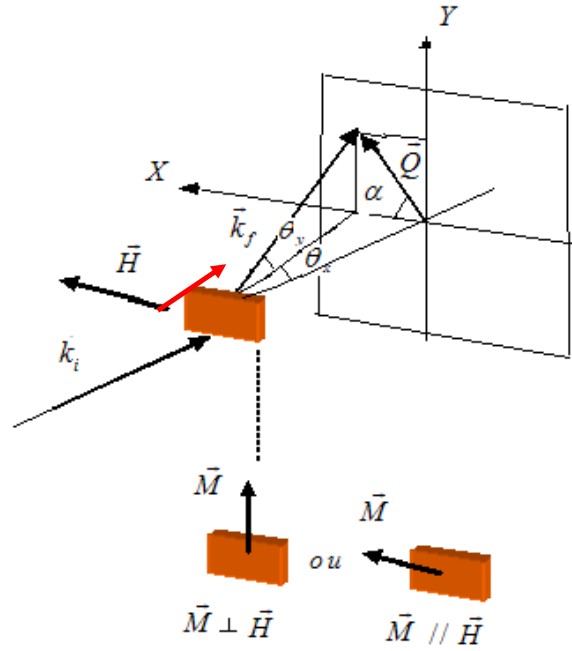
Figure 7.4: Configuration of the applied magnetic field $\overrightarrow{H}$ on the PAPYRUS spectrometer. $\overrightarrow{H}$ can be along (red) or perpendicular (dark) to the incident beam. When the magnetization $\overrightarrow{M}$ is along the incident beam, $\alpha = \pi/2$. When $\overrightarrow{M}$ is perpendicular to the incident beam, α is defined in the detector plane.

These considerations on the direction of the magnetization allows to rewrite the magnetic contrast given by Equation 7.45 for two limit cases (without taking into account the structure factor $S(Q)$):

$$\begin{cases} \triangle I(\overrightarrow{Q}) = -4PF_N(\overrightarrow{Q})F_M(\overrightarrow{Q}) & for\ \overrightarrow{M}\ \|\ \overrightarrow{k_i} \\ \triangle I(\overrightarrow{Q}) = -4PF_N(\overrightarrow{Q})F_M(\overrightarrow{Q})sin^2\alpha & for\ \overrightarrow{M}\ \perp\ \overrightarrow{k_i} \end{cases} \tag{7.52}$$

It indicates that the scattering depends on the angle α only when $\overrightarrow{H}$ is applied perpendicular to the incident wave vector. To illustrate the α-dependence of the magnetic contrast, I performed some simulations via the SpectraProcessor software [Spe] on a nanowire with a diameter of 10 nm for a length of 100 nm and exhibiting a magnetization similar to the one of cobalt ($M = 1400\,kA/m$) (see Figure 7.5). The influence of $sin^2\alpha$ is characterized by the shape of an "butterfly" (see Figure 7.5(b)).
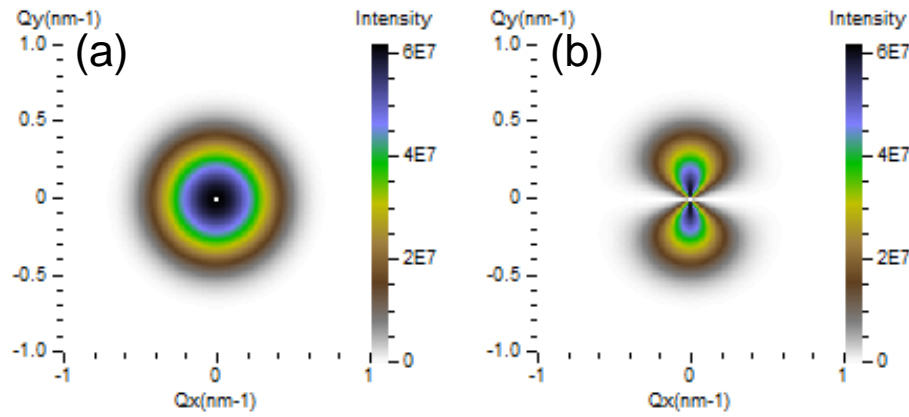
Figure 7.5: Simulations of the magnetic contrast $\triangle I(\overrightarrow{Q})$ performed via the spectraprocessor software for a nanowire with a diameter of $10\,\text{nm}$ and a length of $100\,\text{nm}$ depending on the orientation of its magnetization $\overrightarrow{M}$ to the incident beam: (a) $\alpha = 0$ (aligned to $\overrightarrow{k_i}$), (b) $\alpha = \pi/2$ (perpendicular to $\overrightarrow{k_i}$) .

7.3   Conclusion and perspectives of investigations

Sections 7.2.1 and 7.2.2 focussed on the crucial role of the relative orientation of the investigated nanowires. If the nanowires are not perfectly aligned, one has to take into account their orientation distribution. Nevertheless, the spatial correlations also play a key role in their scattering. The spatial correlations are described by the structure factor $S(\overrightarrow{Q})$ introduced in Equation 7.20. The structure factor may be hard to determine depending on the dispersion of the particles in the medium. That is why I investigated two different systems:

1. I first studied the nanowires synthesized via the polyol process and dispersed in a dilute so that the structure factor can be approximated to $S(\overrightarrow{Q}) = 1$.

2. I then investigated some Co and Ni nanowires which are perfectly aligned in a porous alumina membrane. They present an hexagonal order which is almost perfect so that the structure factor $S(\overrightarrow{Q})$ can be calculated.

Chapter 8

SANS measurements on aligned nanowires in a solvent

In Chapter 7, we have shown that for anisotropic particles the scattering intensity $I(Q)$ depends on the orientation relative to $\vec{k_i}$. Therefore, the treatment of the data tends to be complex in the case of randomly oriented nanowires. That is why the nanowires presented in Part I have been dispersed in a liquid solution and aligned by applying a magnetic field. The fact that the nanowires are dispersed in a solvent allows to neglect the interparticles interactions so that $S(Q) = 1$.

However, many difficulties arose during the investigation of this system so that it appeared hard to deduce quantitative information. In this chapter, the preparation of the samples and the difficulties to study them are first detailed. Then qualitative results are exposed and discussed.

8.1 Preparation of the sample: nanowires dispersed and aligned in a solvent

The nanowires synthesized via the polyol process exhibit very interesting magnetic properties. In particular, their aspect ratios and their high crystalline quality confer to them, respectively, large shape and magnetocrystalline anisotropies. Furthermore, because of their small dimensions, their magnetization reversal process is relatively well modelled within the Stoner-Wohlfarth model.

Unfortunately, Chapter 3 showed that it is difficult to fabricate solid samples with well aligned nanowires. The best results were obtained with nanowires oriented in a toluene solvent where they are freer to rotate. There are however four main difficulties to carry through such a study:

1. When $0.9\,\mathrm{g}$ of nanowires is dispersed in $1\,\mathrm{mL}$ of solvent to obtain a volumic fraction of 10%, some solubility problems may arise. For lower volumic fractions, the scattered signal is essentially coming from the solvent.

2. The chemical synthesis of the nanowires implies the presence of H atoms at their surface, giving rise to a large incoherent scattering (see Section 7.1.3).

3. Working in a solvent can make harder the use of a magnetic field. If the magnetic field is not perfectly homogeneous, one can expect the particles to move from the center to the edges of the sample cell.

4. In a SANS experiment, it takes longer to apply a magnetic field and to cool the sample down than in a magnetometer like a SQUID. Unfortunately, the nanowires tend to aggregate in toluene and fall down within a few minutes. A good dispersion of the particles is only provided by $Co_{80}Ni_{20}$ nanowires dispersed in a solution of DMAC. In this case, the particles can remain dispersed in the solution during many weeks. The origin of their good solubility in the solution of DMAC is attributed to the presence of acetate groups at their surface.

From these remarks, I chose to investigate $0.9\,g$ of $Co_{80}Ni_{20}$ nanowires dispersed in $1.3\,mL$ of DMAC contained in a Helma cell $1\,mm$ thick. The corresponding volumic fraction amounts to 8.5%. The nanowires dispersed in a solution of DMAC were put under a magnetic field so that they could be aligned. The magnetic field was applied perpendicular to the incident beam with an electromagnet allowing fields up to $0.9\,T$. The nanowires are thus expected to be perpendicular to the incident wave vector $\overrightarrow{k_i}$ (see Figure 8.1).
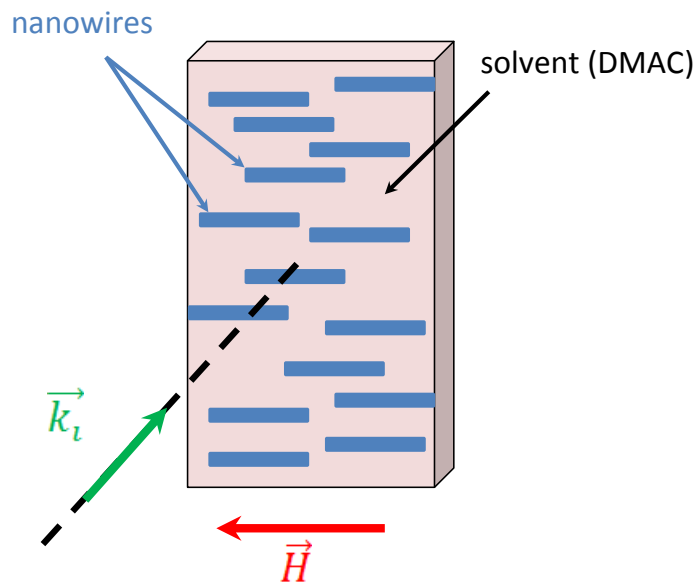
Figure 8.1: Representation of the investigated sample. The nanowires are expected to align along the magnetic field axis and therefore to be perpendicular to the incident beam.

8.2   Non-Polarized SANS measurements

Before focussing on Polarized SANS measurements to obtain information about the magnetism of these nanowires, it is first necessary to consider the non-polarized SANS intensity which can provide information about the dispersion of the particles in the solvent. The measurements have been performed on the PAPYRUS spectrometer for two Q-ranges: at large Q with $0.08\,nm^{-1} < Q < 2.4\,nm^{-1}$ and at small Q with $0.02\,nm^{-1} < Q < 0.62\,nm^{-1}$. The incoherent contribution of the solvent was substracted.

8.2.1 Measurements at large Q

SANS measurements have been performed on the sample at zero field and then with increasing value of H. Figure 8.2(a) shows the scattering spectra before the application of a magnetic field on the sample. A small anisotropy of the 2D spectra can be observed. It reflects a preferential orientation of the nanowires in the toluene, a hint that they tend to self-organize without any external magnetic field. It is then compared to the scattering spectra obtained for a magnetic field of $0.9\,\mathrm{T}$ (see Figure 8.2(b)). The comparison between the two data sets shows that the scattering is stronger at large Q ($1\,\mathrm{nm}^{-1} < Q < 2.4\,\mathrm{nm}^{-1}$) for $H = 0\,\mathrm{T}$ than for $H = 0.9\,\mathrm{T}$ (see Figure 8.2). It reflects the aggregation of the wires. Indeed, bigger aggregates lead to larger scattering at smaller Q values.
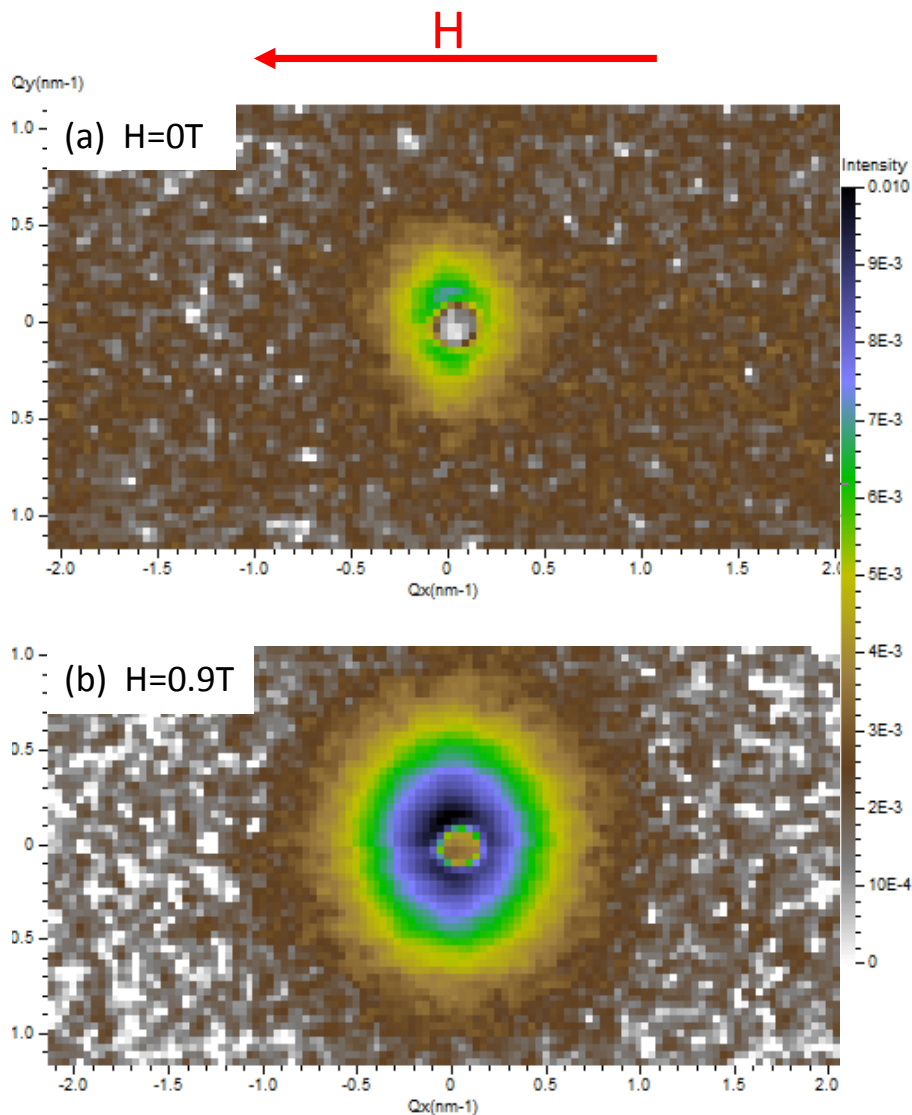
Figure 8.2: Scattering spectra of $I(Q)$ at large Q: (a) before the application of a magnetic field, (b) for a magnetic field $H = 0.9\,\mathrm{T}$.

In order to understand the origin of the difference of scattering at large Q, the SANS intensity integration is presented for some values of the applied magnetic field in Figure

8.3. It indicates that the SANS intensity at large Q varies as a function of the magnetic field. The SANS profiles evolves under the applied field until reaching a stable Q value for $H > 0.72\,\mathrm{T}$. For $H > 0.72\,\mathrm{T}$, the SANS intensity profiles do not evolve any more. Note that when the magnetic field is switched off, the SANS profile remains similar to the one under large magnetic fields.

This suggests the following interpretation. Under a magnetic field, the nanowires move because there is a small field gradient which is applied. They tend to aggregate and form larger structures which exhibit larger scattering at small Q. Then for $H > 0.72\,\mathrm{T}$, the aggregates exhibit a characteristic size which is no more affected by switching off the magnetic field. Once the sample has reached a stable state, it is then possible to study it at smaller Q.
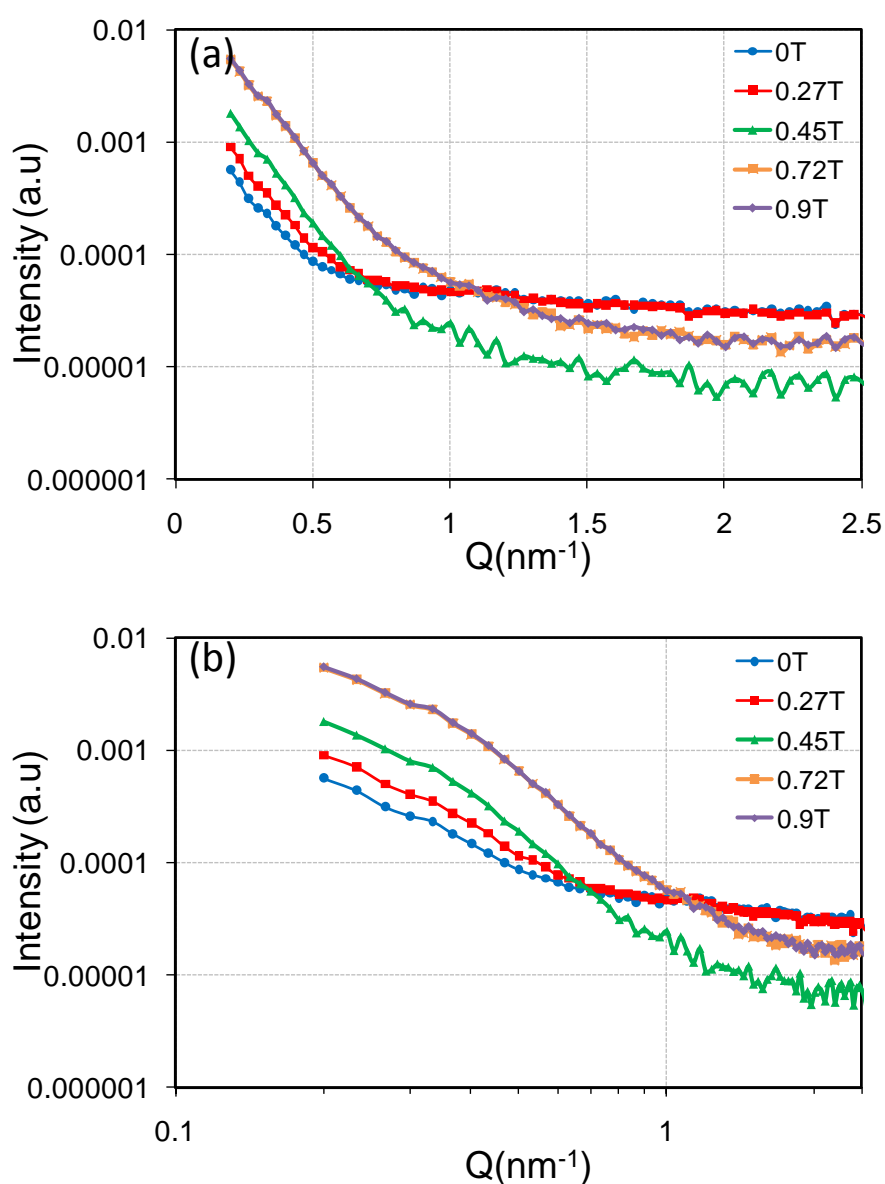
Figure 8.3: Scattering profile of $I(Q)$ at large Q of the sample for different values of the magnetic field: (a) in log-linear scale and (b) in log-log scale.

8.2.2 Measurements at small Q

The scattering intensity has been studied for magnetic fields from $H = 0\,\mathrm{T}$ up to $H = 0.9\,\mathrm{T}$. Figure 8.4 shows the scattering spectra for different magnetic field values. Note that the magnetic field has been applied in a direction perpendicular to the one of Figure 8.2. If the scattering spectra is slightly anisotropic for $H = 0\,\mathrm{T}$ (see Figure 8.4(a)), the anisotropy of the spectra strongly varies with increasing magnetic fields. This indicates that the nanowires align along the magnetic field direction. It is thus necessary to apply a large magnetic field to well align the nanowires.
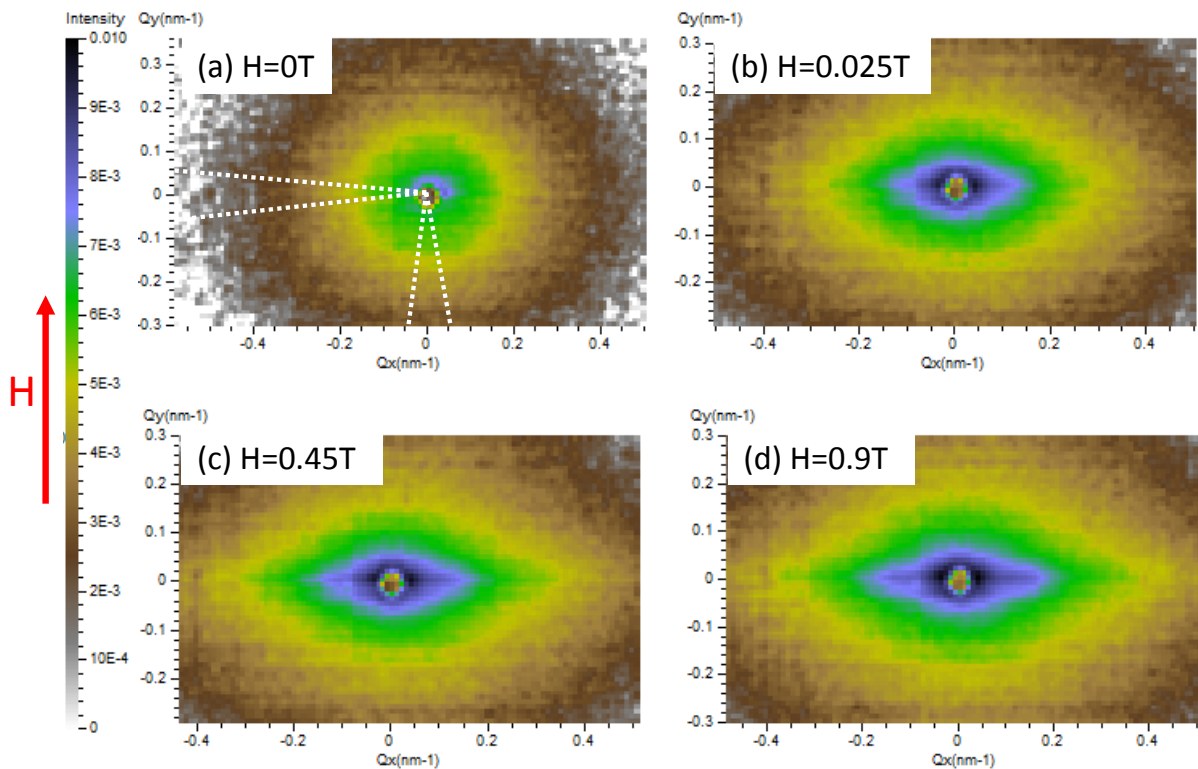
Figure 8.4: Scattering spectra of $I(Q)$ at small Q of the sample: (a) for a magnetic field $H = 0\,\mathrm{T}$, (b) for $H = 0.025\,\mathrm{T}$, (c) for $H = 0.45\,\mathrm{T}$, (d) for $H = 0.9\,\mathrm{T}$. Because of the strong anisotropy of these spectra, the circular integration are made on horizontal (HS) and vertical (VS) sectors with an opening of 10° (indicated with dashed lines in (a)).

We can try to extract information about the dispersion of the particles in the solvent and, in particular, the characteristic size of the aggregates of nanowires in the solvent. In order to obtain this information, the SANS intensity profile as a function of Q has been calculated from the 2D spectra. Since the scattering 2D spectra are anisotropic, I made a circular integration on horizontal (HS) and vertical (VS) sectors with an opening of 10° (see Figure 8.4). Figure 8.5 shows the profile of the SANS intensity for $H = 0\,\mathrm{T}$ and $H = 0.9\,\mathrm{T}$ in linear-logarithmic and in logarithmic-logarithmic scales. The sectors HS and VS allow to evidence the influence of the magnetic field since the direction of HS and VS are respectively perpendicular and parallel to H. These profiles confirm the anisotropy of the scattering intesity when a magnetic field is applied.

Moreover, for particles or aggregates exhibiting a characteristic size ξ, a plateau is expected at small Q [Gri2008, Bro1999] for:

$$Q^* = \frac{2\pi}{\xi} . \tag{8.1}$$

In Figure 8.5, no plateau is observed which underlines that the nanowires form some aggregates with a characteristic size ξ assessed to be at least:

$$\xi \simeq \frac{2\pi}{Q_{min}} \approx 180\,\text{nm} . \tag{8.2}$$

It implies that when these nanowires are dispersed in a slovent, they tend to form large aggregates whose characteristic sizes are at least 180 nm. Besides, the SANS profiles, presented in Figure 8.5, exhibit two different slopes (blue line at small Q and dark line at large Q) corresponding to two different exponents of the following Q-dependence:

$$I(Q) = Q^{-\alpha} . \tag{8.3}$$
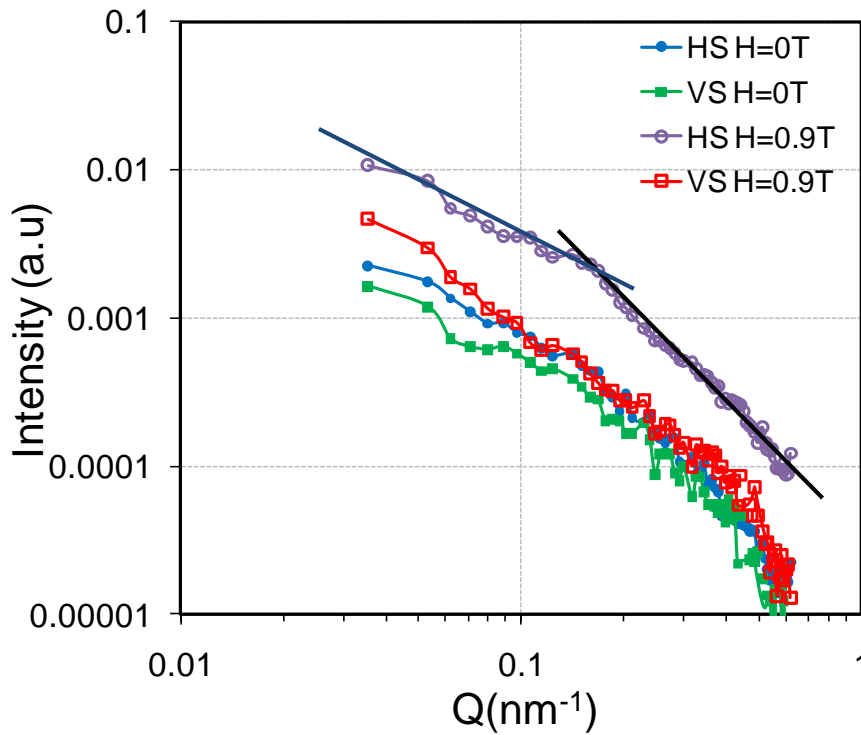
Figure 8.5: Scattering profile of $I(Q)$ at small Q obtained from horizontal (HS) and vertical (VS) sectors with an opening of 10° for $H = 0\,\text{T}$ and $H = 0.9\,\text{T}$.

From Figure 8.5, the value of α is deduced for small Q (α_{SQ}) and for large Q (α_{LQ}):

$$\begin{cases} \alpha_{SQ} \approx 1.1 \\ \alpha_{LQ} \approx 2.3 \end{cases} . \tag{8.4}$$

The value of α_{SQ} is related to the aggregate shape [Gri2008]. As a matter of fact, a Q^{-1} dependence is characteristic of $1D$ objects whereas a Q^{-2} dependence is characteristic of

2*D* objects or locally planar as for example membrane or flat colloidal particles [Gri2008]. Therefore, $\alpha_{SQ} \approx 1.1$ indicates that the nanowires form some large aggregates which exhibit a 1D shape. It allows to conclude that they form some "wires of nanowires". Note that at large Q, α is generally equal to 4 because of the Porod law corresponding to scattering at interfaces. Here, $\alpha_{LQ} \approx 2.3$ probably corresponds to an intermediate regime. To extensively characterize the size of the aggregates, it is necessary to probe smaller Q via a more adapted SANS spectrometer.
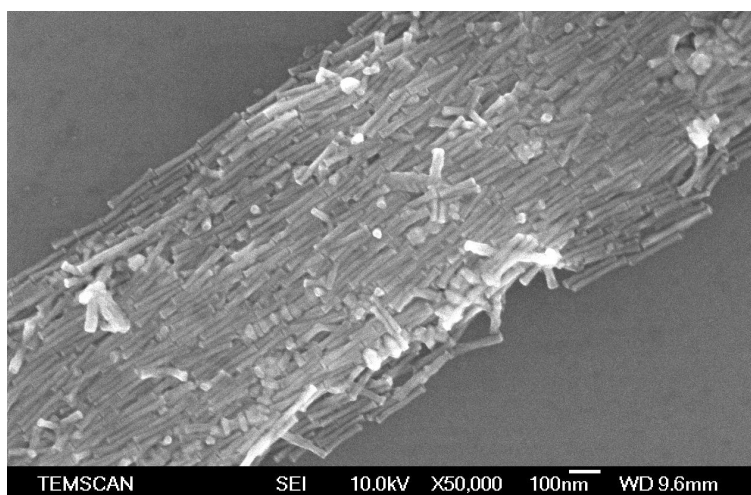
Figure 8.6: Aggregates of nanowires deposited onto a flat surface under a magnetic field.

8.3 Polarized SANS measurements

Polarized SANS measurements have been performed to put into evidence the magnetic form factor of the particles. However, it has been shown in Section 8.2.2 that the nanowires tend to form large aggregates when they are dispersed in the solvent. The information provided by Polarized SANS measurements do not therefore concern the nanowires but the aggregates. That is why these results are qualitatively discussed.

Figure 8.7 presents the scattering spectra for neutrons polarized $|+\rangle$ and $|-\rangle$ and for magnetic fields of $H = 0\,\mathrm{T}$ and $H = 0.9\,\mathrm{T}$. It is apparent that the scattering spectra at zero field for neutrons polarized $|+\rangle$ is similar to the one for neutrons polarized $|-\rangle$. At $H = 0.9\,\mathrm{T}$ is applied, the scattering spectra for neutrons polarized $|+\rangle$ becomes much more anisotropic than for neutrons polarized $|-\rangle$.
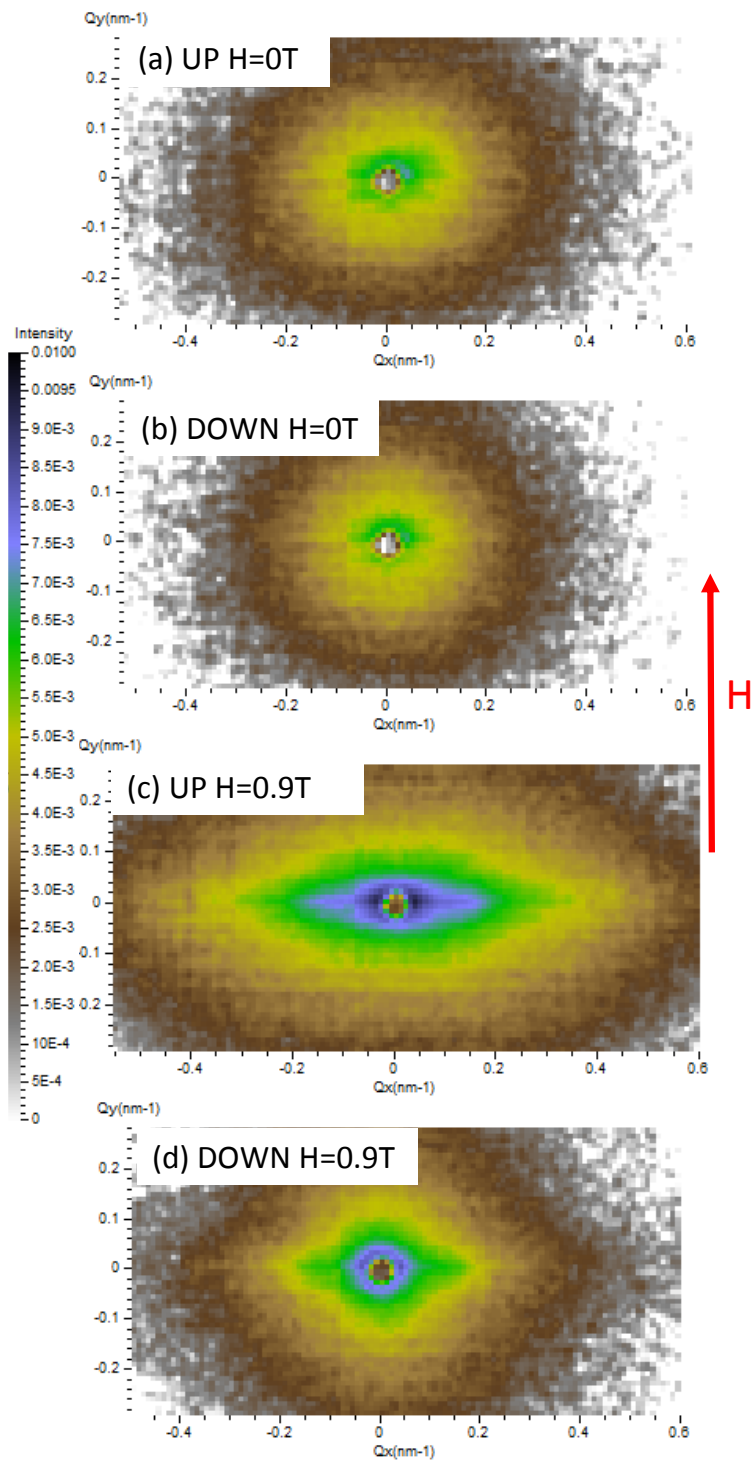
Figure 8.7: Scattering 2D spectra for : (a) neutrons polarized $|+\rangle$ (UP) for $H = 0\,\text{T}$ (b) neutrons polarized $|-\rangle$ (DOWN) for $H = 0\,\text{T}$ (c) neutrons polarized $|+\rangle$ (UP) for $H = 0.9\,\text{T}$ (d) neutrons polarized $|-\rangle$ (DOWN) for $H = 0.9\,\text{T}$.

It is possible to deduce the magnetic contrast $I^+(Q) - I^-(Q)$ for $H = 0\,\text{T}$ and $H = 0.9\,\text{T}$. This is shown in Figure 8.8. The magnetic contrast presents the shape of a "butterfly" which is the signature of $sin^2\alpha$ as previously discussed from Equation 7.52.

This corresponds to the configuration where the magnetic field is perpendicular to the incident beam.
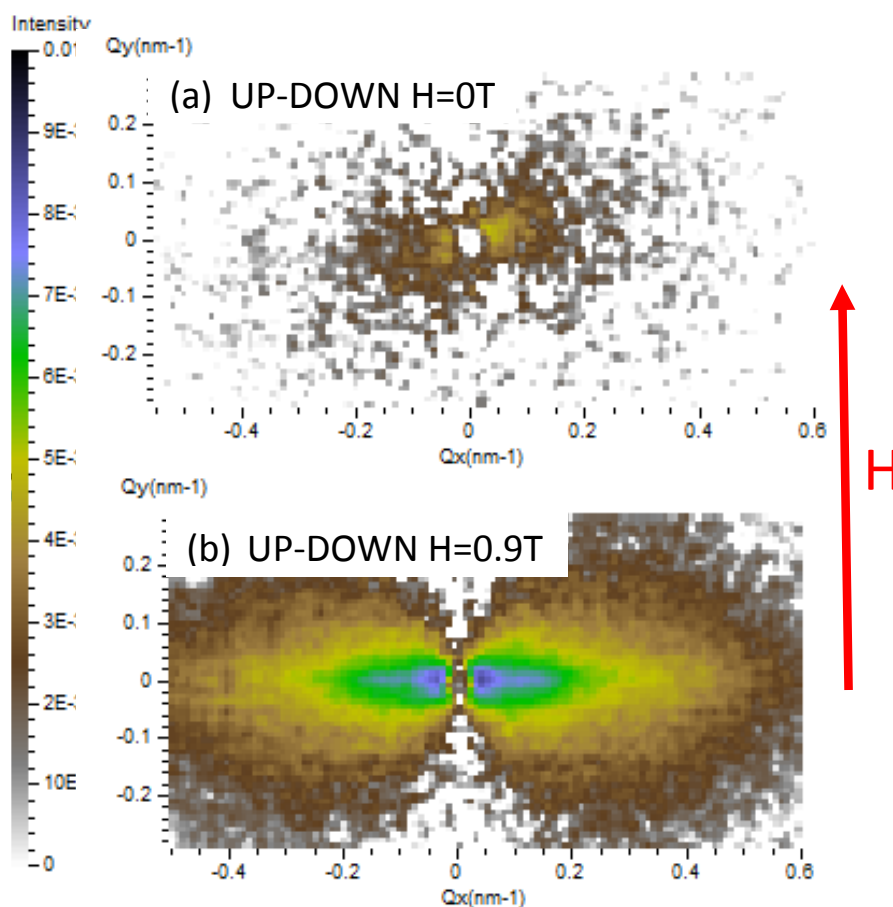
Figure 8.8: Magnetic contrast $I^+(Q) - I^-(Q)$ for: (a) $H = 0\,\mathrm{T}$ and (b) $H = 0.9\,\mathrm{T}$.

8.4 Conclusion

SANS is a valuable tool to study the formation of aggregates under magnetic fields which provides crucial information for the fabrication of composite materials with single nanowires (see Figure 8.6). Further investigations are scheduled to investigate the dispersion of nanowires in polymer solution and the formation of aggregates depending on the value of the applied magnetic field.

In order to probe magnetism of individual nanowires via Polarized SANS experiments, attention has been focused on nanowires included in porous membranes so that the objects are well separated from each other and the geometry of the sample can be controlled. These results are presented in Chapter 9.

Chapter 9

SANS measurements on nanowires ordered in porous membranes

The SANS studies on nanowires aligned in a solvent have proved to be difficult because of the non perfect alignment of the objects and their tendency to aggregate. Consequently, the magnetic information provided by Polarized SANS do not concern individual nanowires but large aggregates of nanowires. In order to overcome this difficulty, SANS measurements have been performed on nanowires included in porous membranes. The nanowires present then the advantage to be perfectly monodisperse, aligned and well separated from each other.

9.1 Presentation of the samples

In order to carry out SANS investigations on nanowires included in porous membranes, a collaboration has been started with Laurent Cagnon (Institut Néel, Grenoble) who provided us with Co and Ni nanowires almost perfectly ordered in porous alumina membranes. This section presents the investigated nanowires and their magnetic properties.

9.1.1 Synthesis of the samples

The process is divided in two steps: the porous alumina synthesis and then the nanowires electrodeposition [Mar1994, Mar1996]. The porous alumina layer is first formed using a double anodization process. The porous alumina synthesis first consists in the deposition of a bulk aluminum plate which is then electrochemically oxidized to form alumina (see Figure 9.1(I)). During the process, the alumina layer self-organizes into organized pores (see Figure 9.1(II-IV)) [Jes1998, Mas1995, Lag2008, Lag2007].

Depending on the acid used to dissolve the matrix and on the exposition time, the diameter of the pores ϕ_P and the distance between them d_P may be adjusted from a few tens of nanometers up to hundreds of nanometers (see Figure 9.2). The different steps involved in the synthesis of porous alumina membranes are extensively detailed in [Lag2008, Jes1998, Lag2007, Fur1989, Mar1996, Mar1994, Rab2003].

It is then possible to deposit materials into these holes to obtain arrays of nano-objects with sizes in the range $5 - 200\,\mathrm{nm}$ [Dah2006, Cag2007]. In the present case, the metallic nanowires have been deposited electrochemically under a constant electric potential $(1\,\mathrm{V})$

155

from the following solution: $0.64M\ H_3BO_3 + 0.38M\ NiSO_4.7H_2O + 0.23M\ NiCl_2$. The bath basicity and electrodeposition current have effects on the crystallographic orientation of electrodeposited *hcp* Co nanowires [Dar2004, Dar2005]. It is thus possible to syntesize *hcp* Co nanowires with the axis $\overrightarrow{c}$ either parallel or perpendicular to the long axis. Moreover, to perform the electrodeposition of the nanowires, it was necessary to start with the deposition of a layer of metal on a side of the membrane to make the electric contact. That is why a 250 nm thick *Au* layer has been sprayed in order to fully block up the pores and provide an electrode far the growth.
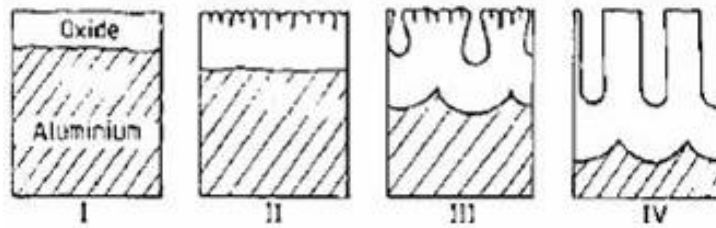
Figure 9.1: Porous alumina synthesis: (I) deposition of a Al_2O_3 layer on an Al film, (II) and (III) dissolution of the Al_2O_3 film and apparition of the first holes, (IV) competition between the Al_2O_3 dissolution and the oxidation of the Al film. Adapted from [Lag2008].
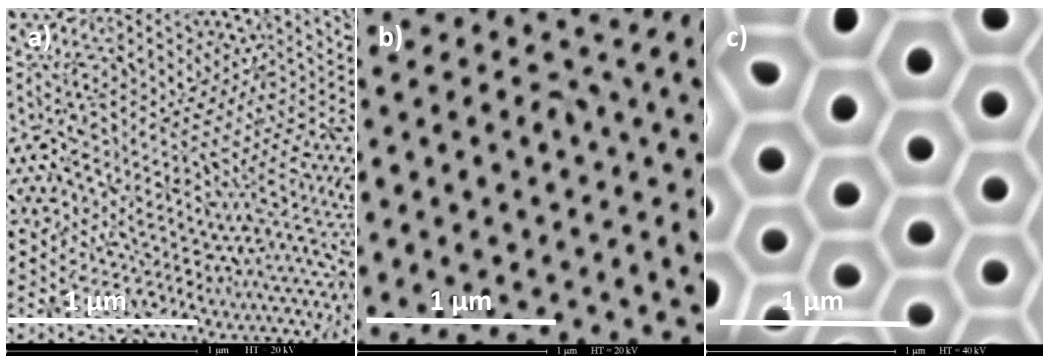
Figure 9.2: SEM images of porous alumina membranes: (a) porous alumina membrane made with H_2SO_4, $\phi_P = 35$ nm and $d_P = 60$ nm, (b) porous alumina membrane made with $(COOH)_2$, $\phi_P = 60$ nm and $d_P = 100$ nm,(c) porous alumina membrane made with H_3PO_4, $\phi_P = 200$ nm and $d_P = 450$ nm. Images from L. Cagnon (Institut Néel, Grenoble).

Four different empty porous alumina membranes with different geometries have been investigated (see Table 9.1 and Figure 9.3). This variety of samples allows to compare the scattering of porous alumina membranes exhibiting different structures or filled in with different materials. Note that the length of the pores is about $50\,\mu$m for all the samples.

Sample	ϕ_P(nm)	d_P(nm)
238	35	65
240	100	160
241	40	70
242	60	105

Table 9.1: Characteristic sizes of the investigated empty porous alumina membranes obtained from SEM images.
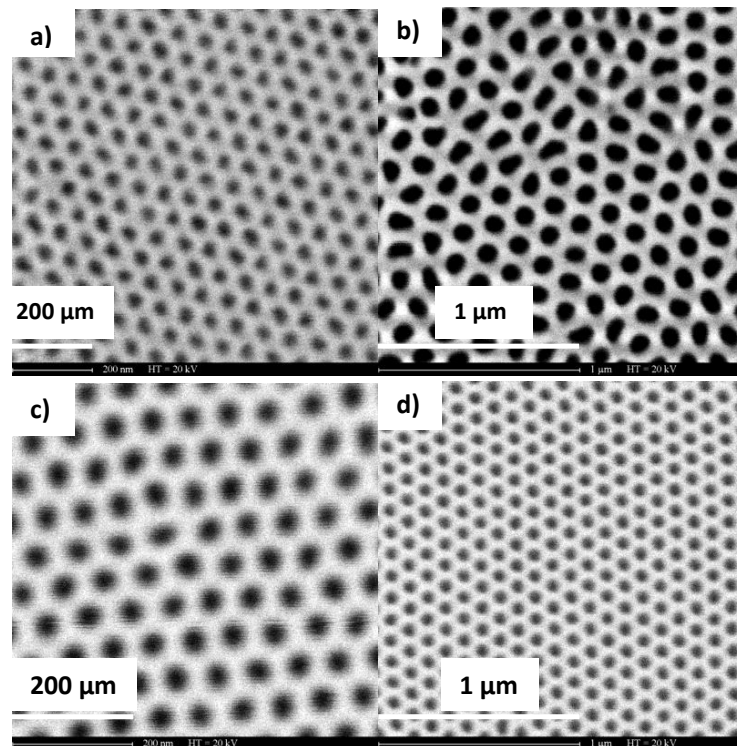
Figure 9.3: SEM images of the investigated porous aluminamembranes: a) n°238, b) n°240, c) n°241 and d) n°242

A fifth porous alumina membranes filled with Co and Ni metals has also been investigated. The membrane which is filled in with nanowires is the n°226 characterized by $\phi_P = 40\,\text{nm}$ and $d_P = 105\,\text{nm}$. The four kinds of nanowires included in the membrane n°226 are Ni nanowires, Co nanowires made with SCN (thiocyanates) and Co nanowires made at $pH = 3.4$ and at $pH = 5.75$. The length of the nanowires depends on the time of electrodeposition. In the present case, they all have a length of about $25\,\mu\text{m}$ which indicates that the pores are half filled. The $Co\ SCN$ nanowires are amorphous while the others are crystallized. The Co nanowires made at $pH = 3.4$ and $pH = 5.75$ are crystallized in the hexagonal compact phase with the axis $\vec{c}$ respectively perpendicular and parallel to the wire axis.

9.1.2   Magnetic characterization of the samples

The four membranes filled with Co and Ni have been magnetically characterized by VSM measurements. The hysteresis cycles for a magnetic field parallel or perpendicular to the wires axis are presented in Figures 9.4, 9.5, 9.6 and 9.7. The values of the coercivity and the remanence for each hysteresis cycle are listed in Table 9.2.

The magnetization of Ni nanowires exhibits an easy and a hard magnetic directions (see Figure 9.4). When the magnetic field is applied along the nanowires, the hysteresis cycle presents a square shape and a remanent magnetization of $0.94\,M_S$. The coercivity of the easy axis hysteresis cycle is $1110\,\text{Oe}$. As for the hard axis hysteresis cycle, it is almost closed: the remanence and the coercivity are about $0.02\,M_S$ and $78\,\text{Oe}$, respectively.
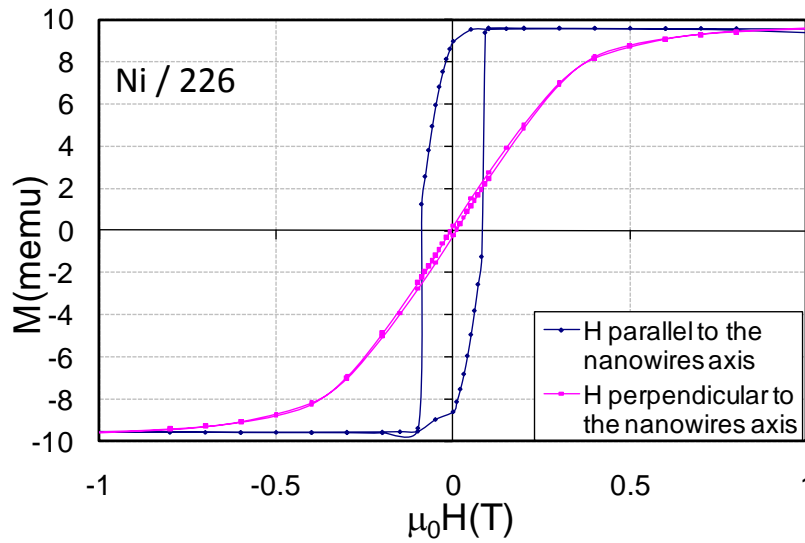
Figure 9.4: Hysteresis loop of Ni nanowires included in the n°226 porous alumina membrane
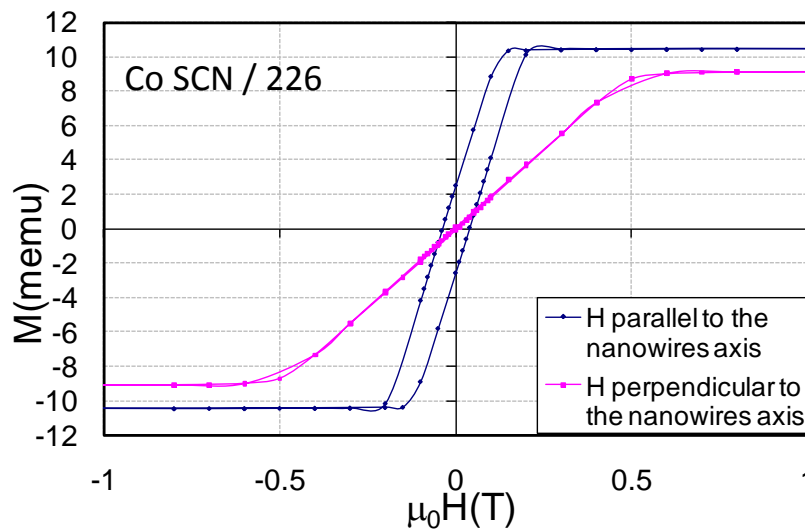
Figure 9.5: Hysteresis loop of amorphous $Co\,SCN$ nanowires included in the n°226 porous alumina membrane

The nanowires made of $Co\,SCN$ also exhibit an easy and a hard magnetic directions (see Figure 9.5). The hysteresis cycle when the magnetic field is applied perpendicular to the wires is almost closed ($H_C = 37\,\text{Oe}$ and $M_R = 0.008\,M_S$). The remanence parallel of the hysteresis cycle is only $0.25\,M_S$. These values can be explained by the amorphous structure of the nanowires. Indeed the only magnetic anisotropy in play is the shape one.
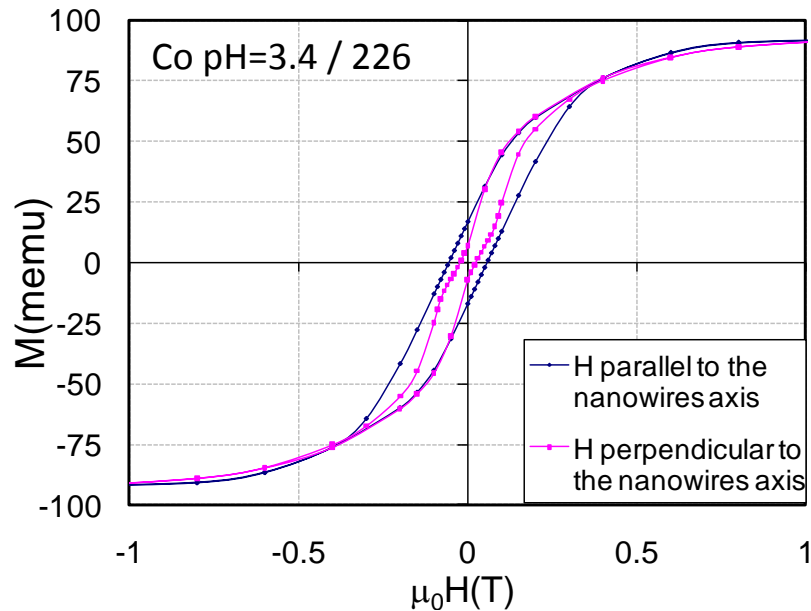
Figure 9.6: Hysteresis loop of Co nanowires synthesized at $pH = 3.4$ included in the n°226 porous alumina membrane
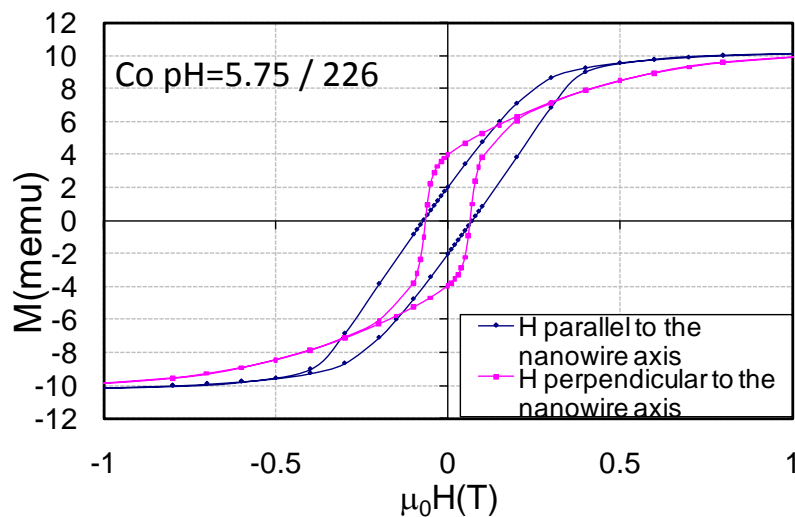
Figure 9.7: Hysteresis loop of Co nanowires synthesized at $pH = 5.75$ included in the n°226 porous alumina membrane

The hysteresis cycles of the Co nanowires made at $pH = 3.4$ are different (see Figure 9.6). The hysteresis cycle when $\overrightarrow{H}$ is applied along the wires exhibit a similar remanence

$(0.18\,M_S)$ than for the $Co\,SCN$ wires but with a larger coercivity $(710\,\text{Oe})$. The hysteresis cycle for $\overrightarrow{H}$ transverse to the wires is however not completely closed in contrast to Ni and $Co\,SCN$ wires. This indicates that the magnetocrystalline anisotropy has a transverse component to the wire axis and that there is competition between the magnetocrystalline and shape anisotropies.

The Co nanowires made at $pH = 5.75$ and $pH = 3.4$ do not present any clear easy or hard directions. When $\overrightarrow{H}$ is applied perpendicular to the wires, the Co nanowires made at $pH = 5.75$ even exhibit a remanence twice larger than when $\overrightarrow{H}$ is applied parallel to the wires (see Figure 9.7). This is surprising since they are expected to crystallize in the hcp phase with the axis $\overrightarrow{c}$ along the geometrical axis (L. Cagnon, Private Communication). As for the coercivity of this sample, it is similar in both directions $(710\,\text{Oe}$ and $647\,\text{Oe}$ for respectively $\overrightarrow{H}$ parallel and perpendicular to the wires).

	$\overrightarrow{H}$ // wires		$\overrightarrow{H}$ ⊥ wires	
Samples	$H_C(\text{Oe})$	M_R/M_S	$H_C(\text{Oe})$	M_R/M_S
Ni	1110	0.95	78	0.024
Co SCN	383	0.25	37	0.008
Co pH=5.75	710	0.2	647	0.4
Co pH=3.4	565	0.18	232	0.076

Table 9.2: Values of the coercivity and the remanence for magnetic field applied parallel of transverse to the nanowire long axis.

9.2   Structure and form factors

A great advantage of these nanowires is that they are embedded in a rigid matrix so that a magnetic field has no effect on their orientation. The samples are very thin since the pores are $50\,\mu$m long and covered with an Au layer of about $250\,\text{nm}$. They present a section of about $5\,\text{mm} \times 5\,\text{mm}$ depending on the sample. For the SANS scattering, we set the samples perpendicular to the incident neutron beam. The nanowires are thus parallel to the beam (see Figure 9.8). In this configuration, we expect to measure the structure and form factors of the wires.
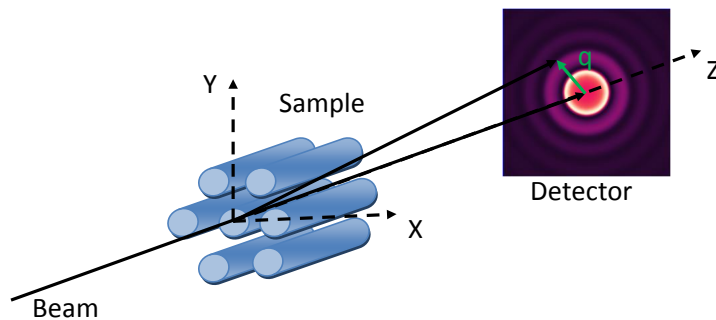
Figure 9.8: Configuration of the SANS experiment on porous alumina membranes

9.2.1 Determination of the structure factor $S(Q)$ from SEM images: Ewald sphere effects

As shown in Figure 9.3, the pores of the investigated porous alumina membranes are hexagonally ordered. The corresponding structure factor is first calculated for a perfect hexagonal assembly of pores. Then orientational disorder is taken into account by introducing the Percus-Yevick model. The structure factor $S(Q)$ provided by this model is compared to the one determined from an analysis of the SEM images.

9.2.1.1 Structure factor $S(Q)$ of a perfect hexagonal assembly of pores

Let's consider a perfect two-dimensional hexagonal assembly of pores. The unit cell of this assembly in the direct space is represented in Figure 9.9. The pores are separated by a distance a. The axes of this assembly are $\overrightarrow{OA}$ and $\overrightarrow{OB}$ so that:

$$OA = OB = a \,, \tag{9.1}$$

$$(\overrightarrow{OA}, \overrightarrow{OB}) = \frac{2\pi}{3} \,. \tag{9.2}$$

The axes of the reciprocal space are $\overrightarrow{OM}$ and $\overrightarrow{ON}$ and are determined by:

$$OM = ON = \frac{2}{\sqrt{3}} \times \frac{2\pi}{a} \,, \tag{9.3}$$

$$(\overrightarrow{OM}, \overrightarrow{ON}) = \frac{\pi}{3} \,. \tag{9.4}$$

We now consider a pore P defined by its coordinates (x, y) in the direct space and numbered via two integers (h, k):

$$\begin{cases} x = h \, \overrightarrow{OA} \\ y = k \, \overrightarrow{OB} \end{cases} . \tag{9.5}$$

The node $P^*(x^*, y^*)$ in the reciprocal space is numbered by:

$$\begin{cases} x^* = h' \, \overrightarrow{OM} \\ y^* = k' \, \overrightarrow{ON} \end{cases} . \tag{9.6}$$

The periodicity of the equidistant reciprocal rows $R_{h',k'}$ is expressed as:

$$R_{h',k'}^2 = |OP^*|^2 = (h'\overrightarrow{OM} + k'\overrightarrow{ON}).(h'\overrightarrow{OM} + k'\overrightarrow{ON}) = \frac{4 \times (2\pi)^2}{3a^2}(h'^2 + k'^2 + h'k') \,. \tag{9.7}$$
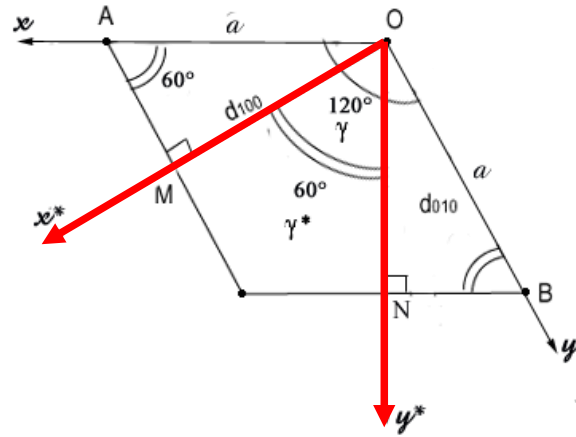
Figure 9.9: Representation of the unit cell for a 2D hexagonal assembly of the pores. (x, y) and (x^*, y^*) (in red) are the axis of the direct space and reciprocal space, respectively.

The structure factor $S(Q)$ of a perfect hexagonal assembly is expressed from Equation 7.20 as:

$$S(Q) = \frac{1}{N} \sum_{h,k} e^{i2\pi(hh' + kk')} .$$ (9.8)

$S(Q)$ is composed of hexagonally ordered Bragg spots. The diffraction pattern of a perfect hexagonal array is made of Bragg peaks localized on the (h', k') nodes of the reciprocal lattice (see Figure 9.9). Note that the reciprocal lattice of an hexagonal assembly of points is an hexagonal assembly of infinite lines. When the array surface is normal to the beam, the Ewald sphere intercepts all the hexagonally ordered lines of the reciprocal lattice so that the final scattered figure is an hexagonal array of points.
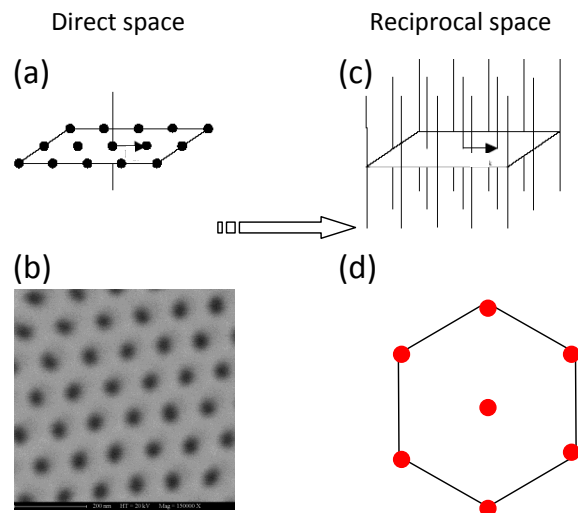
Figure 9.10: Representation of: (a), (b) the direct space of an hexagonal assembly of points and (c), (d) the corresponding reciprocal space.

To illustrate the calculation of the structure factor for an hexagonal assembly of pores,

SEM images of the empty porous alumina membranes synthesized by L. Cagnon have been numerically analyzed by Frédéric Ott. Figure 9.11(a) shows the SEM image of well hexagonally ordered pores. The first step to process the image consists in "binarizing" the image (see Figure 9.11(b)) so that the hole centers can be localized (see Figure 9.11(c)). From this image, a Fourier transform of the holes positions provide the structure factor (see Figure 9.11(d)).
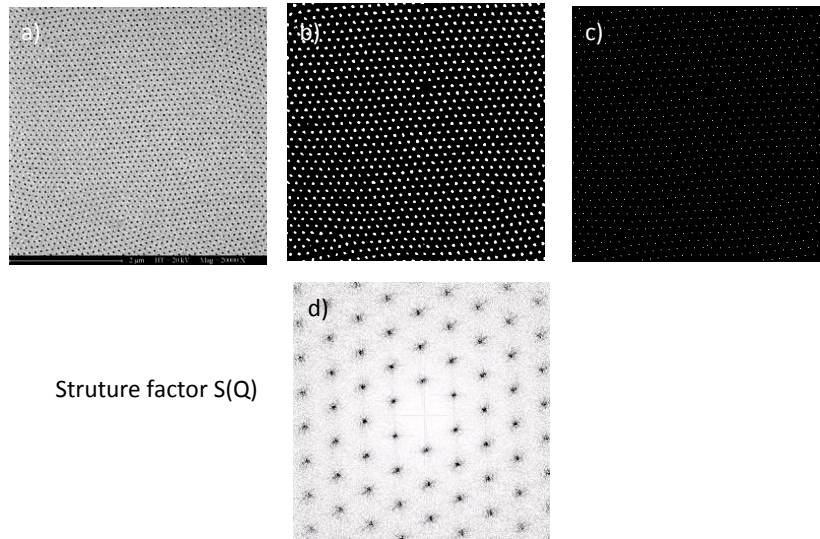
Struture factor S(Q)

Figure 9.11: Numerical treatment of the SEM image of a well hexagonally ordered alumina membrane (fabricated by L. Cagnon) to determine the structure factor : a) SEM image, b) Binarisation of the SEM image, c) Localization of the hole centers, d) Structure factor associated with the initial SEM image.

h'	k'	$\sqrt{h'^2 + k'^2 + h'k'}$	multiplicity
1	0	1	4
1	-1	1	2
1	1	$\sqrt{3}$	2
2	-1	$\sqrt{3}$	4
2	0	2	4
2	-2	2	2
2	1	$\sqrt{7}$	4
3	-1	$\sqrt{7}$	4
3	0	3	4
2	2	$\sqrt{12}$	2
3	1	$\sqrt{13}$	4

Table 9.3: Values of $\sqrt{h^2 + k^2 + hk}$ for different values of (h, k) with taking into account the multiplicity of the solutions. The ratio of these values gives the ratio of the distance from the center of the reciprocal lattice to the different nodes listed.

In order to complete the characterization of the structure factor for an hexagonal array

of pores, we need to calculate the distance from the center of the reciprocal lattice of the reciprocal nodes. This distance $R_{h',k'}$ only depends on (h', k') and is given by Equation 9.7. The distances $R_{h',k'}$ are proportional to $\sqrt{h'^2 + k'^2 + h'k'}$ and are listed in Table 9.3 for the smallest values of (h', k').

9.2.1.2   Influence of orientational disorder on the structure factor $S(Q)$ for an hexagonal array of pores: the Percus-Yevick model

In the previous section, the structure factor for an hexagonal array of pores was determined. However, the arrangement of the pores is not perfect over the whole sample surface. The Percus-Yevick model,which is based on the hard sphere model, allows to take into account orientational disorder in the expression of the structure factor.

In this model, $S(Q)$ is expressed among the hard sphere diameter ϕ_S and the system compacity η as [Ash1966]:

$$S(Q) = K(1 - n\,c(Q\phi_S))^{-1} \; , \tag{9.9}$$

where K, n and $c(Q\phi_S)$ are respectively a constant, the density number and the radial distribution function. The density number n and the radial distribution function are defined by:

$$n = \frac{6\eta}{\pi\phi_S^3} \; , \tag{9.10}$$

$$c(Q\phi_S) = 4\pi\phi_S^3 \int_0^1 x^2 \frac{sin(Q\phi_S)}{xQ\phi_S} \left(\alpha + \beta x + \gamma x^2\right) \; , \tag{9.11}$$

with

$$\alpha = \frac{(1 + 2\eta)^2}{(1 - \eta)^4} \; , \tag{9.12}$$

$$\beta = \frac{6\eta(1 + 0.5\eta)^2}{(1 - \eta)^4} \; , \tag{9.13}$$

$$\gamma = \frac{0.5\eta(1 + 2\eta)^2}{(1 - \eta)^4} \; . \tag{9.14}$$

Of course, the problem here does not correspond to a hard sphere model since the objects are holes but this model is well-known [Lag2008] to particularly suits to the case of the porous alumina membranes by considering $\phi_S = d_P$. This model is here compared to the structure factor determined from the SEM images.
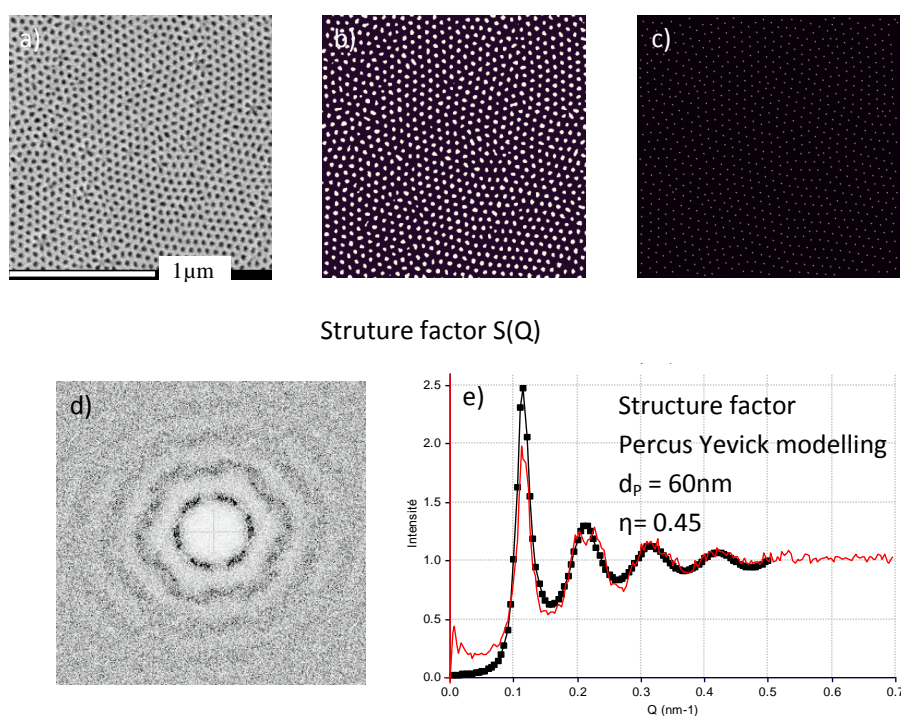
Struture factor S(Q)

Figure 9.12: Numerical processing of the SEM image of a rather well hexagonally ordered alumina membrane (fabricated by L. Cagnon): a) SEM image, b) Binarisation of the SEM image, c) Localization of the hole centers, d) Structure factor associated to the initial SEM image, e) Percus-Yevick modelling (black curve) of the SEM image compared to the calculated structure factor (red curve). In the case of rather well ordered pores the Percus-Yevick model applies moderatly well.

Furthermore, when the Percus-Yevick model is applied to the problem of porous membranes, some precautions have to be taken. First, the system compacity η should not be interpreted as a volume occupation of the holes. It is just an adjustable parameter. Secondly the validity of the model depends on the quality of the holes ordering. The more disordered the system is, the better the model fits. For very well ordered systems such as the one presented in Figure 9.11, one obtains a diffraction image in the reciprocal space so that it is meaningless to make a circular integration. In this case, the Percus-Yevick model cannot be applied. Some other SEM images making appear more disordered holes were provided by L. Cagnon. A similar treatment of the SEM image leads to the 2D-mapping of the structure factor presented in Figure 9.12(d)). In this case, the Percus-Yevick model can be applied even if it fits to the structure factor profile only moderately well. Finally the Percus-Yevick model is known to fit particularly well to very disordered systems. A SEM image of such disordered pores has been provided by K. Lagrené (see Figure 9.13). In this case, the Percus-Yevick model provides an accurate description of the structure factor $S(Q)$.

Furthermore, for hexagonal assemblies of pores exhibiting some orientational disorder, the Bragg spots are no longer observed but are transformed into rings. The rings stems from the superposition of the Bragg spots which correspond to the different orientations of the local perfect hexagonal orders.

MEB image   Struture factor S(Q)
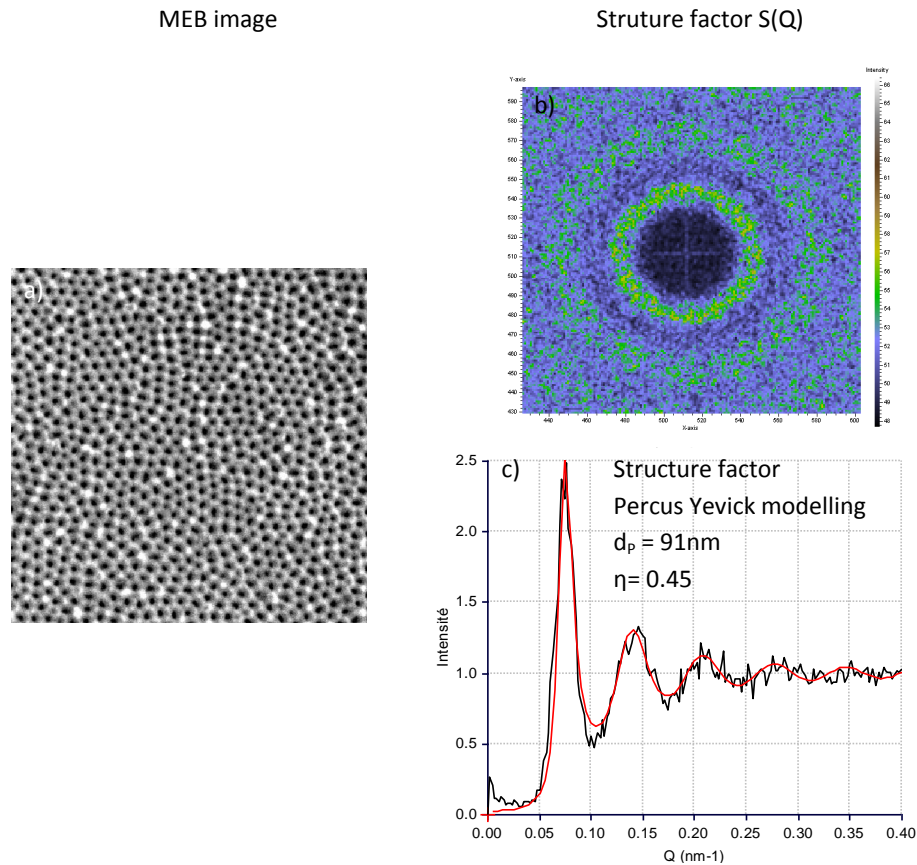
Figure 9.13: Numerical treatment of the SEM image of a disordered alumina membrane (fabricated by K. Lagrené): a) SEM image, b) Structure factor associated to the initial SEM image, c) Percus-Yevick modelling (red curve) of the SEM image compared to the structure factor coming from the integration of image (b) (black curve). In the case of disordered pores the Percus-Yevick model applies well.

9.2.2   Determination of the form factor

Section 7.2 provides the general expression of the form factor $F(Q)$ of a nanowire depending on its orientation β to the incident beam (see Equation 7.49). It has also been shown that in the framework of the experiment ($\beta = 0$), the form factor of the cylinder is similar to the one of a disk given by the square of the Airy function:

$$F(Q) = \frac{2J_1(QR_P)}{QR_P} \, , \qquad (9.15)$$

where $J_1(x)$ is the Bessel function of the first order and R_P the diameter of the pore. When the pores are perfectly aligned along the incident beam, the pores can be seen as holes and therefore as disks (see Figure 9.14a)). This approximation provides a fully isotropic scattering function (see Figure 9.14b)).
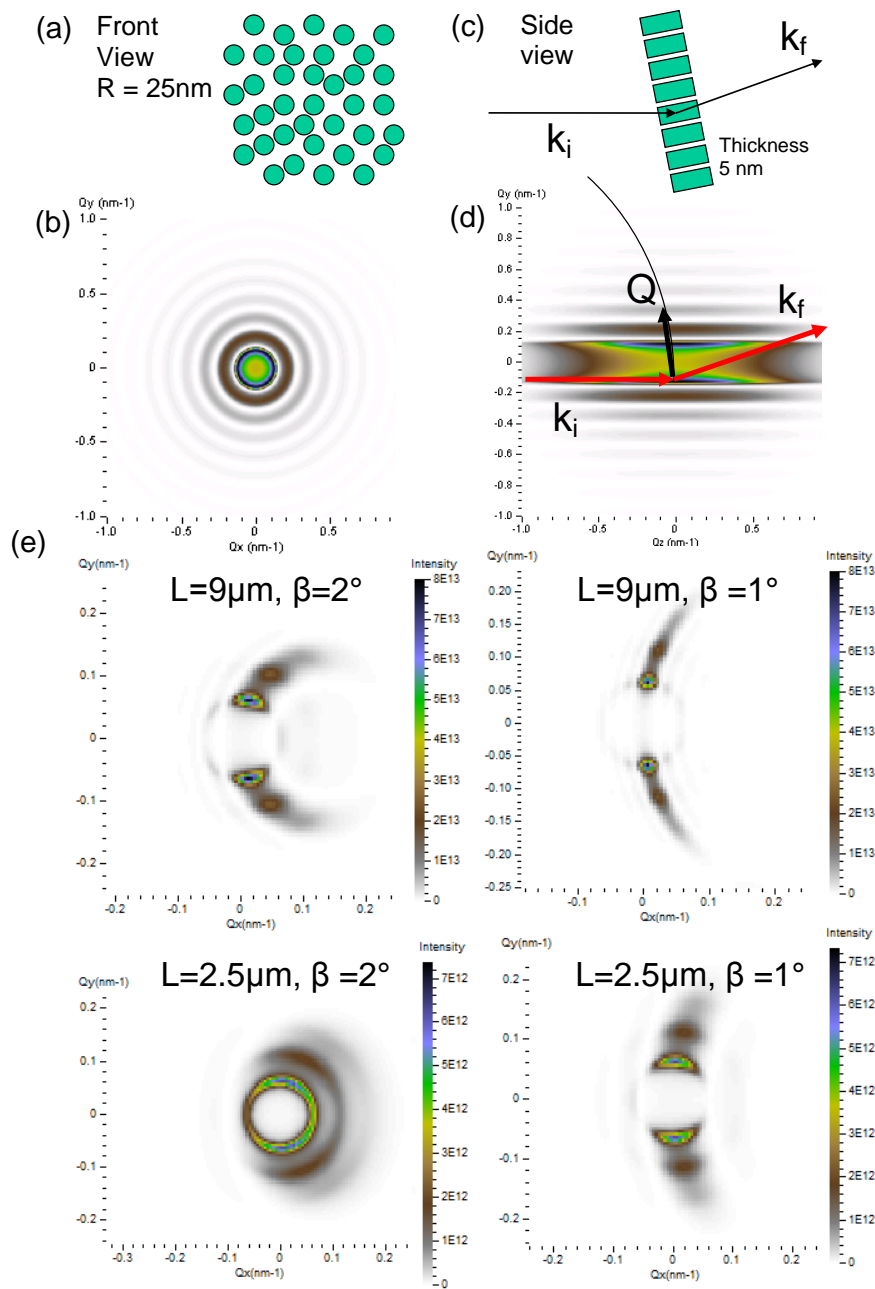
Figure 9.14: *(a) Assembly of disk. (b) Scattering function from this assembly of disks. (c) Incidence geometry when the beam is not perpendicular to the plane of the membrane. (d) 2D scattering function in the above geometry. Along the Q_y direction one has the scattering function of disks but it is modulated along the Q_z direction (incident neutron direction) by a sinc function. (e) 2D scattering function for various thickness of the membrane ($L = 9\,\mu m$ and $L = 2.5\,\mu m$) and for various orientations of the membrane to the incident beam ($\beta = 1°$) and ($\beta = 2.5°$).*

However when the pores are not perfectly aligned with the incident beam, the finite thickness of the pores has to be taken into account (see Figure 9.14c)). As a matter of fact, Equation 7.47 indicates that the form factor is modulated by a *sinc* function corresponding to the apparent thickness $L\cos\beta$ of the membrane which is crossed by the

neutrons. Some examples are given in Figure 9.14. The effect of the Ewald sphere can thus be clearly observed when the sample is rotated and its surface makes the angle β with respect to the incident beam (see Figure 9.14e)).

9.3   SANS measurements of empty porous alumina membranes

These systems are rather complex for scattering studies because they are both dense systems with a marked structure factor as well as very anisotropic since there is a perfect orientation of the holes in one specific direction. The scattering analysis on such structures is thus non trivial to derive.

In order to characterize the structure of the membranes, SANS measurements have been performed on the PAXE spectrometer at the Laboratoire Léon Brillouin. The experimental set-up is described in Annexe 12. As shown in Figure 9.8, the long axis of the nanowires is along the incident beam and the applied magnetic field.

The neutron wavelength and the distance *sample-detector* have been respectively set up at 7Å and 5 m in order to cover a wavelength range from $3.5 \times 10^{-3} \text{Å}^{-1}$ up to $5.5 \times 10^{-2} \text{Å}^{-1}$. The scattering figures have been normalized by the incoherent scattering and the number of incident neutrons.

9.3.1   Description of the SANS figures

In SANS experiments, the use of a beam stop is essential to prevent the transmitted beam to saturate the detector. However in the case of our samples, the transmitted beam represents only 22% of the incident one which is a rather low value due to the very strong scattering of the samples. The use of a beam stop is therefore not essential to perform SANS experiments on such systems.

Figure 9.15 shows the normalized scattering spectra of the four samples. These scattering spectra are isotropic and made of concentric scattering rings as expected from Section 9.2. Since one does not observe any Bragg spots but some concentric rings, it indicates that the pores are not perfectly ordered on the whole sample surface. Indeed, the pores are perfectly ordered over regions whose size can vary from tens to hundreds of nanometers. However on the whole surface of the sample, these domains are disoriented so that the Bragg spots which come from each hexagonally organized domains are turned. The average over all the orientations of these domains leads to a scattering figure made of concentric circles instead of Bragg spots. Of course, the distance between the concentric circles should follow the hexagonal geometry where the positions of the different circles should successively be $|Q^*|$, $\sqrt{3}\,|Q^*|$, $2\,|Q^*|$, $\sqrt{7}\,|Q^*|$, $3\,|Q^*|$, $\sqrt{12}\,|Q^*|$,... with $|Q^*|$ the position of the first circle (see Table 9.3). In practice one does not observe any concentric circles but concentric rings. Indeed, the thickness of the rings is due to the polydispersity of the interpores distance and the finite wavelength resolution $\frac{\triangle\lambda}{\lambda} \sim 10\%$.
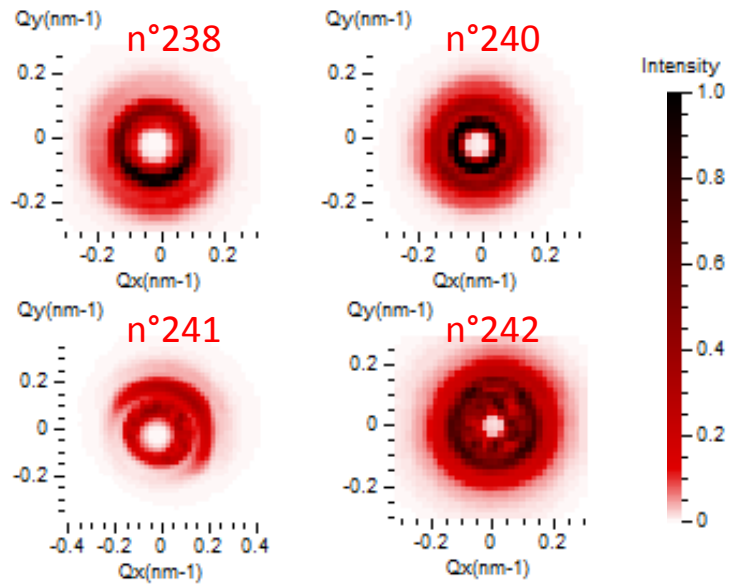
Figure 9.15: Normalized scattering spectra on the PAXE spectrometer of the porous alumina membranes n°238, 240, 241, 242 when the sample surface is perpendicular to the incident beam. Note that the scattering spectrum of the sample n°241 is slightly anisotropic because the sample section is not perfectly perpendicular to the incident beam.
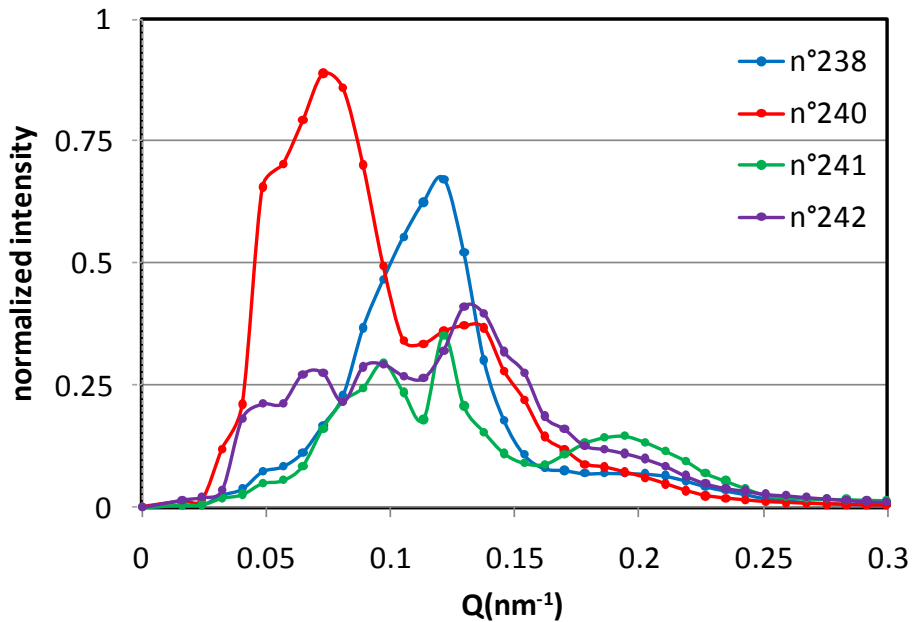
Figure 9.16: Profile of the normalized intensity as a function of the norm of the scattering wave vector Q in lin-lin scale. Note that for each curve the three measured points with the smallest Q correspond to the Beam Stop position.

In order to compare the position of the rings, the profile of the normalized intensity as a function of Q is represented for all samples on Figure 9.16 after a circular integration of

the figures 9.15. These profiles are characterized by the presence of peaks whose positions depend on the structure factor and thus on the interpore distance.

The SEM images of the samples allowed to determine the interpore distance d_P and the diameter of the pores ϕ_P for each sample. The profile of the scattered intensity should give a more accurate estimation of these parameters. The position of the first peak Q^* allows to determine d_P thanks to:

$$Q^* = \frac{2\pi}{d_P} \times \left(\frac{2}{\sqrt{3}}\right) . \qquad (9.16)$$

Sample	d_P(nm) SEM	Q^*(nm^{-1}) SEM	Q^*(nm^{-1}) SANS	d_P(nm) SANS
238	65	0.112	0.121	60
240	160	0.045	<0.048 (0.072)	>151 (174)
241	70	0.103	0.097	75
242	105	0.069	0.064	113

Table 9.4: Comparison of d_P and Q^* from the SEM images and the SANS spectra. Concerning the sample n°240, since the first peak is not accessible in the investigated Q range, the second peak which is indicated into brackets gives an access to the d_P.

It must be underlined that the Q range was not large enough to observe the first peak of the sample n°240. In fact, the probable position of this peak is localized at the edge of the Beam Stop. In order to extract information from the intensity profile of this sample, one thus has to consider the peak localized at $\sqrt{3}Q^*$. The positions of the first peaks and thus the interpore distance are indicated for each sample in Table 9.4 and compared with the values deduced from the SEM images. The values deduced from the SANS measurements are globally in agreement with the values deduced from the SEM images.

In Figure 9.17, from the experimental position of the first peak - or of the second peak for the sample n°240 - the positions of the other peaks ($\sqrt{3}Q^*$, $2Q^*$, $\sqrt{7}Q^*$, $3Q^*$, $\sqrt{12}Q^*$,...) are presented in the case of an hexagonal arrangement. It shows that the second experimental peak is centered between $\sqrt{3}Q^*$ and $2Q^*$ while the third one is centered between $\sqrt{7}Q^*$ and $\sqrt{12}Q^*$ for samples n°238 and 240. It appears that the different peaks include in fact several theoretical peaks. As a matter of fact, the polydispersity of the interpores distance introduces a width of the peaks and the spectrometer resolution does not permit to separate them. Sample n°241 shows two peaks at low Q. However, if the first one is indexed by Q^*, the second one cannot be indexed by $\sqrt{3}Q^*$. This indicates that these two peaks are in fact a single one. The width of this peak comes from the non-perfect orientation of the sample during the experiment (see Figure 9.17).

The orientation of the sample is crucial to extract quantitative information. As a matter of fact, when the pores are not perfectly aligned along the incident beam, the scattering figure becomes clearly anisotropic. Figure 9.18 presents different examples of the shape of the scattering depending on the angle β between the incident beam and the normal to the sample surface. The more the porous alumina membrane is rotated, the more anisotropic its scattering figure becomes. The influence of the angle β stems from the form factor of the objects and corresponds to what has been discussed in Section 7.1 (see Figure 7.3). In order to extract information about the structure of these systems, it

is thus recommended to process carefully and to make sure that the orientation is well under controlled.
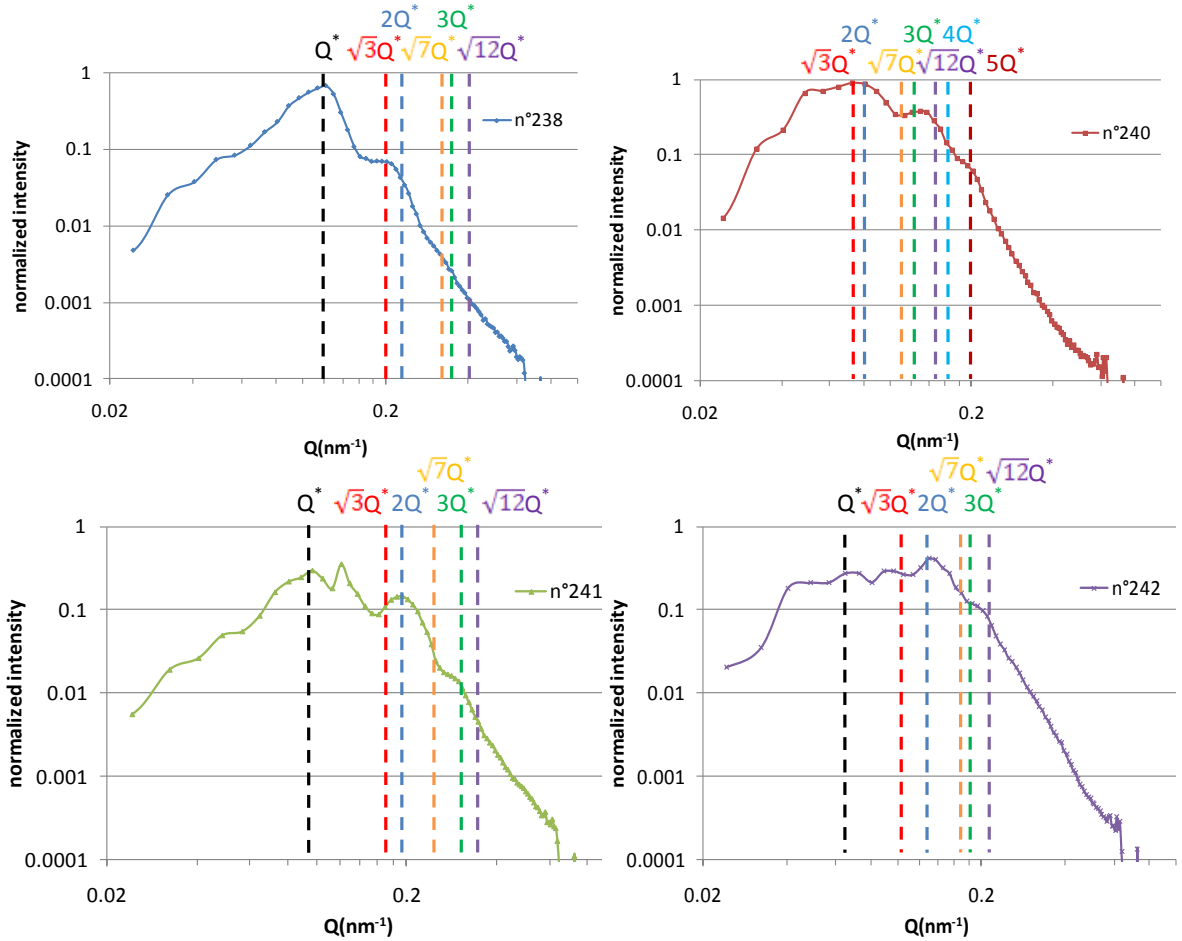
Figure 9.17: Profile of the normalized intensity as a function of the norm of the wave vector Q in log-log scales with an indication of the position of Q^*, $\sqrt{3}Q^*$, $2Q^*$, $\sqrt{7}Q^*$,$3Q^*$, $\sqrt{12}Q^*$...
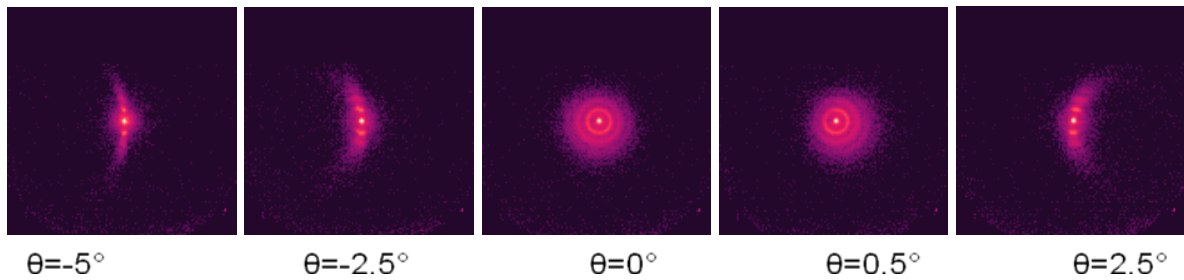
Figure 9.18: Scattering spectra for a porous alumina membrane depending on the angle α between the incident beam and the normal to the surface.

9.3.2   Determination of the alumina membrane neutron scattering length density

It is fundamental to know the value of the neutron scattering length density before starting SANS experiments. For amorphous materials such as alumina Al_2O_3, the neutron scattering length density is given by :

$$\rho = \frac{\mathcal{N}\varrho}{M} b_{coh} \,, \tag{9.17}$$

where $\mathcal{N}$, ϱ, M and b_{coh} are respectively the Avogadro number, the volumic mass, the molar mass and the coherent scattering length. For alumina, the coherent scattering length is expressed as:

$$b_{coh}(Al_2O_3) = \frac{2}{5} b_{coh}(Al) + \frac{3}{5} b_{coh}(O) \,,$$

where $b_{coh}(Al)$ and $b_{coh}(O)$ are respectively the neutron scattering length of Al and O. Knowing that $\varrho_{AL_2O_3}$ is of the order of $3.4\,\mathrm{g.cm^{-3}}$ for porous alumina membranes [Lag2008, Nie2002b], the value of the alumina scattering length density is about :

$$\rho_{Al_2O_3} = 4.22 \times 10^{10}\,\mathrm{cm^{-2}} \,. \tag{9.18}$$

However the amorphous structure of alumina may lead to a slight variation of this value so that we need to determine ρ experimentally. The method is based on the *contrast matching* technique [Gri2007b, Lag2008]. When the porous alumina membrane is empty, the scattering contrast density $\triangle\rho$ is expressed as:

$$\triangle\rho = \rho_{Al_2O_3} - \rho_0 \,, \tag{9.19}$$

where $\rho_{Al_2O_3}$ and ρ_0 are respectively the neutron scattering length densities of the alumina and of the air which fills in the pores. Since the scattered intensity $I(Q)$ (see Section 7.1.2.2) is:

$$I(Q) = \Phi V_P \left(\triangle\rho\right)^2 |F(Q)|^2 S(Q) \,, \tag{9.20}$$

the idea consists in filling the pores with a material which has a scattering length density of $\triangle\rho$, and therefore $I(Q)$ becomes zero. The easiest way consists in filling the pores with a mixing of H_2O and D_2O whose neutron scattering length densities are respectively $\rho_{H_2O} = -0.56 \times 10^{10}\,\mathrm{cm^{-2}}$ and $\rho_{D_2O} = 6.38 \times 10^{10}\,\mathrm{cm^{-2}}$. The neutron scattering length density $\rho_{mix}(x_D)$ depends on the volume fraction of D_20, x_D, is expressed as:

$$\rho_{mix}(x_D) = x_D\rho_{D_2O} + (1 - x_D)\rho_{H_2O} \,. \tag{9.21}$$

The matching point which verifies $I(x_D) = 0$ is noted x_M. Combination of Equations 9.20 and 9.21 suggests that the x_D dependence of $\pm\left(Imax\right)^{1/2}$ is linear with $+$ referring to $0 < x_D < x_M$ (since $\rho_{D_2O} > 0$) and $-$ referring to $x_M < x_D < 1$ (since $\rho_{H_2O} < 0$). Since the x_D dependence of $\pm\left(Imax\right)^{1/2}$ is linear, we only need to investigate a few values of x_D. We have thus measured four different values of x_D: 0, 0.25, 0.75 and 1.

Figure 9.19(a) shows the evolution of the scattered intensity depending on the value of the D_2O volume fraction, x_D . The different intensity profiles are homothetic and

the intensity is minimum for $x_D = 0.75$ which implies that the "matching point", x_M, is localized around this value.

Figure 9.19(b) gives access to the value of x_D by representing the x_D dependence of $\pm (Imax)^{1/2}$. It must be precised that the measurement of $I(Q)$ as a function of x_D is not fully precise for two main reasons: (i) the alignment of the sample with respect to the incident beam is not exactly the same for each measurement and (ii) from a measurement to another, it is requested to well dry the sample so that the pores are well empty before being filled with another mixing. These reasons may explain systematic errors made on the measurement. The value of x_D deduced from the measurement is $x_D \approx 0.68$ which corresponds to:

$$\rho_{Al_2O_3}^{exp} = 4.16 \times 10^{10} \, \text{cm}^{-2} \, . \tag{9.22}$$

The deduced value is very close to the theoretical value which shows that the alumina is very dense.. In the next sections, we will use the theoretical value $\rho_{Al_2O_3} = 4.22 \times 10^{10} \, \text{cm}^{-2}$ which corresponds quite well to the experimental one.
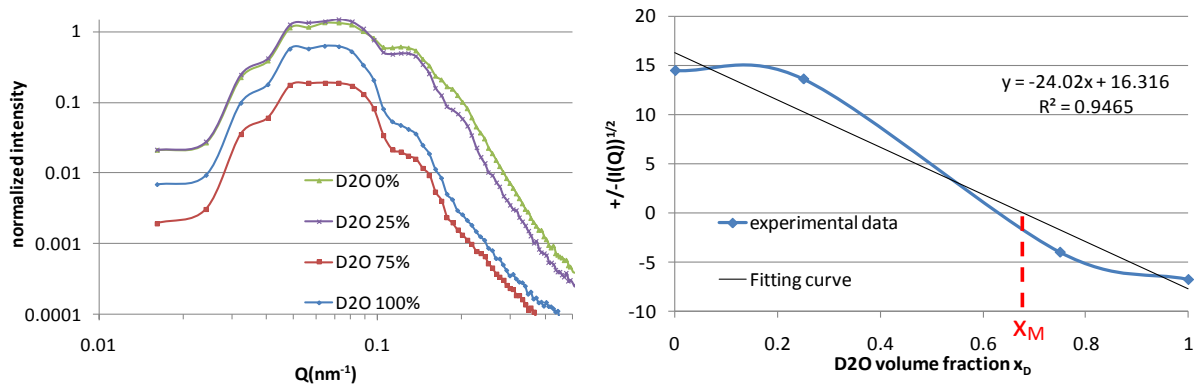
Figure 9.19: The contrast matching method applied to a porous alumina membrane synthesized by L. Cagnon. a) $I(Q)$ for different values of the D_2O volume fraction x, b) $\pm I(Q)^{1/2}$ for different values of the D_2O volume fraction x. $x_M = 0.68$ is the matching point. The linear fit (black) is given by $y = Ax + B$ with $A = -24.02 \pm 4.04$ and $B = 16.316 \pm 2.574$. The goodness of the fit is given by $R^2 = 0.946$.

9.4 SANS measurements of nanowires in porours alumina membranes

SANS measurements have been performed on magnetic nanowires included in membranes. The non-polarized scattering should be similar to the one of the porous alumina membranes since the major change in the expression of $I(Q)$ comes from $\triangle \rho$ (see Equation 9.20). The size and the distribution of the nanowires are indeed imposed by the alumina membrane geometry. The aim of the experiments here is to focus on the magnetic scattering of these nanowires via polarized measurements. Four different batches of nanowires have been extensively studied (see Section 9.3.1). These nanowires are all included in the same type of porous alumina membrane (n°226) so that they all exhibit the same geom-

etry. From SEM measurements (see Figure 9.20), they present a diameter ϕ of 40 nm, an interpore distance d_P of 105 nm and a length of 25 μm.
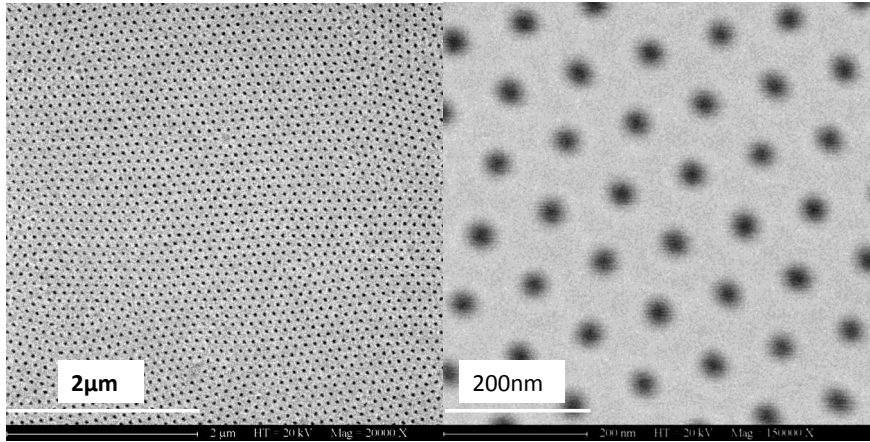
Figure 9.20: SEM images of the porous alumina membrane n°226.

The SANS experiments on these nanowires have been performed on the PAPYRUS (G5.5) spectrometer at the Laboratoire Léon Brillouin. The wavelength of the neutrons was 8Å and the *sample − detector* distance is 4m so that the accessible wavevector Q range was:

$$0.029 \, \text{nm}^{-1} < Q < 0.62 \, \text{nm}^{-1} \, . \tag{9.23}$$

The distance $d \simeq 105$ nm between the nanowires gives a position of the first ring at $Q \approx 0.06 \, \text{nm}^{-1}$. The accessible Q-range is therefore well adapted to the study of these objects.

9.4.1 Non-polarized SANS measurements

As expected, the four samples exhibit SANS spectra similar to the one of the empty porous alumina membranes previously discussed (see Figure 9.21). The samples have been oriented to the best possible so that the nanowires are almost perfectly aligned with respect to the incident beam. Therefore the SANS figures are almost fully isotropic.

The counting time (t=3600s) was long enough to make visible the first three diffraction peaks in the intensity profile $I(Q)$ (see Figure 9.22). One can even guess the fourth one. The diffraction peaks are localized at the same Q position for each sample. The position of the first peak Q^* gives an access to the distance d_P between the centers or the wires (see Table 9.5). The value of d_P is found to be about 115 nm which is in agreement with the SEM images. In fact, the major difference between the four samples stems from the scattering spectrum of the Ni nanowires whose intensity is much larger than for Co nanowires (see Figure 9.22). The difference of scattering intensity between the crystallized Ni nanowires and the crystallized Co ones (samples $Co \, pH = 3.4$ and $pH = 5.75$) are accounted for Equation 9.20 and the difference between the scattering length densities $\triangle \rho$ of the crystallized Co and Ni. The scattering length of Ni and Co are respectively 10.3 fm and 2.49 fm. Since they both exhibit an atomic concentration of $9 \times 10^{28} \, \text{m}^{-3}$, their scattering length densities are $\rho(Ni) = 9.27 \times 10^{10} \, \text{cm}^{-2}$ and $\rho(Co) = 2.24 \times 10^{10} \, \text{cm}^{-2}$.
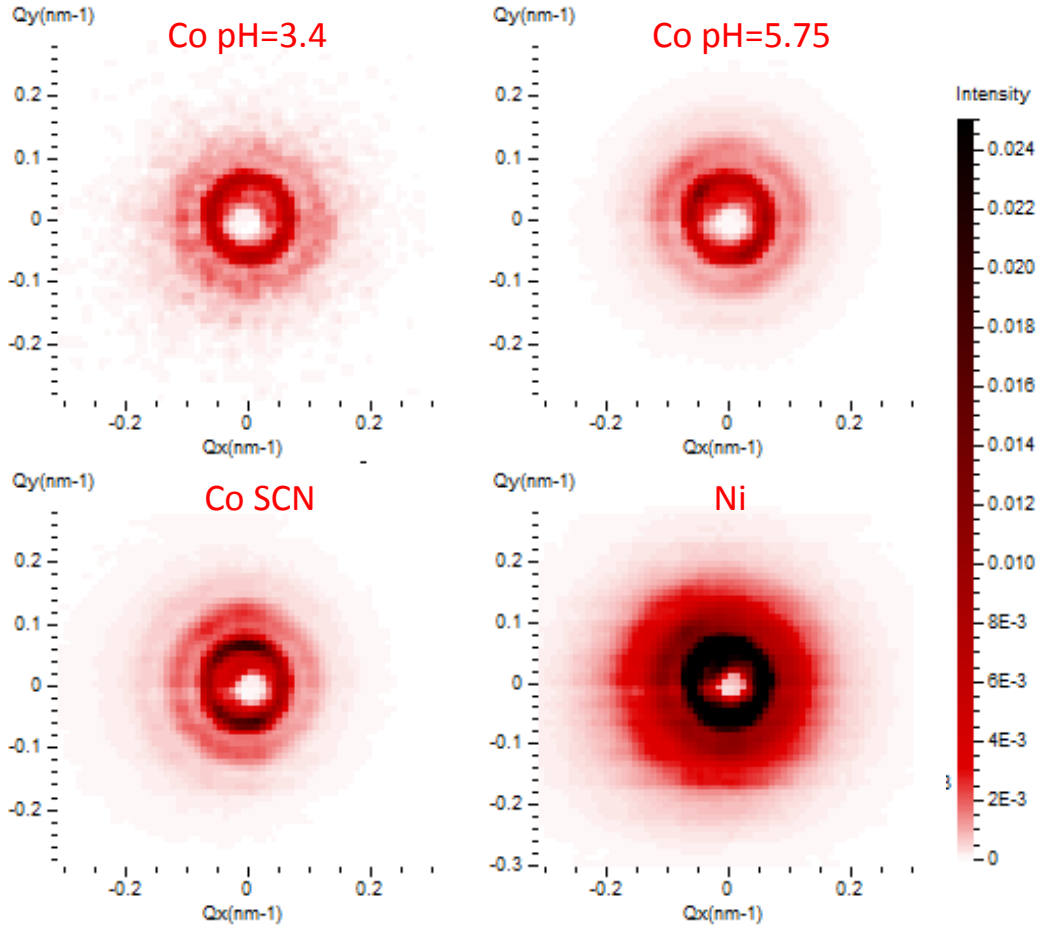
Figure 9.21: SANS spectra of the four samples after normalization by the monitor.

With $\rho(Al_2O_3) = 4.22 \times 10^{10} \, \text{cm}^{-2}$, we obtain the scattering contrast factors:

$$\begin{cases} \rho(Ni) = 9.27 \times 10^{10} \, \text{cm}^{-2} \\ \rho(Co) = 2.24 \times 10^{10} \, \text{cm}^{-2} \end{cases} . \tag{9.24}$$

It implies that the ratio of scattering between $I_{max}(Co)$ and $I_{max}(Ni)$ is expected to be:

$$\frac{I_{max}(Co)}{I_{max}(Ni)} = \left(\frac{\triangle\rho(Co)}{\triangle\rho(Ni)} \right)^2 = 0.15 . \tag{9.25}$$

The predicted value of this ratio corresponds quite well to the experimental value presented in Table 9.5. For $Co \, SCN$ nanowires the experimental value of this ratio is 0.27. This can be accounted for the amorphous structure of these objects making thus the value of the neutron scattering length of crystallized Co ($b = 2.49 \, \text{fm}$) inadequate. Nevertheless the experimental value of $I_{max}(Co \, SCN)/I_{max}(Ni)$ determined here allows to get access to the value of $\rho(Co \, SCN)$ since:

$$\triangle\rho(Co \, SCN) = \triangle\rho(Ni) \left(\frac{I_{max}(Co)}{I_{max}(Ni)} \right)^{\frac{1}{2}} . \tag{9.26}$$

From Equation 9.26, we obtain:

$$\rho(Co\,SCN) = 1.6 \times 10^{-10}\,\text{cm}^{-2}\,. \tag{9.27}$$

This value is about 30% lower than the one of crystallized Co. The difference between these two values is probably due to a variation of the atomic density between the crystallized and amorphous cobalt.
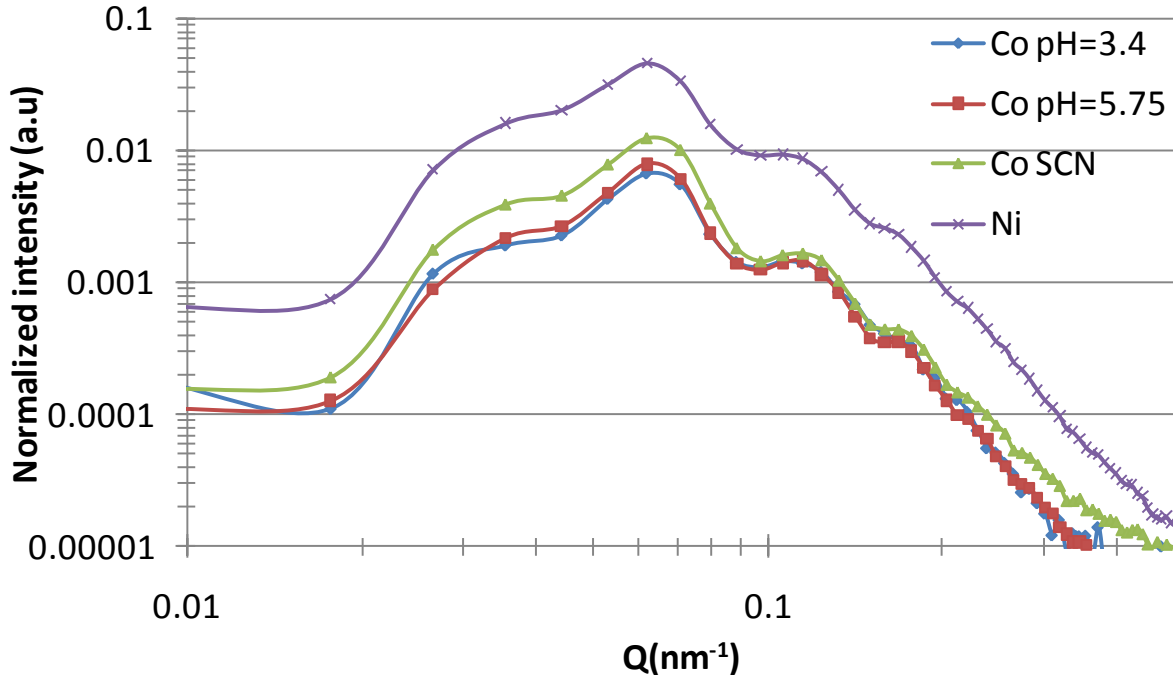
Figure 9.22: Intensity profile $I(Q)$ obtained for the four samples from a circular integration of the spectra presented on Figure 9.21.

Sample	$Q^*(\text{nm}^{-1})$	$d_P(\text{nm})$	$I_{max}(\text{a.u})$	$I_{max}/I_{max}(Ni)$
Co pH=3.4	0.063	115	6.7	0.15
Co pH=5.75	0.063	115	7.9	0.17
Co SCN	0.063	115	12.6	0.27
Ni	0.063	115	46.1	1

Table 9.5: Comparison of Q^*,d_P and I_{max} between the four samples

In order to characterize the structure of the arrays of nanowires, fits have been performed on the Spectraprocessor software [Spe] developed by F.Ott from the Laboratoire Léon Brillouin. This software allows to fit the scattered intensity for arrays of nanowires by modelling the structure factor $S(Q)$ with the Percus-Yevick model presented in Section 9.2.1.2 and the form factor $F(Q)$ of the nanowire section by the Airy function as introduced in Section 6.2.2.3. The scattering spectra of porous membranes filled in with nanowires are similar to the scattering of arrays of disks when the wires are aligned along the incident beam. The finite thickness of the nanowires provides no contribution to the scattering when the sample surface is normal to the incident beam. Furthermore, since

the nuclear scattering is very similar for all the samples, fits have only been made on the sample *Co pH* = 3.4.
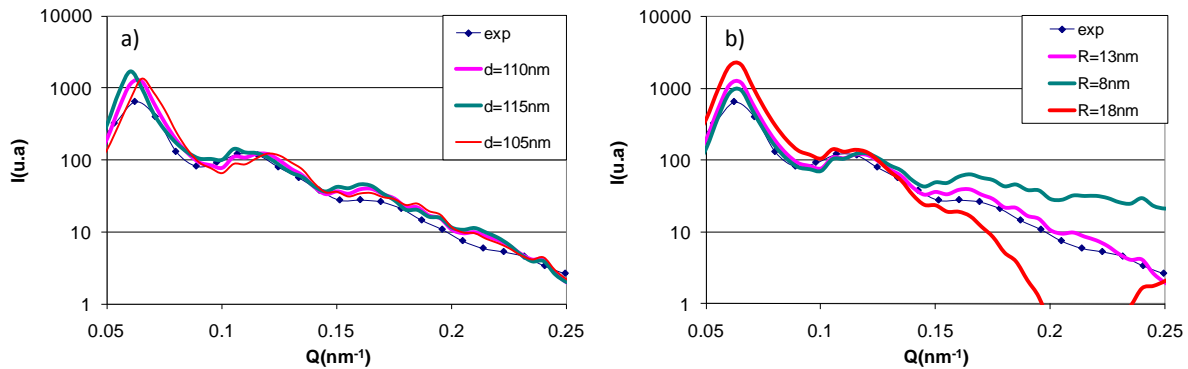
Figure 9.23: SANS modelization of $I(Q)$ for the Co pH=3.4 nanowire array. a) Variation of the distance d_P between the centers of the nanowires, b) Variation of their radii R.

Figure 9.23 shows the effects of the nanowire radius R and the interwire distance d_P as parameters of the scattering. The value of d_P modifies the structure factor profile and thus the positions of the diffraction peaks. A first approximation of the first diffraction peak localization Q^* provided $d_P = 115$ nm. However the graphical estimation of Q^* is not too precise. Fits have been realized with the *Spectraprocessor* software for different values of d_P. It allows to assess a more accurate value of d_P of about 110 nm. The value $d_P = 110$ nm provides the best agreement for the positions of the three main diffraction peaks (see Figure 9.23(a)). As for the value of R, Figure 9.23(b) indicates how strongly the variations of R may affect $I(Q)$. The main effect of R concern the slope of $I(Q)$ at larger Q. This effect is quite drastic and $R = 13$ nm is the most suitable value. This value is compatible with the SEM images (see Figure 9.20) from which only a rough estimate of the pores sizes can be extracted because of the limited resolution. One has to pay attention to estimate the diameter of the pores from the SEM images [Lag2008] because SEM introduces a gaussian high-frequency noise which corresponds to a spread gaussian in the reciprocal space, leading to a blurred zone around the holes on the SEM images.

9.4.2 Polarized SANS measurements

In order to probe the magnetism in the nanowires, Polarized SANS measurements have been performed on the PAPYRUS (G5.5) spectrometer at the Laboratoire Léon Brillouin (see Annexe 12). The aim of the experiment consists in determining the magnetic form factors of the nanowires and in studying their magnetization reversal.
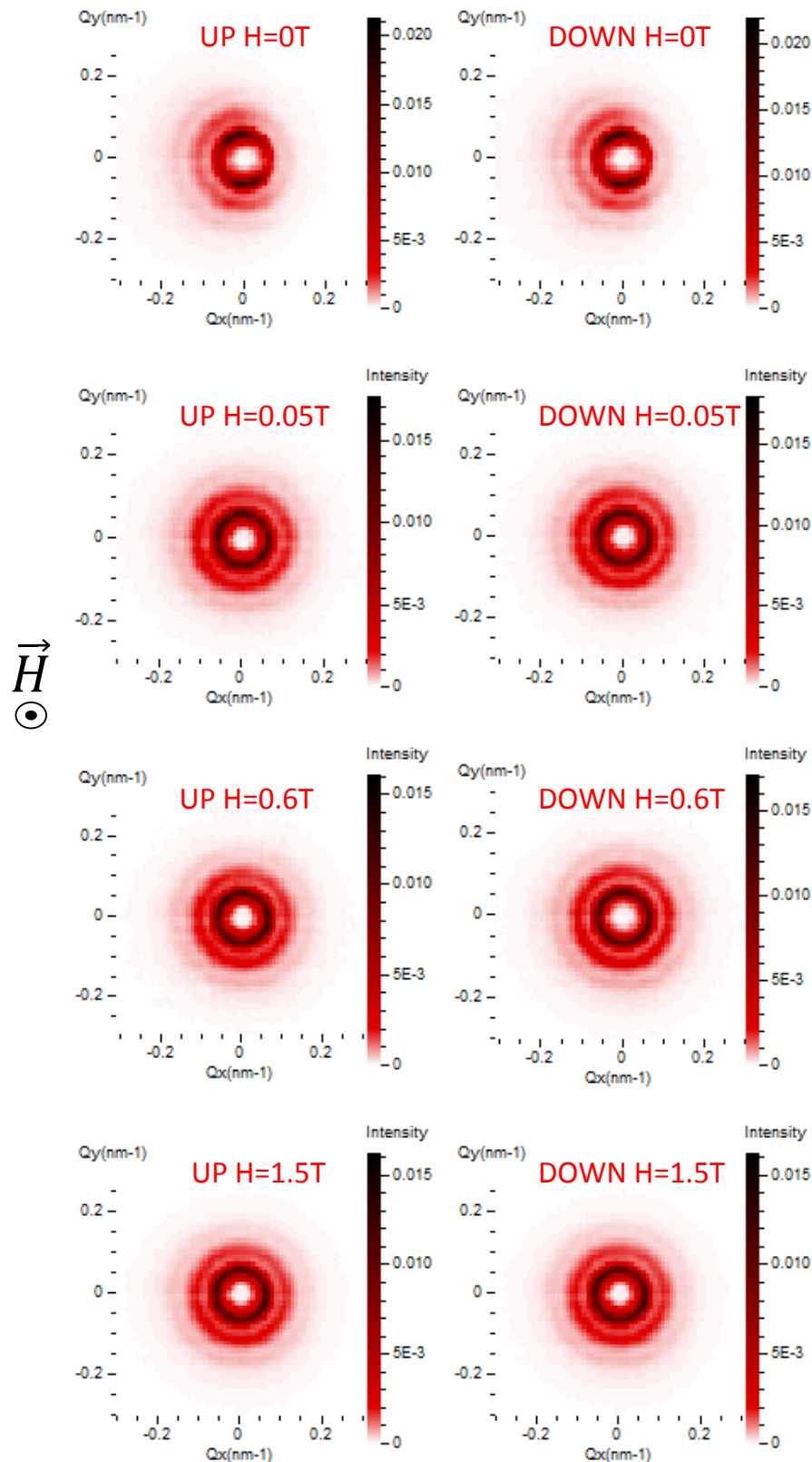
Figure 9.24: Scattering spectra of the Co pH=3.4 nanowires for neutrons polarized UP and DOWN and for different values of the magnetic field applied along the nanowires. Note that in the remanent state, the magnetic configuration does not follow the cylindrical symmetry of the wires.

Figures 9.24 presents the scattering spectra $I^+(Q)$ and $I^-(Q)$ for sample $Co\ pH = 3.4$ and for different values of the applied magnetic field. It is hard to distinguish any differences between these spectra. the polarization contrast is rather low between I^+ and I^-. While the measurements under an applied field are symmetrical which proves the correct alignment of the wires, the measurement in the remanent state $(H = 0\,\mathrm{T})$ shows a marked anisotropy which suggests that the remanent state is not homogeneous and does not follow the cylindrical wire symmetry. This can be accounted for by the magnetometry measurement of Figure 9.6 which showed that the anisotropy axis in this sample was poorly defined and that the remanent state consists of domains. For the other samples in which the magnetic anisotropy is better defined (see Figures 9.4, 9.5 and 9.7), the SANS scattering is isotropic even in the remanent state.

In Section 7.1.3, it has been shown that in the configuration $(\overrightarrow{H} \parallel \overrightarrow{k_i})$, the total SANS intensity $I(Q)$ and the magnetic contrast $\triangle I(Q)$ can be written:

$$
\begin{cases}
I(Q) = S(Q) \times 2 \times (|F_N(Q)|^2 + |F_M(Q)|^2) \\
\triangle I(Q) = I^+(Q) - I^-(Q) = S(Q) \times (-4PF_N(Q)F_M(Q))
\end{cases}
. \tag{9.28}
$$

From Equations 9.28, it is possible to get rid of the structure factor $S(Q)$ by considering the ratio $\triangle I(Q)/I(Q)$:

$$
\frac{\triangle I}{I} = -\frac{2PF_N F_M}{\left(|F_N|^2 + |F_M|^2\right)} . \tag{9.29}
$$

In the following, the experimental results are presentend in two steps. First the stress is put of the dependence on $I(Q)$ on the external magnetic field $\overrightarrow{H}$. The second step consists in putting the magnetic contrast $\triangle I(Q)$ into evidence by studying the ratio $\triangle I/I$ and its dependence on the magnetic field. For the $Co\ (pH = 5.75)$, the $Co\ SCN$ and the Ni nanowires, the values of the applied magnetic field have been applied so that it follows the hysteresis cycle from 0T up to 1T, then down to -1T and then once again up to 1T. As for the $Co\ (pH = 3.4)$ nanowires, the measurements have been performed for only field values from 0T up to 1T. Note that the sample has been previously saturated at H=1T.

Furthermore it must be noted that the temperature of measurement can vary from a sample to another. Table 9.6 sums up the variation of the temperature and of the magnetic field for the different investigated samples.

Sample	Temperature	Applied magnetic field H
Co pH=3.4	20 K	Saturation of the sample at $H = 1\,\mathrm{T}$: from $H = 0\,\mathrm{T}$ up to 1.5 T
Co pH=5.75	200 K	From 0 T up to 1 T down to -1 T and then up to 1 T
Co SCN	200 K	From 0 T up to 1 T down to -1 T and then up to 1 T
Ni	250 K	From 0 T up to 1 T down to -1 T and then up to 1.5 T

Table 9.6: Comparison of the temperature and magnetic field parameters for the four investigated samples

Figures 9.25, 9.26, 9.27 and 9.28 show the circular integration of the 2D SANS patterns $I(Q) = I^+(Q) + I^-(Q)$ as a function of the applied field. It can first be observed that the scattering at small Q is larger for low magnetic fileds. It corresponds to the formation of magnetic domains. Moreover, when the magnetization inside the wires is disordered (small H), the scattering objects are not so well defined anymore and this leads to a blur of the structure factor peaks.
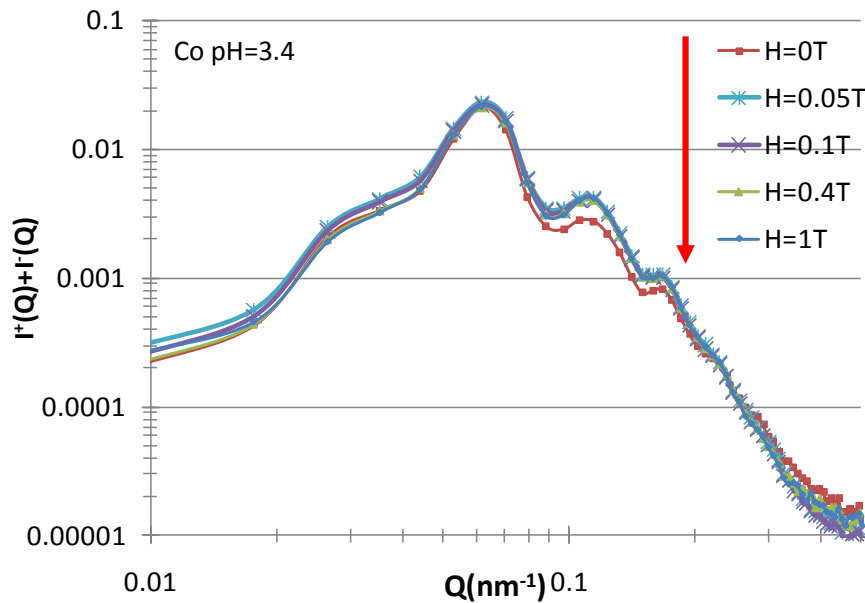
Figure 9.25: Evolution of the scattering function $I(Q)$ of the Co nanowires made at pH=3.4 for different values of the applied magnetic field H
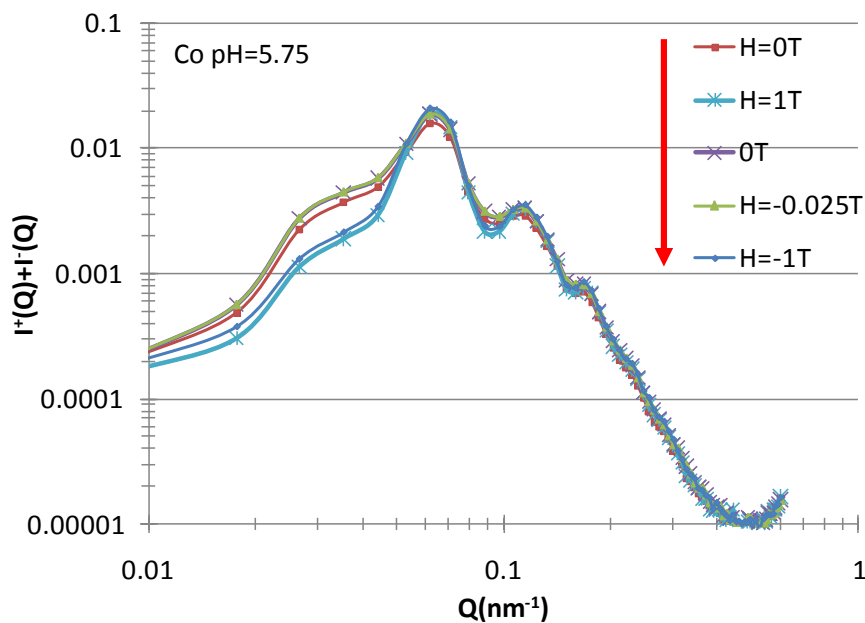
Figure 9.26: Evolution of the scattering function $I(Q)$ of the Co nanowires made at pH=5.75 for different values of the applied magnetic field H
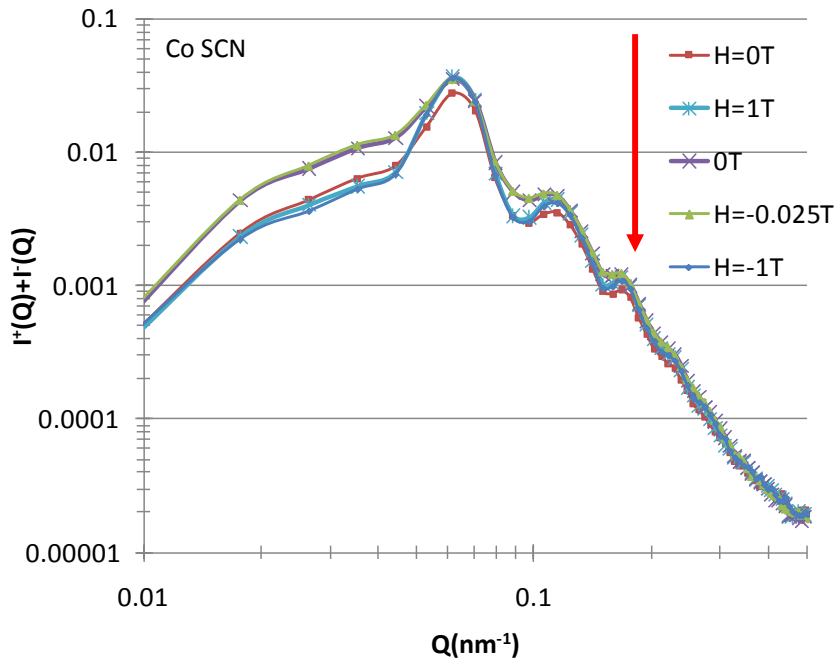
Figure 9.27: Evolution of the scattering function $I(Q)$ of the Co nanowires with SCN for different values of the applied magnetic field H
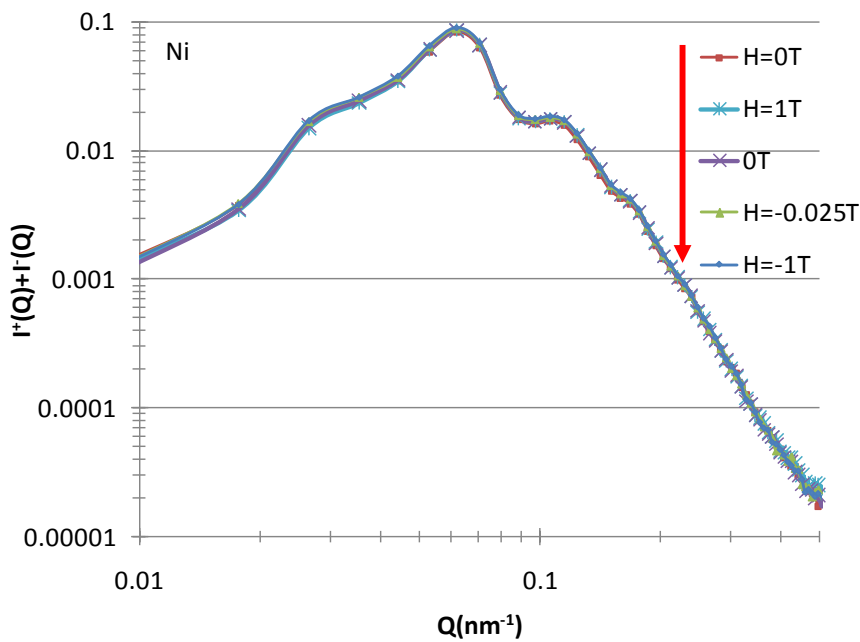
Figure 9.28: Evolution of the scattering function $I(Q)$ of the Ni nanowires for different values of the applied magnetic field H

The non-polarized scattering is thus strongly affected by the magnetic field H and possibly by the formation of magnetic domains inside the wires. However the scattering due to the magnetism of the nanowires becomes more visible when the scattering spectra of the $|+\rangle$ and $|-\rangle$ polarized neutrons are compared. In order to probe the magnetic

properties of the nanowires, the difference between the scattering spectra of $|-\rangle$ and $|+\rangle$ polarized neutrons are presented in Figures 9.29, 9.30, 9.31 and 9.32. These figures put into evidence many inversions of $I^- - I^+$ depending on both Q and H which originate from the $F_N F_M$ dependence of the $\triangle I = I^- - I^+$ quantity (see Equation 7.52).
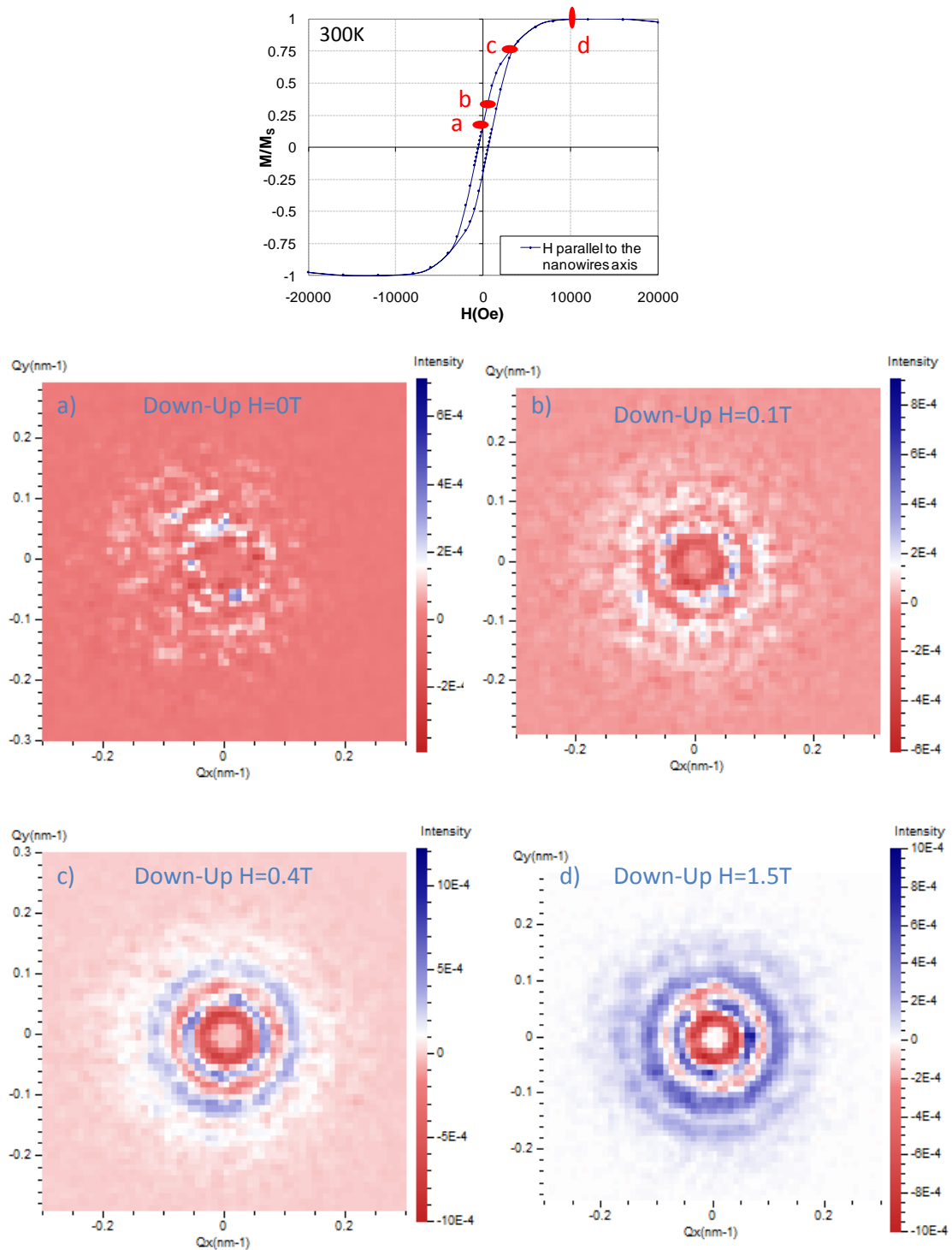
Figure 9.29: $I^-(Q) - I^+(Q)$ for Co nanowires made at $pH = 3.4$ and for different values of the magnetic field at $T = 200\,\mathrm{K}$.
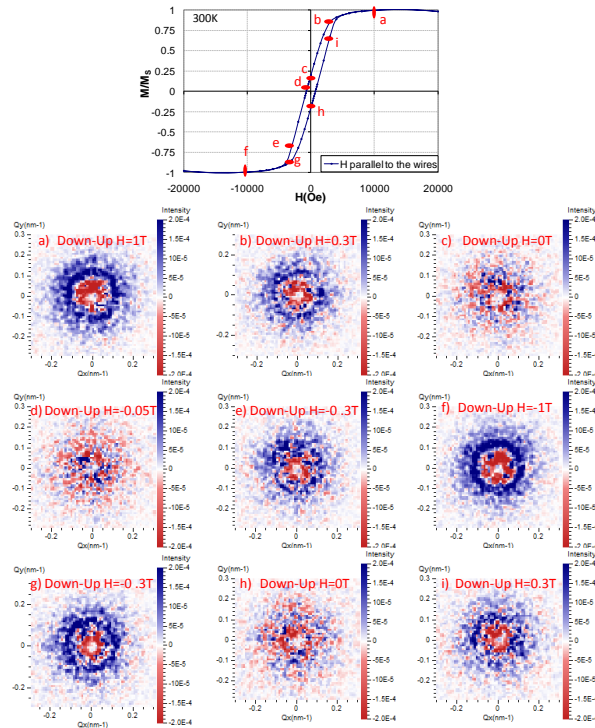
Figure 9.30: $I^-(Q) - I^+(Q)$ for Co nanowires made at $pH = 5.75$ and for different values of the magnetic field at $T = 200\,\mathrm{K}$.
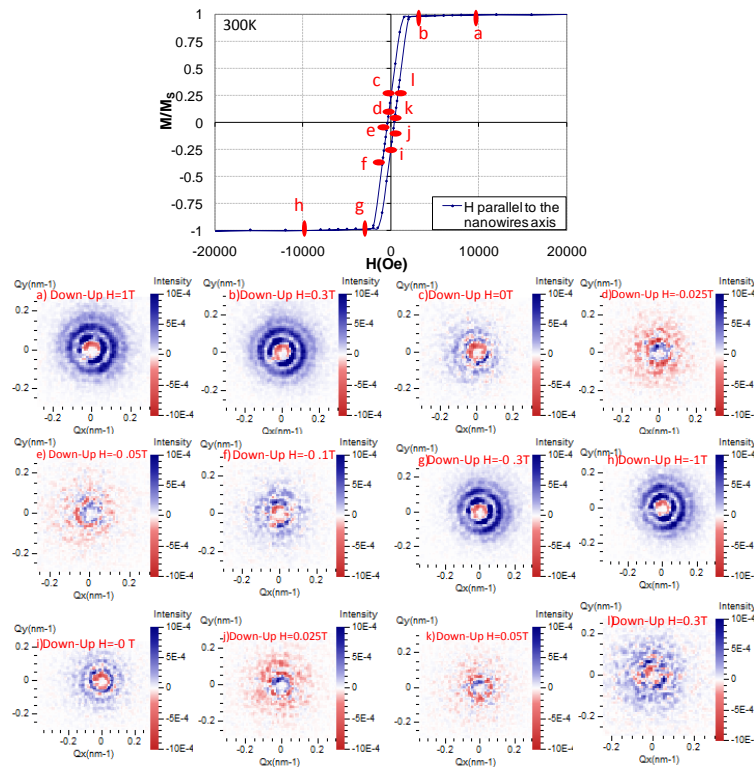
Figure 9.31: $I^-(Q) - I^+(Q)$ for the Co nanowires made with SCN and for different values of the magnetic field at $T = 200\,\mathrm{K}$.
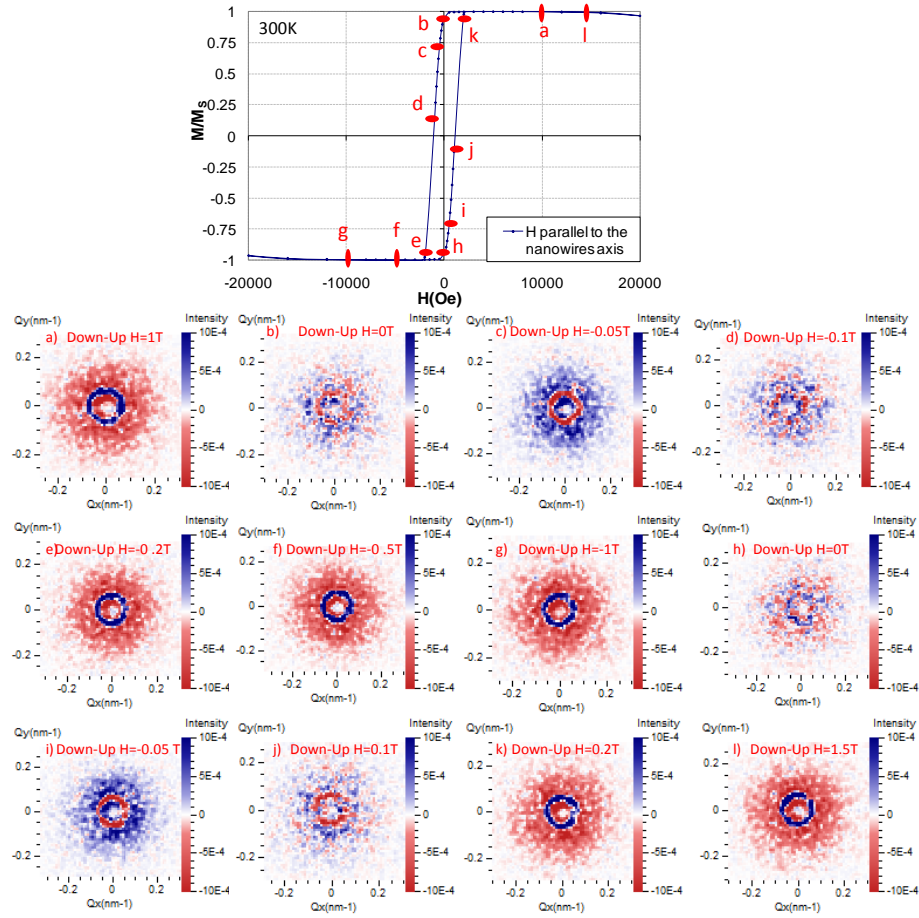
Figure 9.32: $I^-(Q) - I^+(Q)$ for Ni nanowires and for different values of the magnetic field at $T = 250\,\text{K}$.

However from these spectra it is difficult to get an idea of the evolution of the magnetic contrast. The magnetic contrast is indeed hidden by the strong structural scattering stemming from the structure factor. In order to eliminate the structure factor and the geometrical factor, it is useful to study the magnetic field dependence of the asymmetry ratio (see Equation 9.30):

$$R(Q) = \frac{\triangle I}{I} = -\frac{2PF_N F_M}{(F_N^2 + F_M^2)} \, . \tag{9.30}$$

Figures 9.33, 9.34, 9.35 and 9.36 present the evolution of the ratio $R(Q) = \triangle I / I$ as a function of the magnetic field H for each sample. The Q profiles are rather similar insofar as $R(Q)$ are maximum for large magnetic field ($H > 0.3\,\text{T}$) when the samples are saturated. Then when H decreases, $R(Q)$ also globally decreases. An inversion of the sign of $R(Q)$ is also observed for small Q values. Furthermore, the most striking feature of the $R(Q)$ profiles stems from the drop of $R(Q)$ for small Q ($Q < 0.2\,\text{nm}^{-1}$).
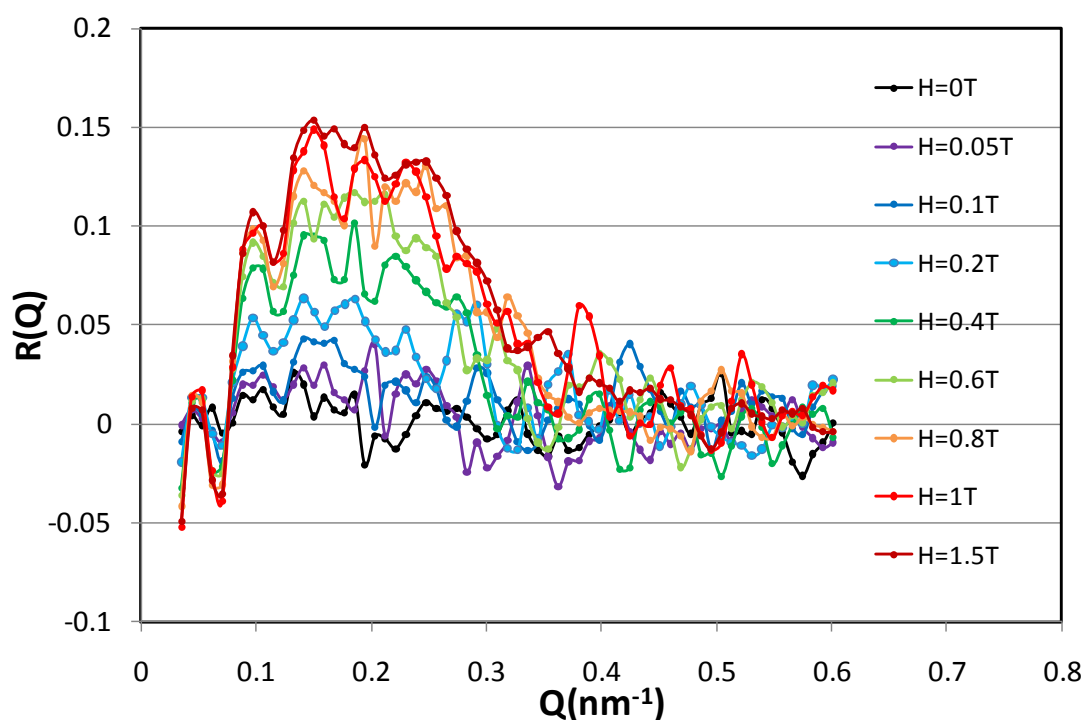
Figure 9.33: Evolution of the ratio function $R(Q) = \triangle I(Q)/I(Q)$ of the Co nanowires made at $pH = 3.4$ for different values of the applied magnetic field H
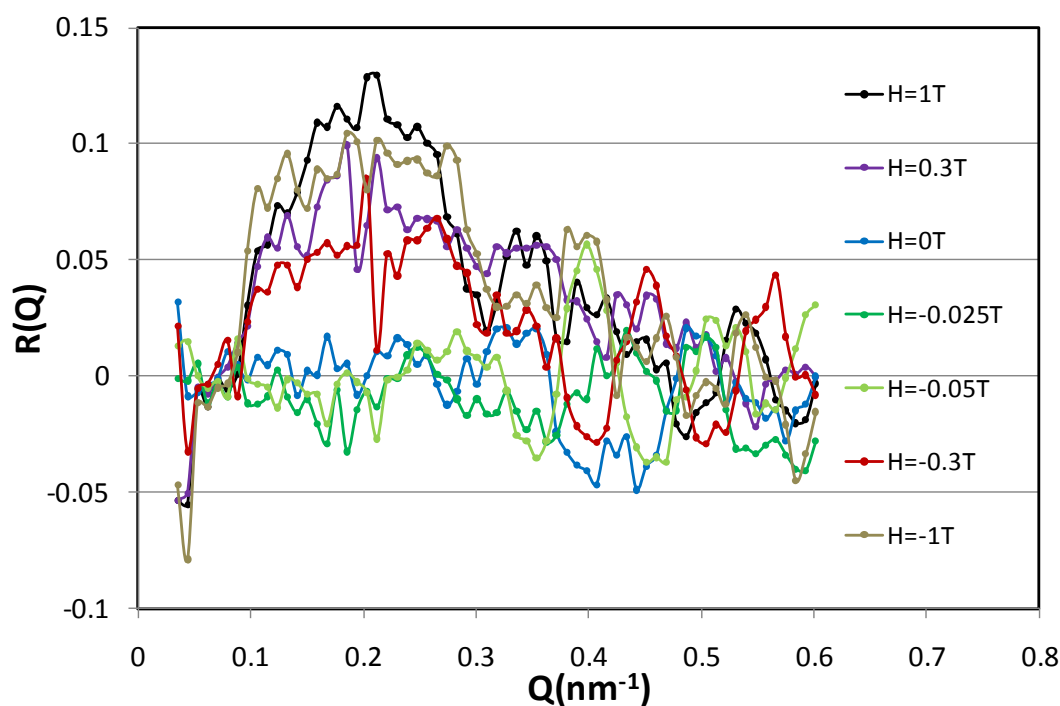
Figure 9.34: Evolution of the ratio function $R(Q) = \triangle I(Q)/I(Q)$ of the Co nanowires made at $pH = 5.75$ for different values of the applied magnetic field H
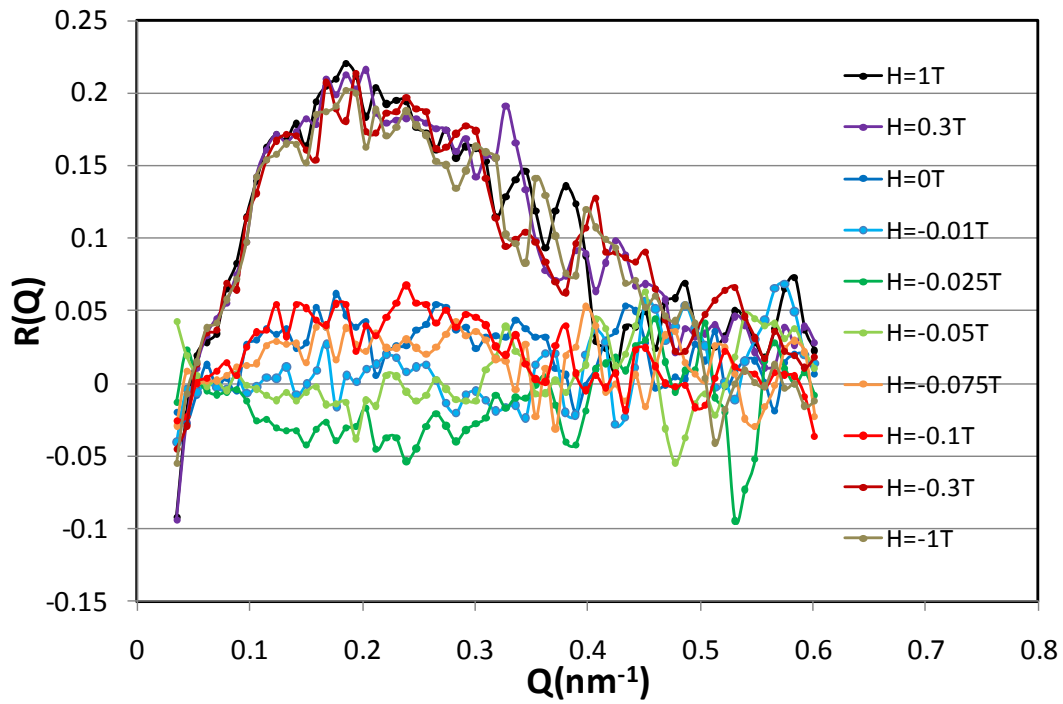
Figure 9.35: Evolution of the ratio function $R(Q) = \triangle I(Q)/I(Q)$ of the Co nanowires made with SCN for different values of the applied magnetic field H
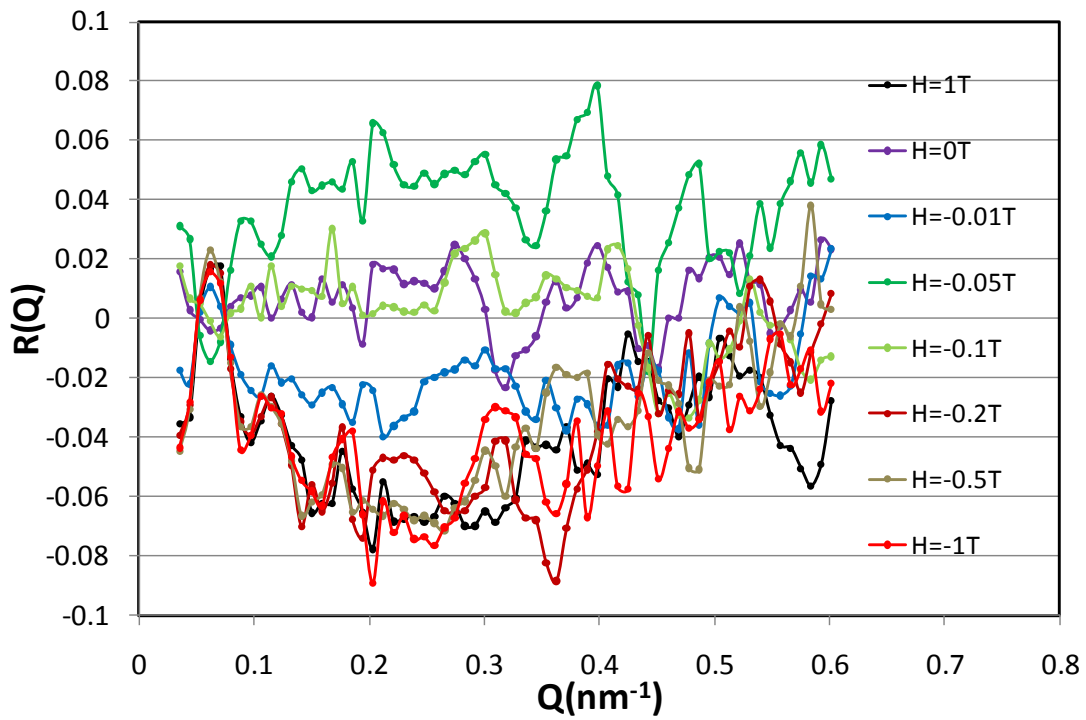
Figure 9.36: Evolution of the ratio function $R(Q) = \triangle I(Q)/I(Q)$ of the Ni nanowires at $T = 250\,\mathrm{K}$ for different values of the applied magnetic field H

In the following, I discuss the qualitative information that can be deduced from the results of the Figure 9.33-9.36.

Let's consider the ideal case where the magnetization is homogeneous inside the wires (see Figure 9.37(a) and (b)). In this case, the component $M_\perp$ measured by SANS is exactly the magnetization along the wires. The geometrical form factor $F_N(Q)$ and the magnetic form factor $F_M(Q)$ are thus strictly proportionnal: $F_M(Q) = \alpha F_N(Q)$. Thus the asymmetry ratio writes:

$$R(Q) = \frac{2P\alpha F_N^2(Q)}{(1+\alpha^2)F_N^2(Q)} = \frac{2P\alpha}{(1+\alpha^2)}$$

In such a case, the asymmetry ratio should thus be constant. This obviously contradicts the measurements presented in Figure 9.33-9.36. It is thus necessary to consider complex magnetic configurations in the wires which either do not match the shape of the wires or present correlations between wires.

For low magnetic fields, the asymmetry ratio $R(Q)$ is globally small and close to zero. From Eq 9.36, this can only originate from the fact that the magnetic form factor $F_M(Q)$ becomes very small or even close to zero since it is the only parameter which can evolve while a magnetic field is applied. This suggests that very small magnetic domains (at the scale of the nanowire, i.e. $20\,nm$) are formed. If long magnetic domains were formed, such as head to head domains along the wires, this would give rise to a finite magnetic contrast in the measured Q-range.

When large magnetic fields, enough to saturate the sample, are applied, the asymmetry ratio grows which corresponds to the apparition of a magnetic contrast. However, this contrast is not constant as a function of Q which suggests that the magnetization distribution does not follow the geometry of the wires (see Figure 9.37(c)).

The simple situation where one assumes that the magnetization of the wires is restricted in a reduced part of the wires, either because the wires edges are rough or because the outer shell of the metallic wires are oxidized (see Figure 9.38) does not allow to reproduce even qualitatively the observed asymmetry ratios presented in Figures 9.34-9.37. Presently, these results strongly indicate that the stray field between the nanowires has to be taken into account in the analysis of Polarized SANS experiments (see Figure 9.37 (d)). In SANS experiments, the influence of the stray field is usually neglected despite no real theoretical justification. Some simulations performed with the FEMM (Finite Element Method Magnetics) software on nanowires with a diameter of 10nm and a length of 100nm clearly indicate that the stray field cannot be neglected in the calculation of the induction for assembly of nanowires (see Figure 9.38). Figure 9.37 (d) suggests that there must be variations of the intensity of the stray field between the nanowires which may affect the magnetic contrast. Recent experiments performed on similar systems but with a magnetic field transverse to the nanowires also exhibits results which can not be explained with usual arguments [Nap2009]. At this stage, more accurate simulations are requested in order to show the role of the stray field in analysis of Polarized SANS experiments.
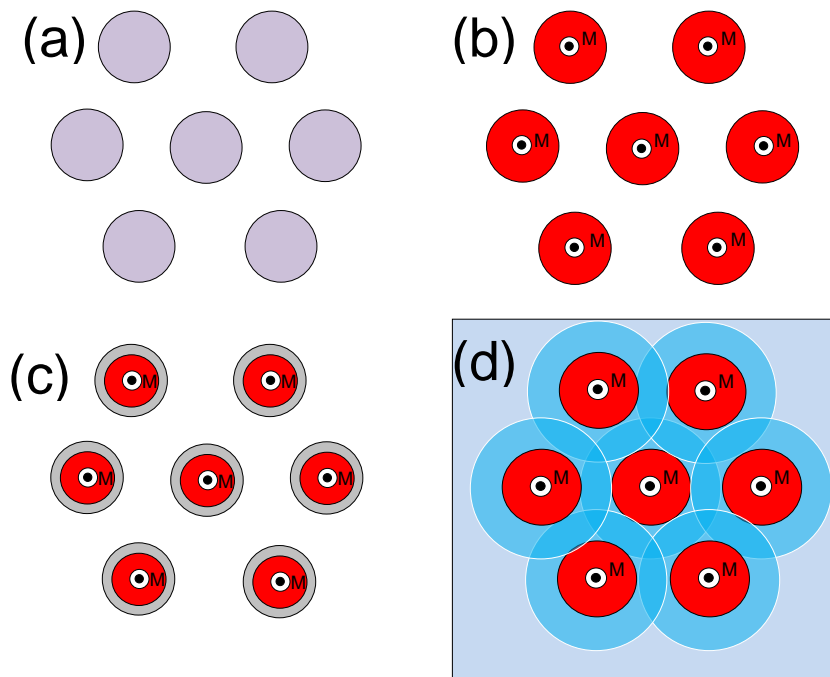
Figure 9.37: (a) hexagonal assembly of nanowires; (b) Ideal case where the magnetization is considered homogeneous in the wires. (c) Non ideal case were only the core of the wires is magnetic. (d) Influence of the demagnetizing field taking into account.
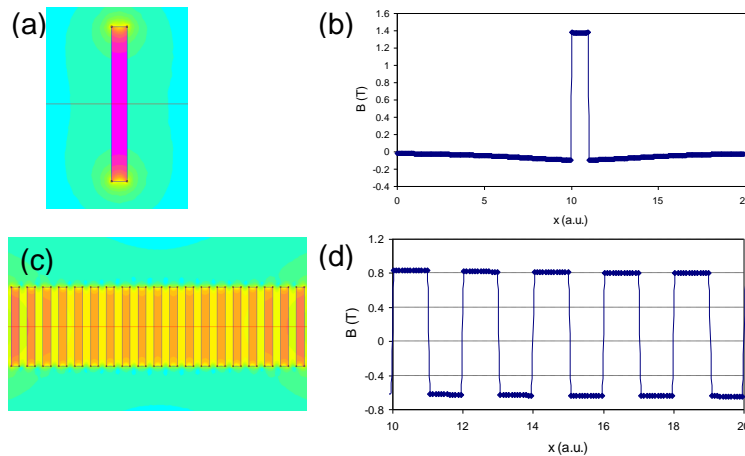
Figure 9.38: (a) Stray field generated by an individual nanowire with a diameter of 10nm and a length of 100nm. The simulation has been performed with the FEMM software. (b) Profile of the induction. It is neglected for an individual nanowire. (c) Stray field generated for an assembly of nanowires with a diameter of 10nm and a length of 100nm. (d) The profile of the induction indicate that the stray field cannot be neglected in the case of an assembly of nanowires.

9.5 Conclusion

To summarize, these measurements on arrays of nanowires have shown that the Ewald sphere effects are very large so that these types of samples must be considered as equivalent to single crystals. The orientation effects can be modelled quantitatively by using the SpectraProcessor software. I have shown that in the non polarized case, it is possible to disentangle the structure factor of the array and the form factor of a single wire. In the polarized case, the measurements allow to qualitatively discuss the micromagnetic behavior under magnetic field but it has until now not been possible to give a detailed description of the magnetic form factor of a single wire.

Conclusion

The aim of this thesis was to study, by using magnetometry, micromagnetic modeling, and Polarized Small Angle Neutron Scattering (PSANS), the magnetic behaviour of magnetic anisotropic nano-objects synthesized via the polyol process. This process provides a large variety of $Co_{1-x}Ni_x$ anisotropic nanowires with a diameter and a length which are respectively in the ranges $7-20$ nm and $100-300$ nm. These magnetic nanowires, because of both their high aspect ratio and their excellent crystallinity, exhibit large shape and magnetocrystalline anisotropies.

I have first shown that by properly ordering these objects, either in liquid solutions or in polymer matrices, it is possible to achieve very large coercive fields and remanence magnetizations (up to $H_C = 0.9$ T and $M_R = 0.95\, M_S$ at 150 K). I have modelled this behavior within the Stoner Wohlfarth model (Chapter 3). This made it possible to disentangle the shape anisotropy and the magneto-crystalline anisotropy contributions to the coercivity. I have shown that both these anisotropies contribute with the same weight to the properties of the wires.

These excellent properties suggest that composite materials based on these wires could be used to fabricate permanent magnet materials. I have studied their high temperature behavior (up to 500 K) and I propose that these materials could compete with existing permanent magnetic materials at high temperature (up to $300°C$) (Chapter 6).

I have shown that the magnetic behavior is strongly controlled by the detailled shape of the wires and especially by the shape of the wire extrmities (Chapter 4). The formation of spherical or conical tips at the end of the wires can lead to a curling reversal mode which promotes the magnetization reversal in the wires when these tips are large enough. Drops in the coercivity as large as 3 kG can be induced. This was demonstrated by micromagnetic simulations and illustrated with bulk magnetic measurements on different types of objects (cylinders, dumbbells, diabolos).

Such nanowires are prone to oxidation which have proved to strongly affect their magnetic properties at low temperature ($T < 200$ K). I have shown by neutron diffraction that a CoO shell forms around the wires. This shell orders anti-ferromagnetically at 230 K and strongly modifies the magnetic properties of the wires at low temperatures via the exchange bias effect. In particular it leads to a drop of the coercive field (of up to 2 kG) in the temperature range (100 K $- 200$ K). I have proposed a model in which the superparamagnetic fluctuations of the antiferromagnetic shell play a key role in this phenomenon. This is supported by micromagnetic simulations. This behaviour is specific to the 1D geometry of cylinders.

I have also used Polarized Small Angle Neutron Scattering to study both nanowires dispersed in solution and ordered arrays of nanowires. I have shown that the technique of PSANS can provide information about the aggregation process in solution of wires subject to an applied field. This can be used to study the fabrication process of composite materials. In the case of arrays of ordered nanowires, I propose that PSANS makes it possible to study the inner magnetic configurations of the nanowires and their magnetic correlations.

Perspectives

This work has tried to show that, in order to develop and study magnetic nano-objects, complementary expertises are required. For instance, organic chemistry could allow to improve the structural and magnetic properties of the objects, physico-chemistry could lead to a better dispersion of the particles in polymers, metallurgy is requested to fabricate composite materials made of these objects, magnetism may give a better understanding of their properties and the way to improve them or expertises in instrumentation could impulse the development of tools such as Polarized Small Angle Neutron Scattering to probe their magnetic properties. The aim of this section is therefore to point to directions in which improvements in the study of these magnetic nano-objects could be made: How to improve their magnetic or structural properties? How to fabricate samples made with such nanowires? How to promote applications based on their use? How to probe in more details their properties?

To make these directions clearly visible, the perspectives are divided into four main stakes: 1) Improving the intrinsic properties of the nanowires, 2) Fabricating composite materials made with such objects, 3) Understanding the details of their magnetic properties and 4) Promoting the use of Polarized Small Angle Neutron Scattering to study magnetic nanowires.

Improving the intrinsic properties of the nanowires

In a first step, two research orientations may be followed: 1) improving the intrinsic magnetic properties of the nanowires and 2) improving their temperature stability. This part of the work is the task of our colleagues chemists.

To improve the intrinsic magnetic properties of these objects, the most promising route might be to consider the fabrication of similar materials based on iron which would both provide a higher saturation magnetization (and thus a larger shape anisotropy) and a cheaper cost for large scale fabrication. The challenge is however very tough since Fe crystallizes in cubic phase which makes the chemical growth of anisotropic Fe nanoparticles harder. Nevertheless one may first consider coating the existing Co nanowires with a Fe shell.

As for the temperature stability of these objects, it is related to both their structural and magnetic properties. A first stake is to prevent the nanowires from sintering at high temperatures. It requires to modify the nanowire surface by, for example, covering it with an oxide or a non magnetic material or to well separate the objects from each other. Furthermore, the magnetic properties of Co nanowires are strongly affected at high temperature by the singular temperature dependence of the Co magnetocrystalline anisotropy. It forces to consider other materials. Once again, the use of Fe could provide a solution to improve the magnetic properties at high temperature.

Fabricating composite materials made of nanowires

The objective is here to fabricate permanent magnets made of nanowires. The key issue is to align the nanowires in a suitable matrix. However, the alignment of the nanowires is far from being easy. Applying an homogeneous external magnetic field is indeed not sufficient. The difficulty stems from the agglomeration of the objects in solution. During

this study, after many attempts, I observed a good stability of $Co_{80}Ni_{20}$ nanowires in the dimethylacetamide (DMAC) solvent. It is still necessary to find a suitable solvent for Co nanowires. It is also imperative to modify the nanowires surface in order to favor their dispersion.

In this context, the research project, MAGAFIL, financed by the Agence Nationale de la Recherche (ANR) aims to fabricate composite materials made with aligned nanowires. It is based on a close collaboration between four laboratories: the Laboratoire Léon Brillouin (LLB, IRAMIS-CNRS) which uses its expertise in magnetism to support the magnetic characterization of the samples and to provide information to improve their synthesis, the Interfaces, Traitements, Organisation et DYnamique des Systèmes (ITODYS, Université Paris Diderot) laboratory and the Laboratoire de Physique et Chimie des Nano-Objets (LPCNO, INSA Toulouse) which both focus on the incorporation of the magnetic nanowires in a polymer host and the Laboratoire des Propriétés Mécaniques et Thermodynamiques des Matériaux (LPMTM, Université Paris 13) which works on dispersing and aligning the objects in well-chosen metals.

To incorporate and align the nanowires in a polymer host, the nanowire surface must be modified in order to maximize the nanoparticle/polymer interaction. It can consist in grafting surfactants. However, the surfactants tested during this work such as laurate did not conduct to satisfactory alignment of the nanowires in the polymer matrices. The strategy which is now developed is based on the Atom Transfer Radical Polymerization (ATRP). This process allows to form uniform polymer chains at the surface of the objects so that they become covered with a polymer brush which tends to favor their dispersion in a polymer host. This method has proved to be an efficient and versatile method [Li2007]. It must be underlined that the preparation of metal (Fe) surfaces coated with polymers by ATRP has been successfully developed at ITODYS [Mat2005].

The other strategy to fabricate composite materials made with such nanowires consists in dispersing and aligning them in metals using high pressure and high temperature equipments. It requires a metal with a low melting point such as Sn ($T_F = 232°C$) or Pb ($T_F = 327.5°C$).

Finally, it must also be precised that the LPMTM owns a Hot Isostatic Pressure (HIP) equipment which is devoted to the consolidation of powders in order to obtain dense materials. Our project consists in adding a permanent magnet in this equipment in order to compress nanowire powder under a magnetic field so that the nanowires will be aligned. Such compact aligned powders should exhibit both large coercivity and remanence.

Understanding the detailled magnetic properties

This work opens the way to three main research orientations: 1) the role of the nanowire geometry in the magnetization reversal, 2) the influence of the oxidation on their magnetic properties and 3) the behaviour of interacting wires.

The polyol process has been improved for the last two years so that it is now possible to provide nanowires exhibiting a whole set of shapes. One of the crucial parameters in the geometry of the synthesized nanowires is the temperature ramp during the heating of the butanediol solution. A temperature ramp of $3.5°C.min^{-1}$ leads to average diameter and length of respectively 35 nm and 140 nm *i.e.* aspect ratio of 4 while a temperature ramp of $7°C.min^{-1}$ leads to average diameter and length of respectively 17 nm and 330 nm

i.e. aspect ratio of 19. Therefore, this large range of aspect ratios should allow to fully characterize the role of the geometry in both the magnetization reversal and the influence of the oxide shell formation. A systematic study is now required to more accurately identify the role of the aspect ratio and of the detailed shape in the magnetic properties of the nano-objects. This systematic study may be supplemented, if necessary, by a mapping of the magnetization configuration via electron holography by Christophe Gatel (CEMES, Toulouse). This can evidence, experimentally, the role of the tip shape in the nanowire magnetization.

Furthermore, one of the main results of this work is the modification of the nanowire magnetic properties at low temperature when they oxidize. Many experimental measurements have been performed by magnetometry but there still remains to understand the role of the CoO grain sizes. This is why I started a collaboration with Pr. Jean-Philippe Ansermet. As a matter of fact, V. Scarani and Pr. Ansermet performed Nuclear Magnetic Resonance (NMR) experiments in 2000 [Sca2000] which showed that oxidized Co nanowires exhibit a temperature dependence of the spin-lattice relaxation which evidenced the thermal fluctuations of the uncompensated moments of the CoO grains at the surface of the nanowires. Such an experiment is thus perfectly adapted to the samples which have been presented in Annexe III and which exhibit different degrees of oxidation.

These magnetic characterizations could be complemented by electrical characterization and magneto-transport measurements. I only had the opportunity to perform very few magnetoresistance measurements which showed very limited effects (3% of magnetoresistance at room temperature). However, once a better control of the oxidation is achieved, one may expect spectacular tunnel magnetoresistive effects similar to [Tan2007].

Moreover, in order to better understand experimental measurements on these nanowires, micromagnetic simulations have been performed using the Nmag software. What is at stake here is to probe the role of interactions in the magnetic properties of nanowires. This problematic is presently the post-doc work of Fatih Zighem at the Laboratoire Léon Brillouin.

Besides these three research projects, two other work directions are intended to characterize the dynamic magnetic modes inside the nanowires.

The first one is based on a collaboration with Michel Viret (SPEC, CEA Saclay) and consists in isolating a nanowire to make a single-nanowire electrical contact. This should allow to obtain information about the magnetization configuration and the magnetic excitations inside the objects. This could also give evidence for magnetoresistance effects due to the interface between the CoO oxide shell (antiferromagnetic) and the Co core (ferromagnetic).

The second project consists in performing Inelastic Neutron Scattering (INS) using Time of Flight spectrometers to study the quantized spin wave modes in magnetic nanowires. Recent Brillouin Light Scattering [Rou2001, Wan2002] have indeed demonstrated the existence of transverse spin waves modes controlled by the reduced diameters and saturation magnetization in the energy range $0 - 0.1\,\mathrm{meV}$. We here propose to perform INS experiments to probe a larger Q-range. It will consist in probing spin-wave excitations in well-defined and aligned thin $(7 - 15\,\mathrm{nm})$ nanowires at zero field and with an applied magnetic field along the wire axis. The magnetic field will be strong enough (above $1\,\mathrm{T}$) to ensure that we can explore the regime where the spin waves mode energies increase linearly with the field [Tar2006, Tar2005]. We made some attempts on the $IN6$

spectrometer at the Institut Laue-Langevin. Two difficulties appeared: the presence of hydrogen at the surface of the nanowires which led to a large incoherent "background" scattering which is a great handicap to make inelastic signals visible and the difficulty in aligning the nanowires. Consequently we still need to progress in the fabrication of the samples. The fabrication of pressed aligned nanowire powders or composite materials made with aligned nanowires in Sn or Pb (which are metals adapted to neutron scattering) could make possible such a study. Another possibility may also be the study of Co nanowires included and aligned in alumina membranes. However, because of the small quantities of matter, it requires to superpose tens of membranes which would require a lot of work.

That is why a good alternative could consist in probing the magnetic excitations inside nanowires via Spin-Polarized STM. During the European Workshop on Self-organized nanomagnets which took place in Aussois in 2009, Wulf Wulfhekel from the Physikalisches Institut in Karlsruhe presented some interesting results about this recent technique. It is based on the spin transfer torque: the injection of a polarized electric current creates a collective excitation of the spins in the ferromagnet. Via Inelastic Scanning Tunneling Spectroscopy (ISTS), magnon dispersions and lifetimes in thin Mn, Co and Ni films have been obtained with precision similar to inelastic neutron scattering [Gao2008]. This technique might be applied to the study of individual nanowires.

Promoting the use of Polarized Small Angle Neutron Scattering to study magnetic nanowires

The Polarized Small Angle Neutron Scattering studies performed during this work emphasized different limitations to investigate the nanowires synthesized via a polyol process, mainly (i) the difficulty to align them and (ii) the presence of hydrogen at their surface. This has prevented the realization of quantitative PSANS studies on such nanowires. The collaboration with LPMTM could provide aligned nanowires dispersed in Sn or Pb matrices which exhibit low scattering cross sections and are therefore well adapted for such studies. In the meantime, I intend to align the nanowires as well as possible in a polymer matrix under a magnetic field and then to stretch the polymer film in order to promote the nanowire alignment. In situ film deformation equipment is available at the Laboratoire Léon Brillouin. It is often used to study the strengthening of polymer films loaded with silica nanospheres and the role of stretching onto the mechanical properties [Jou2009].

Nevertheless the best PSANS results have been obtained on Co and Ni nanowires aligned in alumina membranes. We notably observed an inversion of the polarized signal around the minimum of the spectrometer Q-range. It would thus be very interesting to investigate the lower Q values which is not possible for the moment on the PAPYRUS spectrometer. The idea therefore consists in investigating a sample exhibiting larger distances between the objects. This could be part of a more general work consisting in studying a set of membranes with different distances between the pores in order to probe the exact role of this parameter.

Furthermore, it must be precised that in the near future, it will be possible to probe smaller Q-range with PSANS. As a matter of fact, Grégory Chaboussant and Sylvain

Désert are currently developing PA20 (Petits Angles 20 mètres) which is a new SANS spectrometer with polarization option. It should allow to probe Q-values from $2 - 3 \times 10^{-4} \mathring{A}^{-1}$ up to $0.5 \mathring{A}^{-1}$. This spectrometer will make PSANS studies at the Laboratoire Léon Brillouin much easier to perform by having a far more versatile spectrometer.

From the previous discussions, it can be seen that these nanowires offer a wealth of research opportunities in magnetism.

Part III

Annexe: Complementary study on the Exchange Bias effect in nanowires

Chapter 10

Exchange Bias effect in nanowires depending on the degree of oxidation

In chapter 5, the exchange bias effect in nanowires has been investigated. The nanowires were dried in an oven until passivation occurs. This annexe considers the role of the CoO thickness in the Exchange Bias phenomenon. From an initial dialcohol solution of nanowires, three different batches of nanowires exhibiting three different degrees of oxidation have been investigated. The investigated objects are Co nanowires exhibiting a diameter $d = 18\,$nm for a length $L = 250\,$nm. The three investigated samples were extracted from the same original butanediol solution of nanowires but were oxidized differently:

1. The first sample was washed several times with ethanol, then dried in a oven at $60°C$ during three days and finally dried in the air during four other days. Then it was covered with a non magnetic varnish to prevent the nanowires from oxidation. The mass of nanowire powder was $5.3\,$mg. This sample is named "Sample A".

2. The second one was also washed several times with ethanol and then dried in the air during one week. Then it was also covered with a non magnetic varnish. The mass of nanowire powder is $2.3\,$mg. This sample is named "Sample B" and is expected to be less oxidized than Sample A.

3. The last one was a few mL of the initial butandiol solution containing the nanowires. It was however in contact with air during several weeks so that it was not perfectly preserved from air. A very slight oxidation can thus be expected. This sample is named "Sample C". Note that comparisons with the above samples can only be made below $200\,$K since above this temperature the butandiol is no longer frozen and magnetometry measurements cannot be performed.

Different kinds of measurements have been performed on these samples and are presented in this section: hysteresis cycles and Field Cooled (FC)/ Zero Field Cooled (ZFC) curves.

10.1 Hysteresis cycles

To quantitatively compare the hysteresis cycles of the different samples, the quantity of magnetic nanowires in each sample needs to be determined. The difficulty is to assess the

quantity of organic matter. This has been evidenced by the neutron measurements which showed large incoherent scattering - due to the presence of hydrogen- even after heating under vacuum at $T = 130°C$ during several days.

For Sample A, if we first assume that the mass of $5.3 \, \text{mg}$ corresponds to only Co and CoO. If the oxide shell thickness is assumed to be about $1.5 \, \text{nm}$, the total mass comes for three quarters from the Co cores and for the last quarter from the CoO shells. Moreover at $240 \, \text{K} - 260 \, \text{K}$, the temperature is above T_N (see Section 5.1.1) and the contribution to the hysteresis cycle only stems from Co. At $T = 240 \, \text{K}$, $M = 2.32 \times 10^{-4} \, \text{A.m}^2$ for $N = \frac{m_{Co}}{M_{Co} N_A} = 4.06 \times 10^{19} \, Co$ atoms. It implies that $M = 0.62 \, \mu_\text{B}/\text{at}$ which is about the third of the Co bulk value ($1.7 \, \mu_\text{B}/\text{at}$). This confirms that there probably remains a significant amount of organic matter at the surface of the nanowires.

Sample B has not been totally dried so that there remains more organic matter than for Sample A. While the sample mass is about twice smaller, its magnetization is about ten times smaller. this suggests that Sample B consists mostly of organic matter and solvent. An absolute determination of the samples magnetization is thus impossible to perform.

In the following, we make the assumption that the level of surface oxidation does not modify the saturation magnetization of the Co core at high temperature since there is no interaction between the Co core and the CoO shell. the hysteresis curves of the different samples have thus been normalized by the magnetization measured at high temperature ($250 \, \text{K}$) and high field ($5 \, T$) (see Figure 10.1). The normalization factors were then kept constant when the temperature was decreased.

The samples have been cooled down to $T = 2.5K$ under a magnetic field $H = 5 \, \text{T}$. Then hysteresis cycles have been measured while increasing the temperature from $5 \, \text{K}$ to $300 \, \text{K}$. At $T = 240 - 260 \, \text{K}$, the samples A and B saturate above $H = 3 \, \text{T}$. In the case of Sample C, the nanowires in solution have been field cooled which explains the square shape of the hysteresis cycle indicating that the nanowires are aligned.

Below $T = 200 \, \text{K}$, the hysteresis cycles start to be different for the three samples. The hysteresis cycles of Sample A remain quite well saturated at $H = 5 \, \text{T}$. The major changes with decreasing temperatures occur for the samples B and C which are a priori less oxidized. Both the coercivity and the saturated magnetization vary in large proportions with decreasing temperatures for these samples. The coercivity drops at low temperatures while the saturation magnetization significantly increases. Another interesting feature is that the variations of coercivity and saturated magnetization for Sample C occur for lower temperatures than for sample B but seem to make up for their lag at very low temperatures ($T = 2.5 \, \text{K}$). Furthermore, below $100 \, \text{K}$, the hysteresis cycles of the samples B and C exhibit a positive slope at large fields which increases in large proportions with decreasing temperature. This positive slope could stem from the superparamagnetic fluctuations of the antiferromagnetic grains of the oxide shell. Finally, a "wasp" shape can also be seen at low fields for Sample B when the temperature is below $10 \, \text{K}$. The shape of the hysteresis cycles will be more deeply analyzed later.
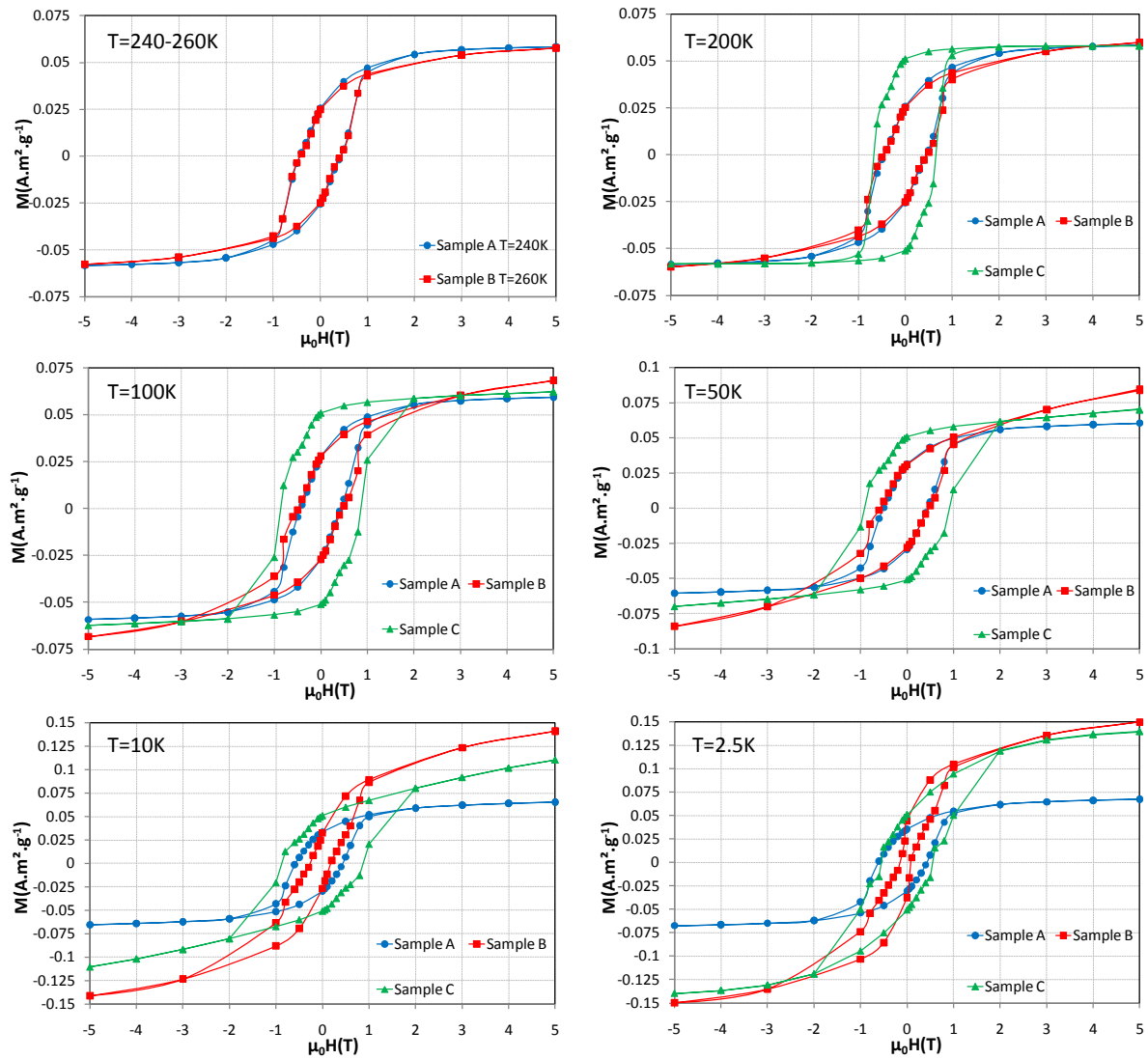
Figure 10.1: Hysteresis cycles for samples A, B and C at different temperatures. Note that at $T = 240 - 260 \, \text{K}$, butandiol is liquid so that the measurement can not be performed for Sample C.

10.2 Temperature dependence of H_C and H_E

The temperature dependence of the coercive field H_C and the exchange field H_E for the three samples, obtained from the hysteresis cycles, are presented in Figure 10.2.

For Sample A, the temperature dependence of H_C and H_E is similar to the one observed in Section 5.1.2. The Exchange Bias temperature is $T_{EB} = 100 \, \text{K}$ and $H_E = -815 \, \text{Oe}$ at $T = 5 \, \text{K}$. As for H_C, there is still a coercivity drop with decreasing temperature from $T = 200 \, \text{K}$ down to $T \approx 120 \, \text{K}$. However, this coercivity drop is smaller than the one reported in Section 5.1.2.

The temperature dependence of H_C and H_E for Sample B is very different from Sample A and from the ones reported in Section 5.1.2. The Exchange Bias temperature T_{EB} is the same as for Sample A (T_{EB} 100 K). For $T < T_{EB}$, H_E increases with decreasing

temperature from T_{EB} downto 20 K as expected but then decreases from 20 K ($H_E = -575$ Oe) down to 7.5 K ($H_E = -230$ Oe) and finally increases again down to 2.5 K ($H_E = -325$ Oe). The exchange field drop from 20 K down to 7.5 K is very unexpected and no similar report in the literature could be found.

As for H_C, going from 200 K down to 100 K, there is no longer a coercivity drop but rather a coercivity plateau. Below T_{EB}, H_C begins to follow the same variations as for Sample A. Nevertheless below 50 K, a drastic coercivity drop occurs since $H_C = 5230$ Oe at $T = 50$ K and 1110 Oe at $T = 5$ K. This represents a giant coercivity drop of about 80%. Then H_C slightly increases again from 5 K down to 2.5 K. The coercivity and exchange field drops seem to be nearly concommitant in temperature like their rebound at very low temperature.
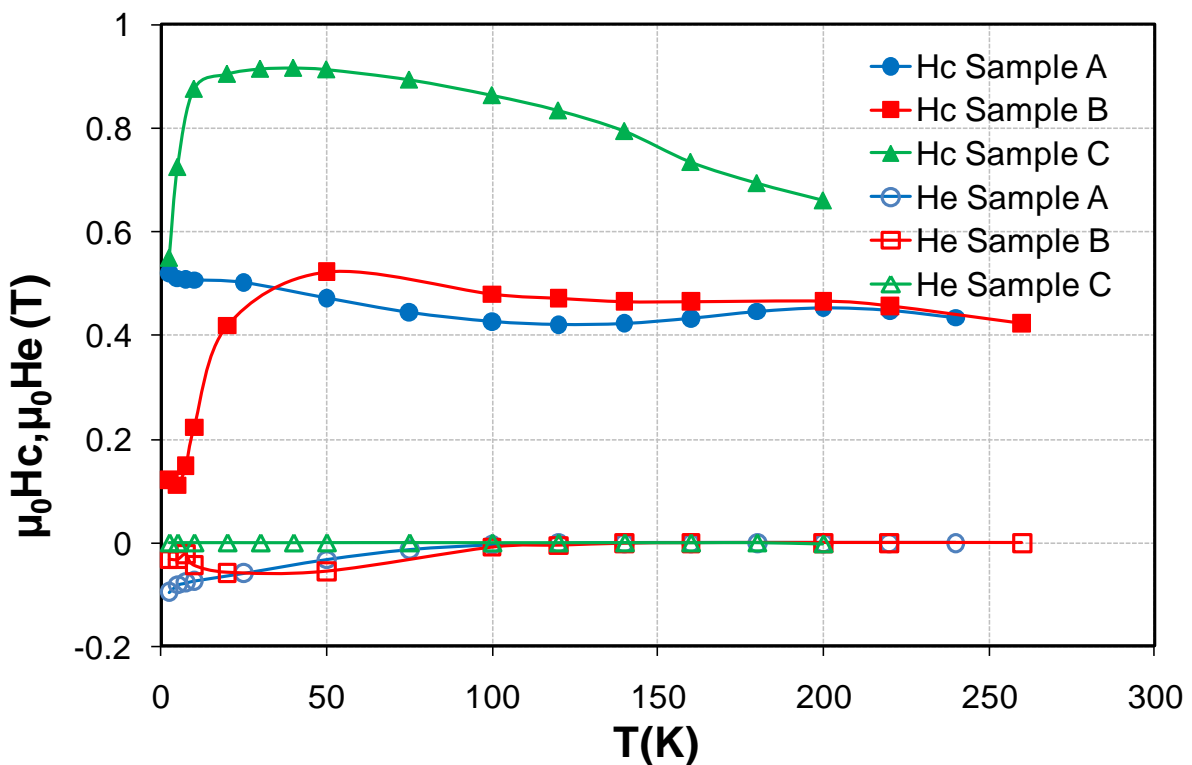
Figure 10.2: Temperature dependence of H_C and H_E for samples A, B and C after a field cooled procedure: a magnetic field $H = 5$ T has been applied while decreasing the temperature down to 2.5K, then the measurements have been performed with increasing temperatures. Note that H_C is much larger for Sample C since the nanowires aligned themselves in the butandiol solution during the Field Cooled procedure.

In order to have a better understanding of the results for Sample B, the Field Cooled (FC) and Zero Field Cooled (ZFC) procedures have been compared (see Figure 10.3). As expected, the exchange field H_E is equal to zero for all temperatures under the ZFC procedure. The ordered antiferromagnetic CoO do not indeed show any preferential orientation. The most striking feature of the comparison between the ZFC and FC measurements is the similitude between the temperature dependence of H_C. It implies that the blocked antiferromagnetic CoO grains play no role in the coercivity drop of Sample B.
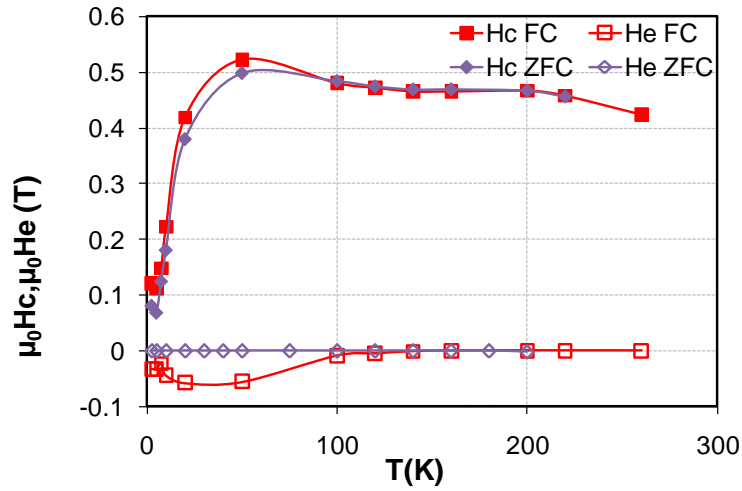
Figure 10.3: Comparison between the temperature dependencies of H_C and H_E of Sample B for a zero Field Cooled procedure and a Field Cooled one under $H = 5\,\text{T}$. The measurements are performed with increasing temperature from 2.5 K up to 260 K.

As for Sample C, Figure 10.2 shows that H_E is equal to zero for all the temperatures. The large coercivity which has been measured for this sample stems from the alignment of the nanowires in the solution during the Field Cooled procedure. However a large coercivity drop is observed from 10 K ($H_C = 8770\,\text{Oe}$) down to 2.5 K ($H_C = 5520\,\text{Oe}$) while there is no coercivity plateau at higher temperatures. Since the coercivity drop at low temperature looks like the one of Sample B, the first question consists here to determine whether the nanowires of this sample are oxidized or not. Figure 10.4 compares $H_C(T)$ for Sample C and non-oxidized nanowires (previously shown in Figure 5.3) . The temperature dependence is similar from room temperature down to 20 K where the coercivity drop sets in for Sample C. This drastic coercivity drop, occuring at a temperature lower than in the case of Sample B, suggests that if the nanowires of Sample C are oxidized, the *CoO* grains are smaller than the ones of Sample B.

Sample	oxidation	T_{EB}	H_{EB}	H_C
A	dried in a oven (60°C during 3days)	100 K	monotonous increase with decreasing T	drop from T_N down to T_{EB}
B	dried in the air during one week	100 K	decrease from $T \approx 50\,\text{K}$ down to $T = 7.5\,\text{K}$	large drop from $T \approx 50\,\text{K}$ down to $T = 5\,\text{K}$
C	very slight oxidation expected	-	$H_{EB} = 0$	large drop from $T \approx 10\,\text{K}$ down to $T = 2.5\,\text{K}$

Table 10.1: Characteristics of Samples A, B and C.

The comparison between samples A, B and C leads to several questions (see Table 10.1):

- Why is the Exchange Bias T_{EB} temperature identical for the samples A and B?

- Why is there -for Sample B- a plateau instead of an expected coercivity drop from $200\,\mathrm{K}$ down to T_{EB}?

- Is the coercivity drop observed for Sample B and C at low temperatures also coming from the superparamagnetic fluctuations of the antiferromagnetic grains of the oxide shell?

- How is it possible to explain the exchange field drop with decreasing temperature from $20\,\mathrm{K}$ down to $7.5\,\mathrm{K}$ for Sample B?

- What is the reason for the rebound of H_C and H_E at very low temperature for Sample B?

- Why no bias is observed for Sample C if it also oxidized?

The challenge is therefore to determine whether these phenomena are, like the coercivity drop of Sample A at high temperature, linked to the superparamagnetic fluctuations of the antiferromagnetic grains inside the oxide shell.
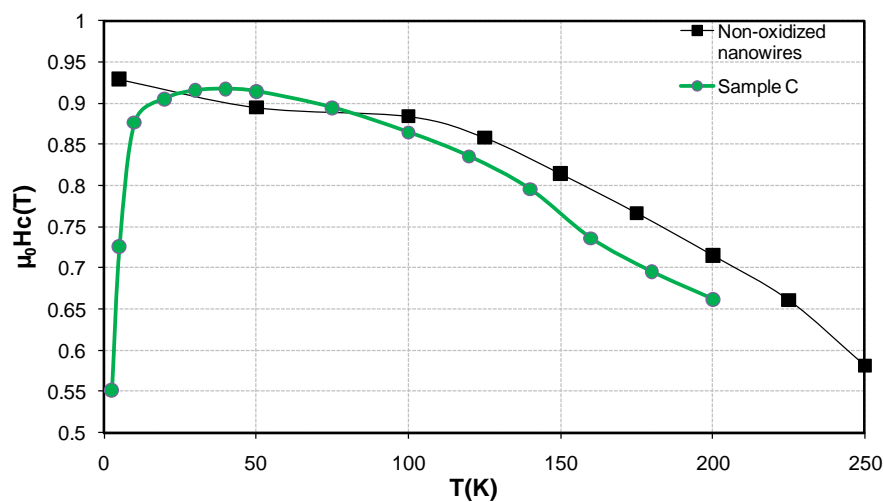
Figure 10.4: Comparison between the temperature dependence of H_C for Sample C and non-oxidized nanowires.

10.3　Temperature dependence of saturation and remanent magnetizations

The temperature dependence of the saturation magnetization M_S is reported for each of the three samples (see Figure 10.5). In fact, the term of "saturated magnetization" is not appropriate. The measurements were made at $H = 5\,\mathrm{T}$ but the hysteresis cycles (presented in Figure 10.1) showed that the samples B and C were not saturated at low temperature for $H = 5\,\mathrm{T}$. However, the temperature dependence of M_S or $M(H = 5\,\mathrm{T})$ gives some information about the net magnetization. An increase of net magnetization with decreasing temperature can stem from:

1. the uncompensated moments of antiferromagnetic particles which become blocked with decreasing temperature .

2. some phenomena like spin glass. It can be imagined that the blocked antiferromagnetic grains keep the ferromagnetic moments fixed because of exhange interaction.

For Sample A, at $T = 2.5\,\mathrm{K}$, we observe an increase of $M(H = 5\,\mathrm{T})$ of about 15% compared to the value at high temperature (above T_N). The most striking feature comes from the two other samples which are less oxidized. They exhibit a very large increase of $M(H = 5\,\mathrm{T})$ with decreasing temperature: for these samples $M(H = 5\,\mathrm{T})$ is about 2.5 times higher at $T = 2.5\,\mathrm{K}$ than at room temperature.

Furthermore, the increase of $M(H = 5\,\mathrm{T})$ occurs at lower temperature for Sample C than for Sample B. Indeed the CoO grains of Sample B are larger than the ones of Sample C so that they become blocked for higher temperature. However at $T = 2.5\,\mathrm{K}$, the difference of magnetization between these two samples is small. Moreover $M(H = 5\,\mathrm{T})$ increases progressively down to T_{EB} but increases much more below T_{EB} when the CoO grains begin to be blocked. The question here is to know whether the very large increase of $M(H = 5\,\mathrm{T})$ for the samples B and C can stem from only the uncompensated moments of the antiferromagnetic grains.
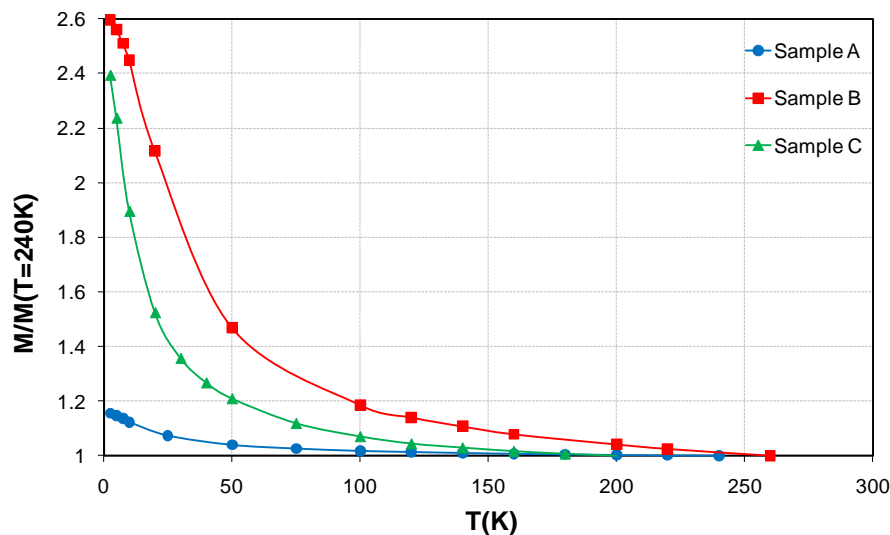
Figure 10.5: Temperature dependence of $M/M(T = 240\,\mathrm{K})$ at $H = 5\,\mathrm{T}$ for the samples A, B and C.

FC/ZFC magnetization curves have been measured to probe the configuration of the magnetic moments at $H = 0\,\mathrm{T}$. Figure 10.6 compares the FC/ZFC curves of the samples A and B. The curves are similar for both samples from room temperature down to about 10 K. The remanence ($M(\mu_0 H = 3mT)$) remains almost constant from room temperature down to 150 K. When $T \approx T_{EB}$, the remanence begins to increase. For both samples, the curves obtained after cooling the sample under $H = 5\,\mathrm{T}$ increases by 40% from 150 K down to 10 K. Moreover, we observe that the remanence of Sample A is larger than that of Sample B between 100 K and 10 K. This can be explained by the fact that the CoO grains of Sample A are larger than that of Sample B so that they will be blocked at higher temperatures.

Furthermore the main difference between samples A and B occurs below $10\,\mathrm{K}$ where the remanence of Sample B increases from 1.4 at $T = 10\,\mathrm{K}$ up to 1.95 at $T = 2.5\,\mathrm{K}$. Compared to the temperature dependence of both H_E and H_C, this large increase of the remanence for Sample B happens below 10K when H_E and H_C both rebound (see figure 10.3). This could be attributed to the blocking of very small antiferromagnetic grains exhibiting a large fraction of uncompensated moments. The question then is: can the blocking of antiferromagnetic CoO grains be the only explanation for such a drastic remanence increase?
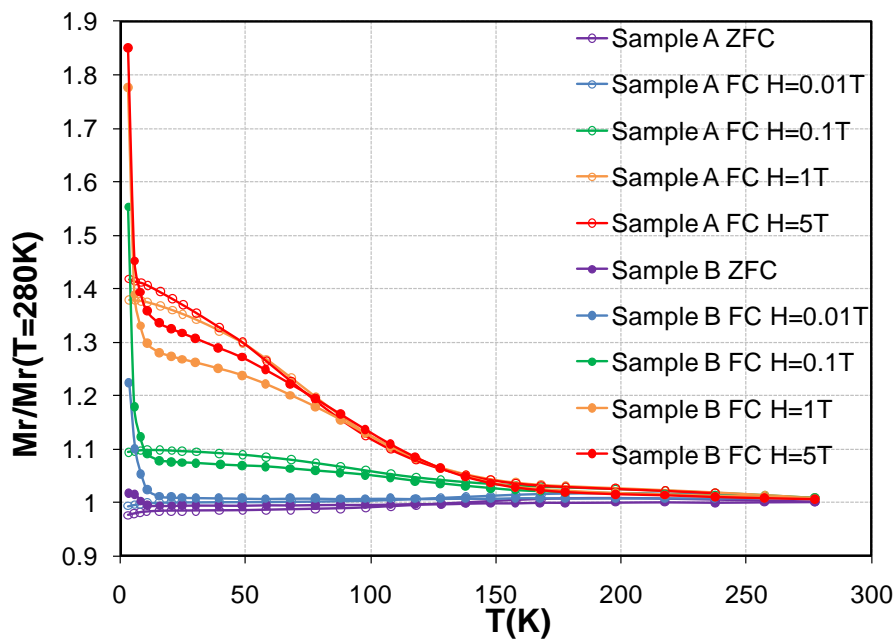
Figure 10.6: Field Cooled / Zero Field Cooled curves for both the samples A (empty circles) and B (filled circles). The curves are normalized by the value of the magnetization at $T = 280\,\mathrm{K}$.

Figure 10.7 shows the FC/ZFC of Sample C. Contrary to the measurements made on the sample A and B, the sample was cooled from only $T = 180\,\mathrm{K}$ since the butandiol has to be frozen during the whole experiment to prevent the nanowires from moving. In the FC procedure under $H = 5\,\mathrm{T}$, the remanence increases by 16% from $180\,\mathrm{K}$ down to $2.5\,\mathrm{K}$. Compared to the samples A and B, the increase of the remanence sets in at lower temperature and in slighter proportions. These measurements indicate that few CoO grains remain blocked with no external field in the temperature range $50\,\mathrm{K} - T_{EB}$. An explanation might be the very small size of the CoO grains which compose the oxide shell of Sample C.
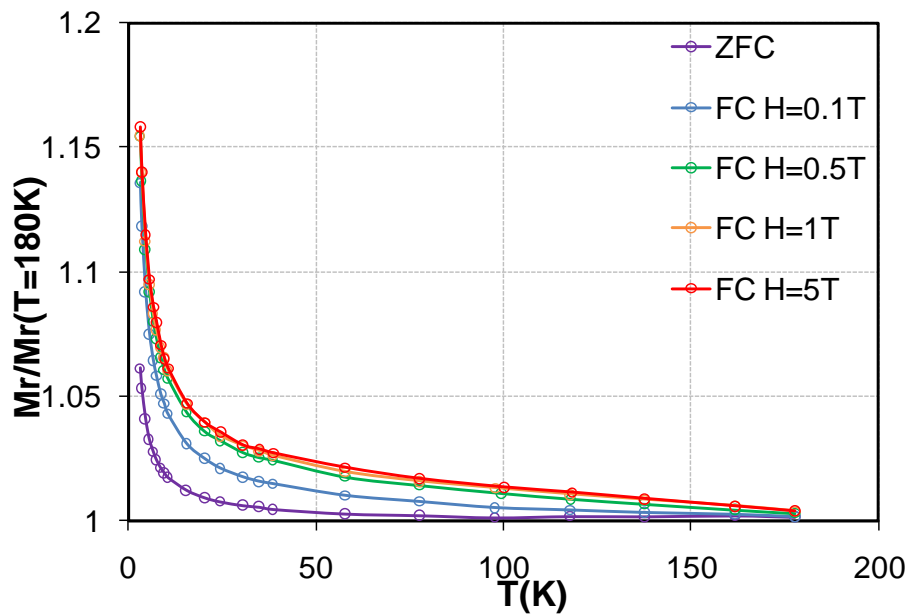
Figure 10.7: Field Cooled / Zero Field Cooled curves for Sample C. The curves are normalized by the value of the magnetization at $T = 180\,\text{K}$.

10.4 Conclusion

In this annexe, it has been shown large differences in the magnetic behaviour of nanowires depending on their degree of oxidation. As a matter of fact, when nanowires are not dried in a oven but only dried in the air, there is no more a coercivity drop from $T = 220 - 240\,\text{K}$ down to $T_{EB} \approx 100\,\text{K}$. In fact, in this case, a large coercivity drop is observed with decreasing temperatures below T_{EB}. A more surprising feature is the decrease of the exchange field with decreasing temperatures in the same temperature range. Moreover, it can be noted that for this sample, the magnetization is about 2.5 time larger at $2.5\,\text{K}$ than at room temperature. From these experimental results, many questions are arisen but no reasonable model allows to explain them for the moment.

Part IV

Annexes: Techniques and Methods

Several experimental techniques have been performed personally or by coworkers during this work. The most interesting results came from: magnetometry, Small Angle Neutron Scattering and neutron diffraction, X-Ray diffraction, TEM and SEM. Here the choice is made to only present neutron scattering techniques. Indeed, magnetometry techniques such as VSM or SQUID are quite well-known and microscopy techniques have been performed by co-workers. In fact, one of the main part of this work consists in developing SANS as a tool to probe magnetic anisotropic nanostructures. That is why this part of the manuscript only focuses on neutron scattering and especially on SANS technique with or without polarized neutron beam. In a first chapter, neutron scattering theory is detailed and compared to X-ray scattering in order to underline the power of neutron scattering to probe magnetic properties. Then, SANS technique is presented so that the experimental results presented in Part II can be well understood.

218

Chapter 11

Neutron Scattering

The physical objects used in scattering techniques can be either particles like neutrons or photons like X-rays. As described in [Lév1984], these objects are called "quantons" and can behave either as particles or as waves. Here the basics of scattering techniques and the similarities and differences between X-Rays and neutrons are discussed. The mathematical formalism of neutron scattering will be introduced in details at the end of the present section.

11.1 Basics of X-ray and neutron scattering

The properties of X-Rays and neutrons are presented in the following Table 11.1 [Rav2006]. X-Rays interact with electrons via the electromagnetic interaction. As for neutrons, they interact with the spins of the electrons via the electromagnetic interaction and with the nuclei via the strong interaction. These interactions lead to weak scattering which means that the probability that such events occur is very small. In fact, scattering can only be observed thanks to the giant flux produced by synchrotrons and neutron reactors. In the following sections, similarities between X-rays and neutrons will be underlined. For instance, the Bragg law is valid for both quantons since diffraction only depends on the wavelength. Nevertheless, some processes need a specific formalism like X-rays absorption or neutron magnetic scattering.

11.2 Interaction processes

When particles (neutrons or photons) hit matter, two main interaction processes come into play: absorption and scattering processes. Absorption refers to processes where the energy of quantons is absorbed by another entity and these quantons destroyed. Scattering refers to processes where a beam of quantons is deflected in multiple directions by a target. Scattering process may be elastic or inelastic depending if the target energy is changed or not during the process. It must be noted that refraction and reflection are not considered as fundamental interaction processes since they are a particular case of scattering. However, few words will be written about them since reflection gives rise to very useful techniques such as reflectivity.

	Neutrons	X-Rays
Description	Particle Wave function Ψ $\Psi \sim exp(i(\overrightarrow{k}.\overrightarrow{r}))$	Field $E = E_0\, e\, exp(i(\overrightarrow{k}.\overrightarrow{r} - \omega t))$ $e : polarisation$
Energy	$E = \frac{p^2}{2m}$	$E = \hbar\omega = \frac{\hbar c}{\lambda}$
Wavelength $\lambda(\text{Å}) =$ $\lambda = 1\text{Å}$	$\frac{0.286}{\sqrt{E(eV)}}$ $E = 81.8\,meV$	$\frac{12.4}{E(keV)}$ $E = 12.4\,keV$
Impulsion	$p = \hbar k = mv$	$p = \hbar k = \frac{h\nu}{c}$
$\frac{k_B T(300\,\text{K})}{E(1\text{Å})}$	0.32	2.1×10^{-6}
Interaction	Strong (nuclei) electromagnetic (spins of electrons)	electromagnetic (electrons)
Scattering cross section	$\sigma_{nuclear} \sim 5\,barn$ $\sigma_{magnetic} \sim 3barn$	$0.32\sigma_{thomson} \sim Z^2 barn$ $\sigma_{magnetic} \sim 10^{-6}\,\sigma_{th}$
Absorption cross section	$\sigma_a \sim 0.1 - 10\,barn$ for most elements	σ depends on k and Z

Table 11.1: Properties of neutrons and X-Rays [Rav2006]. Note that $1\,barn = 10^{-28}\,\text{m}^2$ and that $k_B T(300\,\text{K}) = 25.2\,\text{meV}$.

11.2.1   Absorption process

The absorption of incident quantons by matter is given by the Beer-Lambert law. It implies that a beam of intensity I (proportional to N incident quantons per time unit) which cross a matter length dz (see Figure 11.1) varies from a quantity dI given by:

$$\frac{dI}{I} = \frac{dN}{N} = -\mu\,dz \tag{11.1}$$

where μ is defined as the absorption linear coefficient which is homogeneous to the inverse of a length and whose value depends on materials. When this formula is integrated over the total length L of the sample, it becomes [Sch2003]:

$$I = I_0\,exp(-\mu L) \tag{11.2}$$

where I_0 is the incident intensity. It must be noted that μ which is a macroscopic variable comes from a microscopic variable, the absorption cross section σ_a defined by the following relationship in a volume $dV = S\,dz$:

$$dN = -\Phi_i\,dN_a\,\sigma_a \tag{11.3}$$

where S , Φ_i and dN_a are respectively the cross surface of dV, the incident flux and the number of absorbing centers. In the case of a volume V characterized by a density of absorbing centers ρ_a:

$$dN_a = \rho_a\,S\,dz \tag{11.4}$$

From these equations, the relationship linking μ to σ_a is:

$$\mu = \sigma_a \rho_a \qquad (11.5)$$

Note that σ_a is homogeneous to a surface and is generally expressed in barn. A barn amounts to $10^{-28}\,\text{m}^2$ and an absorbing cross section σ_a of $1\,\text{barn}$ conveys a low probability of absorption.
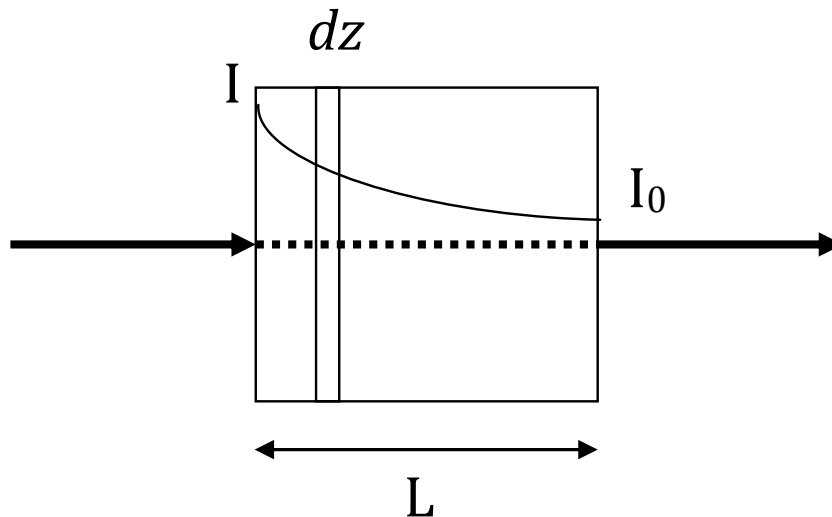
Figure 11.1: Definition of the variables in an absorbing process

11.2.1.1 X-Rays absorption

Several mechanisms lead to X-Rays absorption. At low energies ($\sim 1\,\text{keV}$), the main origin of absorption is the creation of a photoelectron which comes from the photoelectric effect. For energies above the rest energy of electrons ($E_0 = m\,c^2 = 511\,\text{keV}$), the X-photon is disintegrated in an electron-positron pair. X-Ray absorption is a complex phenomenon and can be discontinuous as a function of the energy. It must however be reminded that between two absorption levels, the absorption cross section is proportional to Z^4 and k^{-3}. The consequence is that X-Ray absorption is larger at low energy and for heavy elements. For instance, for X-Rays whose wavelength is $1.542\text{Å}(CuK_\alpha ray)$ [Rav2006], $\sigma_a(Li) = 5.7\,\text{barn}$, $\sigma_a(Ni) = 4760\,\text{barn}$ and $\sigma_a(Pb) = 79800\,\text{barn}$.

11.2.1.2 Neutron absorption

Neutrons are usually weakly absorbed by matter since they weakly interact with electrons. When neutrons are absorbed by matter, the process is a nuclear one. For instance, $^3He^3$ absorbs neutrons via the neutron reaction:

$$^3He + n \rightarrow {}^3H^- + p + 0.764\,\text{MeV} \qquad (11.6)$$
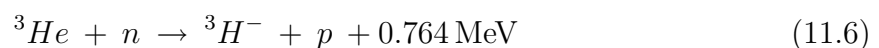
Few elements give rise to such nuclear reactions. ^3He, ^6Li, ^{10}B, Gd or Cd are one of the most neutron absorbing elements. For example, the absorbing cross section σ_a of ^6Li, ^{10}B and Gd are respectively 520, 2100 and 74000 barn for $\lambda = 1.8\text{Å}$. Such efficient absorbing elements are used to build neutron detectors or protecting screens [Sch2003].

Finally, contrary to X-rays, in most neutron scattering experiments, absorption is not a major problem.

11.2.1.3   Scattering process

Scattering is a term characterizing the deflection of quantons in multiple directions. Scattering and diffraction processes must not be mixed up. Scattering indicates the elementary interaction process between a quanton and a target (See Figure 11.2). As for diffraction, it is a particular case of scattering in precise directions.

Note that the scattering process of a quanton comes from the interaction with a target. The corresponding interaction potential is written $\mathcal{V}(\overrightarrow{r})$ and will be defined later in Equation 11.24.
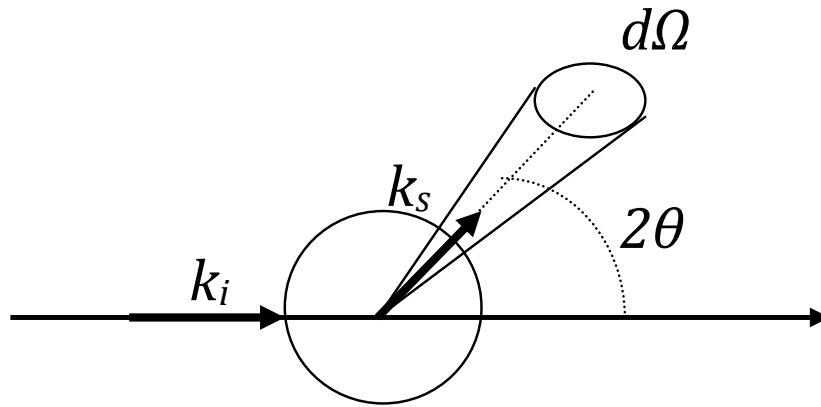
Figure 11.2: Definition of variables in a scattering process

11.2.1.4   The scattering length b

An incident beam of quantons is now considered in order to put into form the mathematical formalism. The flux of quantons is noted Φ_0. $\overrightarrow{k_s}$ and $\overrightarrow{k_i}$ are respectively the scattered and the incident wave vectors and 2θ is the angle between $\overrightarrow{k_s}$ and $\overrightarrow{k_i}$. The scattering wave vector $\overrightarrow{Q}$ is defined by:

$$\overrightarrow{Q} = \overrightarrow{k_s} - \overrightarrow{k_i} \tag{11.7}$$

The number of quantons scattered per time unit dN_s in the solid angle $d\Omega$ is given by:

$$dN_s = \Phi_0 \frac{d\sigma_s}{d\Omega} d\Omega \tag{11.8}$$

where $\frac{d\sigma_s}{d\Omega}$ is the differential scattering cross section of the target. This is a variable linked to the scattering length b which is measured during a scattering experiment.

Consider now a target which is a single scattering center. The incident quanton is a plane wave defined by the wave function normalized on a volume V [Coh1973]:

$$\varphi_i(\overrightarrow{r}) = \frac{1}{\sqrt{V}} exp(i\,\overrightarrow{k_i}.\overrightarrow{r})$$

The wave function of the scattered quanton becomes:

$$\varphi_s = -\frac{1}{\sqrt{V}}\frac{b(Q)}{r}exp(i\overrightarrow{k_s}.\overrightarrow{r})$$

In the above expression, the negative sign comes from a convention which defines that when $b > 0$, the quanton is subjected to a phase difference of π. Mathematical developments [Rav2006] lead to the following expression linking $\frac{d\sigma_s}{d\Omega}$ to b:

$$\frac{d\sigma_s}{d\Omega} = \frac{k_s}{k_i}\,|b(Q)|^2 \tag{11.9}$$

In elastic scattering processes, this equation can be simplified into:

$$\frac{d\sigma_s}{d\Omega} = |b(Q)|^2 \tag{11.10}$$

The function $b(Q)$ characterizes the intensity of the interaction between the quanton and the atom. It *a priori* depends on the wave vector Q. When $b(Q)$ is constant (case of neutrons), it is called the *scattering length*.

11.2.1.5 X-Ray scattering

In the case of X-Rays [Her], the total scattering cross section varies following:

$$\sigma_s \sim Z^2 \tag{11.11}$$

where Z is the atomic number of the considered element. It directly implies that the contrast between two elements exhibiting a similar atomic number will be quite weak. This can appear as a real limitation in some studies.

11.2.1.6 Neutron scattering

Contrary to X-Rays, the neutron scattering length is a real constant and does not depend on Q. The total neutron scattering length becomes

$$\sigma_s = 4\pi\,|b|^2$$

The sign of b cannot be measured via a scattering experiment. To proceed to the sign determination of b, reflectivity measurements are required (see Section 11.2.2).
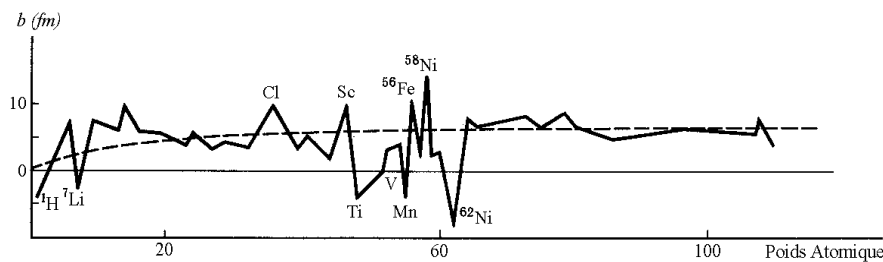
Figure 11.3: The neutron scattering length as a function of the atomic number.

Finally the great advantage of neutrons compared to X-Rays comes from the dependence of b as a function of Z. As a matter of fact, while σ_s is proportional to Z^2 for X-Rays, it strongly varies from one element to another for neutrons (see Figure 11.3) and the sign of b can even be opposite for two elements which are neighbours in the classification table. This property allows to obtain large contrasts between elements presenting similar atomic numbers. For instance, it thus becomes possible to easily distinguish Fe from Co or Ni. Another example is the matching technique which consists in replacing H atoms ($b_H = -3.74\,\text{fm}$) by D atoms ($b_D = 6.57\,\text{fm}$) in order to tune the scattering contrast (see Section 9.3.2).

11.2.2 Refraction

As previously explained, refraction is not a fundamental interaction process but just a particular case of scattering phenomenon. It can give rise to very interesting experiments which are described in the following section. Let us imagine an incident quanton hitting a surface with an incident wave vector $\overrightarrow{k_i}$ making an angle α with the normal to the surface. $\overrightarrow{k_r}$ is the reflected wave vector and $\overrightarrow{k_t}$ the transmitted one making an angle β with the normal to the surface. It can be shown [Her] that the refraction index n is written:

$$n = 1 - \delta = 1 - \frac{2\pi}{k^2}\,\rho_s\,b(0) \tag{11.12}$$

ρ_s is the density of scattering centers and $b(0)$ is the b value for $Q = 0$ (remind that $b(Q) = b(0) = b$ for neutrons). In both cases, neutrons and X-Rays, δ is very small and amounts to about 10^{-5}. From the Snell-Descartes law $\cos\alpha = n\cos\beta$, it can be deduced that $\alpha \simeq \beta$ and the refraction process is eventually negligible for both neutrons and X-Rays.

Nevertheless, the expression of δ shows that in reflectivity experiments, the sign of $b(0)$ becomes critical. Indeed, when $b(0) > 0$, $n < 1$ and there is a critical angle α_c below which the reflection is total. When $b(0) < 0$, $n > 1$ and there cannot be any total reflection observed. Note that the total reflection phenomenon is always observed for X-Rays since $b(0)$ is always positive for such quantons. As previously discussed, b can be either positive or negative for neutrons.

Finally reflectivity measurements are necessary as soon as the aim of a study is to measure b and its sign which is not possible via scattering techniques which only give an access to $|b|^2$. Reflectivity experiments are very useful to probe surface structures and interfaces.

11.3 From interaction processes to experimental techniques

To probe the structure of matter, experimental techniques can be classified following the fundamental interaction processes listed in Figure 11.4. However other quantons such as electrons or light photons can lie at the root of these experimental techniques. The advantages of neutrons have been exposed in Chapter 1. Very briefly, it can be reminded that neutrons have a few advantages compared to other quantons:

1. Neutrons can easily penetrate thick materials because they are electrically neutral. Contrary to X-rays or electrons, the study of condensed matter via neutron techniques is not limited to surfaces, interfaces or thin films.

2. Neutrons can interact totally differently with atoms whose atomic number is very close or even with different isotopes from the same atom species.

3. Neutron wavelength range $(0.5 - 20\,\text{nm})$ gives an access to interatomic distances or correlation lengths in larger structures like polymer or liquid crystals. As for neutron energy range $(1 - 100\,\text{meV})$, it corresponds to the energy of excitations in condensed matter.

4. Neutrons have a spin which interacts with the magnetic moments of atoms. This lie at the root of magnetic studies in condensed matter.

5. Isotopic labelling (especially deuteration) which is of outmost importance in the study of polymere science.

Neutrons are thus a very powerful tool to probe structures, magnetism and excitations in condensed matter. However, the main limitation to their use is their low flux compared to the X-rays.

EMISSION :
- **X-Rays**
  - Fluorescence (Chemical analysis)

REFRACTION :
- **X-Rays**
  - Reflectivity (Surfaces, interfaces)
  - Surface diffraction
- **Neutrons**
  - (Polarized) Reflectivity ((magnetic) surfaces and interfaces)

Quantons :
- X-Rays
- Neutrons

Matter :
- Crystal
- Liquid, liquid crystal
- Polymer
- Surface

ABSORPTION:
- **X-Rays**
  - Absorption spectroscopies (EXAFS, XANES)
  - Dichroïsm (magnetism, thin films)

SCATTERING:
- **X-Rays**
  - Diffraction (structures)
  - Diffuse scattering (desorder in liquid crystal)
  - Compton scattering (electronic structures)
  - SAXS (polymers, aggregates...)
  - Magnetic or Inelastic scatterings (synchrotron)
- **Neutrons**
  - Diffraction, Diffused scattering (structures, H presence)
  - (Polarized) SANS (polymer, aggregates, magnetic particles...)
  - Inelastic scattering (excitations: phonons, magnons)
  - Magnetic scattering (structures, interactions)

Figure 11.4: X-Ray and neutron experimental techniques to probe condensed matter. Adapted from[Rav2006].

11.4 Mathematical formalism of thermal neutron scattering

The neutrons produced to probe matter exhibit some energies comprised between 1 and $200\,\text{meV}$ $(12 - 2400\,\text{K})$. For energies below $10\,\text{meV}$, neutrons are referred to as *cold.* Up

to 100 meV, they are qualified as *thermal*. Above 100 meV, they are called *hot*. This large energy range suits particularly well to all kinds of studies in condensed matter, from crystal structure determination to the dynamics of polymers or proteins. The mathematical formalism of thermal neutron scattering will be introduced afterwards as follow. First, Fermi's golden rule gives the probability per time unit for a system quanton-target to change its initial state into another final state. This law allows to express the partial differential cross section within the Born approximation. Then the consideration of a target including N nuclei lead to the *Van Hove* formula which defines the coherent and incoherent cross sections. The meaning and the importance of these quantities are discussed. Finally the nuclear and magnetic scattering will be detailed.

11.4.1   Born approximation and Fermi's golden rule

In quantum mechanics, scattering processes can be modelled via the resolution of the Schrödinger equation applied to a neutron submitted to an interaction potential $\mathcal{V}(\overrightarrow{r})$ independent of time. One approach consists in calculating the stationary states with the energy $E = \frac{\hbar^2 k^2}{2m}$ via the eigenvalues equation [Coh1973]:

$$\left[-\frac{\hbar^2}{2m}\triangle + \mathcal{V}(\overrightarrow{r}) \right] \varphi(\overrightarrow{r}) = E\,\varphi(\overrightarrow{r}) \tag{11.13}$$

By normalizing the interaction potential into $U(\overrightarrow{r}) = -\frac{2m}{\hbar^2}\mathcal{V}(\overrightarrow{r})$, this equation becomes:

$$\left[\triangle + k^2 - U(\overrightarrow{r}) \right] \varphi(\overrightarrow{r}) = 0 \tag{11.14}$$

Within this approach, the particles can be described as wave packets resulting from the superposition of the stationary states. The Born approximation consists in considering an interaction potential small enough to assume that only one scattering process occurs in the target. Finally the solutions of the eigenvalues equation within the Born approximation becomes [Rav2006]:

$$\varphi(\vec{r}) \sim e^{i\,\overrightarrow{k_i}.\overrightarrow{r}} + b(\overrightarrow{Q})\,\frac{e^{i\,\overrightarrow{k_s}.\overrightarrow{r}}}{r},\ for\ r \to \infty$$

This solution is the sum of an incident plane wave and a scattered spherical wave. Note that the Born approximation is all the more true as the total wave function is similar to the incident one, which is only valid for weak interaction potentials. It implies that this approximation is false around the Bragg peaks in diffraction but also near the total reflectivity in reflectivity experiments. As for the SANS experiments, it is only valid as soon as the scattered intensity is low compared to the incident beam.

Of course, the interaction between a neutron and an atom is time dependent. The interaction potential is thus considered to grow when the neutron gets closer to the target. The interaction potential is said to be "switched on". The scattered cross section of the neutron will thus be determined by the time-dependent perturbation theory which requires to determine the interaction hamiltonian H between the neutron and the target. The initial state of the system neutron-target is characterized by the energy ε_i and described by the wave function $|\psi_i\rangle$. As for the final (scattered) state, it is characterized by the

energy ε_s and described by the wave function $|\psi_s\rangle$. The initial state of the neutron is always a plane wave with a wave vector $\overrightarrow{k_i}$.

In the Born approximation, the cross sections can be deduced from Fermi's golden rule which gives explicitly the probability per unit time that the system moves from the initial state $|\psi_i\rangle$ to the final state $|\psi_s\rangle$:

$$\mathcal{P}_{i,s} = \frac{2\pi}{\hbar}\, |\langle \psi_s\, |H|\, \psi_i\rangle|^2\, \delta(\varepsilon_i - \varepsilon_s) \tag{11.15}$$

The Fermi's golden rule has been written in its general form and thus depends on the kind of quantons considered. The energies and wave functions of the initial and final states for the neutron-target system are listed below:

$$initial\ state\ |\psi_i\rangle\ :\ \psi_i = \frac{1}{\sqrt{V}}e^{i\,\overrightarrow{k_i}.\overrightarrow{r}}\,\phi_i \quad \varepsilon_i = E_i + \frac{p_i^2}{2m} \tag{11.16}$$

$$final\ state\ \ |\psi_s\rangle\ :\ \psi_s = \frac{1}{\sqrt{V}}e^{i\,\overrightarrow{k_s}.\overrightarrow{r}}\,\phi_s \quad \varepsilon_s = E_s + \frac{p_s^2}{2m} \tag{11.17}$$

V is a volume normalizing the wave functions of the neutron. Note that it has no influence on the final result (Van Hove formula). ϕ_i and ϕ_s are respectively the initial and final wave functions of the target. E_i, E_s, $\frac{p_i^2}{2m}$ and $\frac{p_f^2}{2m}$ are respectively the energies of the initial and final states of the target and of the neutron. From the energy and momentum conservation, the energy and momentum transfers are:

$$\hbar\omega = E_s - E_i \tag{11.18}$$

$$\hbar\overrightarrow{Q} = \hbar\overrightarrow{k_s} - \hbar\overrightarrow{k_i} \tag{11.19}$$

Finally, when Fermi's golden rule is applied to neutrons and mathematically developed, the partial scattering cross section can be written as:

$$\frac{d^2\sigma}{d\Omega dE} = \frac{k_s}{k_i}\left(\frac{V\,m}{2\pi\hbar^2}\right)^2 \sum_i \mathcal{P}_i \sum_s |\langle \psi_s\, |H|\, \psi_i\rangle|^2\, \delta(E_s - E_i + \hbar\omega) \tag{11.20}$$

where $\mathcal{P}_i$ is the probability of each initial state $|\psi_i\rangle$ of the system.

11.4.2   Definition of the neutron scattering length b

The neutron-nucleus interaction potential is written $H = \mathcal{V}(\overrightarrow{r})$. For an elastic scattering process, the integration of the partial scattering cross section over the energy E leads to:

$$\frac{d\sigma}{d\Omega} = \left(\frac{V\,m}{2\pi\hbar^2}\right)^2 \left|\int \mathcal{V}(r)e^{-i\overrightarrow{Q}.\overrightarrow{r}}d^3r\right|^2 \tag{11.21}$$

Neutrons and nuclei interact via the strong interaction whose range -about 10^{-15} m- is very short compared to the neutron wavelength. Therefore the neutron-nucleus interaction potential can be expressed as:

$$\mathcal{V}(\overrightarrow{r}) = a\,\delta(\overrightarrow{r}) \tag{11.22}$$

where a is the quantity to determine. Once re-injected in the expression of $\frac{d\sigma}{d\Omega}$, one obtains:

$$\frac{d\sigma}{d\Omega} = \left(\frac{m}{2\pi\hbar^2}\right)^2 a^2 \tag{11.23}$$

which has to be compared to $\frac{d\sigma}{d\Omega} = |b|^2$, expression introduced in Section 11.2.1.4. Consequently the neutron-nucleus interaction potential $\mathcal{V}(\overrightarrow{r})$, named the Fermi pseudo-potential, can be expressed as:

$$\mathcal{V}(r) = \frac{2\pi\hbar^2}{m} b\delta(r) \tag{11.24}$$

Finally the neutron scattering length is defined from the Fourier transform of the Fermi pseudo-potential and does not depend on the scattering angle. This feature is a non-negligible advantage to carry through neutron scattering studies.

11.4.3   Coherent and incoherent scattering: Van Hove formula

A target constituted of N atoms is now considered. The total interaction hamiltonian can be written:

$$H(\overrightarrow{r}) = \sum_n \mathcal{V}_n(\overrightarrow{r} - \overrightarrow{r_n})$$

where the sum is over all the positions $\overrightarrow{r_n}$ of the atoms in the target. Note that there is no reason for that $\overrightarrow{r_n}$ should not be time dependent. The neutron scattering length of each atom n is written b_n so that:

$$\langle k_s | \mathcal{V}_n(\overrightarrow{r} - \overrightarrow{r_n}) | k_i \rangle = \frac{2\pi\hbar^2}{V\,m} b_n\, e^{-i\overrightarrow{Q}.\overrightarrow{r_n}} \tag{11.25}$$

Thus,

$$\langle \psi_s | H | \psi_i \rangle = \frac{2\tau\hbar^2}{V\,m} \left\langle \phi_s \left| \sum_n b_n\, e^{-i\overrightarrow{Q}.\overrightarrow{r_n}} \right| \phi_i \right\rangle \tag{11.26}$$

A calculation of the partial scattering cross section leads to [Rav2006]:

$$\frac{d^2\sigma}{d\Omega dE} = \frac{k_s}{k_i} \frac{N}{2\pi\hbar} \int \sum_m \langle b_n b_{n+m} \rangle \left\langle e^{-i\overrightarrow{Q}.\vec{r}_{n+m}(t)} e^{i\overrightarrow{Q}.\vec{r}_n(0)} \right\rangle e^{i\omega t} dt \tag{11.27}$$

In the above expression, $\langle ... \rangle$ represents the spatial and statistic average. Since b_n exhibits no spatial correlation, it can be written:

$$\langle b_n b_{n+m} \rangle = \langle b \rangle^2 \ \ for\ m \neq 0 \tag{11.28}$$

$$and\ \langle b_n b_{n+m} \rangle = \langle b \rangle^2 + \left(\langle b^2 \rangle - \langle b \rangle^2 \right)\ for\ m = 0 \tag{11.29}$$

It implies that the partial scattering cross section is the sum of two contributions: one is called the coherent cross section and the other one the incoherent cross section. These quantities have been expressed by Van Hove in 1954 and are written:

$$\frac{d^2\sigma_{coh}}{d\Omega dE} = \frac{k_s}{k_i} \frac{N\,\langle b \rangle^2}{2\pi\hbar} \int \sum_m \left\langle e^{-i\overrightarrow{Q}.\vec{r}_{n+m}(t)} e^{i\overrightarrow{Q}.\vec{r}_n(0)} \right\rangle e^{i\omega t} dt \tag{11.30}$$

$$\frac{d^2\sigma_{incoh}}{d\Omega dE} = \frac{k_s}{k_i} \frac{N\left(\langle b^2 \rangle - \langle b \rangle^2\right)}{2\pi\hbar} \int \left\langle e^{-i\overrightarrow{Q}.\vec{r}_{n+m}(t)} e^{i\overrightarrow{Q}.\vec{r}_n(0)} \right\rangle e^{i\omega t} dt \qquad (11.31)$$

From these expressions, it is possible to introduce the coherent and incoherent scattering functions:

$$S_{coh}(\overrightarrow{Q},\omega) = \frac{1}{2\pi\hbar} \int \sum_m \left\langle e^{-i\overrightarrow{Q}.\vec{r}_{n+m}(t)} e^{i\overrightarrow{Q}.\vec{r}_n(0)} \right\rangle e^{i\omega t} dt \qquad (11.32)$$

$$S_{incoh}(\overrightarrow{Q},\omega) = \frac{1}{2\pi\hbar} \int \left\langle e^{-i\overrightarrow{Q}.\vec{r}_{n+m}(t)} e^{i\overrightarrow{Q}.\vec{r}_n(0)} \right\rangle e^{i\omega t} dt \qquad (11.33)$$

By introducing the time dependent correlation function, mathematical developments [Rav2006] lead to the expression of the coherent and incoherent partial scattering cross sections:

$$\frac{d^2\sigma_{coh}}{d\Omega dE} = \frac{k_s}{k_i} N \langle b \rangle^2 S_{coh}(\overrightarrow{Q},\omega) \qquad (11.34)$$

$$\frac{d^2\sigma_{incoh}}{d\Omega dE} = \frac{k_s}{k_i} N \left(\langle b^2 \rangle - \langle b \rangle^2\right) S_{incoh}(\overrightarrow{Q},\omega) \qquad (11.35)$$

Physically, the coherent scattering corresponds to a system where all the nuclei exhibit the same scattering length. As for the incoherent scattering, it is similar to the diffuse scattering and corresponds to a random distribution of the scattering lengths over the different scattering centers. They are two origins in the incoherent scattering. First, isotopes of the same element have different scattering lengths. Secondly, the scattering length of isotopes carrying a nuclear spin (H in particular) depends on whether the neutron and nuclear spins are parallel or antiparallel. Except at very low temperature ($T \ll 1\,\mathrm{K}$), nuclear spins are disordered. Note that the incoherent scattering gives rise to a continuous background in neutron scattering experiments.

11.5 An example of neutron scattering technique: neutron diffraction

In the present section, neutron diffraction technique is briefly described as some neutron diffraction measurements are presented in Chapter 4.

Let's consider a crystal. The positions of the atoms are given by the following relation:

$$r_n(t) = R_n + u_n(t)$$

where R_n and u_n represent respectively the average position in time and the small deviation in time from the average position. From, the results detailed in the previous section, the expression of the partial coherent neutron scattering cross section in this scope is:

$$\frac{d^2\sigma_{coh}}{d\Omega dE} = \frac{k_s}{k_i} \frac{N \langle b \rangle^2}{2\pi\hbar} \int \sum_m e^{-i\overrightarrow{Q}.\overrightarrow{r_m}} \left\langle e^{-i\overrightarrow{Q}.\vec{u}_{n+m}(t)} e^{i\overrightarrow{Q}.\vec{u}_n(0)} \right\rangle e^{i\omega t} dt \qquad (11.36)$$

An approximate value of $\left\langle e^{-i\overrightarrow{Q}.\vec{u}_{n+m}(t)}e^{i\overrightarrow{Q}.\vec{u}_n(0)}\right\rangle$ is given by the following development into series:

$$\left\langle e^{-i\overrightarrow{Q}.(\vec{u}_{n+m}(t)-\overrightarrow{u_n}(0))}\right\rangle = 1 - \left\langle i\overrightarrow{Q}.(\vec{u}_{n+m}(t) - \vec{u}_n(0))\right\rangle - \frac{1}{2}\left\langle\left(\overrightarrow{Q}.(\vec{u}_{n+m}(t) - \vec{u}_n(0))\right)^2\right\rangle \tag{11.37}$$

Since the second term is equal to zero, we have:

$$\left\langle e^{-i\overrightarrow{Q}.(\vec{u}_{n+m}(t)-\overrightarrow{u_n}(0))}\right\rangle = e^{-\frac{1}{2}\left\langle\left(\overrightarrow{Q}.(\vec{u}_{n+m}(t)-\vec{u}_n(0))\right)^2\right\rangle} \tag{11.38}$$

The introduction of the Debye-Waller factor, $W = \frac{1}{2}\left\langle\left(\overrightarrow{Q}.\overrightarrow{u_n}\right)^2\right\rangle$, allows to simplify this expression into:

$$\left\langle e^{-i\overrightarrow{Q}.(\vec{u}_{n+m}(t)-\overrightarrow{u_n}(0))}\right\rangle = e^{-2W}e^{\left\langle\overrightarrow{Q}.(\vec{u}_{n+m}(t).\vec{u}_n(0))\right\rangle} \tag{11.39}$$

Then, the term $e^{\left\langle\overrightarrow{Q}.(\vec{u}_{n+m}(t).\vec{u}_n(0))\right\rangle}$ can be expressed as:

$$e^{\left\langle\overrightarrow{Q}.(\vec{u}_{n+m}(t).\vec{u}_n(0))\right\rangle} = 1 + \left\langle\overrightarrow{Q}.(\vec{u}_{n+m}(t).\vec{u}_n(0))\right\rangle + ... \tag{11.40}$$

This development allows to separate elastic scattering from inelastic one. Indeed, the fist term which time-independent and named *zero-phonon* term is the dominant term and corresponds to an elastic scattering. The second term is named *one-phonon* term, etc. Thus these other terms correspond to inelastic scattering. If the *zero-phonon* term is now isolated from the others considering only the elastic scattering, the elastic partial coherent neutron scattering cross section can be reduced to [Rav2006]:

$$\frac{d^2\sigma_{coh}}{d\Omega dE} = \frac{N\left\langle b\right\rangle^2}{2\pi\hbar}e^{-2W}\sum_m e^{-i\overrightarrow{Q}.\overrightarrow{r_m}}\int e^{i\omega t}dt = N\left\langle b\right\rangle^2 e^{-2W}\sum_m e^{-i\overrightarrow{Q}.\overrightarrow{r_m}}\delta(\hbar\omega) \tag{11.41}$$

After integration over the energy- the elastic coherent scattering cross section becomes:

$$\frac{d\sigma_{coh}}{d\Omega} = \left\langle b\right\rangle^2 e^{-2W}\frac{\left|F(\overrightarrow{Q})\right|^2}{v^2} * \sum_{hkl}\delta(\overrightarrow{Q} - \overrightarrow{Q_{hkl}}) \tag{11.42}$$

where v is the volume of the elementary cell and $\overrightarrow{Q_{hkl}}$ the wave vectors of the reciprocal lattice nodes. $\left|F(\overrightarrow{Q})\right|$ is the Fourier transform of the form function $\sigma(\overrightarrow{r})$ which is defined as follow: $\sigma(\overrightarrow{r}) = 1$ if the extremity of $\overrightarrow{r}$ is inside the volume of the sample otherwise it is equal to 0. When the crystal contains several atoms, it is necessary to introduce the structure factor $S(\overrightarrow{Q})$:

$$S(\overrightarrow{Q}) = \left|\sum_j\left\langle b_j\right\rangle e^{-W_j}e^{-i\overrightarrow{Q}.\overrightarrow{r_j}}\right|^2$$

In this case, the scattering cross section becomes:

$$\frac{d\sigma_{coh}}{d\Omega} = S(\overrightarrow{Q})\frac{\left|F(\overrightarrow{Q})\right|^2}{v^2} * \sum_{hkl}\delta(\overrightarrow{Q} - \overrightarrow{Q_{hkl}}) \tag{11.43}$$

This formula of the scattering cross section allows to interpret neutron diffraction experiments. In crystals, the average distances between atoms do not vary that is why some Bragg spots can be observed. To characterize structures, it is possible to use spectrometers similar to X-rays ones like powder diffractometers or 4-circles spectrometers [Mul2003].

Chapter 12

Small Angle Neutron Scattering (SANS)

This chapter first exposes why SANS is a technique which suits particularly well to the study of magnetic nanoparticles. Then SANS spectrometers used during this work and typical experiments are detailed.

12.1 Polarized SANS: a unique tool to probe magnetism of nano-objects

SAS encompasses three techniques: Small Angle Light Scattering (SALS), Small Angle X-Ray Scattering (SAXS) and Small Angle Neutron Scattering (SANS). SALS does not allow to study opaque systems and it is unfortunately a real limitation since a non negligible part of individual nano-objects are opaque and especially the objects studied during this work. As for SAXS, it appears very useful to probe nano-objects as soon as the sample is not too thick. The great advantage of SAXS is the high brilliance of the beam. However, the magnetic diffraction intensity of X-rays is about four orders of magnitude lower than the charge scattering intensity. It means that X-rays is far from being the ideal tool to carry magnetic measurements.

In fact, even if the neutron brilliance is low compared to the X-rays one, SANS is a unique technique to study magnetic nanoparticles. Of course, the Q range probed by both SAXS and SANS corresponds well to the typical sizes of nano-objects. Moreover, the added value of neutrons here are the interaction of their spins with the magnetic moments of the atoms in the matter. This property is crucial to probe the magnetic properties of nanoparticles.

Finally, SALS, SAXS and SANS are complementary techniques to study nano-objects. The choice of the technique depends on the kind of objects studied. What is the accessible Q range? Are the objects opaque? Are they magnetic?

Both SAXS and SANS allow to get access to structural information about the shape, the size and the orientation of the objects. However SANS really appears to be the more suitable tool to probe the magnetic properties of nano-objects because of the intrinsic properties of neutrons.

233

12.2   Instrumentation: SANS spectrometers

This section aims to give a short overview about SANS spectrometers. The choice of the spectrometer depends on the objectives of the study. The wavelength and the distance *sample-detectors* define the accessible Q range. Typically SANS spectrometers such as PAXE at the LLB allow to study objects with sizes ranging from a few nanometers to tens of nanometers. However Very Small and Ultra Small Angle Scattering spectrometers recently developed such as TPA at the LLB can give information on micro-sized systems. However as soon as the goal is to study magnetic systems, Polarized SANS (PSANS) is required. The idea consists in polarizing the beam and in observing the difference of scattering between spin $|+\rangle$ and spin $|-\rangle$ neutrons. The difference between the scattered intensities of neutrons polarized UP and DOWN is directly linked to the magnetic contrast which gives access to the static magnetic properties of the sample.

In this section the technical characteristics of SANS spectrometers are given. PAXE and PAPYRUS are typical examples of respectively non-polarized and polarized spectrometers.

12.2.1   Transmitted Intensity: necessity of a Beam Stop

During a SANS experiment, neutrons can be either absorbed, reflected or scattered. The sample is placed perpendicular to the incident beam so that the reflection can be considered as negligible. As for the absorption of neutrons by the sample, it is given by the Beer-Lambert law which implies that it increases exponentially with the thickness of the sample. For this reason the samples are usually less than 2 mm thick.

The use of a Beam Stop is crucial to prevent the detector from being saturated by transmitted neutrons. A Beam Stop is a piece of cadmium which is a strong absorber. The aim is to center it so that neutrons which are not deflected are absorbed. Finally, the measured signal will be only constituted of scattered neutrons.

Note that during the scattering processes some energy can be lost or transferred to neutrons. In this case the scattering process is qualified of *inelastic*. In the contrary it is qualified of *elastic*. The inelastic scattering is much lower in intensity than the elastic one. In a SANS experiment, the inelastic scattering is thus neglected.

12.2.2   Wavelength and sample-detector distance: determination of the accessible Q range.

The scattering wave vector is defined as:

$$Q = \frac{4\pi}{\lambda} sin\theta \tag{12.1}$$

From this formula, the accessible Q range strongly depends on the wavelength and on the accessible θ range.

12.2.2.1   Choice of the wavelength

For the PAPYRUS spectrometer, the wavelength is fixed to 8Å by a monochromator made of Ni-Ti multilayers on Si (see Figure 12.1). However, for other spectrometers, the

wavelength can be tuned. For instance, on the PAXE spectrometer the wavelength can vary from 4Å to 20Å. The wavelength is defined by a velocity selector. A velocity selector is a rotating drum with helically curved and absorbing slits. The selected wavelength depends on the rotation speed of the chopper. The wavelength spread is around $\frac{\triangle\lambda}{\lambda} = 10\%$.

12.2.2.2 Choice of the sample-detector distance

The accessible Q range depends on the maximum 2θ value which is itself directly linked to the sample-detector distance D and the surface S of the detector. For the PAPYRUS spectrometer, D can be set to 1, 2, 3 or 4 m and S is equal to 64×64 cm. For other spectrometers D can vary continuously. For the PAXE spectrometer, it can vary from 0.8 to 5 m and S is equal to 64×64 cm.

12.2.2.3 Accessible Q range

For the PAPYRUS spectrometer, the accessible Q range is respectively $0.008\text{Å}^{-1} < Q < 0.24\text{Å}^{-1}$ and $0.002\text{Å}^{-1} < Q < 0.06\text{Å}^{-1}$ for $D = 1$ m and $D = 4$ m. For the PAXE spectrometer, the accessible Q range is $0.001\text{Å}^{-1} < Q < 0.5\text{Å}^{-1}$. These accessible Q ranges allow to probe structures whose characteristic size is given by:

$$\xi = \frac{2\pi}{Q} \tag{12.2}$$

The typical sizes corresponding to these Q range have been listed in Table 7.1. This table shows that SANS experiments are well adapted to the study of nanostructures.
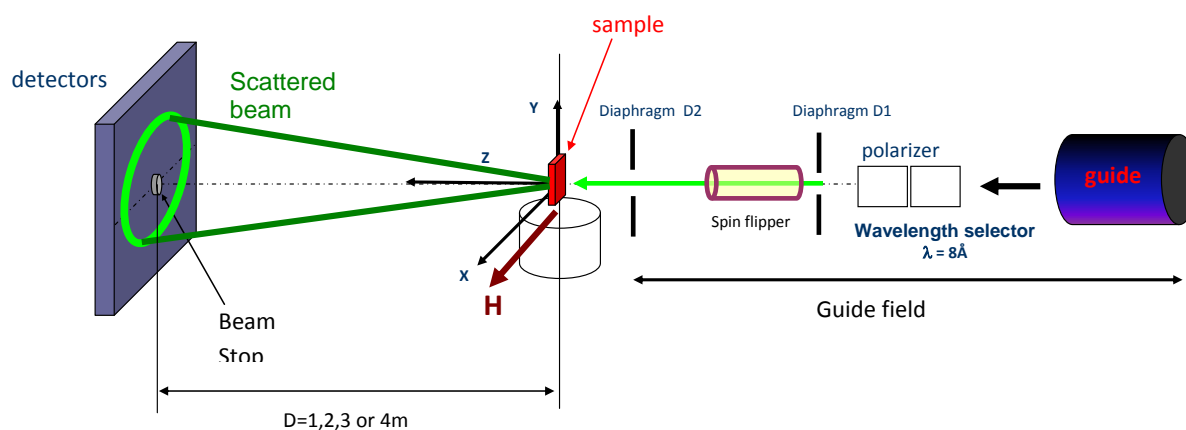

Figure 12.1: Configuration of PAPYRUS, the Polarized SANS spectrometer at the LLB

12.2.3 Collimation: a compromise between flux and resolution

The choice of collimation results from a compromise between the resolution and the neutron flux. The resolution should be set to the largest possible value compatible with

the phenomenon to be studied in order to maximize the flux. This choice strongly depends on the nature of the sample.

12.2.4   Detectors for SANS spectrometers

For the moment, most detectors are made of gas counters. One of the most commonly used mixture is made of ^3He as detection gas and CF_4 as stopping gas. The technical details are discussed in [Kno1989]. On the PAXE and PAPYRUS spectrometers, the counting gas is BF_3. The principle is based on an neutron-alpha interaction [Sch2003]. Neutrons are absorbed by the boron atoms as follow:

$$ {}^1_0n \ + \ {}^{10}_5B \ \longrightarrow \ \alpha \ + \ {}^7_3Li $$
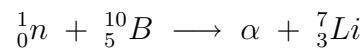
The charges created during this reaction are located using a wire grid. For the PA-PYRUS spectrometer, the wire grid defines 128×128 pixels of $5 \times 5\,\mathrm{mm}$.

12.2.5   Polarization of neutrons

Few spectrometers are implemented with a neutron polarizer. The PAPYRUS spectrometer is equipped with [Fe/Si] supermirrors which allows to polarize the incident neutrons and with a radio-frequency flipper which allows to adiabatically reverse their polarization (see Figure 12.1). The polarization is about 94%.

12.3   Setting-up a typical SANS experiment

12.3.1   Experimental settings

Before starting an experiment, it is recommended to calculate the Q-range which should be probed depending on the size of the particles [Gri2008]. Then the wavelength of the incident beam and the distance sample-detector distance can be set. The second step consists in setting the collimation. As explained above, this choice results from a compromise between flux and resolution. After that, it is required to center the beam so that it hits the middle of the detector area. Once these settings have been processed, the transmission at $Q = 0$ (in the direct beam) must first be determined. Then, the detectors efficiency has to be measured. A material which exhibits mainly incoherent scattering is used. This material is usually vanadium or Plexiglas. The last step consists in putting the sample in the beam and in centering the beam stop. If the particles are dispersed in a solution or in a matrix, it is strongly recommended to measure the scattering from the solvent or the matrix without the particles.

12.3.2   Multiple scattering: a precaution to take

Multiple scattering comes from the probability for a neutron to be scattered more than once by the sample. It implies that the final deflection of the neutron which has been scattered several times is ill defined. Consequently the more multiple scattering occurs, the worse becomes the result. In order to prevent from multiple scattering, a possibility consists in using thin or dilute samples.

12.3.3 From raw to normalized data.

The first information is given by the transmission of the signal T. Indeed when a volume V of the sample is illuminated by a beam with a flux Φ_0 during a time t, the fraction $\triangle N$ of the incident flux which is elastically scattered in the direction Q within a solid angle $\triangle\Omega$ is given by [Gri2008]:

$$\triangle N = \Phi_0\, t\, T\, \frac{d\sigma}{d\Omega}(Q)\, \triangle\Omega \tag{12.3}$$

In this formula, $\frac{d\sigma}{d\Omega}(Q)$ is defined as the differential scattering cross section. This term characterizes the elastic interaction between neutrons and the sample. A SANS experiment consists in determining this term since the scattered intensity per unit volume is given by

$$I = \left(\frac{d\Sigma}{d\Omega}\right)_{total} = \frac{1}{V}\frac{d\sigma}{d\Omega}(Q) = \frac{\triangle N(Q)}{\Phi_0 T\, t\, V\, \triangle\Omega} \tag{12.4}$$

The total differential cross section per unit volume $\left(\frac{d\Sigma}{d\Omega}\right)_{total}$ includes the neutrons scattered by the particles but also by the empty cell and the solvent or matrix which contains the particles. That is why as explained above a measurement on the empty cell and the solvent have to be performed so that the contribution $\left(\frac{d\Sigma}{d\Omega}\right)_{empty\ cell\ +\ solvent}$ can be subtracted to the total scattered intensity.

Bibliography

[Aff1989] I. Affleck, J. Phys.: Condens. Matter. **1** (1989) 3047-3072.

[Aha1966] A. Aharoni, Phys. Status Solidi **16**, 1 (1966).

[Aha1986] A. Aharoni, IEEE Trans. Mag. **22**, 478 (1986).

[Aha1997] A. Aharoni, J. Phys.: Cond. Matter **9** (1997) 10009-10021.

[Ala2004] R. Alayan, L. Arnaud, A. Bourgey, M. Broyer, E. Cottancin, J. R. Huntzinger, J. Lermé, J. L. Vialle, M. Pellarin and G. Guiraud, Rev. Sci. Instrum. **75**, 2461 (2004).

[And1950] P. W. Anderson, Phys. Rev. **79**, 2 (2009) 350-356.

[Ash1966] N. W. Ashcroft and J. Lekner, Phys. Rev **145** (1966).

[Bal2008] T. Balashov, A. F. Takács, M. Däne, A. Ernst, P. Bruno and W. Wulfhekel , Phys. Rev. B **78**, 174404 (2008).

[Bal2009] T. Balashov, T. Schuh, A. F. Takács, A. Ernst, S. Ostanin, J. Henk, I. Mertig, P. Bruno, T. Miyamachi, S. Suga, and W. Wulfhekel, Phys. Rev. Lett. **102**, 257203 (2009).

[Ban2005] J. Bansmann, S. H. Baker, C. Binns, J. A. Blackman, J.-P. Bucher, J. Dorantes-Davila, V. Dupuis, L. Favre, D. Kechrakos, A. Kleibert et al., Surface Science reports **56** (2005) 189.

[Bea1956] C. P. Bean and I. S. Jacobs, J. Appl. Phys. **27** (1956) 1448J. J. Becker, F. E. Luborsky and D. L. Martin, IEEE Trans. Mag., VOL. MAG-4, N°. 2 (1968).

[Ber1972] F. de Bergevin and M. Brunel, Phys. Lett. A39, 141 (1972).

[Ber1999] A.E. Berkowitz and K. Takano, J. Magn. Magn. Mater. **200**, 552 (1999).

[Ber1974] W. Berkson, Fields of Force- The Development of a World View from Faraday to Einstein, New-York (1974).

[Bis2006] F. Bisio, R. Moroni, F. Buatier de Mongeot; M. Canepa and L. Mattera, APL **89**, 052507 (2006).

[Bis2007] F. Bisio, A. Toma, R. Moroni, R. Pasero, F. Buatier de mongeot, C. Boragno, M. Canepa, U. Valbusa and L. Mattera, Phys. Rev. B 75, 054407 (2007).

[Bla2008] E. Blackburn, C. Sanchez-Hanke, S. Roy, D. J. Smith, J.-I. Hong, K. T. Chan, A. E. Berkowitz, and S. K. Sinha , Phys. Rev. B **78**, 180408 (2008).

[Blü2005] S. Blügel, T. Brückel and C. M. Schneider, Magnetism goes Nano, Lecture Manuscripts of the 36th Spring School of the Institute of Solide State Research (2005).

[Bon1988] G.L. Bona, F. Meier, H.C. Siegmann, R.J. Gambino, Appl. Phys. Lett. **52** (1988) 166.

[Bor2007] B. Borca, O. Fruchart, Ph. David, A. Rousseau and C. Meyer, Appl. Phys. Lett. 90, 142507 (2007).

[Bro1999] S. L. Brock, M. Sanabria, S. L. Suib, V. Urban, P. Thiyagarajan and D. I. Potter, J. Phys. Chem. B **103** (1999) 7416-7428.

[Bro1970] W. Brodkorb, W. Haubenreisser, Phys. Stat. Sol. A **3** (1970) 333W. F. Brown, Phys. Rev. **105**, 1479 (1957).

[Brü2002] T. Brückel and W. Schweika (Editors), Polarized Neutron Scattering, Lectures of the 1st Summer School held at the Forschungszentrum Jülich from 10 to 14 September 2002, Materie und Material.

[Cag2007] L. Cagnon, Y. Dahmane, J. Voiron, S. Pairis, M. Bacia, L. Ortega, N. Benbrahim and A. Kadri, J. Magn. Magn. Mater. **310**, 2 (2007) 2428-2430.

[Car1958] W.J. Carr, Phys. Rev., **109** (1958), R1971-R1976.

[Cha2003] N. Chakroune, G. Viau, C. Ricolleau, F. Fiévet-Vincent and F. Fiévet, J. Mater. Chem., 2003, 13, 312.

[Cha1985] R. W. Chantrell, N. Y. Ayoub and J. Popplewell, J. Magn. Magn. Mater. **53** (1985) 199-207

[Coe2009] J.M. Coey, *Histoire du magnétisme en sept moments magnétiques depuis la Chine prédynastique jusqu'à aujourd'hui*, cycle de conférences sur le magnétisme, *Université de tous les savoirs*, Paris (2009), available at the following website: http://www.canal-u.tv/producteurs/universite_de_tous_les_savoirs.

[Coh1973] C. Cohen-Tannoudji, B. Diu and F. Laloë, *Mécanique Quantique*, Editions Herrmann, Paris (1973).

[Cot1999] J. P. Cotton, Journal de Physique IV, **9** (1999) 21-49.

[Cra1967] D. J. Craik and R. Lane, J. Appl. Phys. **18**, R1269 (1967).

[Cro1966] E. R. Cronk, J. Appl. Phys. **37** (1966), R1097.

[Dag1999] E. Dagotto, Rep. Prog. Phys. **62** (1999) 1525-1571.

[Dah2006] Y. Dahmane, L. Cagnon, J. Voiron, S. Pairis, M. Bacia, L. Ortega, N. Benbrahim and A. Kadri, J. Phys. D: Appl. Phys. **39** (2006) 4523-4528.

[Dar2004] M. Darques, A. Encinas-Oropesa, L. Villa and L. Piraux, J. Phys. D: Appl. Phys. **37** (2004) R1411-R1416.

[Dar2005] M. Darques et al, APL **86**, 072508-1 (2005).

[Deg2001] J. Degauque, Matériaux à Propriétés Magnétiques Dures: Matériaux industriels M4601 Techniques de l'Ingénieur, Paris (2001) p. 1.

[DeL2009] J. De La Torre Medina, M. Darques, and L. Piraux, J. Appl. Phys. **106**, 023921 (2009).

[Dev1997] A.J. Devasahayam, K.R. MountÞeld, M.H. Kryder, IEEE Trans. Magn. 33 (1997) 2881.

[Die1991a] Diény, V. S. Speriosu, S. S. P. Parkin, B. A. Gurney, D. R. Wilhoit, and D. Mauri , Phys. Rev. B **43**, 1297 (1991).

[Die1991b] B. Dieny, V.S. Speriosu, S. Metin, S. S. P. Parkin, B. A. Gurney, P. Gaumart and D. R. Wilhoit, J. Appl. Phys. **69** 4774 (1991).

[Dir1926] P. A. M. Dirac, *On the Theory of Quantum Mechanics*, Proceedings of the Royal Society of London, Series A 112 (1926).

[Dob2009] A. N. Dobrynin, V. M. T. S. Barthem and D. Givord, APL **95**, 052511 (2009) .

[Dor1981] J. L. Dormann, Revue Phys. Appl. **16** (1981) 275-301.

[Dür2009] T. Dürr et al., IEEE Trans. Magn., vol. 45, N°1 (2009).

[Dut2008] D.P. Dutta, G. Sharma, A.K. Tyagi, S.M. Yusuf, Nanotechnology **19**, 245609 (2008).

[Eft2005] E. Eftaxias and K.N. Trohidou, Phys. Rev. B **71**, 134406 (2005).

[Enc2001] A. Encinas-Oropesa, M. Demand, L. Piraux, I. Huynen and U. Ebels, Phys. Rev. B **63**, 104415 (2001).

[Esc2007] J. Escrig, M. daub, P. Landeros, K. Nielsch and D. Altbir, Nanotechnology **18** (2007) 445706.

[FaL1966] R. B. Falk, J. Appl. Phys. **37**, R1108 (1966).

[Fer2003] E. Ferain and R. Legras, Nucl. Instrum. Methods Phys. Res. B **208**, 115 (2003).

[Fié1989] F. Fiévet, J. P. Lagier, B. Blin, B. Beaudoin and M. Figlarz, Sol. St. Ion. **32**, 3 (1989) 198-205.

[Fig] M. Figlarz, F. Fiévet, J. P. Lagier, Europe n°0113281; USA n°4539041.

[Fis2007] T. Fischbacher, M. Franchin, G. Bordignon and H. Fangohr, IEEE Trans. Mag. **43**, 2896 (2007).

[Fru2002] O. Fruchart, P.- O. Jubert, C. Meyer, M. Klaua, J. Barthel and J. Kirschner, J. Magn. Magn. Mater. **239** (2002) 224-227

[Fru2005] O. Fruchart and A. Thiaville, C. R. Physique 6 (9) (2005).

[Fru2007] O. Fruchart, Techniques de l'Ingénieur, Dossiers NM 1 201 et 202 (2007).

[Ful1972] E. Fulcomer and S. H. Charap, J. Appl. Phys. **43**, 4184 (1972).

[Fur1989] R. C. Furneaux et al, Nature **337**, 147 (1989).

[Gal2005] D. Gallant and S. Simard, Corr. Sci. **47**, 1810 (2005).

[Gan1992] S. Gangopadhyay, G.C. Hadjipanayis, C.M. Sorensen, K.J. Klabunde, IEEE Trans. Magn. **28** (1992) 3174.

[Gan1993] S. Gangopadhyay, G.C. Hadjipanayis, C.M. Sorensen and K .J. Klabunde, J. Appl. Phys. **73**, 6964 (1993).

[Gao2008] C.L. Gao, A. Ernst, G. Fischer, W. Hergert, P. Bruno, W. Wulfhekel, and J. Kirschner , Phys. Rev. Lett. **101**, 167201 (2008).

[Gau1986] P. Gaunt, J. Appl. Phys. **59**, 4219 (1986).

[Gib1985] D. Gibbs, D. E. Moncton, K. L. D'Amico, J. Bohr, and B. H. Grier , Phys. Rev. Lett 55, 234 (1985).

[Gla1982] O. Glatter and O. Kratky, Small-Angle X-ray Scattering, Academic Press, London (1982).

[Gla1982] O. Glatter and O. Kratky, Small-Angle X-ray Scattering, Academic Press, London (1982).

[Gla2001] H. Glättli, *La diffusion de neutrons aux petits angles*, J. Phys. IV France **11** (2001).

[Gla1972] A. A. Glazer, A. P. Potapov, R. I. Tagirov, Sov. Phys. JETP. Lett. **15** (1972) 259.

[Gol1999] A. Goldoni, A. Baraldi, G. Comelli, S. Lizzit and G. Paolucci, Phys. Rev. Lett. **82**, 3156 (1999).

[Gou1926] S. Goudsmit and G.E. Uhlenbeck, Physica **6** (1926) 273.

[Gri2007a] N. A. Grigoryeva, S. V. Grigoriev, H. Eckerlebe, A. A. Eliseev, A. V. Lukashin and A. S. Vyacheslavov, Physica **B** 397 (2007) 82–84.

[Gri2007b] Grigorieva et al, J. Appl. Cryst. **40** (2007) 532.

[Gri2008] I. Grillo, Small-Angle neutron scattering and applications in soft condensed matter, Springer-Verlag, Berlin Heidelberg (2008).

[GruPat] P. Grünberg, US Patent N° 4949039.

[Gri2003] M. Grimsditch, A. Hoffmann, P. Vavassori, Hongtao Shi and D. Lederman, Phys. Rev. Lett. **90**, 257201 (2003).

[Gru1986] P. Grunberg, R. Schreiber, Y. Pang, M.B. Brodsky, and H. Sowers., Phys. Rev. Lett. **57**, 2442 (1986).

[Gru2000] M. Gruyters and D. Riegel, Phys. Rev. B **63**, 052401 (2000).

[Gru2007] M. Gruyters, Europhys. Lett. **77**, 57006 (2007).

[Gui1939] A. Guinier, Ann. Phys. Paris **12** (1939) R161-R237.

[Gui1955] A.Guinier and G. Fournet, *Small Angle Scattering of X-Rays*, Wiley, New-York (1955).

[Gut2000] O. Gutfleisch, J. Phys. D 33 (2000) R157.

[Har1992] K. Haraaguchi, T. Katsuyama, K. Hiruma and K. Ogawa, Appl. Phys. Lett. **60** (1992).

[Hei1926] W. Heisenberg, *Mehrkörperproblem und Resonanz in der Quantenmechanik*, Zeitschrift für Physik **38** (1926) R411-426.

[Her] Neutron and Synchrotron Radiation for Condensed Matter Studies, Vol. 1, Cours de l'école HERCULES (Higher European Research Course for Users of Large Experimental Systems) Ed. J. Baruchel, J. L. Hodeau, M.S. Lehmann, J. P. Regnard et C. Shlenker, Les éditions de physique/Springer Verlag (1993).

[Her2002] R. Hertel, J. Magn. Magn. Mater. **249** (2002) 251-256.

[Her2005] R. Hertel et al., Phys. Rev. B **72**, 214409 (2005).

[Hoe2009] M. Hoesch, A. Bosak, D. Chernyshov, H. Berger, and M. Krisch,Phys. Rev. Lett. **102**, 086402 (2009).

[Hou2000] C. Hou, H. Fujiwara, K. Zhang, A. Tanaka, and Y. Shimizu, Phys. Rev. B **63**, 024411 (2000).

[Hua1998] L. Huang, S. Jay Chey and J. H. Weaver, Phys. Rev. Lett. **80**, 4095 - 4098 (1998).

[Igl2008] O. Iglesias, A. Labarta and X. Battle, J. Nanosci. Nanotechnol.,**8**,6 (2008).

[Ind2008] S. E. Inderhees, J. A. Borchers, K. S. Green, M. S. Kim, K. Sun, G. L. Strycker and M. C. Aronson, Phys. Rev. Lett.. **101**, 117202 (2008).

[Jam2001] M. Jamet, W. Wernsdorfer, C. Thirion, D. Mailly, V. Dupuis and P. Mélinon, Phys. Rev. Lett. **86** (2001) 4676.

[Jau2001] W. Jauch, M. Reehuis, H.J. Bleif and F. Kubanek, Phys. Rev. B **64**, 052102 (2001).

[JCPD] JCPDS file n° 00-048-1719.

[Jes1998] O. Jessensky, F. Müller and U. Gösele, Appl. Phys. Lett. **72** (1998) 1173-1175.

[Jou2009] N. Jouault, P. Vallat, F. Dalmas, S. Said, J. Jestin and F. Boué, Macro-molecules **42** (2009) 2031-2040.

[Juh2005] R. Juhasz, N. Elfström and J. Linros, Nano. Lett. **5** (2005) R275-280.

[Jun1994] R. Jungblut, R. Coehoorn, M.T. Johnson, J. aan de Stegge, A. Reinders, J. Appl. Phys. **75** (1994) 6659.

[Kho2009] X. Khou, X. Fan, H. Zhu and J. Q. Xiao, APL **94**, 112509 (2009).

[Kne1962] E. Kneller, Ferromagnetismus (Berlin, Springer, 1962).

[Kno2008] M. Knobel, W. C. Nunes, L. M. Socolovsky, E. De Biasi, J. M. Vargas, and J. C. Denardin, J. Nanosci. Nanotechnol. **8** (2008) R2836-R2857.

[Kno1989] G.F. Knoll and J. Wihley, *Radiation Detection and Measurement,* Academic Press, New-York (1989).

[Koo1996] J. C. S. Kools, IEEE Trans. Magn., Vol **32**, N° 4 (1996).

[Kra1934] H. A. Kramers, Physica **1**, 182 (1934).

[Lag2007] K. Lagrené and J. M. Zanotti, European Physical Journal - Special Topics **141** (2007) 261-265.

[Lag2008] K. Lagrené, Etude dynamique de polymères sous confinement quasi-uniaxial, Thèse de doctorat de l'université Paris-Sud Orsay (2008).

[Lah2006] M. Lahmani, C. Dupas and P. Houdy, Les nanosciences: Nanotechnologies et nanophysique, Editions Belin (2006).

[Lei2002] C. Leighton, H. Suhl, J. Nogués, M. J. Pechan, R. Compton and I. K. Schuller, J. Appl. Phys. **92**, 1483 (2002).

[Lév1984] Jean-Marc Lévy-Leblond et Françoise Balibar, *Quantique, Rudiments*, InterEd-itions, Paris (1984).

[Li2007] D. Li, Q. He, Y. Cui, J. Li, Chem. Mater. **19** (2007) 412.

[Löf2005] J. F. Löffler, H. B. Braun, W. Wagner, G. Kostorz and A. Wiedenman, Phys. B. **71**, 134410 (2005).

[LuB1962] F.S. Luborsky, Electro-Technology (1962) 107.

[Lun2004] C. Luna , M. del Puerto Morales, C.J. Serna and M. Vazquez, Nanotechnology **15**, 293 (2004).

[Mal1974] M.G. Malbin, V.I. Saprykin, Phys. Met. Metall. **38** (1974) 63.

[Mal1987] A. P. Malozemoff, Phys. Rev. B **35**, 3679 (1987).

[Mar1994] C. R. Martin, Science **266**, 1961 (1994).

[Mar1996] C. R. Martin, Chem. Mater. **8**, 1739 (1996).

[Mas1995] H. Masuda and K. Fukuda, Science **268** (1995) 1466-1468.

[Mat2005] T. Matrab, M. M. Chehimi, C. Perruchot, A. Adenier, A. Guillez, M. Save, B. Charleux, E. Cabet-Deliry and J. Pinson, Langmuir **21** (2005) 4686.

[Mau2007] T. Maurer, F. Ott, G. Chaboussant, Y. Soumare, J.-Y. Piquemal and G. Viau, Appl. Phys. Lett. **91**, 172501 (2007).

[Mau2009] T. Maurer, F. Zighem, F. Ott, G. Chaboussant, G. André, Y. Soumare, J.Y. Piquemal, G. Viau and C. Gatel, Phys. Rev. B **80**, 064427 (2009).

[Mau1987] D. Mauri, H.C. Siegmann, P.S. Bagus, E. Kay, J. Appl. Phys. **62** (1987) 3047.

[Mau1987(2)] D. Mauri, E. Kay, D. Scholl and J. K. Howard, J. Appl. Phys. 62 (1987) R2929-2932.

[Mei1956] W.H. Meiklejohn, C.P. Bean, Phys. Rev. **102** (1956) 1413.

[Men1955] L. I. Mendelsohn, F. E. Luborsky, and T. O. Paine, J. Appl. Phys. **26**, R1274 (1955).

[Mei1957] W. H. Meiklejohn and C. P. Bean, Phys. Rev. **105**, 904 (1957).

[Mig2009] J. Miguel et al., J. Phys.: Condens. Matter. **21** (2009) 185004.

[Mul2003] C. Muller, *Diffraction des neutrons : principe, dispositifs expérimentaux et applications*, J. Phys. IV France **103** (2003).

[Nap2009] K.S. Napolskii et al., Physica B **404** (2009).

[Née1967] L. Néel, Ann. Phys. (France) **1** (1967) 61.

[Net] http://www.hpfem.jku.at/netgen/.

[Nie2001] K. Nielsch, R. B. Wehrspohn, J. Barthel, J. Kirschner, U. Gosele, S. F. Fischer and H. Kronmuller., Appl. Phys. Lett. **79**, N°9 (2001).

[Nie2002a] K. Nielsch, R. Hertel, R.B. Wehrspohn, J. Barthel, J. Kirschner, U. Gösele, S. F. Fischer and H. Kronmüller, IEEE Transactions on Magnetics **38**, N°5 (2002).

[Nie2002b] K. Nielsch, J. Choi, K. Schwirn, R. B. Wehrspohn and U. Gösele, Nanoletters **2** (7) (2002).

[Nis1996] K. Nishioka, C. Hou, H. Fujiwara, R.D. Metzger, J. Appl. Phys. 80 (1996) 4528.

[Nis1998] K. Nishioka, S. Shigematsu, T. Imagawa, and S. Narishige, J. Appl. Phys. **83**, 3233 (1998).

[Nmag] http://nmag.soton.ac.uk/nmag/.

[Nog1999] J. Nogues and I. K. Schuller, J. Magn. Magn. Mater. **192**, 203 (1999).

[Nog2005] J. Nogués, J. Sort, V. Langlais, V. Skumryev, S. Suriñach, J.S. Muñoz, M.D. Baró, Phys. Rep. **422**, 65 (2005).

[O'H2000] R. C. O'Handley, *Modern Magnetic Materials- Principles and Applications*, A Wiley-Interscience publication, New-York (1942).

[Oli1997] N.J. Oliveira, J.L. Ferreira, J. Pinheiro, A.M. Fernandes, O. Redon, S.X. Li, P. ten Berge, T.S. Plaskett, P.P. Freitas, J. Appl. Phys. **81** (1997) 4903.

[Ono1979] F. Ono and O. Yamada, J. Phys. Soc. Jap. **46**, 462 (1979).

[Ono1980] F. Ono, J. Phys. Soc. Jap. **50**, 2564 (1980).

[Ons1944] L. Onsager, Phys. Rev. **65**, 117-149 (1944).

[Ott2009] F. Ott, T. Maurer, G. Chaboussant, Y. Soumare, J.-Y. Piquemal and G. Viau, J. Appl. Phys. ***105***, 013915 (2009).

[Paj2007] D. Pajic, K. Zadro, R. Ristic, I. Zivkovic, Z. Skoko, E. Babic, J. Phys.: Cond. Matter **19**, 296207 (2007).

[Pap2002] P.Papon, J. Leblond and P. H. E. Meijer, Physique des Transitions de Phases, Dunod (2002).

[Par2002] W. I. Park, D. H. Kim, S. W. Jung and G. C. Yi, Appl. Phys. Lett. 80, 22 (2002).

[Pen2000] D. L. Peng, K. Sumiyama, T. Hihara, S. Yamamuro, and T.J. Konno, Phys. Rev. B **61**, 3103 (2000).

[Per1997] A. Perez, P. Malinon, V. Dupuis, P. Jensen, B. Prevel, J. Tuaillon, L. Bardotti, C. Martet, M. Treilleux, M. Broyer, M. Pellarin, J.L. Vialle, B. Palpant and J. Lerme, J. Phys. D: Appl. Phys. **30** (1997) 709-721.

[Qi2000] S. R. Qi, X. T. Huang, Z. W. Gan, X. X. Ding and Y. Cheng, J. Cryst. Growth **219** (2000) R485-R488.

[Rab2003] O. Rabin et al, Adv. Funct. Mater. 13, 631 (2003).

[Rad2007] F. Radu and H. Zabel, arXiv:0705.2055v (2007).

[Rad2008] F. Radu and H. Zabel, Magn. Heterostruct. **227**, 97 (2008).

[Ram1997] R. Ramirez, M. Kiwi, D. Lederman, Bull. Am. Phys. Soc. **42** (1997) 445.

[Rau1986] C. Rau, C. Liu, A. Schmalzbauer and G. Xing, Phys. Rev. Lett. **57**, 2311 (1986).

[Rav2006] Sylvain Ravy, Cours "Structure de la Matière Condensée" du master M2 de Physique de la Matière Condensée de l'Ecole Doctorale de physique de la région parisienne (2006). *http://www.lps.u-psud.fr/Utilisateurs/ravy/*.

[Rep2002] V. Repain, G. Baudot, H. Ellmer and S. Rousset, Europhys. Lett. **58**, 730 (2002).

[Rou2001] Y. Roussigné, S. M. Chérif, C. Dugautier, and P. Moch, Phys. Rev. B **63**, 134429 (2001).

[Roy2005] S. Roy, S. S. Yu, E. Henestroza, A. Anders, F. M. Bieniosek, J. Coleman, S. Eylon, W. G. Greenway, M. Leitner, B. G. Logan, W. L. Waldron, D. R. Welch, C. Thoma, A. B. Sefkow, E. P. Gilson, P. C. Efthimion, and R. C. Davidson , Phys. Rev. Lett. **95**, 047201 (2005).

[Roy2007] S. Roy, C. Sanchez-Hanke, S. Park, M. R. Fitzsimmons, Y. J. Tang, J. I. Hong, David J. Smith, B. J. Taylor, X. Liu, M. B. Maple, A. E. Berkowitz, C.-C. Kao, and S. K. Sinha, Phys. Rev. B **75**, 014442 (2007).

[Sal1976] N.M. Salansky, E.G. Khasanov, K.M. Mukimov, Sov. Phys. Solid State **17** (1976) 1865.

[Sal2005] V. Salgueirino-Maceira, M. A. Correa-Duarte and M. Farle, Small **1**, 11 (2005).

[San2003] S. Sanders, R. Gronsky, T. Sands and A. M. Stacy, Chem. Mater. 15, 335-339 (2003).

[San1974] Y.S. Sanoyan, K.A. Yegiyan, Phys. Met. Metall. **38** (1974) 231.

[Sca2000] V. Scarani, H. De Riedmatten and J.-Ph. Ansermet, Appl. phys. Lett. **76**, 903-905 (2000).

[Sch1951] C. G. Shull, W. A. Strauser and E. O.Wollan, Phys. Rev. **83**, 333 (1951). Note that the 2θ scales of Fig. 9 and 10 are not correct.

[Sch2003] J. Schweizer, *Neutrons et matériaux: introduction*, J. Phys. IV France **103** (2003).

[Sel2000] D. J. Sellmyer, M. Zheng, and R. Skomski, J. Phys.: Condens. Matter **13**, (2000) R433.

[Sha1994] M. P. Sharrock, J. Appl. Phys. **76** (1994) 6413.

[Sko1999] R. Skomski and J. M. D. Coey, *Permanent Magnetism*, Institute of Physics Publishing, Bristol and Philadelphia (1999).

[Sko2000] R. Skomski, H. Zeng, M. Zheng and D.J. Sellmyer, Phys. Rev. B **62**, N°6 (2000).

[Sko2002] R. Skomski, H. Zeng, and D.J. Sellmyer, JMMM **249** (2002) 175-180.

[Sku2003] V. Skumryev, S. Stoyanov, Y. Zhang, G. Hadjipanayis, D. Givord and J. Nogues, Nature **43**, 850 (2003).

[Sno2008] E.Snoeck, C. Gatel, L.M. Lacroix, T. Blon, S. Lachaize, J. Carrey, M. Respaud and B. Chaudret, Nanolett. **8**, 4293 (2008).

[Soul2009] K. Soulantica, F. Wetz, J. Maynadié, A. Falqui, R.P. Tan, T. Blon, B. Chaudret and M. Respaud, Appl. Phys. Lett **95**, 152504 (2009).

[Sou2008] Y. Soumare, J.-Y. Piquemal, T. Maurer, F. Ott, G. Chaboussant, A. Falqui and G. Viau , J. Mater. Chem. **18**,1-8 (2008).

[Sou2009a] Y. Soumare, C. Garcia, T. Maurer, G. Chaboussant, F. Ott, F. Fiévet, J.-Y. Piquemal and G. Viau, Adv. Func. Mater. **19,** 1-7 (2009).

[Sou2009b] Y. Soumare, Thèse de l'Université Paris 7 (2009).

[Spe] http://www-llb.cea.fr/prism/programs/spectraprocessor/spectraprocessor.htm.

[Sta2000] R. L. Stamps, J. Phys. D: Appl. Phys. **33** R247 (2000).

[StP2001] T.G. St. Pierre, N.T. Gorham, P.D. Allen, J.L. Costa-Krämer, K.V. Rao, Phys. Rev. B **65**, 024436 (2001).

[Str1999] Strbac, O. M. Magnussen, and R. J. Behm, Phys. Rev. Lett. **83**, 3246 (1999).

[Sun2000] Sun, C. B. Murray, D. Weller, L. Folks and A. Moser, Science **287** , 1989 (2000).

[Tak1997] K. Takano, R.H. Kodama, A.E. Berkowitz, W. Cao, G. Thomas, Phys. Rev. Lett. **79** (1997) 1130.

[Tan2007] R. P. Tan, J. Carrey, C. Desvaux, J. Grisolia, P. Renaud, B. Chaudret and M. Respaud, Phys. Rev. Lett. **99** (2007) 176805.

[Tan1984] C. Tang, J. Appl. Phys. **55** (1984) 2226.

[Tan1961] P. E. Tannenwald and R. Weber, Phys. Rev. **121**, 715 (1961).

[Tar2005] E. Tartakovskaya, Phys. Rev. B **71**, 180404 (2005).

[Tar2006] E. Tartakovskaya, Phys. Rev. B **73**, 092415 (2006).

[Thi1998] A. Thiaville, J. Magn. Magn. Mater. **182** (1998) 5-18.

[Thi2000] A. Thiaville, Phys. Rev. B **61**, 18 (2000).

[Thi2002] C. Thirion, W. Wernsdorfer, M. Jamet, V. Dupuis, P. Melinon, A. Perez, and D. Mailly, J. Magn. Magn. Mater. **242-245** (2002) R993-995.

[Tom2004] K. Tomiyasu, T. Inami and N. Ikeda, Phys. Rev. B **70**, 184411 (2004).

[Tom2006] A. Tomou, D. Gournis, I. Panagiotopoulos, Y. Huang, G. C. Hadjipanayis, and B. J. Kooi, J. Appl. Phys. **99**, 123915 (2006).

[Uhl1925] G.E. Uhlenbeck and S. Goudsmit, Naturwissenschaften **47** (1925) 953.

[Uhl2004] W. C. Uhlig and J. Shi, Appli. Phys. Lett. **84**, N°5 (2004).

[Ung2005] D. Ung, G. Viau, C. Ricolleau, F. Warmont, P. Gredin, and F. Fiévet, Adv. Mater., **17**, 338(2005).

[Ung2005b] D. Ung, G. Viau, F. Fiévet-Vincent, F. Herbst, V. Richard and F. Fiévet, Progr. Sol. St. Chem. **33** (2005) 137-145.

[UngPhD] D. Ung, thèse de l'Université Paris 7 (2005).

[Ung2007] D. Ung, Y. Soumare, N. Chakroune, G. Viau, M.-J. Vaulay, V. Richard and F. Fiévet, Chem. Mater., **19**, 2084(2007).

[Uso1994] N. A. Usov and S. E. Peschany, JMMM ***130*** (1994) 275-287.

[VAC] http://www.vacuumschmelze.de, manufactor of the Croval permanent magnets.

[VdZ2000] P. J. van der Zaag, Y. Ijiri, J. A. Borchers, L. F. Feiner, R. M.Wolf, J. M. Gaines, R. W. Erwin and M. A. Verheijen, Phys. Rev. Lett. **84**, 6102 (2000).

[Vaz2004] M. Vazquez, M. Hernández-Vélez, K. Pirota, A. Asenjo, D. Navas, J. Velázquez, P. Vargas and C. Ramos , Eur. Phys. J. B **40**, 489-497 (2004).

[Via1996] G. Viau, F. Fiévet-Vincent,F. Fiévet, Solid State Ionics **84** (1996) 259.

[Via2009] G. Viau, T. Maurer, F. Ott, G. Chaboussant, Y. Soumare, J.- P. Piquemal and F. Schoenstein, High temperature magnetism of Co nanorods and $Co_{80}Ni_{20}$ nanowires, Proceedings of the Joint Europen Magnetic Symposia 2008, submitted to J. Magn. Magn. Mater.

[Wan2002]] Z. K. Wang, M. H. Kuok, S. C. Ng, D. J. Lockwood, M. G. Cottam, K. Nielsch, R. B. Wehrspohn and U. Gosele, Phys. Rev. Lett. **89** , 027201 (2002).

[Wan2007] C. Wang, Y. Hou, J. Kim, and S. Sun, Angew. Chem., Int. Ed. **46** (2007), R1.

[Wan2008] T. Wang, Y. Wang, Y. Fu, T. Hasegawa, H. Oshima, K. Itoh, K. Nishio, H. Masuda, F.S. Li, H. Saito and S. Ishio, Nanotechnology **19** (2008) 455703.

[Wan2009] T. Wang, Y. Wang, Y. Fu, T. Hasegawa, F. S. Li, H. Saito and S. Ishio, Nanotechnology **20** (2009) 105707.

[War1990] B. E. Warren, X-ray Diffraction, Dover Publications, New York, 1990, p. 298.

[Whi1996] S. R. White, Phys. Rev. B. **53**, 52 (1996).

[Woh1984] E.P. Wohlfarth, J. Phys. F: Met. Phys. **14**, L155 (1984).

[Wu1994] S. C. Wu, K. Garrison, A. Begley, F. Joan and P. Johnson, Phys. Rev. B **49**, 14081 (1994).

[Wu2001] Y. Wu and P. Yang, J. Am. Chem. Soc. **123** (2001) 3165-3166.

[Xu2000] D.S Xu, Y.J. Xu, D. P. Chen, G. Guo, L. Gui and Y. Tang, Adv. Mater. **12**, 520 (2000).

[Zac2000] M. Zach, Science 290, 2120-2123 (2000).

[Zak1971] Y.V. Zakharov, V.A. Ignatchenko, Sov. Phys. JETP **32** (1971) 517.

[Zen1954] C. Zener, Phys. Rev. **96**, 1335 (1954).

[Zen2000] H. Zeng, M. Zheng, R. Skomski, D.J. Sellmeyer, Y. Liu, L. Menon and S. Bandyopadhay, J. Appl. Phys. **87**, 4718 (2000).

[Zen2002] H. Zeng, R. Skomski, L. Menon, Y. Liu, S. Bandyopadhyay and D. J. Sellmeyer, Phys. Rev B **65**, 134426 (2002).

[Zha2008] J. Zhang, V. Sessi, C. H. Michaelis, I. Brihuega, J. Honolka, K. Kern, R. Skomski, X. Chen, G. Rojas, and A. Enders, Phys. Rev. B **78**, 165430 (2008).

[Zhe2000] M. Zheng, L. Menon, H. Zeng, Y. Liu, S. Bandyopadhyay, R.D. Kirby and D. J. Sellmayer, Phys. Rev. B **62**, 12282 (2000).

[Zig] F. Zighem and C. Gatel, to be published.

PUBLICATIONS ET COMMUNICATIONS

PUBLICATIONS

Publications dans des revues internationals à comité de lecture:

1. *Magnetic nanowires as permanent magnets.*
   T. Maurer, F. Ott, G. Chaboussant, Y. Soumare, J-Y. Piquemal and G. Viau, Appl. Phys. Lett. **91**, 172501 (2007)
   Sélectionné dans *Virtual Journal of Nanoscale Science & Technology 16(19) (Nov. 5, 2007 issue), www.nanotechweb.org*

2. *Oriented magnetic nanowires with high coercivities.*
   Y. Soumare, J.-Y. Piquemal, T. Maurer, F. Ott, G. Chaboussant, A. Falqui and G. Viau, J. Mater. Chem. **18** (2008) 5696 – 5702

3. *Effects of the shape of elongated magnetic particles on the coercive field.*
   F. Ott, T. Maurer, G. Chaboussant, Y. Soumare, J-Y. Piquemal and G. Viau, J. Appl. Phys. **105**, 013915 (2009)

4. *Kinetically controlled synthesis of hexagonally close-packked cobalt nanorods with high magnetic coercivit*y.
   Y. Soumare, C. Garcia, T. Maurer, G. Chaboussant, F. Ott, F. Fiévet, J-Y. Piquemal and G. Viau , Advanced Functional Materials **19** (2009) 1-7

5. *Exchange-Bias in Co1-xNix/CoO core-shell nanowires: role of the antiferromagnetic superparamagnetic fluctuations.*
   T. Maurer, F. Zighem, F. Ott, G. Chaboussant, G. André, Y. soumare, J-Y. Piquemal, G. Viau and C. Garcia, Phys. Rev. B **80**, 064427 (2009)

Papiers de conference avec comité de lecture:

1. G. Viau, C. Garcia, T. Maurer, G. Chaboussant, F. Ott, Y. Soumare and J-Y. Piquemal, Physica Status Solidi A, **206,** N°4, 663 (2009)
   International Workshop on Magnetic Wires, 9-10 Mai 2008, Zumaia, Spain.

CONFERENCES INTERNATIONALES

Communications orales:

1. 11th Joint MMM-Intermag Conference, Washington (Etats-Unis) 18-22 Janvier
   Magnetic configurations of iron nanocubes and Co nanowires studied by electron holography
   C. Gatel, E. Snoeck, E. Javon, L. Lacroix, T. Blon, J. Carrey, M. Respaud, S. Lachaize, B. Chaudret, G. Viau, T. Maurer, F. Zighem and F. Ott

2. PNSXM 2009 (Polarized Neutron and Synchrotron X-rays for Magnetism), Bonn (Allemagne), 2-5 Août 2009.
   Polarized Small Angle Neutron Scattering of Co nanowires.

T. Maurer, F. Zighem, G. Chaboussant, F. Ott, Y. Soumare, J-Y. Piquemal, G. Viau and L. Cagnon.

3. Nanomagnets 2009, Aussois (France), 29 Mars - 3Avril 2009
Exchange bias in CoNi nanowires.
T. Maurer, F. Zighem, G. Chaboussant, F. Ott, Y. Soumare, J-Y. Piquemal and G. Viau

4. JEMS 08 (Joint European Magnetic Symposium), Dublin (Irlande) 13-19 Septembre 2008
Role of the antiferromagnetic fluctuations in the exchange bias mechanism. Study on magnetic nanowires.
T. Maurer, G. Chaboussant, F. Ott, Y. Soumare, J-Y. Piquemal and G. Viau

5. JEMS 08, Dublin (Irlande) 13-19 Septembre 2008
Magnetic nanowires as permanent magnets.
T. Maurer, F. Ott, G. Chaboussant, Y. Soumare, J-Y. Piquemal and G. Viau

6. EPS-CMD (European Physical Society- Condensed Matter Division), Rome (Italie) 25-29 Août 2008
Coercivity drop in exchange biased Co nanowires induced by antiferromagnetic fluctuations.
T. Maurer, F. Ott, G. Chaboussant, Y. Soumare, J-Y. Piquemal and G. Viau

7. MRS Fall Meeting 2008, Boston (Etats-Unis), 1-5 Décembre 2008
Cobalt Rods and Dumbbells : Shape Control, Assembly and Hard Magnetic Properties.
<u>G. Viau</u>, C. Garcia, Y. Soumare, J.-Y. Piquemal, T. Maurer, G. Chaboussant, F. Ott

8. Particles 2008, Orlando (Etats-Unis), 10-13 Mai 2008
An easy procedure for the preparation of ferromagnetic cobalt nanorods via the polyol process: towards the formation of permanent magnets.
Y. Soumare, <u>J.-Y. Piquemal</u>, G. Viau, T. Maurer, F. Ott, G. Chaboussant et F. Fiévet.

9. International Workshop on Magnetic Wires, Zumaia (Espagne), 9-10 Mai 2008
Synthesis and Magnetic Properties of Cobalt Nanowires with High Coercivity.
<u>G. Viau</u>, C. Garcia, T. Maurer, G. Chaboussant, F. Ott, Y. Soumare et J.-Y. Piquemal.

Communications par affiche :

1. ICM 2009, Karlsruhe (Allemagne), 26-31 Juillet 2009
Exchange Bias in magnetic $Co_{1-x}Ni_x$ nanowires
T. Maurer, F. Ott, <u>G. Chabousssant</u>, F. Zighem, Y. Soumare, J.-Y. Piquemal et G. Viau .

2. ICMFS, Berlin (Allemagne), 20-24 Juillet 2009
Dipolar magnetic interactions in arrays of ferromagnetic nanowires: a micromagnetic study
<u>F. Zighem</u>, F. Ott, T. Maurer et G. Chaboussant

3. INTERMAG, Madrid (Espagne), 5-8 Mai 2008
   Synthesis and Magnetic Properties of Cobalt Nanowires with High Coercivity.
   <u>G. Viau</u>, Y. Soumare, J.-Y. Piquemal, T. Maurer, F. Ott et G. Chaboussant.

CONFERENCES NATIONALES

Communciations orales:

1. Congrès SFP 2009, Palaiseau, 6-10 juillet 2009.
   Exchange Bias dans des nanofils de CoNi.
   <u>T. Maurer</u>, F. Zighem, F. Ott, G. Chaboussant, Y. Soumare, J-Y. Piquemal and G. Viau

2. 17èmes Journées de la Diffusion Neutronique, La Grande Motte, 27-29 Mai 2009.
   Etude de nano-objets magnétiques $Co_{1-x}Ni_x$ anisotropes par diffusion de neutrons polarisés aux petits angles (DNPA).
   <u>T. Maurer</u>, F. Zighem, G. Chaboussant, F. Ott, Y. Soumare, J-Y. Piquemal, G. Viau and L. Cagnon.

3. 9èmes journées francophones des jeunes physico-chimistes, 2-5 Octobre 2007, Maubuisson (Gironde), France.
   Synthèse et propriétés magnétiques des nanoparticules anisotropes
   <u>Y.Soumare</u>, G. Viau, J-Y. Piquemal, T. Maurer, F. Ott et G. Chaboussant

Communications par affiche :

1. Colloque Louis Néel, Albé, 30 Mars – 2 Avril 2010
   ExchangeBias dans des nanofils Co/CoO.
   <u>T. Maurer</u>, F. Zighem, G. Chaboussant, F. Ott, , Y. Soumare, J-Y. Piquemal and G. Viau

2. J3N, Journées Nationales en Nanosciences et Nanotechnologies, 21-23 Octobre 2009, Toulouse, France.
   Elaboration d'aimants permanents haute-température à base de nanofils organisés par une approche bottom-up.
   G. Viau, T. Maurer, <u>F. Zighem</u>, F. Ott, G. Chaboussant, J.-Y. Piquemal, F. Fiévet, Y. Soumare, N. Jouini, F. Schoenstein et C. Gatel.

3. Colloque Louis Néel, La Grande Motte, 1er-3 Octobre 2008
   Rôle des fluctuations antiferromagnétiques dans le phénomène d'exchange bias. Etude sur des nanofils magnétiques.
   <u>T. Maurer</u>, G. Chaboussant, F. Ott, , Y. Soumare, J-Y. Piquemal and G. Viau

4. 16èmes Journées de la diffusion neutroniques, Albé, 28-30 Mai 2008
   Etude de nano-objets magnétiques $Co_{1-x}Ni_x$ anisotropes par diffusion de neutrons polarisés
   <u>T. Maurer</u>, G. Chaboussant, F. Ott, Y. Soumare and G. Viau

5. Colloque Louis Néel, Lyon, 14-16 Mars 2007
   Etude de nano-objets magnétiques $Co_{1-x}Ni_x$ anisotropes par diffusion de neutrons polarisés.
   T. Maurer, G. Chaboussant, F. Ott, G. Viau, Y. Soumare and J-Y. Piquemal.

6. J3N, Journées Nationales en Nanosciences et Nanotechnologies, 20-22 Octobre 2008, Grenoble, France.
   Elaboration d'aimants permanents haute-température à base de nanofils organisés par une approche bottom-up.
   J.-Y. Piquemal, Y. Soumare, F. Fiévet, G. Viau, C. Garcia, T. Maurer, F. Ott, G. Chaboussant, N. Jouini et F. Schoenstein.

Magnetism of individual nano-objects is a very active research field thanks to the development of original synthesis routes and investigation tools. This thesis aims at probing the magnetism of nanowires synthesized via a pure chemical route, the polyol process. This process provides a large variety and an excellent crystallinity of the synthesized nanowires. This process allows to tune the diameter of the nanowires from 7nm to 20nm leading to coherent magnetization reversal in the nanowires. I show how the large shape and magnetocrystalline anisotropies provide large coercivities compared to magnetic nanowires synthesized via other routes. Furthermore, the oxidation of such objects has also been investigated. Magnetic measurements has revealed unsual temperature dependencies of both the coercive and exchange fields, emphasizing the role of the superparamagnetic fluctuations of the CoO antiferromagnetic grains in the Exchange Bias effect. Finally, this thesis also aims at developing Polarized Small Angle Neutron Scattering to probe magnetism in complex nano-objects. Such a technique has been ignored until now to study magnetic anisotropic nano-objects despite being well adapted. The key ingredient to carry through such a study is the perfect alignment of the nanowires. This is why, besides the nanowires synthesized via the polyol process, Polarized Small Angle neutron Scattering measurements have been performed on arrays of magnetic nanowires included in porous alumina membranes.

Key words: nanomagnetism, nanowire, Exchange Bias, permanent magnets, Polarized Small Angle Neutron Scattering.

Le nanomagnétisme est actuellement un champ d'investigation très actif grâce aux développements de méthodes de synthèse et d'investigation originales. Cette thèse s'attache à sonder le magnétisme de nanofils magnétiques synthétisés par un procédé polyol. Ce procédé présente l'avantage de fournir un large éventail d'objets magnétiques anisotropes présentant une très bonne qualité cristalline. Les nanofils ainsi synthétisés présentent des diamètres variant de 7nm à 20nm, leur conférant un mode de renversement de l'aimantation cohérent. Cette thèse montre que les nanofils ainsi synthétisés ont des coercivités élevées comparées à celles de nanofils synthétisés par d'autres voies. Par ailleurs, les effets de l'oxydation de ces nanofils sur leurs propriétés magnétiques ont été étudiés. Les mesures magnétiques ont révélé une dépendance en température des champs d'échange et coercitif non reportée jusqu'à présent dans la littérature. Cela a permis de mettre en lumière le rôle prépondérant des fluctuations superparamagnétiques des grains antiferromagnétiques d'oxyde de cobalt dans le phénomène d'Exchange Bias. Enfin, cette thèse a aussi eu pour objectif de développer la technique de Diffusion de Neutrons Polarisés aux Petits Angles pour sonder le magnétisme de nanofils. Jusqu'à présent, cette technique a été surtout réservée à l'étude d'objets magnétiques isotropes. En effet, l'alignement des nanofils est crucial pour extraire des informations quantitatives d'une telle étude. C'est pour cela, qu'outre les nanofils synthétisés par procédé polyol, des nanofils inclus dans des matrices d'alumine poreuse ont aussi été étudiés par cette technique. Cette étude a ainsi montré la nécessité de prendre en compte le champ dipolaire- habituellement négligé- dans l'analyse des figures de diffusion.

Mots-clefs: nanomagnétisme, nanofil, Exchange Bias, aimants permanents, Diffusion de Neutrons Polarisés aux Petits Angles.